

Thesis submission for the qualification of Doctor rerum naturalium

---

# Modern Mass Spectrometry of Functional Molecules

## Moderne Massenspektrometrie Funktioneller Moleküle

---

by

**Jing Li**

*April 2013*

*Nanjing, China*

Physical Chemistry I

Department of Chemistry and Pharmacy

Friedrich-Alexander-University Erlangen-Nuremberg



# **Moderne Massenspektrometrie Funktioneller Moleküle**

Der Naturwissenschaftlichen Fakultät der Friedrich-Alexander-Universität Erlangen-  
Nürnberg  
zur Erlangung des Doktorgrades Dr. rer. nat.

2013

vorgelegt von

**Jing Li**

aus Nanjing, China

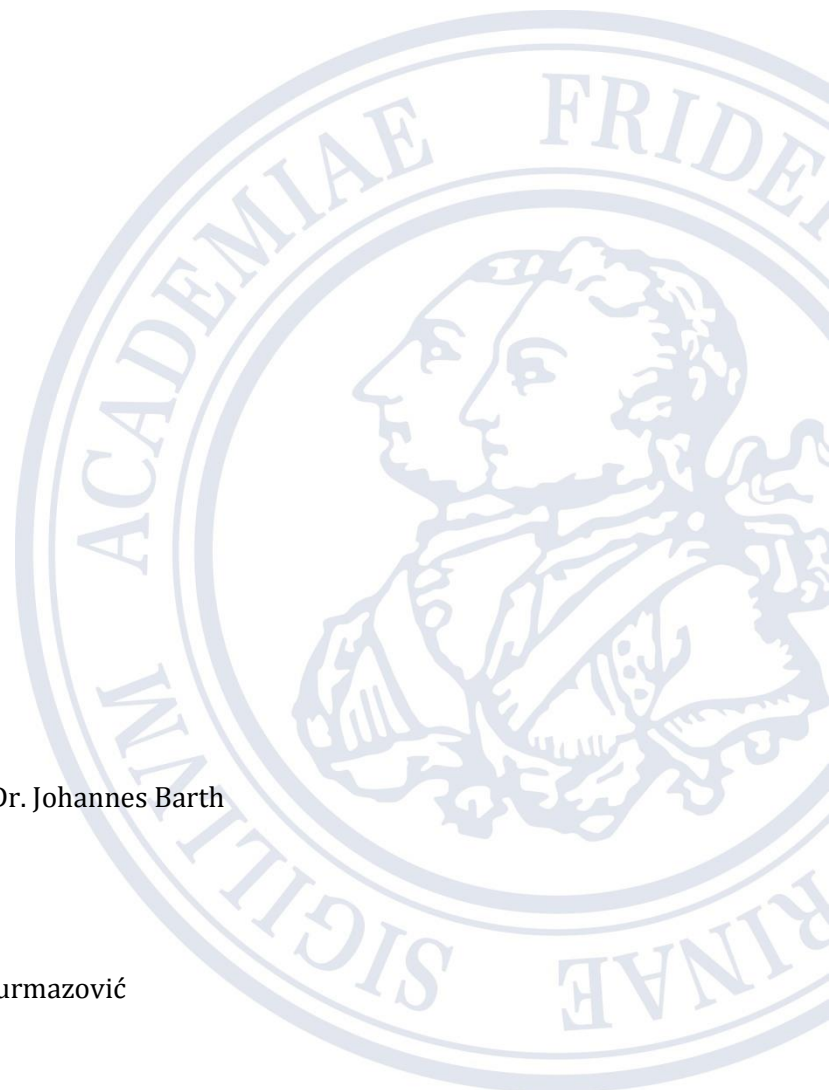
Als Dissertation genehmigt von der Naturwissenschaftlichen Fakultät  
der Friedrich-Alexander-Universität Erlangen-Nürnberg

Tag der mündlichen Prüfung: 20. Aug. 2013

Vorsitzender der Promotionskommission: Prof. Dr. Johannes Barth

Erstberichterstatter: Prof. Dr. Thomas Drewello

Zweitberichterstatter: Prof. Dr. Ivana Ivanović-Burmazović



## ACKNOWLEDGEMENT

First of all, I would like to express my sincere thanks to my supervisor, **Prof. Thomas Drewello**, for the doctoral opportunity in Germany and his academic guidance during my doctoral research period.

Special thanks to go our chair, **Prof. Dirk Guldi**, whose constant support of my work has been an essential component for the success of my research. I thank the whole Guldi group for the many inter-group collaborations.

The work with **Dr. Katharina Dürr** and **Prof. Ivana Ivanović-Burmazović** on the porphyrin-crown ether projects has been an enthusiastic and fruitful experience from which my first two publications resulted and which led to further investigation of porphyrins. I thank **Prof. Dr. Norbert Jux** for contributing many of his exciting porphyrin derivatives. Many interesting findings resulted from the generous access I had to the maXis-mass spectrometer provided by **Prof. Ivanović-Burmazović**, with many experience that were often conducted together with **Dr. Leanne Nye**.

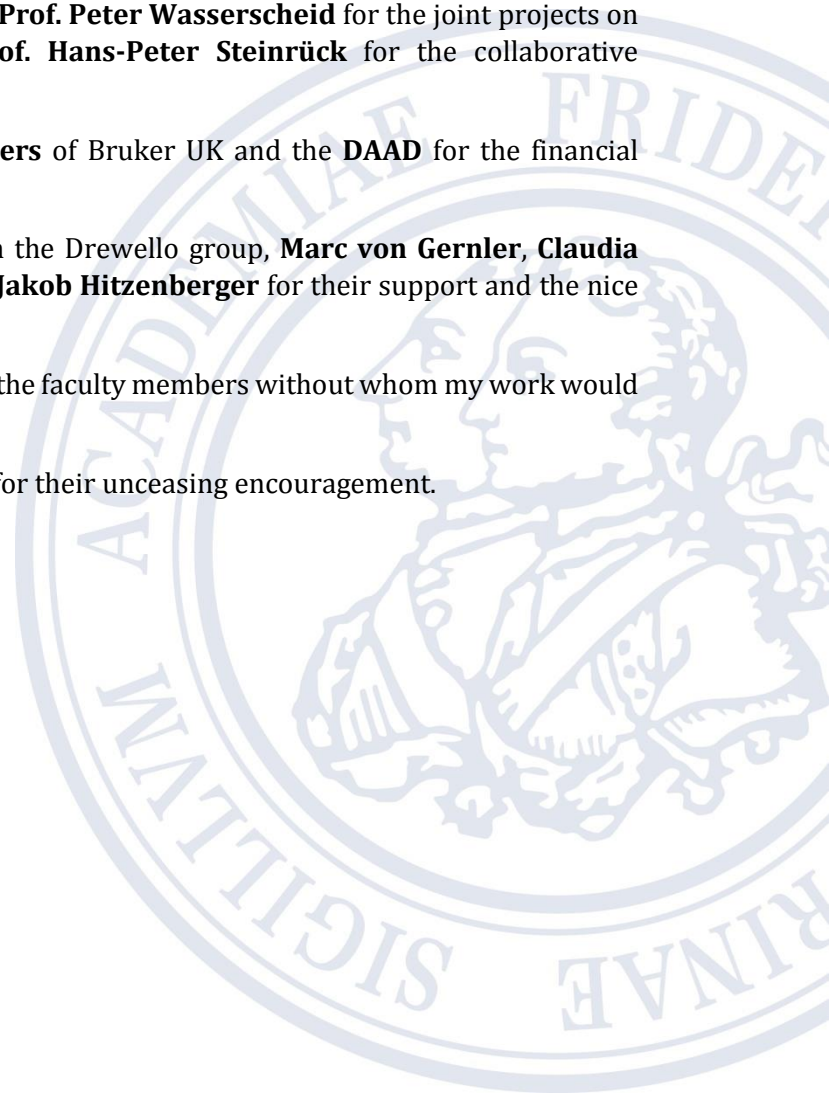
I share the credit of my work with **Wei Wei** and **Prof. Peter Wasserscheid** for the joint projects on ionic liquids and **Dr. Florian Maier** and **Prof. Hans-Peter Steinrück** for the collaborative investigations into the behavior of ionic liquids.

I am indebted to **John Kelly** and **Dr. Ian Sanders** of Bruker UK and the **DAAD** for the financial support through a matching fund stipend.

I owe my deepest gratitude to my colleagues in the Drewello group, **Marc von Gernler**, **Claudia Dammann**, **Rolf Kirschbaum**, **Ina Kellner** and **Jakob Hitzenberger** for their support and the nice working atmosphere.

I take this opportunity to record my thanks to all the faculty members without whom my work would have been a distant reality.

Last but not the least, I want to thank my family for their unceasing encouragement.





**In youth we learn,  
in age we understand.**

*Marie von Ebner-Eschenbach*

## TABLE OF CONTENT

---

List of Figures.....	I
List of Abbreviations .....	II
1 Introduction .....	1
1.1 Aims .....	1
1.2 Fundamentals of Ionisation .....	1
1.2.1 Gas Phase Ion Chemistry .....	1
1.2.2 Isotopes .....	1
1.2.3 Resolution in Mass Spectrometry .....	3
1.2.4 Ionisation Energies and Gas Phase Basicity .....	4
1.2.5 Electron Affinity and Gas Phase Acidity.....	5
1.2.6 Ionisation Methodology .....	6
1.2.7 Types of Analyzers .....	10
1.2.8 Tandem Mass Spectrometry .....	18
1.3 Nature of Investigated Compounds.....	22
1.3.1 Fullerene Derivatives.....	22
1.3.2 Ionic Liquids .....	26
1.3.3 Porphyrins.....	30
1.4 Instrumental.....	31
1.4.1 Esquire6000 (Bruker Daltonics).....	31
1.4.2 maXis (Bruker Daltonics).....	34
1.4.3 Axima Confidence (Shimadzu).....	35
2 Reference.....	38
3 Appendix.....	42

## LIST OF FIGURES

Figure 1-1: Isotopic pattern of the element chlorine. a) Simulated mass spectrum of the chloride anion and; b) Simulated mass spectrum of the chlorine cation. ....	3
Figure 1-2: 10% valley definition of resolution.....	4
Figure 1-3: Full Width at Half Maximum definition.....	4
Figure 1-4: Scheme of an ESI source.....	6
Figure 1-5: MALDI ionisation process.....	7
Figure 1-6: Scheme of a linear time-of-flight mass spectrometer (ToF-MS).....	11
Figure 1-7: Scheme of a reflectron ToF mass spectrometer.....	12
Figure 1-8: Schematic of a quadrupole ion trap mass analyzer.....	12
Figure 1-9: Potential surface for a quadrupole ion trap (QIT). ....	13
Figure 1-10: Mathieu stability regions for the ion trap. a) The stability regions corresponding to stable solutions in the $z$ direction. b) The stability regions corresponding to stable solutions in the $r$ direction. ....	14
Figure 1-11: Mathieu stability diagram in three dimensions. The overlapped regions are of stability in both $r$ - and $z$ -direction, labelled A and B. ....	15
Figure 1-12: Stability diagram of $(a_z, q_z)$ with the iso- $\beta_r$ and iso- $\beta_z$ lines. ....	16
Figure 1-13: Operating line of the QIT. a) Operating line with RF only; b) Operating line with RF and auxiliary frequency. ....	16
Figure 1-14: The Wahrhaftig diagram showing the relationship between internal energy and unimolecular ion decomposition for a hypothetical ion $ABCD^+$ .....	18
Figure 1-15: Post source decay (PSD) process in the linear mode.....	20
Figure 1-16: Post source decay (PSD) process in reflectron mode.....	20
Figure 1-17: Potentials applied in the different types of reflectrons. ....	21
Figure 1-18: Fullerene- $C_{20}$ .....	23
Figure 1-19: Fullerene- $C_{60}$ .....	23
Figure 1-20: Schlegel diagram of $C_{60}$ .....	23
Figure 1-21: Fullerene- $C_{70}$ .....	24
Figure 1-22: Schlegel diagramme of $C_{70}$ .....	24
Figure 1-23: $C_{60}$ -mono.....	25
Figure 1-24: $C_{70}$ -mono.....	25
Figure 1-25: Hydrogenated fullerene-2.....	25
Figure 1-26: Schlegel diagram of $C_{60}F_{48}$ ; (● = F).....	25
Figure 1-27: Open-cage fullerene OCF-1.....	26
Figure 1-28: Open-cage fullerene OCF-2.....	26
Figure 1-29: He@ $C_{60}$ .....	26
Figure 1-30: Sc $_3$ N@ $C_{80}$ - $D_{5h}$ .....	26
Figure 1-31: MALDI ionic liquid matrix: $\alpha$ -cyano-4-hydroxycinnamic acid (CHCA) and 1-methyl-imidazole.....	29
Figure 1-32: Structures of investigated porphyrins.....	30
Figure 1-33: Metalation of porphyrin complex.....	30
Figure 1-34: Photos of the Esquire6000.....	31
Figure 1-35: Schematic figure of Esquire6000.....	32
Figure 1-36: Electron amplifier through a serie of dynodes.....	33
Figure 1-37: Scheme of the maXis.....	34
Figure 1-38: Diagram of the MALDI-ToF instrument from Shimadzu AXIMA Confidence.....	36
Figure 1-39: Photo of a MALDI sample plate from Shimadzu.....	37

## LIST OF ABBREVIATIONS

---

<b>atm</b>	<b>Atmosphere</b>
<b>CID</b>	<b>Collision-Induced Dissociation</b>
<b>Da</b>	<b>Dalton (1Da= <math>1.6605402 \times 10^{-27}</math> kg)</b>
<b>DFT</b>	<b>Density Functional Theory</b>
<b>ESI</b>	<b>Electrospray Ionisation</b>
<b>eV</b>	<b>Electron Volt</b>
<b>FWHM</b>	<b>Full Width Half-height Maximum</b>
<b>Hz</b>	<b>Hertz</b>
<b>ISD</b>	<b>In Source Decay</b>
<b>kV</b>	<b>kilo Volt</b>
<b>LDI</b>	<b>Laser Desorption Ionisation</b>
<b>M</b>	<b>Molecular mass</b>
<b>MALDI</b>	<b>Matrix-Assisted Laser Desorption/Ionisation</b>
<b>maXis</b>	<b>A Bruker high-resolution mass spectrometer</b>
<b>MS</b>	<b>Mass Spectrum/ Mass Spectrometry</b>
<b>MS/MS (MS<sup>2</sup>)</b>	<b>Daughter Ion Mass Spectrum (Fragmentation)</b>
<b>m/z</b>	<b>Mass-to-charge ratio of an ion</b>
<b>M<sup>+</sup></b>	<b>Molecular Ion</b>
<b>MH<sup>+</sup></b>	<b>Protonated molecular ion</b>
<b>QIT</b>	<b>Quadrupole Ion Trap</b>
<b>Tandem-MS</b>	<b>Tandem Mass Spectrometry (= MS/MS)</b>
<b>Torr</b>	<b>1 Torr = 133.3224 Pa</b>
<b>PSD</b>	<b>Post Source Decay</b>
<b>ToF</b>	<b>Time-of-Flight</b>
<b>V</b>	<b>Volt</b>

# 1 INTRODUCTION

---

## 1.1 AIMS

---

The present PhD thesis comprises investigations into the gas phase behaviour of several novel compounds by modern mass spectrometry. The objectives of the work are the improvement of our understanding of the underlying ionisation mechanisms and fragmentation pathways. The research can be divided into four main parts, according to the investigated compound classes. These parts consist of 1.) fullerene derivatives; 2.) porphyrin complexes with different transition metals <sup>[1, 2]</sup>; 3.) novel ionic liquids <sup>[3, 4]</sup> and 4.) polycationic molecules.

The ion formation mechanisms are studied by electrospray ionisation (ESI) and matrix-assisted laser desorption / ionisation (MALDI) mass spectrometry, while the fragmentation behaviour of the resulting ions is examined by tandem mass spectrometry (MS/MS).

## 1.2 FUNDAMENTALS OF IONISATION

---

### 1.2.1 GAS PHASE ION CHEMISTRY

---

Ions in the gas phase are the main subject when the mass spectrometer is used as a reaction vessel. <sup>[5-9]</sup> Through the study of fragmentation pathways, mass spectrometry represents a powerful analytical tool to obtain structural information. In a mass spectrometer almost all processes occur under high vacuum conditions, as a result the chemistry of isolated ions in the elusive gas phase is sampled. For instance, the energy of an ion is mainly redistributed internally and not as it is in solution or the condensed phase through a partner or a chemical reaction. The gas phase ion may undergo unimolecular reactions such as isomerisation and fragmentation. This has been described by the *quasi-equilibrium theory* (QET), which has been developed as an adaptation of Rice-Ramsperger-Marcus-Kassel (RRMK) theory. Assumptions are made that the internal energy of an isolated ion is statistically distributed over the ion. Bond breaking of the weakest bonds occurs as a result of vibrational excitation. This monomolecular nature of the isolated ion has to be borne in mind throughout this study. <sup>[10]</sup>

### 1.2.2 ISOTOPES

---

Isotopes of an element consist of the same amount of protons but have a different number of neutrons in the nucleus, which provides them with a different mass and makes them distinguishable with a mass spectrometer. An ion composed of different elements provides an isotope pattern in the mass spectrum. This, in turn, can be used to establish the elemental composition of an unknown ion. The elemental composition of a compound is more reliably established when the accurate mass measurement is accompanied by the evaluation of the isotope pattern. As a consequence, it is also true that if the isotopic pattern can be established, the mass of an ion does not necessarily have to be determined with such a high accuracy in order to positively identify the composition of the ion.

The nominal mass of an isotope is given as a superscript at the upper left of the elemental symbol, e.g., <sup>12</sup>C and <sup>13</sup>C. The elements have been simply categorized by Gross into three groups of **monoisotopic elements**, **di-isotopic elements**, and **polyisotopic elements**, which are described in detail as follows. <sup>[11]</sup>

**MONOISOTOPIC ELEMENTS** exist in only one naturally stable isotope. For instance, fluorine ( $^{19}\text{F}$ ), sodium ( $^{23}\text{Na}$ ), phosphorus ( $^{31}\text{P}$ ) and iodine ( $^{127}\text{I}$ ) are prominently involved in organic mass spectrometry. However, there also exists monoisotopic metals, for instance: beryllium ( $^9\text{Be}$ ), aluminium ( $^{27}\text{Al}$ ) as well as some transition metals such as scandium ( $^{45}\text{Sc}$ ), manganese ( $^{55}\text{Mn}$ ), cobalt ( $^{59}\text{Co}$ ), rhodium ( $^{103}\text{Rh}$ ) and caesium ( $^{133}\text{Cs}$ ) etc. The elements of this group show the simplest pattern in the mass spectrum. While increasing complexity in the isotope pattern allows for an easier characterisation of an element or the elemental composition. Cluster ions of monoisotopic elements are often used to calibrate the mass scale of the mass spectrometer.

**DI-ISOTOPIC ELEMENTS** are elements which exist in two isotopes. These have been further sub-classified into *X+1 elements*, *X+2 elements* and *X-1 elements*. Carbon is the most prominent representative of the X+1 elements with an isotopic composition of  $^{12}\text{C}$  (100%) and  $^{13}\text{C}$  (1.08%). Among the X+2 elements, there often exists a very characteristic pattern, such as for chlorine ( $^{35}\text{Cl}$ -100%,  $^{37}\text{Cl}$ -31.96%), bromine ( $^{79}\text{Br}$ -100%,  $^{81}\text{Br}$ -97.28%), and silver ( $^{107}\text{Ag}$ -100%  $^{109}\text{Ag}$ -92.90%). The existence of two isotopes with high abundances often facilitates the interpretation of the mass spectrum, as a consequence of the resulting characteristic pattern. When the lighter isotope is of lower abundance than the heavier one with a mass difference of one Da, the element represents the X-1 form, such as lithium ( $^6\text{Li}$ -8.11%,  $^7\text{Li}$ -100%), boron ( $^{10}\text{B}$ -24.84%,  $^{11}\text{B}$ -100%), and vanadium ( $^{50}\text{V}$ -0.25%,  $^{51}\text{V}$ -99.75%).

The majority of elements are **POLYISOTOPIC ELEMENTS**. They are characterised by a complex isotope pattern with three or more isotopes. The isotopic classifications and isotopic compositions of some common elements are listed below (Table 1.1). A more detailed isotopic abundance table can be found at IUPAC.<sup>[12]</sup>

Table 1: Isotopic classifications and isotopic compositions of some common elements [IUPAC2001] <sup>[12]</sup>

Classification	Atomic Symbol	Atomic No.	Mass No.	Isotopic Composition	Isotopic Mass/[u]
<b>X-1</b>	Li	3	6	8.21	6.015122
			7	100	7.016004
	B	5	10	24.8	10.012937
			11	100	11.009306
<b>X</b>	Na	11	23	100	22.989769
	I	53	127	100	126.904468
<b>X+1</b>	C	6	12	100	12.000000
			13	1.08	13.003355
	N	7	14	100	14.003070
			15	0.369	15.000109
<b>X+2</b>	Cl	17	35	100	34.968853
			37	31.96	36.965903
	Br	35	79	100	78.918338
			81	97.28	80.916291
	Ag	47	107	100	106.905094
			109	92.90	108.904756

The isotope pattern reflects the distribution of stable isotopes of the elements within a chemical compound. Chlorine may function as an example; Figure 1-1.a shows a simulated mass spectrum for the chloride anion ( $\text{Cl}^-$ ) and Figure 1-1.b depicts the simulated mass spectrum of the chlorine cation ( $\text{Cl}_2^+$ ).

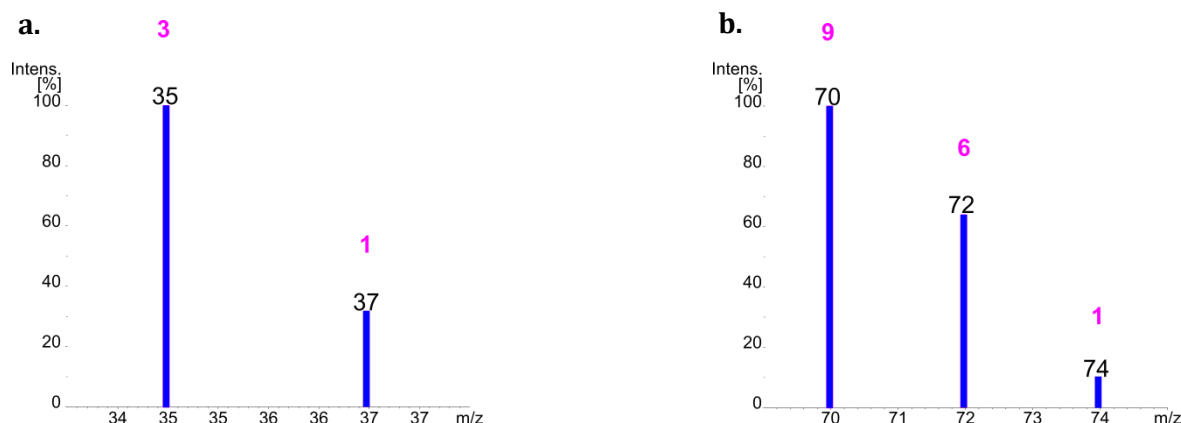


FIGURE 1-1: Isotopic pattern of the element chlorine. a) Simulated mass spectrum of the chloride anion and; b) Simulated mass spectrum of the chlorine cation.

The isotopic pattern of  $\text{Cl}^-$  is simply generated by the relative abundance (approximately 3:1) of the chlorine isotopes in nature, namely  $^{35}\text{Cl}$  (75.77%) and  $^{37}\text{Cl}$  (24.23%). However, when there is more than one chlorine atom present in the chemical formula, the isotopic pattern will also be affected by the amount of chlorine atoms in the ion. The chlorine cation ( $\text{Cl}_2^+$ ) as an example in Figure 1-1.b, shows the possible combinations of  $^{35}\text{Cl}$  and  $^{37}\text{Cl}$  atoms in a  $\text{Cl}_2^+$  ion as:  $[^{35}\text{Cl}^{35}\text{Cl}]^+$ ,  $[^{35}\text{Cl}^{37}\text{Cl}]^+$  and  $[^{37}\text{Cl}^{37}\text{Cl}]^+$  leading to the peaks, at m/z 70, m/z 72 and m/z 74. The ratio of 9:6:1 for the relative abundances of these ions is a consequence of the relative probability by which the different isotopes will contribute to the ions and is calculated by  $(a+b)^n$  with a:b representing the relative abundances of the isotopes (3:1 for chlorine) and n representing the number of chlorine atoms in the ion ( $n=2$  for  $\text{Cl}_2^+$ )

### 1.2.3 RESOLUTION IN MASS SPECTROMETRY

Two singly charged ion peaks of equal height in a mass spectrum at masses  $M$  and  $M + \Delta M$  separated by a valley which at its lowest point is just 10% of the height of either peak are considered resolved. The resolution ( $R$ ) of the mass spectrometer is generally defined as:

$$R = \frac{M}{\Delta M}$$

The value of  $\Delta M$  varies according to the different ways of defining resolution. One is called *the valley definition*, where  $\Delta M$  is equal to the peak width at 10% height of the maximum peak height, as shown in Figure 1-2.



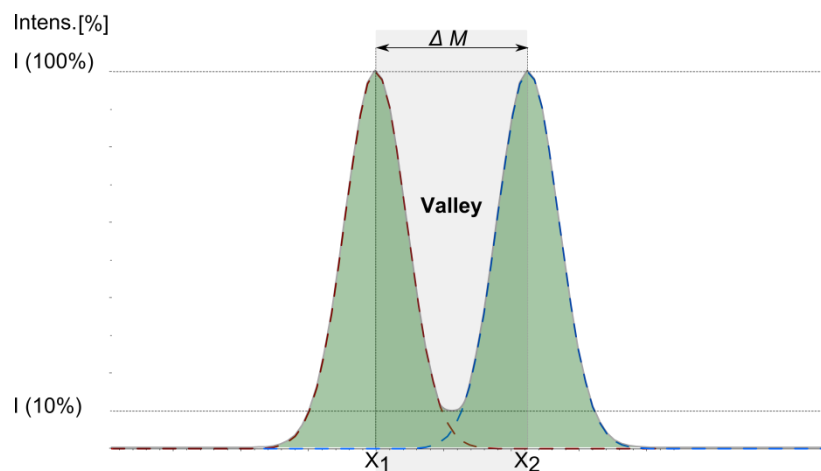


Figure 1-2: 10% valley definition of resolution

Another widely used definition of resolution is the *peak width definition*, where  $\Delta M$  equals to the peak width at a fraction of the maximum peak height. The most commonly used fraction is 50% and it is called Full Width at Half Maximum (FWHM), as shown in Figure 1-3.

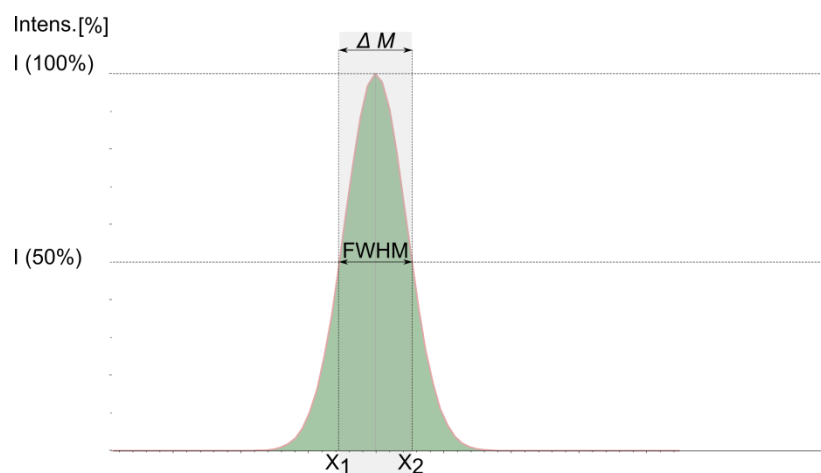
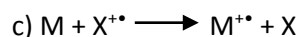
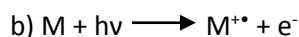
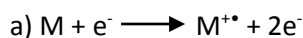


Figure 1-3: Full Width at Half Maximum definition

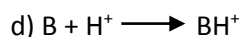
#### 1.2.4 IONISATION ENERGIES AND GAS PHASE BASICITY

Only ions can be detected by mass spectrometry, therefore, the formation of ions plays a significant role in the process of generating an informative mass spectrum. Positively charged ions can be produced by depleting electron(s) from the target molecule. A certain energy is needed for this process. The energy required for the removal of the  $n^{\text{th}}$  electron from a gaseous atom or molecule after  $n-1$  electrons have been removed is called the  $n^{\text{th}}$  ionisation energy (IE). The first ionisation energy is of enormous significance and for molecules, it refers to the energy required to stripe off an electron from the highest occupied molecular orbital (HOMO). In the periodic table of elements, the first ionisation energy shows periodicity, which means that the IE generally decreases when the atomic electron shell becomes bigger. Therefore, the general trend for ionisation energies is to increase across a period and to decrease down the same

group. Most values of the first IEs are in the range of 6-10 eV, which is approximately 580-970 kJ/mol. For hydrocarbons, the IEs of alkanes, alkenes, and alkynes increase with increasing chain length, whereas the IEs decrease when there are more branches present with a given elemental composition. The ionisation into a radical cation can be achieved in several ways. Besides the previously discussed electron ionisation (process *a*), it is also possible to ionise by photoionisation (process *b*), whereby the neutral interacts with light (photons) that possesses energies above the ionisation energies of the neutral *M*. Ionisation may also occur through interaction with a cation that possesses a recombination energy which is larger than the ionisation energy of the neutral *M* (Process *c*).



Besides the removal of electrons, another fundamental approach to produce cations is via protonation. The ability of neutrals to gain a proton to form stable cations can be described in two ways, namely, the gas-phase basicity (GPB) of *B* referring to the negative of the Gibbs free energy for reaction *d*) and the proton affinity (PA) which refers to the enthalpy of reaction *d*)<sup>[13]</sup>.



Therefore, often proton-releasing reagents (e.g. acids) are deliberately added to the ion source; however, the analytes have to possess higher proton affinities than the chosen reagents.

---

### 1.2.5 ELECTRON AFFINITY AND GAS PHASE ACIDITY

---

Electron affinity ( $E_{ea}$ ) is the energy gained by creating a negatively charged ion by adding an electron to the neutral as shown in reaction *e*). Whilst the removal of an electron from the neutral is linked to the ionisation energy; the addition of an electron to the neutral is linked to the electron affinity of the neutral. Both processes describe the opposite directions of the electron transfer process which lead to the formation of positive and negative ions.



The  $E_{ea}$  is defined as the negative value of the energy (enthalpy) of the electron attachment reaction *e*). If the electron attachment is accompanied by an energy release, a positive  $E_{ea}$  is obtained. The  $E_{ea}$  of most non-metals, especially of the halogens is highly positive, which characterizes the resulting anions as highly stable. Alkali metal atoms possess only small positive  $E_{ea}$  values. In the present study, the  $E_{ea}$  values of large organic/organometallic molecules are of interest, as these are the target molecules of the present investigations. Fullerenes and porphyrins, as the main representatives of the large molecular systems, normally possess large positive  $E_{ea}$  values and therefore often readily produce stable anions.

Additionally, when analytes are neutral Brønsted acids, the term gas phase acidities, referring to reaction *f*), must be discussed due to its great impact on ionisation methods such as chemical ionisation (CI), electrospray ionisation (ESI) and matrix-assisted laser desorption ionisation (MALDI).



### 1.2.6 IONISATION METHODOLOGY

ELECTROSPRAY IONISATION (ESI) is a crucial soft ionisation method in mass spectrometry that allows the transfer of ions from the liquid phase to the gas phase, thus it is of significant importance as close to half of chemical and biochemical processes involve ions in solution or in the solid state. Electrospray affords ion transfer of a wide variety of ions dissolved in a wide variety of solvents. Electrospray mass spectrometry was introduced by Yamashita and Fenn<sup>[14]</sup> in 1984. A very similar, independent development was reported at approximately the same time by Aleksandrov and co-workers<sup>[15]</sup>. However, it was actually proposed much earlier by Dole<sup>[16, 17]</sup> that electrospray functions as a source of gas phase ions and their analysis was narrowly focused on polymeric species such as polystyrenes. The transfer of ions from solution to the gas phase is a strongly endothermic and endoergic process. This is because the ion in solution is interacting with a number of solvent molecules which form a solvation 'sphere' around the ion. Compared to other ionisation methods, the desolvation in ESI is achieved gradually by thermal energy at relatively low temperatures in order to avoid fragmentation as much as possible; so that it is mostly intact molecular ions which survive the gas phase transfer/ionisation process, which makes ESI a gentler method than other MS ionisation methods.

The whole ESI process can be divided into three steps: 1) ion formation (nebulisation), creating electrically charged droplets from the sample solution; 2) desolvation, depleting solvent molecules from the droplet, and 3) ion transportation, guiding ions from the atmospheric pressure ion source into the high vacuum of the mass analyzer. The ion transfer and formation from solution to the gas phase has been studied by many research groups.<sup>[18-22]</sup> In practice, it is as depicted schematically in Figure 1-4. The sample is introduced and cationic droplets (in positive mode) emerge at the tip of the nebuliser and are then "sprayed" (forming a mist of highly charged droplets) under an intensive electric field between the nebuliser and the counter electrode at the entrance of the transport region. In the meantime, anions migrate inside the nebulizer and flow away from the tip. Nitrogen gas is usually applied along the side of the spray as the nebuliser gas and also as a drying gas, which has a counter flow to the ion movement, helping to deplete solvent from the charged droplets. As the charged droplets shrink, the repulsive Coulombic forces exceed the droplet surface tension, causing splitting of the droplets into smaller and highly charged droplets. Ions are thus released after constant desolvation and fission, and transported into a mass analyzer via regions with successively reduced pressure. Different polarities in electrospray analysis can be achieved by switching the polarity of the applied electrical fields.

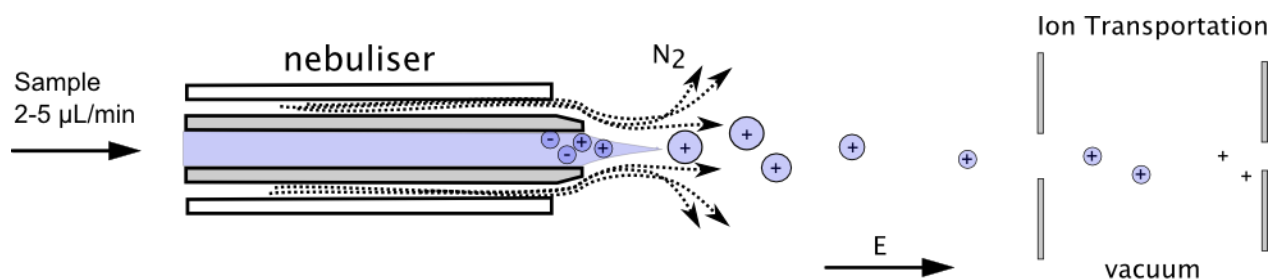


Figure 1-4: Scheme of an ESI source

LASER DESORPTION/IONISATION (LDI) was introduced in the late 1960s. The method easily generates ions from light absorbing organic molecules and low-mass salts by shining laser light upon the samples. Pulsed lasers frequently used in LDI are the Nd:YAG laser (355 nm or 266 nm, pulse width between 1 and 10 ns) or the CO<sub>2</sub> laser (10.6  $\mu$ m, pulse width between 6 and 100  $\mu$ s). Direct LDI may cause either stable ions or excessive unintentional fragmentation, depending upon the light absorbing nature of the analyte (strong absorbing vs. transparent) and its stability. Therefore, light harvesting matrices that absorb at the wavelength of laser have been introduced to this method resulting in MALDI (MATRIX-ASSISTED LDI), which made it possible for non-light-absorbing compounds to be ionised by appropriate energy intake from activated matrices. MALDI has revolutionised the means by which large molecules are studied and opened the door to investigations of proteins and polymers of masses in excess of 200 kDa with greatly improved sensitivity. The MALDI experiment is initiated by depositing a mixture of matrix and analyte (the usual matrix-to-analyte ratio range is from 50-10,000:1, depending on the nature of analyte and matrix) onto a specifically designed sample target plate. The laser beam shines upon the analyte/matrix-crystals (which are formed by evaporation of the solvent from the mixture deposited onto the target plate) which results in the energy from the laser activation being absorbed by the matrix molecules, which is then partially transferred to analyte molecules, which then permits vaporisation and ionisation of the sample as shown in Figure 1-5. For MALDI to occur efficiently it is not necessary for the analyte and the matrix to form crystals, the close proximity of matrix and analyte is sufficient<sup>[23]</sup>. Subsequently, ions are extracted and detected with the mass spectrometer, which in most cases is coupled with a time-of-flight analyzer. The entire process takes no more than a few hundred microseconds. There are common features in MALDI, these include the formation of mainly singly charged ions and the frequent formation of adducts of analyte with alkali metal ions, such as Na<sup>+</sup> and K<sup>+</sup>. Matrix suppression is frequently observed when the reaction of matrix ions with the analyte to produce analyte ions is very efficient.<sup>[24, 25]</sup> In these cases, the matrix ions completely react away to produce analyte ions and only analyte ions are observed, while matrix ions are “suppressed”. Normally, however, both matrix and analyte show ions in the MALDI mass spectrum.

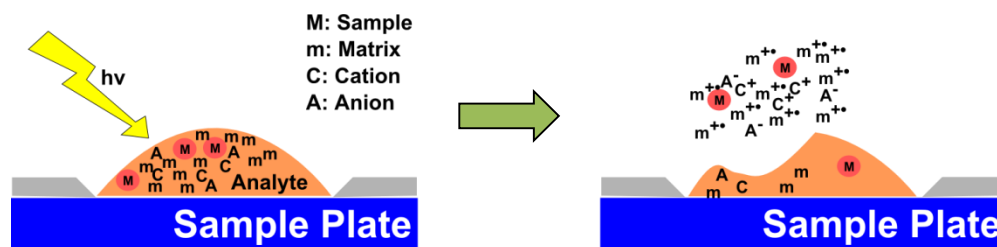
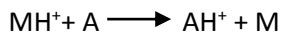


Figure 1-5: MALDI ionisation process

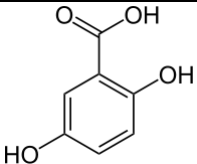
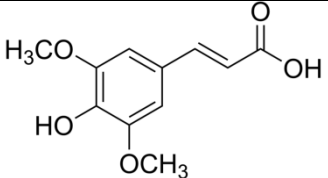
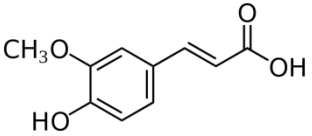
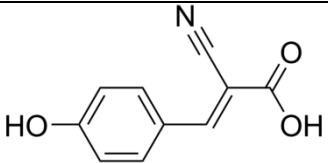
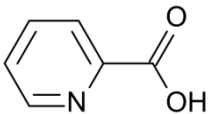
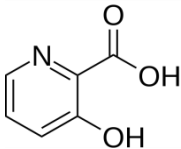
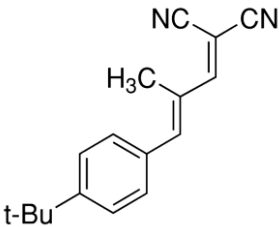
The exact mechanism of ion formation in MALDI is widely discussed, however, a broadly accepted view is that MALDI undergoes a two-step process: ionisation of the primary matrix molecules, followed by in-plume secondary ion-molecule reactions.<sup>[26-29]</sup> The analyte ions are formed in the expanding gas plume which extends from just above the matrix/analyte-crystal surface into vacuum. In the plume ion/molecule-reactions occur and energy is redistributed. Analyte ions are formed in secondary ion/molecule-reactions between the primary formed matrix ions and neutral analyte molecules. The analyte ion can be formed by different processes. These processes may include, for instance, proton

transfer (addition) as shown below, but may also proceed via proton abstraction, cation or anion attachment, or electron transfer.



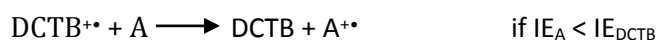
Owing to the diversity of approaches for the charge transfer from matrix to analyte, various matrices have been developed for MALDI, shown in Table 1-2, for different applications.

Table 1-2: Frequently used matrices

Name of matrix	Common name/ abbreviations	Structure	Solvents	Excitation wavelength/nm	Application
2,5-dihydroxybenzoic acid	DHB		Acetonitrile, water, methanol, acetone, chloroform	337, 355, 266	Peptides, nucleotides, oligonucleotides, oligosaccharides
3-(4-hydroxy-3,5-dimethoxyphenyl)prop-2-enoic acid	Sinapinic acid		Acetonitrile, water, acetone, chloroform	337, 355, 266	Peptides, proteins, lipids
(E)-3-(4-hydroxy-3-methoxy-phenyl)prop-2-enoic acid	Ferulic acid		Acetonitrile, water, propanol	337, 355, 266	Proteins
(E)-2-cyano-3-(4-hydroxyphenyl)prop-2-enoate	CHCA, <i>alpha</i> -cyano-4-hydroxycinnamic acid		Acetonitrile, water, ethanol, acetone	337, 355	Peptides, lipids, nucleotides
pyridine-2-carboxylic acid	Picolinic acid		Ethanol	266	Oligonucleotides
3-hydroxypyridine-2-carboxylic acid	3-Hydroxy picolinic acid		Ethanol	337, 355	Oligonucleotides
trans-2-[3-(4-tert-butylphenyl)-2-methyl-2-propenylidene]malononitrile	DCTB		Dichloromethane, toluene,	337, 355	Fullerene derivatives <sup>[30, 31]</sup>

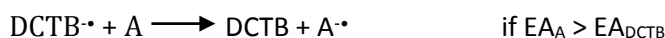
## CHOICE OF MATRIX:

- A strong optical absorption in the UV range from the MALDI matrices enables them to absorb the laser irradiation rapidly and efficiently.
- Vapour pressure from matrix should be low enough to avoid evaporation in the mass spectrometer, however; the matrix molecule should also be small to allow facile evaporation and avoid overlap with the measuring range of the analyte.
- Most MALDI matrices are acidic to encourage ionisation of the analyte via protonation.
- DCTB has shown excellent performance as a matrix for the analysis of fullerenes and their derivatives. DCTB promotes formation of analyte ions at very low laser fluencies and acts as an electron transfer matrix so that analyte ions are formed by electron transfer. DCTB ions seem to fit very well into a thermochemical framework that allows electron transfer without too much unwanted decompositions of the resulting ions. Positive analyte ions are formed by the reaction:



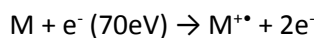
The IE of A must be lower than the recombination energy of DCTB<sup>•+</sup>, which for simplicity is regarded as being equal to the IE of DCTB. In fact, the IE of DCTB ( $\text{IE}_{\text{DCTB}} = 8.47 \text{ eV}^{[31]}$ ) is relatively high and allows the ionisation of most fullerenes and many of their derivatives.

Negative analyte ions are formed by the reaction:



The electron affinity of DCTB has been determined as  $\text{EA}_{\text{DCTB}} = 2.31 \text{ eV}$ , which is lower than the  $\text{EA}_{\text{A}}$  of fullerene ( $\text{EA}_{\text{C}_{60}} = 2.65 \text{ eV}^{[32]}$ ) and many of their derivatives, so that analyte anions are often be formed very efficiently.

ELECTRON IONISATION (EI) is the classic method in (organic) mass spectrometry to form ions and was developed in the early 20<sup>th</sup> century. In EI, electrons carrying tens of electron volts (70 eV) of kinetic energy collided with neutral molecules, which turn into radical cations by ejection of an electron from the neutral molecule.



In rare cases, multiply charged ions can also be generated. In order to allow the comparison of EI mass spectra of different compounds, EI is performed at 70 eV, which also induces a high degree of dissociation, but the appearance of the mass spectrum is around this energy not affected by small deviations of the electron energy, therefore the spectra remain comparable. EI is thus a relatively harsh ionisation method.

Besides the methods mentioned above, a wide variety of ionisation techniques have become available over the years during the development of mass spectrometry. However, none can be applied universally. In Table 1-3, different ionisation approaches have been listed and roughly categorized.

Table 1-3: Choice of molecular ionisation methods.

Molecular Ionisation		
Sample phase	Ionisation Method	Pressure*
Gas phase	Electron ionisation	HV
	Chemical ionisation (CI)	IV
	Photo ionisation (PI)	HV
	Field ionisation	HV
	Metastable atom bombardment	HV
Solution phase	Thermospray	LV
	Atmospheric-pressure CI	AP
	Atmospheric-pressure PI	AP
	Electrospray	AP
Solid phase	Plasma desorption	HV
	Field desorption	HV
	Secondary-ion MS (SIMS)	HV
	Fast atom bombardment	HV
	Matrix-assisted laser desorption	HV

\* HV (HIGH VACCUM), IV (INTERMEDIATE VACCUM), LV (LOW VACCUM), AP (ATMOSPHERIC PRESSURE).

## 1.2.7 TYPES OF ANALYZERS

### TIME-OF-FLIGHT (TOF)

A time-of-flight mass spectrometer (ToF-MS) is a type of mass spectrometer that measures the mass-to-charge ratio of ions based on the time they take to pass a field-free flight tube (usually 1 - 3 metres in length) after a preceding acceleration. In the ToF-MS, ions of mass  $m$  and charge  $z$ , are accelerated by a potential  $V$ , to certain velocities  $v$ . As they leave the ion source, fully accelerated ions of the same charge possess the same initial kinetic energy (taking no account of spatial distribution of ions):

$$E_k = zV = \frac{1}{2}mv^2 \quad 1-1$$

The time,  $t$ , is the time for the ions to pass through the flight tube, which has a length of  $d$ . Substituting for  $v = d/t$  in the previous equation gives

$$t^2 = \frac{m}{z} \left( \frac{d^2}{2V} \right)$$

or

$$t = \text{Const.} \sqrt{\frac{m}{z}} \quad 1-2$$



Since the length of the flight tube ( $d$ ), and the accelerating voltage ( $V$ ) are constant, the time it takes for the ions to reach the detector depends only on their mass and charge. This equation also indicates that, for ions of the same charge state, those with lower masses will be detected sooner.

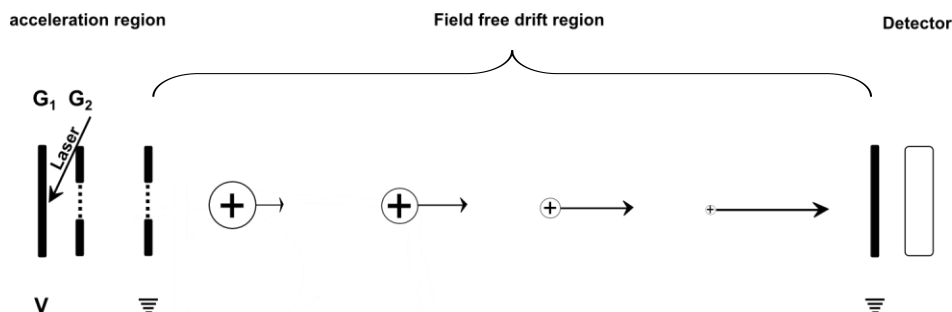


Figure 1-6: Scheme of a linear time-of-flight mass spectrometer (ToF-MS)

A linear ToF-MS has a significant drawback, which is its poor mass resolution. The mass resolution is affected by factors that create a distribution in flight times among ions with the same mass-to-charge ratio. One solution is to lengthen the flight tube as the mass resolution will improve with increasing flight time. It is also possible to increase the flight time by lowering the acceleration voltage. But lowering this voltage decreases the sensitivity. An additional complication arises from the spatial distribution of ions in the ion source and their proximity to the applied electric field, as not all the ions receive the same initial kinetic energy which may result in broad peaks. To overcome these problems, several features are built into most modern ToF mass analyzers that considerably improve mass resolution and in turn help to improve mass accuracies. The first of these is a reflectron which is constructed by a series of ring electrodes to which a high voltage is applied in such a way that it creates a retarding field, which acts as an ion mirror by deflecting the ions and sending them back through the flight tube to a detector. In reflectron ToF, improvements in mass resolution are achieved because the reflectron corrects the energy dispersion of the ions with the same  $m/z$  ratio, as shown in Figure 1-7. Ions with more kinetic energy will penetrate the reflectron more deeply and will spend more time in the reflectron. Thus, they reach the detector at the same time as slower ions (of lower kinetic energy) of the same  $m/z$ , which spend less time in the reflectron. Moreover, the reflectron effectively extends the flight tube to almost twice its length.

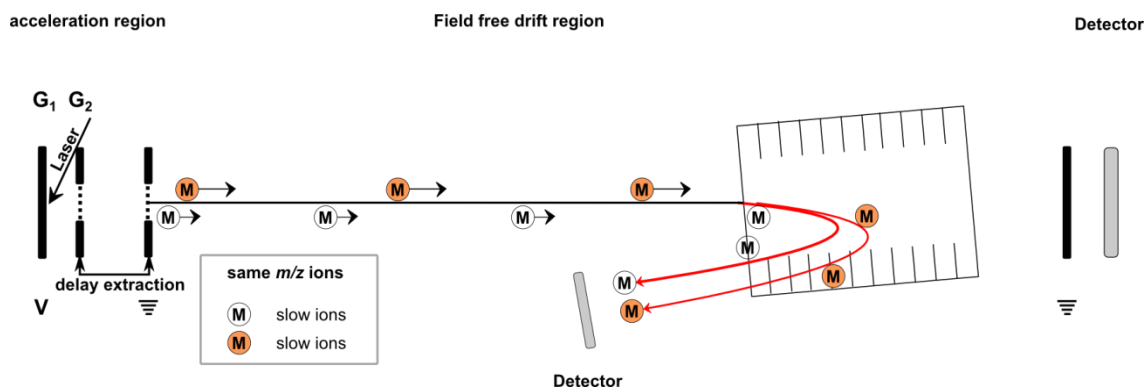


Figure 1-7: Scheme of a reflectron ToF mass spectrometer

A second item that improves the mass resolution in ToF is an ion source, which allows “delayed extraction” of ions. This approach was initially developed as “time-lag energy focusing” by Wiley and McLaren.<sup>[33]</sup> A time lag (in microseconds) is introduced between the formation of the ions and the application of the accelerating pulse. This is achieved, as shown in Figure 1-7, by an acceleration region with two regions. The first region has a very low potential, followed by the second region which provides the main acceleration voltage. At a sacrifice of part of the space resolution, most of the energy time spread is eliminated with delayed extraction, therefore over all resolution is improved.

## ION TRAP

The three-dimensional ion trap, well known as the quadrupole ion trap (QIT), was invented by Wolfgang Paul in 1953, who was later awarded the 1989 Nobel Prize in Physics for this work. It was modified to a mass spectrometer after development of the mass-selective instability mode of mass analysis by Stafford, Kelley and Stephens and commercially introduced as an ion trap mass spectrometer in 1983 by Finnigan Corporation. An illustrative introduction of ion trap mass spectrometry was written by March.<sup>[34, 35]</sup>

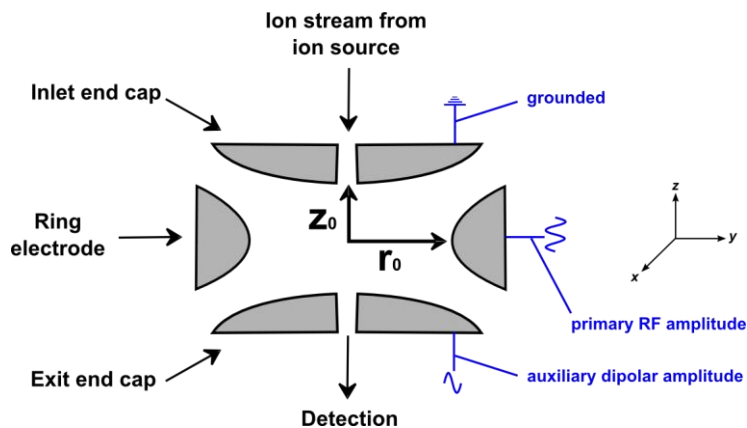


Figure 1-8: Schematic of a quadrupole ion trap mass analyzer

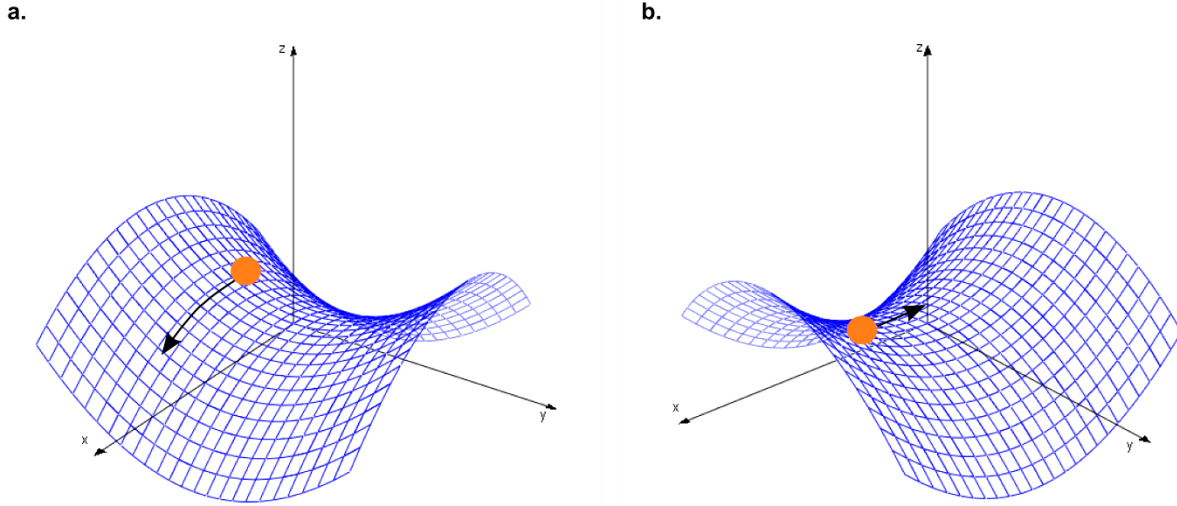


Figure 1-9: Potential surface for a quadrupole ion trap (QIT).

The quadrupole ion trap consists of a central ring electrode and two identical end cap electrodes with an internal hyperboloidal geometry shown in Figure 1-8. This geometry has been chosen so as to create an ideal three dimensional quadrupole field by applying a potential  $\Phi_0 = U - V \cos \omega t$  to the ring electrode while the end cap electrodes remain grounded, where  $U$  and  $V$  are amplitudes of the dc and rf potentials, respectively, and  $\omega$  is the angular frequency. The oscillating potential difference established between the ring and end cap electrodes allows ions of a particular mass range to be trapped in the ion trap, as shown in Figure 1-9. Ions are in general focused towards the centre of the ion trap and ions that tend to fall off from the centre of the potential surface will be focused later with the alternating periodical potential field. Therefore, the trapped ions undergo periodic motions in both the radial as well as the axial direction. This harmonic oscillatory motion of ions, with the major component being the “secular frequency”, is essentially determined by the mass-to-charge ratio of the ion and the rf level. Nevertheless, ion loss, which was due to their initial thermal energy in the ion trap, was also reported.<sup>[36-38]</sup>

The internal radius,  $r_0$ , of the central ring electrode is related to the distance of the centre to one of the end cap electrodes,  $z_0$ , as  $r_0^2 = 2z_0^2$ . To form a stable trajectory during the storage time, the movement of the ion cloud must never reach or exceed  $r_0$  and  $z_0$  and helium with a pressure of  $10^{-3}$  torr is commonly filled in the trap as a buffer gas to slow and cool the ions. The motion of an ion in the trap can be described mathematically by the solutions to the *Mathieu equation*

$$\frac{d^2u}{d\xi^2} + (a_u - 2q_u \cos 2\xi)u = 0 \quad 1-3$$

where  $u$  stands for either  $z$ - or  $r$ -axis and  $\xi$  is equal to  $\omega t/2$ .

Thus two dimensionless variables can be solved from the Mathieu equation, which are

$$a_u = a_z = -2a_r = \frac{-16zeU}{m\omega^2(r_0^2 + 2z_0^2)} \quad 1-4$$

$$q_u = q_z = -2q_r = \frac{8zeV}{m\omega^2(r_0^2 + 2z_0^2)} \quad 1-5$$

It is important to note that  $z$  is the number of charges ( $\pm 1, \pm 2, \dots$ ),  $e = 1.602 \times 10^{-19}C$ ,  $m$  should be expressed in kg per ion and  $\omega = 2\pi\nu$  should be expressed in  $\text{rad s}^{-1}$ . ( $\nu$  is the fundamental RF frequency, which equals to 781 kHz in the case of the QIT used in this study.)

Plots of  $a_u$  versus  $q_u$  in the  $r$ - and  $z$ - directions, respectively (Figure 1-10 a. and b.) show Mathieu stability regions for the three-dimensional quadrupole field. Ion trajectories must be stable in both the  $r$ - and  $z$ -directions simultaneously when they are stored in the trap. Therefore, combining the plots from Figure 1-10 leads to a plot of  $a_u$  versus  $q_u$  as shown in Figure 1-11 and the areas A and B in Figure 1-11 are referred to as the simultaneous stability regions in three dimensions.

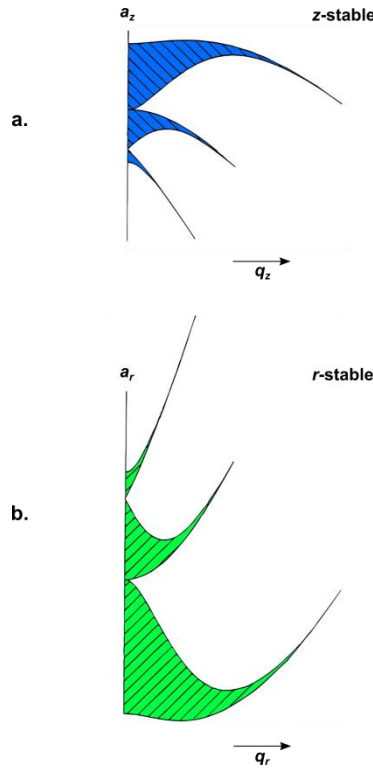


Figure 1-10: Mathieu stability regions for the ion trap. a) The stability regions corresponding to stable solutions in the  $z$  direction. b) The stability regions corresponding to stable solutions in the  $r$  direction.

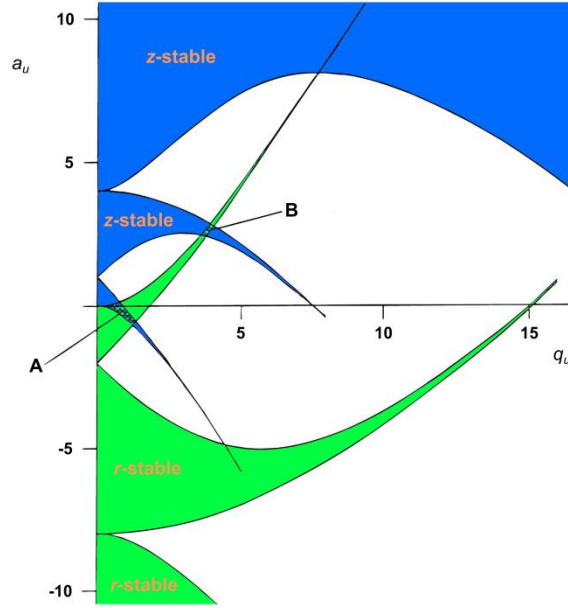


Figure 1-11: Mathieu stability diagram in three dimensions. The overlapped regions are of stability in both  $r$ - and  $z$ - direction, labelled A and B.

Region A in Figure 1-11 is of tremendous significance in practice. Instead of plotting  $a_u$  against  $q_u$ , it is more perceivable to plot  $a_z$  against  $q_z$  as the stability in  $z$  axis directly correlates to the ejection of ions. A new parameter,  $\beta_u$ , has to be introduced here which indicates the boundaries of unstable regions in the stability diagram. The value  $\beta_u$  is dependent on  $a_u$  and  $q_u$ . The borders of the stability regions are defined with  $0 < \beta_u < 1$  shown in Figure 1-11.

$$\beta_u = a_u + \frac{q_u^2}{(2 + \beta_u)^2 - a_u + \frac{q_u^2}{(4 + \beta_u)^2 - a_u + \frac{q_u^2}{(6 + \beta_u)^2 - a_u + \frac{q_u^2}{\dots}}}} \quad 1-6$$

Most commercial instruments apply the mass analysis approach whereby the trap behaves purely as a storage device with an oscillatory field when only the rf voltage is employed, which means the dc voltage is not applied, thus  $a_z=0$ . Therefore, the dashed line in Figure 1-12 becomes the so-called “operating line” of the instrument. The intersection of the  $\beta_z = 1$  stability boundary with the  $q_z$  axis at  $q_z=0.908$  indicates the low-mass cutoff, given by

$$\frac{m}{z} = \frac{4eV}{q_{eject}\omega^2 r_0^2}$$

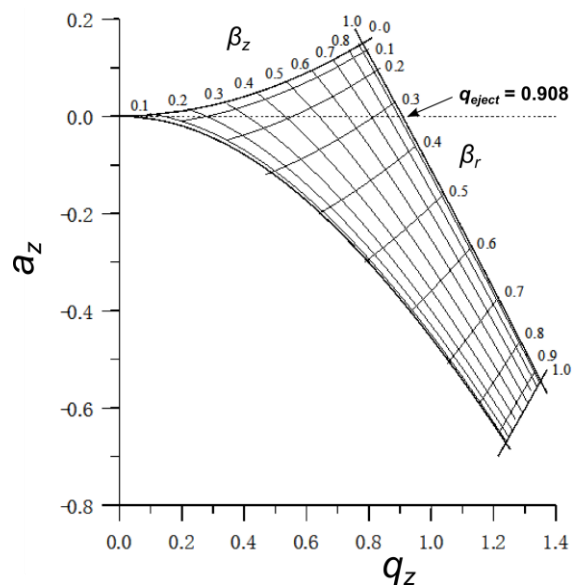


Figure 1-12: Stability diagram of  $(a_z, q_z)$  with the iso- $\beta_r$  and iso- $\beta_z$  lines.

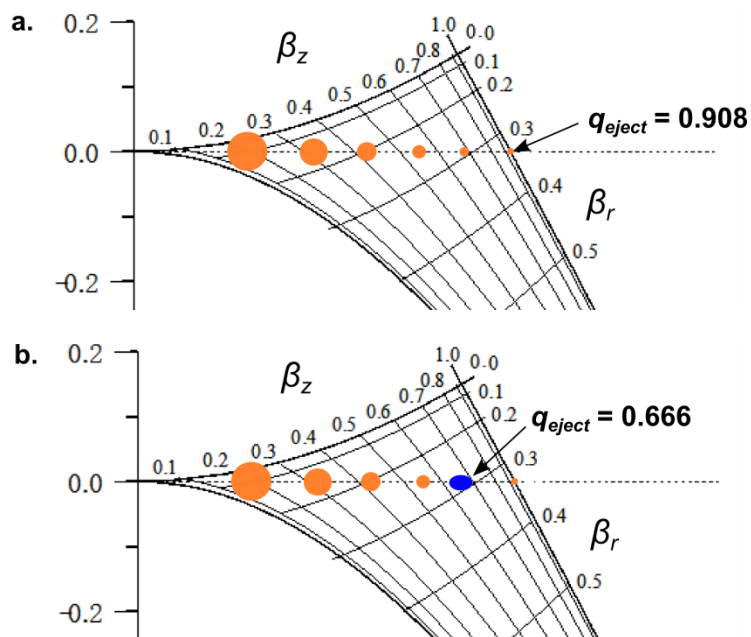


Figure 1-13: Operating line of the QIT. a) Operating line with RF only; b) Operating line with RF and auxiliary frequency.

As discussed in equation 1-5, that ions with smaller mass-to-charge ratio possess higher  $q_z$  values; as a result, when the rf amplitude is increased, the  $q_z$  value will increase for all the ions in general. Therefore, as soon as the  $q_z$  values of the ions reach 0.908, these ions will leave the stability region and are thus eventually ejected sequentially. Nevertheless, with the increase of the rf amplitude, some larger ions are not effectively ejected in terms of the time frame and may also dissociate due to an excessive energy uptake. Hence, an auxiliary frequency is employed between the end caps, which induces non-linear resonances of ions, allowing ions to take up energy very quickly, so that the ions would leave the trap before the occurrence of fragmentation. This procedure is creating a “black hole” at the operating line, as shown in Figure 1-13 b. These non-linear resonances occur when the ion secular frequency and the auxiliary frequency have an integer relationship.

All in all, a full mass spectrum is generated with the QIT instrument by the following steps:

- Ions enter the trap with the help of a repelling voltage on the vacuum partition.
- Voltage on the vacuum partition is then increased to prevent more ions from entering the trap after a given accumulation time.
- Accumulated ions are “cooled down” by buffer gas in the trap and trapped in the rf field with a low amplitude
- Ramping of both quadrupolar and dipolar fields eject ions of increasing  $m/z$  out of the trap accordingly.
- The quadrupolar field is dropped to zero to clear the remaining ions out from the trap.

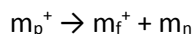
Moreover, the ion trap is well known for its multiple MS/MS capability. The QIT is able to directly eject all ions simultaneously except for the ion of interest as each particular ion with a specific mass-to-charge ratio is resonated by a certain dipolar frequency. To induce fragmentation from the precursor ion, a dipolar field is applied with smaller amplitude than that used for ejection which is typically around 1 - 3 Volts. Accumulated ions quickly take up energy from the dipolar field and collide with the buffer gas resulting in dissociation. For this collision process, it is important to note that only the precursor ions are activated at the applied dipolar frequency. Upon fragmentation there is little energy uptake by the offspring ions. Furthermore, product ions do not respond to the dipolar frequency applied, so they are not excited. Therefore, subsequent fragmentations are not often observed in QIT. This feature of selective excitation of the parent ion without further activation of daughter ions is fairly unique to the QIT analyzer. In other instruments, the successive fragmentation of daughter ions can be frequently observed as a consequence of further activation of the initially generated fragment ions. Such successive activation is, for instance, common when the parent ion is activated by kinetic collisions in a collision cell. Thereafter, the so-called  $MS^2$  spectrum is acquired by ramping of both quadrupolar and dipolar fields ejecting ions in the same manner as during the recording of a full mass spectrum ( $MS^1$ ). Instead of ejecting all the fragment ions, a further isolation of daughter ions of interest with a certain  $m/z$  is possible with the QIT. The fragmentation of the isolated daughter ion results in a so-called  $MS^3$  spectrum. The procedure can be continued as long as the abundance of the daughter ion is of a high enough level. This  $MS^n$  capability is a powerful feature of QIT, and is particularly useful for ion structure elucidation and mechanistic investigations into the fragmentation pathways.



## 1.2.8 TANDEM MASS SPECTROMETRY

Tandem mass spectrometry, abbreviated as MS/MS or MS<sup>2</sup>, is a powerful tool which provides structural information and insight into the fragmentation dynamics of ions in mass spectrometry. In general, this is a two stage process, which involves the isolation of a precursor ion of a certain  $m/z$  ratio, followed by activation and dissociation of the selected precursor ion. The name “tandem mass spectrometry” resulted from the historic use of sector field analyzers, which required the coupling of two mass analyzers (one for isolation and one for the dissociation) to conduct this experiment.

A selected (isolated) ion may fragment without further activation, simply as a consequence of its high internal energy content. A spontaneous dissociation of this type is referred to as unimolecular fragmentation.



Illustrative studies of the internal energy content of ions have been performed by Vékey.<sup>[39-45]</sup> The Wahraftig diagram (Figure 1-14) correlates the internal energy and the unimolecular fragmentation behaviour of ions and is discussed below.

The x axis represents the internal energy of the ion whereas the upper part of the y axis,  $P(E)$ , is the proportion of the ions with the energy represented on the x axis. The lower part of the y axis shows the logarithm of the rate constant  $k$  for unimolecular dissociation. The intake of energy to the ion in excess of IE does not cause decomposition immediately. The ion survives for a certain time until a critical energy,  $E_0$ , is reached.  $E_0$  is the minimum internal energy of the ion ABCD<sup>++</sup> required to dissociate into the respective daughter ions. Beyond  $E_0$ , fragmentation occurs.

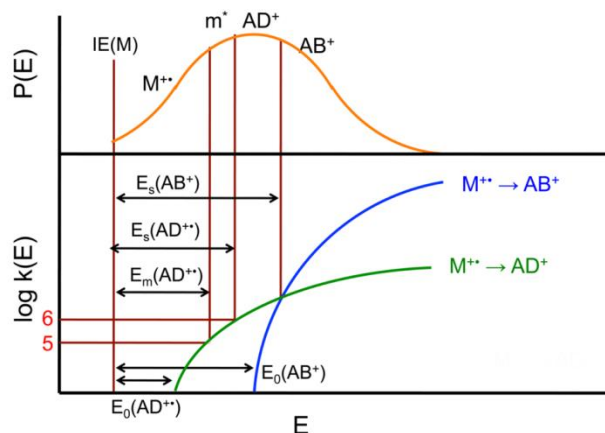
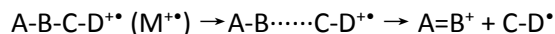
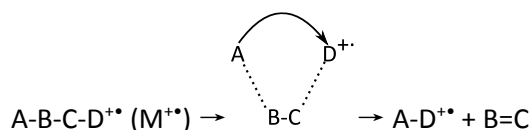


Figure 1-14: The Wahraftig diagram showing the relationship between internal energy and unimolecular ion decomposition for a hypothetical ion ABCD<sup>+</sup>

The blue trace (Figure 1-14) suggests the rate of a direct cleavage reaction:



whilst the green trace represents a rearrangement reaction:



The fragment  $AD^{+*}$  displays a lower critical energy  $E_0(AD^{+*})$  due to its transit cyclic geometry. This prevents one or more rotations from occurring. Additionally, a part of the energy required for bond cleavage (e.g. bond between A and B) is compensated by the energy which is released during the formation of the new bond A-D. However, the rearrangement is less likely to happen due to the lower entropy of the intermediate state. With higher internal energy, direct bond cleavage is much more favoured with a faster rate constant. When the internal energy of  $ABCD^{+*}$  is larger than  $E_m(AD^{+*})$ ,  $ABCD^{+*}$  becomes metastable with a log  $k$  near 5. A detectable amount of daughter ions  $AD^{+*}$  will start to arise when  $E_s(AD^{+*})$  is reached, i.e. when internal energy is excessively accumulated into metastable  $ABCD^{+*}$  with a log  $k$  close to 6.

For sector-type mass spectrometers, ions leaving the ion source can be categorized into three classes according to their lifetime and depending on the distribution of their internal energy shown in the Warhaftig diagram. The first category of ions  $M^{+*}$ , with a rate constant value  $< 10^6 \text{ s}^{-1}$  and a lifetime of  $10^{-5}$  s or longer, will reach the detector intact and are called stable ions. Ions in the second category are unstable ions, with a  $k$  value  $> 10^6 \text{ s}^{-1}$  and lifetime shorter than  $10^{-7}$  s, dissociate before leaving the source and only fragments reach the detector. The third category, is the one of the so-called metastable ions ( $m^*$ )<sup>[46]</sup> which have an intermediate lifetime with a  $k$  in the range  $10^5$  to  $10^6 \text{ s}^{-1}$ . Metastable ions survive the time in the ion source intact, where they acquire excess internal energy, which allows them to fragment after they have been accelerated and continued their flight through the instrument towards the detector. Before reaching the detector, however, they will decompose, so that only fragments will be detected. The experiment of recording metastable ion dissociations with time-of-flight MS is referred to as **Post Source Decay (PSD)**. The PSD experiment will be discussed next in more detail. In cases, where metastable decay is not occurring efficiently, fragmentation can be promoted by collision. The process is referred to as **Collision-Induced Dissociation (CID)** and the details of this will be discussed following the discussion of the PSD process.

## POST SOURCE DECAY

Post source decay (PSD) refers to the recording of daughter ion spectra of a selected parent ion ( $MS^2$ ) in time-of-flight MS. The dissociating parent ion can be regarded as a metastable ion, as it fragments without additional activation in the analyzer region of the ToF-MS. For the selection of the parent ion, an ion gate is placed between the ion source and the flight tube allowing the deflection of all unwanted ions (ion gate on). Only the ion of interest is allowed to pass through (ion gate off). A linear detector is, however, unable to distinguish the selected parent ion from its fragment ions, which are produced during the flight towards the detector in the flight tube region. This is because the parent ion and its daughter ions continue their flight through the instrument with the same velocity. As a consequence they reach the linear detector all at the same time, namely at the arrival time of the parent ion. Interestingly, a completely dissociated parent ion for which only fragment ions would reach the linear detector would still produce a signal for the “intact” parent ion. The linear detector is therefore analytically valuable, as it can reveal ions that have long since fragmented and may no longer exist. Figure 1-15 illustrates this process. As mentioned in the ionisation section, this work has been studied by many research groups<sup>[47, 48]</sup>.

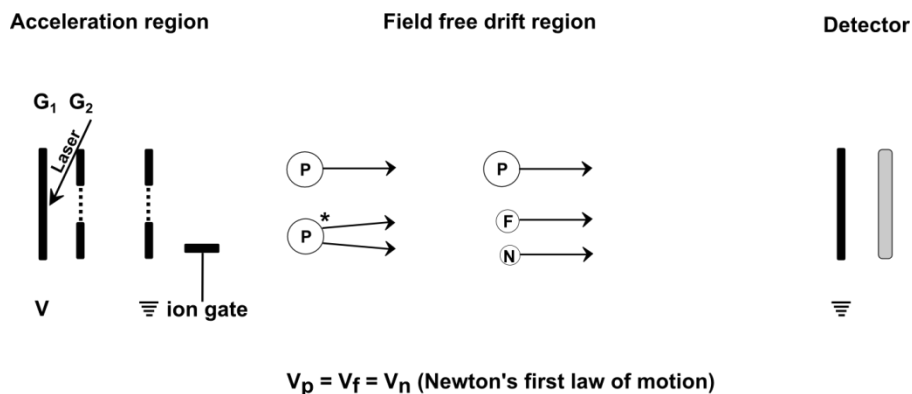


Figure 1-15: Post source decay (PSD) process in the linear mode

In order to distinguish the parent ion from the PSD fragment ion, a reflectron is necessary. The reflectron was first introduced by Mamyrin as an energy filter to compensate for the velocity spread of the ions obtained during their formation and acceleration, in order to improve resolution. An in-depth review by Mamyrin can be read.<sup>[49]</sup> A reflectron is an ion optical device composed of evenly spaced ring electrodes on which a retarding electrostatic field is applied. The reflectron as shown in Figure 1-16, operates as a kinetic energy filter. Although the PSD parent and daughter ions possess the same velocities, their kinetic energy is directly proportional to their mass and, therefore, is distinctly different for the parent and each of the fragment ions. The parent ion with the largest kinetic energy penetrates the reflectron the deepest and spends also the longest time in it. Therefore, the PSD parent, if it survives, will appear at the highest mass in the PSD-MS and the fragments at shorter detection times, corresponding to smaller masses.

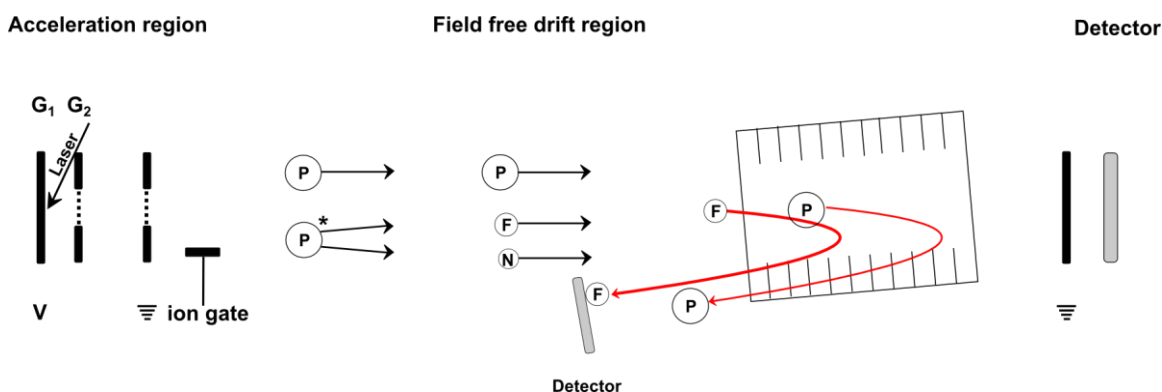


Figure 1-16: Post source decay (PSD) process in reflectron mode

The reflectron does not only improve the resolution, but as previously mentioned, it is essential to distinguish PSD fragment ions from the parent ion. According to the electric field applied, reflectrons can be categorized into three types: single-stage reflectron, dual-stage reflectron and curved-field reflectron shown in Figure 1-17. The dual-stage reflectron has advantages over the single-stage/linear reflectron such as reduced size of the reflectron. However, either will not focus all of the daughter ions onto the detector. With a linear reflectron, ions of less energy than 70% of the parent ions' energy will neither hit the detector nor are focused in time. Therefore, alternative methods have been developed such as a multi

stepping approach, whereby the reflectron voltages are adjusted for different mass regions of the PSD spectrum which are later stitched together to give a full PSD-MS containing all fragment ions. This method is however time- and sample-consuming as the recording of each segment requires time and the activation of new sample areas for each segment requires a sufficient amount of sample.

A more modern approach is the so-called “LIFT”-method. The name resulted from the fact that ions are energetically lifted. In LIFT the parent ion undergoes a collisional dissociation at a collision energy of about 8 keV after which the parent and its daughter ions are “lifted” by further acceleration to 27 keV. This energy lift reduces the energy difference between parent and fragment ions, so that almost all fragment ions are allowed to pass the reflectron and will now also reach the detector.

A further approach to facilitate the recording of PSD spectra is the curved-field reflectron, which operates with potentials that increase exponentially in the reflectron. This “curved field” allows the focus of parent and all daughter ions onto the detector. In principle, only one laser shot can lead to a full PSD mass spectrum. In practice, commercially available reflectrons of this type are slightly less sensitive and of slightly lower resolving power compared to the linear/dual-stage reflectron. The successful application of curved-field reflectrons have been proved by Cotter.<sup>[50-54]</sup>

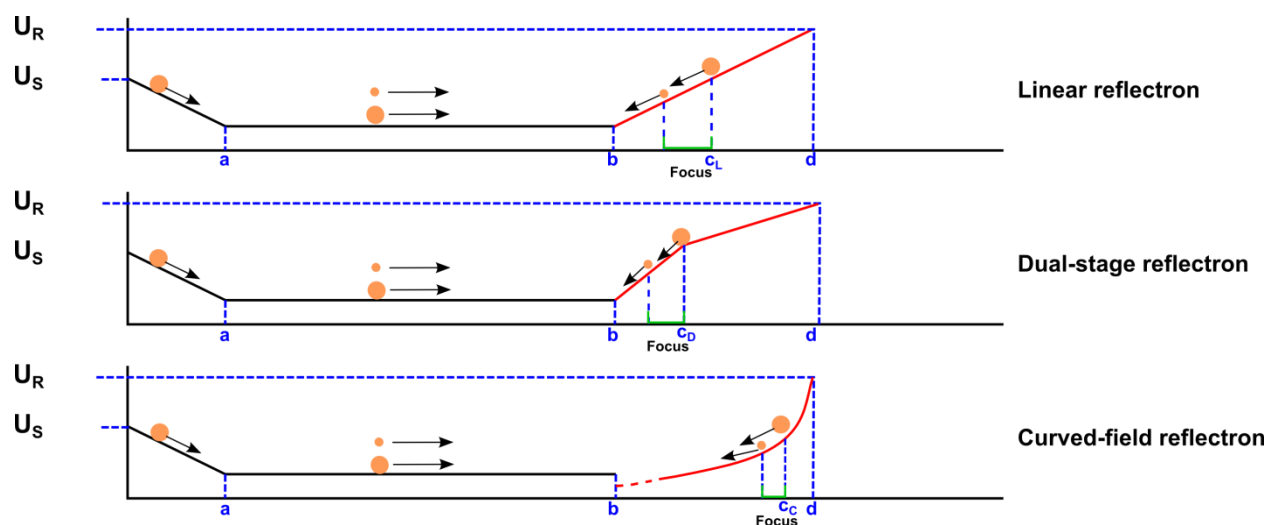


Figure 1-17: Potentials applied in the different types of reflectrons.

Up to point a, ions are accelerated and continue to drift in region a-b. Region b-d is the whole length of reflectron. The parent ion is stopped at point c while smaller fragments are stopped earlier, with the spatial difference between them called “focus” here. Then ions are reaccelerated in the opposite direction of the original ion movement towards the detector.

## COLLISION-INDUCED DISSOCIATION (CID)

This method is also known as collision-activated dissociation (CAD), which allows ions of interest to collide with neutral gas atoms or molecules. In these types of collision, a certain amount of the ion’s kinetic energy is converted into internal energy, which results in bond breakage and thus fragmentation into smaller ions. The CID process can be sequentially divided into two steps. The first step is the collision between precursor ions and the target, which is very fast ( $10^{-14}$ - $10^{-16}$  s), whereby, the translational energy of the precursor ions is converted into internal energy which excites the precursor ions. The second step

is the unimolecular decomposition of the excited precursor ion according to the quasi-equilibrium or Rice-Ramsperger-Kassel-Marcus (RRKM) theories, which assumes that there is no equilibrium with the surroundings and the isolated ion may only undergo unimolecular reactions such as isomerisation and/or dissociation.

The energy to be converted into internal energy in this process is called the centre-of-mass collision energy ( $E_{cm}$ ). The relationship between centre-of-mass collision energy and the ion kinetic energy in the laboratory frame ( $E_{lab}$ ) is described with the following equation<sup>[55]</sup>:

$$E_{cm} = [m_t/(m_p+m_t)]E_{lab}$$

where  $m_p$  is the precursor ion mass and  $m_t$  is the target gas mass. Obviously, increasing the ion kinetic energy ( $E_{lab}$ ) or the target gas mass enhances the energy available for the conversion ( $E_{cm}$ ), which induces more fragmentation.

It is essential to note that in practice there are two collision regimes which should be taken into account, as these are the most common collision regions currently available with the current commercial mass spectrometers. There is the low collision energy range from 1 up to several hundreds of eV, as for instance, occurring in an ion trap instrument, and the high collision energy range which extends up to thousands of eV as implemented in ToF instruments. The purpose of performing CID is to promote fragmentation of an ion of interest, in order to allow the elucidation of its structure by fragment ion analysis.

## 1.3 NATURE OF INVESTIGATED COMPOUNDS

---

### 1.3.1 FULLERENE DERIVATIVES

---

The earliest fullerene,  $C_{60}$  is named after the architect Richard Buckminster Fuller as “buckminsterfullerene” because of its structural similarity to his buildings. It is also known as “buckybal”.  $C_{60}$  was discovered in 1985 at Rice University in Houston by Richard Smalley, Harold Kroto, Robert Curl and their co-workers<sup>[56]</sup>. The first detection of  $C_{60}$  was achieved by laser ablation of graphite followed by expansion and detection of ions by mass spectrometry, which produced  $C_{60}$  in minute quantities.  $C_{60}$  became available in macroscopic amounts in 1990 by the so-called Krätschmer-Huffman process, in which graphite electrodes are evaporated in an atmosphere of about 100 Torr of helium.<sup>[57]</sup> The resulting carbon soot contains fullerenes, with  $C_{60}$  as the major component, which can be isolated by extraction with an appropriate solvent (benzene) and separation. Following the greater availability of fullerenes, the chemistry of fullerenes developed fast into a new scientific area, in which the  $C_{60}$  could be synthetically modified in order to produce new materials with tailor-made properties. The all-carbon  $C_{60}$  molecule has a spherical cage, composed of hexagons and pentagons, so that it possesses the shape of a football. Fullerenes and their derivatives have gained increasing attention due to their potential applications, such as: superconductors, lubricants, catalysts, drug delivery systems, hydrogen storage device, organic semiconductor in photovoltaic, chemical sensors, antioxidants, and polymer additives etc..

Buckminsterfullerene is the most prominent member of the family of structurally related, hollow carbon cages composed merely of five- or six- membered rings formed from threefold-coordinated carbon atoms. There is no specific upper limit on size, however, each fullerene must contain  $2(10+N)$  carbon atoms corresponding to exactly 12 five-membered rings and N six-membered rings. Hence, all fullerenes must

contain an even number of carbon atoms and the smallest fullerene is  $C_{20}$  which contains 12 five-membered rings only.<sup>[58]</sup>

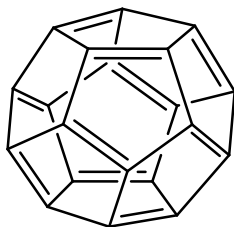
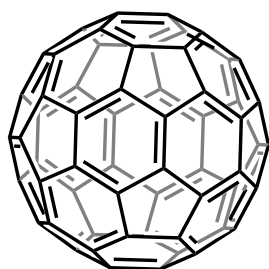


Figure 1-18: Fullerene- $C_{20}$

Buckminsterfullerene,  $C_{60}$ , is a truncated icosahedron with 32 faces of which there are 12 five-membered rings and 20 six-membered rings. The diameter of  $C_{60}$  was initially reported as  $\sim 7 \text{ \AA}$  by Smalley *et al.* in 1985<sup>[56]</sup>; later this value was measured by different research groups and allocated a revised value of  $\sim 10.42 \pm 0.04 \text{ \AA}$ .<sup>[59-62]</sup>



Chemical Formula:  $C_{60}$   
Exact Mass: 720,00

Figure 1-19: Fullerene- $C_{60}$

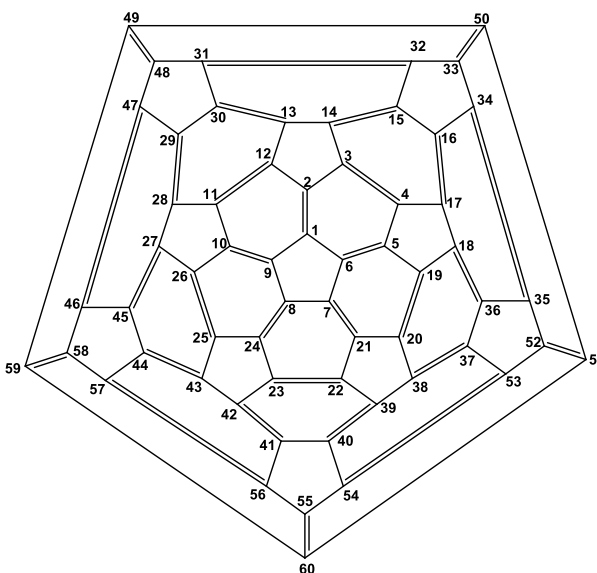
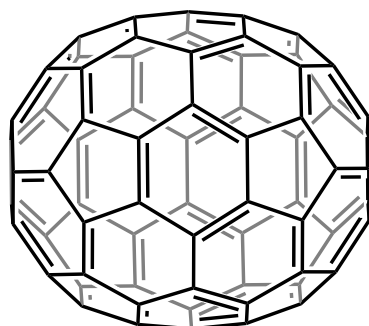


Figure 1-20: Schlegel diagram of  $C_{60}$

$C_{70}$  consists of 70 carbon atoms in a cage-like structure in the shape of a rugby ball and, contains 25 hexagons and 12 pentagons. It was co-generated in the pioneering laser ablation experiments that led to the discovery of the fullerenes, for which the 1996 Nobel Prize in Chemistry was awarded to Kroto, Smalley and Curl.<sup>[63]</sup> The diameter at the short axis of  $C_{70}$  is reported by Tomiyama *et al.* with a value of  $10.94 \pm 0.07 \text{ \AA}$  which is in a good agreement with other groups' measurements.<sup>[59, 60, 62, 64, 65]</sup>



Chemical Formula:  $C_{70}$   
Exact Mass: 840,00

Figure 1-21: Fullerene- $C_{70}$

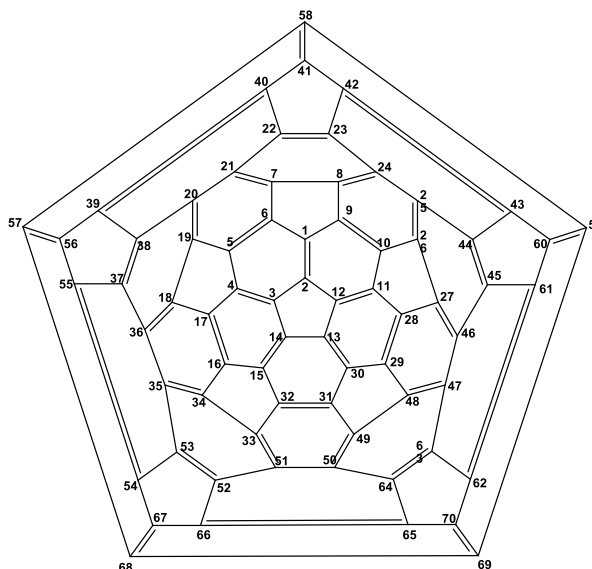


Figure 1-22: Schlegel diagram of  $C_{70}$

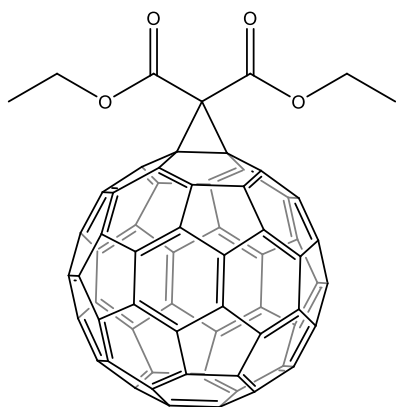
A fullerene is defined as a three-dimensional network of  $sp^2$  hybridized carbon atoms in which each atom is connected by a double bond (one  $\sigma$ -bond and one  $\pi$ -bond) within the six-membered ring and two single bonds ( $\sigma$ -bonds) within two five-membered rings, respectively. In other words, the tetravalency of carbon is satisfied by formation of a  $\pi$ -bond within the six-membered ring. The  $\pi$  bonds are localised within the 6-membered rings, which leads to different bond lengths for the double bonds (1.391 Å) and single bonds (1.455 Å) in  $C_{60}$ <sup>[66]</sup>. The high symmetry of  $C_{60}$  means all of its atoms are equivalent. However, and this is also for  $C_{70}$  and larger fullerenes, it appears that the spherical shape, rather than symmetry is the most important structural requirement. The spherical shape can distribute the strain more evenly, minimizing the anisotropic contribution to strain energy. Beyond  $C_{70}$ , larger fullerenes are known. They are formed by the formal addition of successive  $C_2$  moieties. However, their symmetry and stability varies.  $C_{76}$ ,  $C_{78}$  and,  $C_{84}$  are additionally generated in low amounts during the synthesis of  $C_{60}$  and  $C_{70}$ , and are therefore also commercially available.

The  $C_{60}$  molecule is the most stable fullerene, being able to withstand high temperatures and pressures. However, the  $\pi$ -bonds on the exposed surface of the structure are able to react with other species while retaining the spherical geometry. Therefore, synthesis and characterization of functionalized fullerene derivatives have become broad research fields. Several types of functionalized fullerene derivatives are in existence. Some typical representatives are shown in Figure 1-23 - 28 below. These include exohedrally (at the outer surface) modified fullerenes. Figure 1-23 shows a mono-ligated  $C_{60}$  in its only isomeric form, which can also be produced as bis-ligated (or even higher-ligated) species with several possible isomers, which have been characterised by Hirsch *et al.* <sup>[67]</sup>, as shown in Figure 1-24. Figure 1-25 shows the addition of a crown ether and a hydrogen atom to a double bond<sup>[68]</sup>. Figure 1-26 depicts the Schlegel diagram of  $C_{60}F_{48}$  resulting from fluorination of  $C_{60}$ <sup>[69]</sup>. Figure 1-27 and Figure 1-28 display two so-called open cage fullerenes (OCF). These feature a hole in the carbon sphere which is held open by synthetically introduced heteroatoms. These are currently tested as storage/transport devices for guest entities to be placed inside the sphere <sup>[70-74]</sup>. Finally, endohedral fullerenes are shown, which



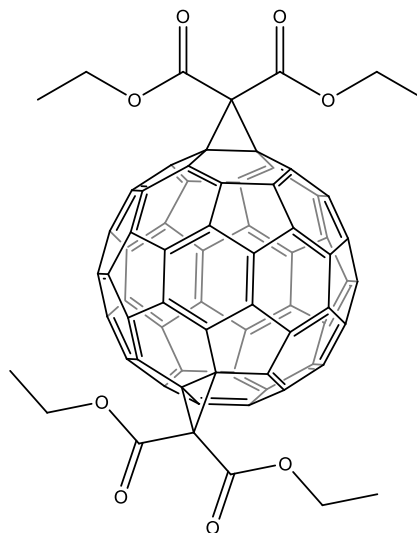
carry guest entities inside the intact sphere. Figure 1-29 shows  $\text{He@C}_{60}$  (" $\text{X@C}_n$ " denotes the moiety X which is inside  $\text{C}_n$ ), for which the He atom has been introduced into an existing  $\text{C}_{60}$ . Figure 1-30 shows  $\text{Sc}_3\text{N@C}_{80}$  [75, 76], for which the  $\text{C}_{80}$  cage has been formed around a  $\text{Sc}_3\text{N}$  molecule which stabilizes the  $\text{C}_{80}$  cage which is normally (as a pure fullerene-cage) not known to possess enhanced stability.

### Ligated fullerenes



Chemical Formula:  $\text{C}_{67}\text{H}_{10}\text{O}_4$   
Exact Mass: 878,06

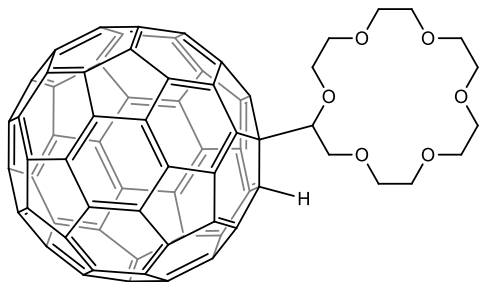
Figure 1-23:  $\text{C}_{60}$ -mono



Chemical Formula:  $\text{C}_{74}\text{H}_{20}\text{O}_8$   
Exact Mass: 1036,12

Figure 1-24:  $\text{C}_{70}$ -mono

### Hydrogenated fullerenes



Chemical Formula:  $\text{C}_{72}\text{H}_{24}\text{O}_6$   
Exact Mass: 984,15729

Figure 1-25: Hydrogenated fullerene-2

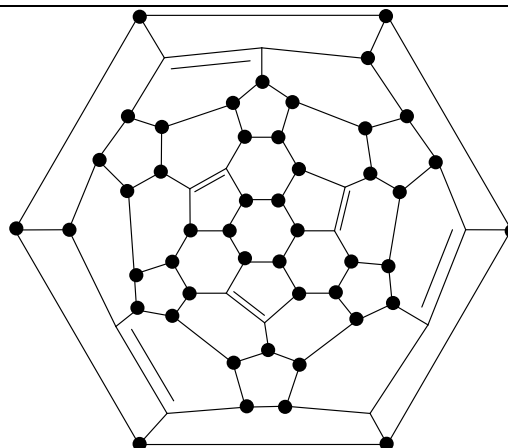
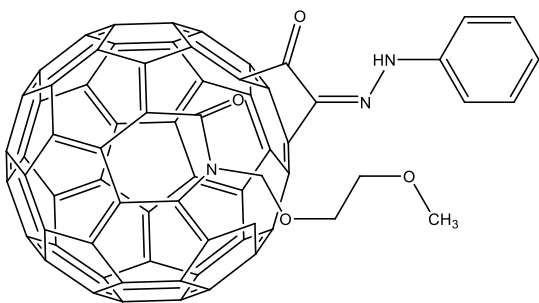


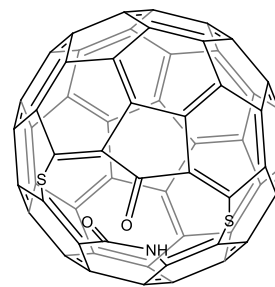
Figure 1-26: Schlegel diagram of  $\text{C}_{60}\text{F}_{48}$ ; (● = F)

## Open-Cage Fullerenes



Chemical Formula:  $C_{70}H_{17}N_3O_4$   
Exact Mass: 963,12

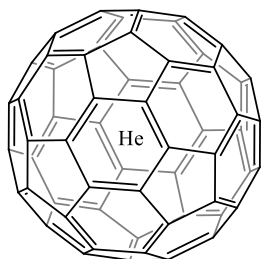
Figure 1-27: Open-cage fullerene OCF-1



Chemical Formula:  $C_{60}HNO_2S_2$   
Exact Mass: 830,94

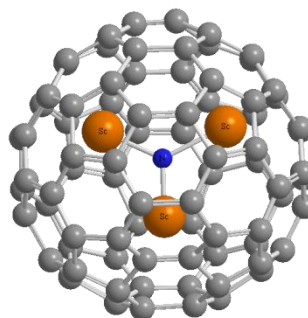
Figure 1-28: Open-cage fullerene OCF-2

## Endohedral fullerenes



Chemical Formula:  $C_{60}He$   
Exact Mass: 724,00

[77]

Figure 1-29: He@C<sub>60</sub>Figure 1-30: Sc<sub>3</sub>N@C<sub>80</sub>-D<sub>5h</sub>

## 1.3.2 IONIC LIQUIDS

Ionic liquids (ILs) are composed of an organic cation and an inorganic anion. They are salt-like compounds, however, displaying unusually low melting points. Most of these salts are actually liquid at temperatures below 100 °C, thus the name: ionic liquids. Charge delocalisation and steric effects prevent the formation of a crystal lattice at these temperatures. The fact that ionic liquids are composed of oppositely charged ions forming ion pairs results in an array of interesting properties which has led to many applications. ILs display low vapour pressures, ionic conductivities, wide liquidus range, properties such as thermo-stability and a good ability for recycling. This had led to applications such as powerful solvents, as reaction media for catalysis, electrically conducting fluids and sealants. The most common cations and anions are displayed in the following tables: [78]

Table 1-4: Common ionic liquid cations:

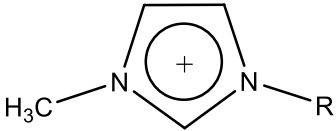
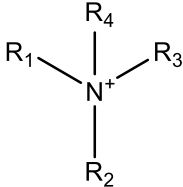
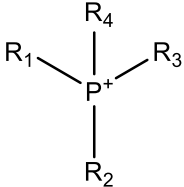
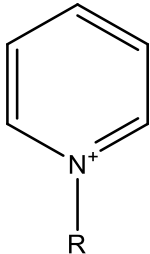
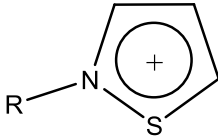
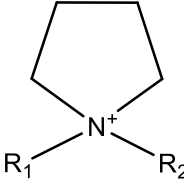
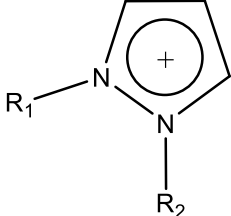
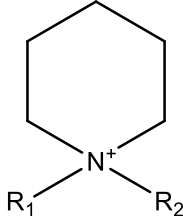
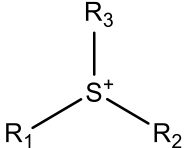



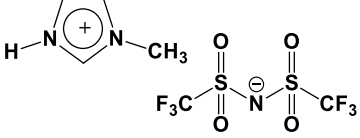

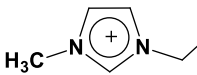

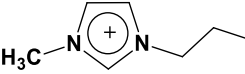

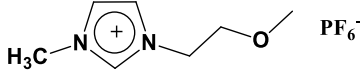
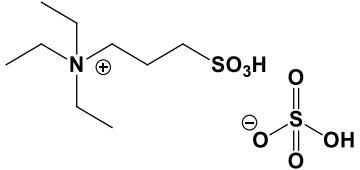
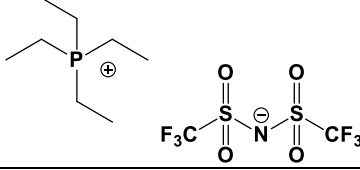
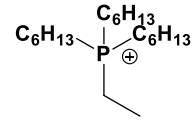
		
1-Alkyl-3-methylimidazolium	Tetraalkylammonium	Tetraalkylphosphonium
		
N-Alkylpyridinium	N-Alkyl-thiazolium	N, N-Dialkylpyrrolidinium
		
1,2-Dialkylpyrazolium	N,N-Dialkylpiperidinium	Trialkylsulfonium

Table 1-5: Common ionic liquid anions:

Halides:	<b>Br<sup>-</sup>, Cl<sup>-</sup></b>
Nitrate:	<b>[NO<sub>3</sub>]<sup>-</sup></b>
Chloroaluminates:	<b>[AlCl<sub>4</sub>]<sup>-</sup>, [Al<sub>2</sub>Cl<sub>7</sub>]<sup>-</sup></b>
Hexafluorophosphate:	<b>[PF<sub>6</sub>]<sup>-</sup></b>
Tetrafluoroborate:	<b>[BF<sub>4</sub>]<sup>-</sup></b>
Alkyl sulfates:	<b>[RSO<sub>4</sub>]<sup>-</sup>, e.g. [C<sub>2</sub>H<sub>5</sub>SO<sub>4</sub>]<sup>-</sup></b>
Alkylcarboxylates:	<b>[RCO<sub>2</sub>]<sup>-</sup></b>
<i>p</i> -toluenesulfonate:	<b>[CH<sub>3</sub>C<sub>6</sub>H<sub>4</sub>SO<sub>3</sub>]<sup>-</sup>, known as tosylate[OTs]<sup>-</sup></b>
Trifluoromethylsulfonate:	<b>CF<sub>3</sub>SO<sub>3</sub><sup>-</sup></b>
bis(trifluoromethylsulfonyl)imide(NTf <sub>2</sub> ):	<b>(CF<sub>3</sub>SO<sub>2</sub>)<sub>2</sub>N<sup>-</sup></b>

To illustrate the “molten salt” character, the following table contrasts the composition of the ion pairs of the ionic liquids with their corresponding melting points.

Table 1-6: Melting points of common ionic liquids:

Ionic liquid	Elemental composition	Structure	Melting point <sup>[79]</sup>
[C <sub>1</sub> Im]Cl	C <sub>4</sub> H <sub>7</sub> ClN <sub>2</sub>		345.15 K 72 °C
[C <sub>1</sub> Im]Br	C <sub>4</sub> H <sub>7</sub> BrN <sub>2</sub>		314.15 K 41 °C
[C <sub>1</sub> Im][BF <sub>4</sub> ]	C <sub>4</sub> H <sub>7</sub> BF <sub>4</sub> N <sub>2</sub>		310.15 37 °C
[C <sub>1</sub> Im][NTf <sub>2</sub> ]	C <sub>6</sub> H <sub>7</sub> F <sub>6</sub> N <sub>3</sub> O <sub>4</sub> S <sub>2</sub>		282.15 K 9 °C
[C <sub>2</sub> Im]Cl	C <sub>5</sub> H <sub>9</sub> ClN <sub>2</sub>		331.15 K 58 °C
[C <sub>2</sub> MIm] Cl ([EMIM] Cl)	C <sub>6</sub> H <sub>11</sub> ClN <sub>2</sub>		357.15 K 84 °C
[C <sub>2</sub> MIm][AlCl <sub>4</sub> ] ([EMIM][AlCl <sub>4</sub> ])	C <sub>6</sub> H <sub>11</sub> Cl <sub>4</sub> N <sub>2</sub> Al		280.15 K 7 °C
[C <sub>3</sub> MIm][PF <sub>6</sub> ]	C <sub>7</sub> H <sub>13</sub> F <sub>6</sub> N <sub>2</sub> P		294.15 K 21 °C
[ <i>i</i> -C <sub>3</sub> MIm][PF <sub>6</sub> ]	C <sub>7</sub> H <sub>13</sub> F <sub>6</sub> N <sub>2</sub> P		375.15 K 102 °C
[C <sub>2</sub> OCMIm][PF <sub>6</sub> ]	C <sub>7</sub> H <sub>13</sub> F <sub>6</sub> N <sub>2</sub> OP		299.15 K 26 °C
[N222,(CH <sub>2</sub> ) <sub>3</sub> SO <sub>3</sub> H][HSO <sub>4</sub> ]	C <sub>9</sub> H <sub>23</sub> NO <sub>7</sub> S <sub>2</sub>		264.15 K -9 °C
[P2222][TFSI]	C <sub>10</sub> H <sub>20</sub> F <sub>6</sub> NO <sub>4</sub> PS <sub>2</sub>		391.15 K 118 °C
[P666,2]Br	C <sub>20</sub> H <sub>44</sub> PBr		332.65 K 59.5 °C

In this study, electrospray ionisation mass spectrometry (ESI) and matrix assisted laser desorption ionisation (MALDI) mass spectrometry were applied to investigate novel ionic liquids. In general, the ionic species that form the ionic liquid ion pair are abundantly observed. That means the cationic component is detected in the positive-ion mode and the anionic component in the negative-ion mode. While this is true for both MALDI and ESI, occasionally clusters with the generic composition of  $\text{Cat}(\text{CatAn})_n^+$  and  $\text{An}(\text{CatAn})_n^-$  with Cat = cationic and An = anionic component of the ionic liquid have been observed. [80-91] Clusters have also been observed with zwitterions [3, 92-94]. The use of ionic liquids for special applications with ESI has been highlighted by Henderson, McIndoe and Dyson. [95]

Besides the use of MALDI purely for the analysis of ionic liquids, there has been also the usage of ionic liquids with the aim of improving the MALDI method. In 2001, Gross and co-workers reported the successful use of ionic liquid-based matrices for MALDI-MS. [96] There are certain requirements for successful MALDI matrices: they must cocrystallize with the sample or remain in close proximity to it, absorb at the wavelength of the applied laser, remain in the condensed phase under high vacuum, promote ionisation of the sample and prevent degradation of the sample. The most common sample preparation method in MALDI analysis is the dried-droplet method in which the crystallisation of sample and matrix takes place as the solvent evaporates. [97] Hence, some “hotspots”, from which sufficient sample signals can be generated, are found during experiments whereas other spots on the target plate cannot produce decent signals owing to the heterogeneous dispersion. This is because sample/matrix crystals formed upon solvent evaporation are often inhomogeneous and unevenly dispersed on the target plate. This “hotspots”-effect highly restrains the reproducibility of MALDI measurements. [98] It is suggested that ionic liquid matrices can remarkably enhance the homogeneity in the sample and form a thin liquid layer on the target plate with negligible vapour pressure, which leads to increasingly reproducibility and possibility of sample quantitation. Gross and co-workers pointed out that classical ionic liquids are not suitable for the usage as MALDI matrices owing to their poor laser absorption ability and the lack of transferable protons. However, successful ionic liquid-based MALDI matrices were obtained when the cation is a typical organic cation known from “classic” ionic liquids, such as 1-methyl-imidazole in combination with a typical conventional MALDI matrix that can function as organic base, such as  $\alpha$ -cyano-4-hydroxycinnamic acid (CHCA). An example is displayed in Figure 1-31. [96] Subsequent success of applying ionic liquids as MALDI matrices in the above mentioned manner has additionally been reported by many other groups. [99-104]

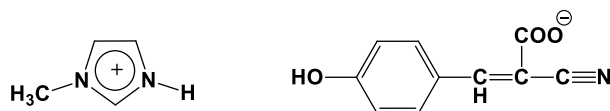


Figure 1-31: MALDI ionic liquid matrix:  $\alpha$ -cyano-4-hydroxycinnamic acid (CHCA) and 1-methyl-imidazole

### 1.3.3 PORPHYRINS

Porphyrins represent an important class of organic molecules for their unique role in supporting aerobic life in addition to functioning as dyes and catalysts for solar cells. Porphyrins are characterized by a tetrapyrrolic core structure, in which four pyrroles are bridged by methine units (=CH-) under formation of an aromatic macrocycle. In this study, the following porphyrins, which were synthesised in the group of Privatdozent Dr. N. Jux at University of Erlangen, have been investigated. These studies of porphyrins were initiated alongside the research group of Prof. Ivanović-Burmazović to investigate the interaction of Fe/Mn porphyrins and superoxide in order to enhance the understanding of their roles in transportation of oxygen in the biological system. Of particular interest in our study has been the influence of the covalently attached aza-crown ether as a neighbouring complexation moiety.

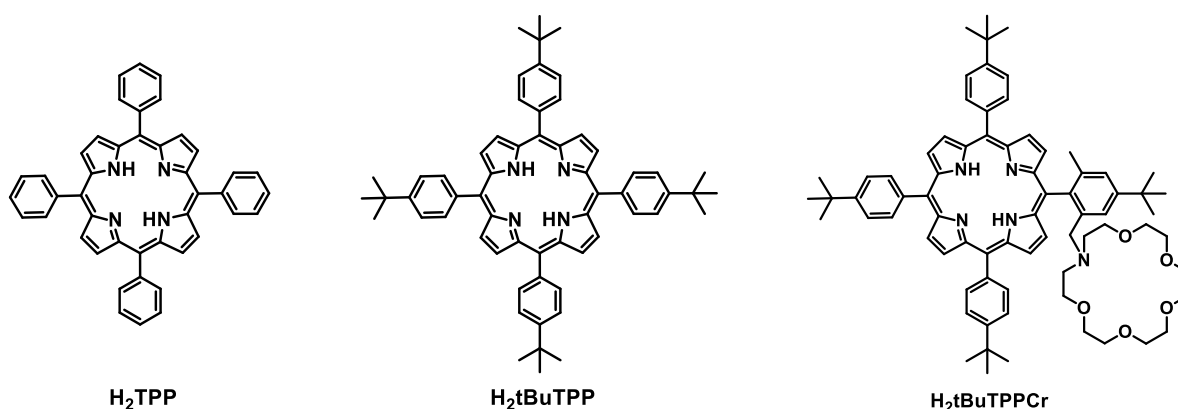


Figure 1-32: Structures of investigated porphyrins

The porphyrins mentioned above were later metallated for further investigation through the method of Borovkov et al. as shown in Figure 1-33.

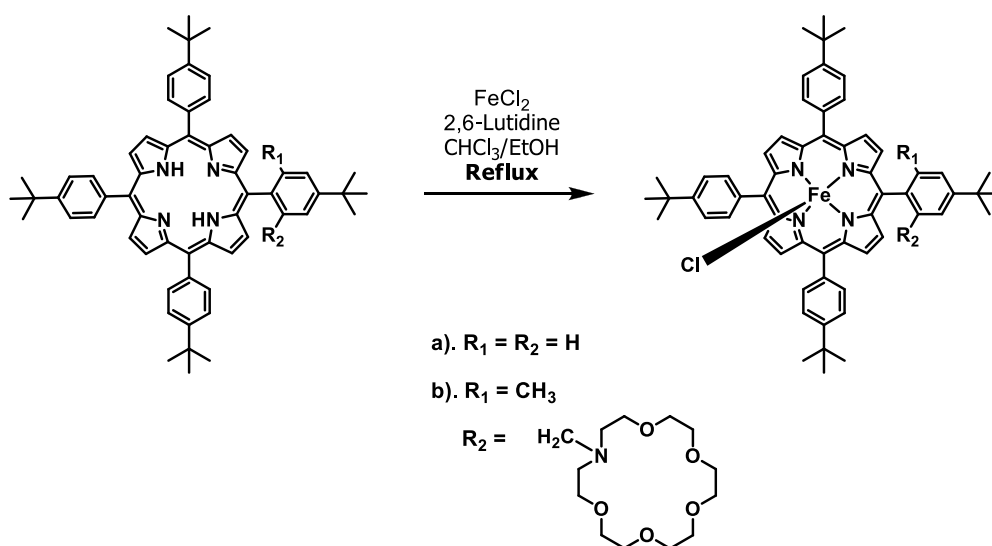


Figure 1-33: Metalation of porphyrin complex

For the ESI investigation of the porphyrin compounds, DMSO was used as solvent, which is rather unusual. However, this was done for reasons of consistency, as earlier solution-based investigations on the reactions of porphyrins with (su)peroxide were also performed in DMSO.<sup>[105]</sup> Successful ESI experiments with DMSO as a solvent have been previously reported in the literature.<sup>[106]</sup>

## 1.4 INSTRUMENTAL

A mass spectrometer is an instrument which generates ions, separates and detects them according to their mass-to-charge ratios. Depending on the ion-separating analyzer used, mass spectrometers can be distinguished; they can also be coupled with different ionisation methods to provide a variety of instrumentation. In the following, the mass spectrometers used in the present investigations are discussed.

### 1.4.1 ESQUIRE6000 (BRUKER DALTONICS)

#### ESQUIRE6000 (BRUKER DALTONICS)

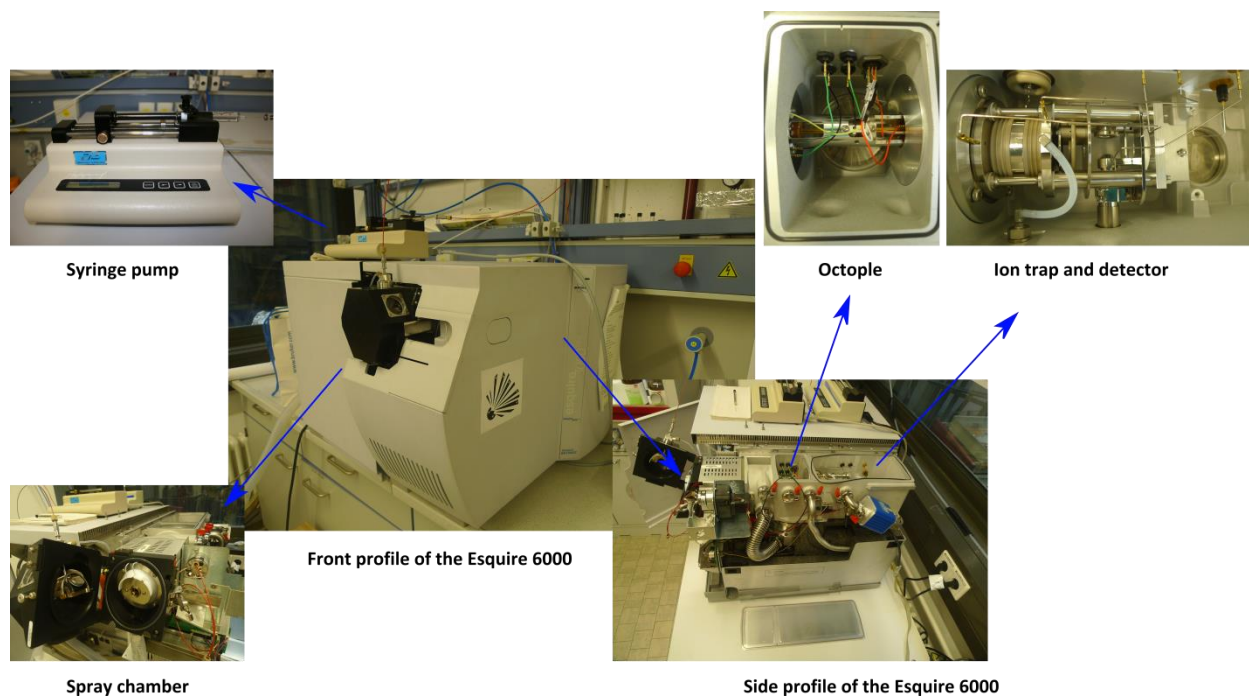


Figure 1-34: Photos of the Esquire6000

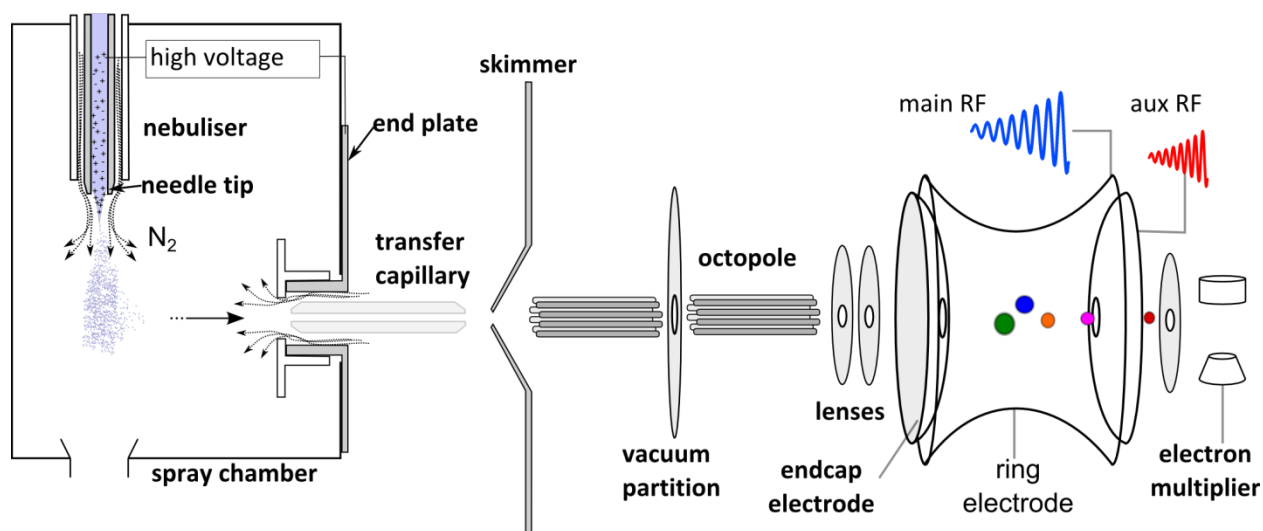


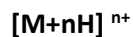
Figure 1-35: Schematic figure of Esquire6000

For ESI experiments, the compounds were introduced into the mass spectrometer Esquire6000 (*Bruker Daltonic*, shown in Figure 1-34) via an infusion pump (*Cole Parmer*) with a liquid flow rate of 240  $\mu\text{L}/\text{min}$ . Different settings of the pump have to be employed according to the size of the selected syringe. Pure acetonitrile (ACN) and methanol or their mixtures with dichloromethane (DCM) were generally applied as solvent to provide a stable spray. DMSO was employed as solvent in porphyrin investigations and ionic liquids were studied in water. Solvent addition to analyte ions is occasionally observed in ESI experiments with the Esquire6000. The origin of such additions is often the occurrence of analyte ion/solvent reactions inside the ion trap analyzer of the instrument.<sup>[107]</sup>

The Esquire6000 connects an electrospray ion source with a quadrupole in trap analyzer. The ESI source and the analyzer are orthogonal to each other and connected with a transfer region for the ions. As shown in Figure 1-35, the ions are introduced to the spray chamber along with nitrogen nebulizer gas. A high voltage is applied at the end plate while the needle tip of the nebulizer is grounded, so that a fine aerosol of charged droplets is produced along a steady electrostatic gradient. By a counter-flow of heated nitrogen gas, the charged droplets are “dried” through solvent evaporation and become highly charged at the surface. Ions are formed and emitted into the gas phase when the repulsion created by the ions at the surface of the droplet exceeds the surface tension. Typical ions that result in the ESI process are:

#### Positive Ion Mode

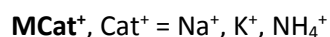
*Formation of protonated molecular ions*



*Formation of oxidized molecular ions*

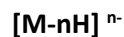


*Formation of cation addition*



#### Negative Ion Mode

*Formation of deprotonated species*



*Formation of reduced molecular ions*



*Formation of anion addition*





Multi-protonation and deprotonation are the most commonly observed process of ion formation when the sample is a biological molecule and their occurrence can be promoted by the choice of the solvent and by addition of acids or bases. Similarly, addition of charge-providing cations and anions can enhance the formation of the respective adduct ions. The formation of radical cations/anions is a special case and such electron transfer reactions occur when the analyte is easily oxidised or reduced and when the ion source conditions allow the ESI source to operate as an electrochemical cell.<sup>[108]</sup>

After the ions of interest are ionised, they are transported and guided into a quadrupole ion trap where they are stored and separated according to their mass to charge ratio. The principle of the storage and separation of ions has been outlined on previous pages. Various experiments that are possible with an ion trap have also been outlined earlier.

Eventually, ions are detected by an electron multiplier, which converts the kinetic energy of the arriving particles into electrical signals. The incoming ions strike a metal surface called a dynode, which is capable of releasing secondary electrons when struck by a particle processing energy above a certain level. There is a series of dynodes within the detector and released electrons are accelerated towards the next dynode (shown in Figure 1-36), by which further electrons are generated. The same process is successively repeated until a blizzard of electrons strikes the final dynode, producing a detectable current which is amplified further. By repeating this input and release process many times, the number of electrons increases by a factor of  $10^6$  to  $10^8$ .

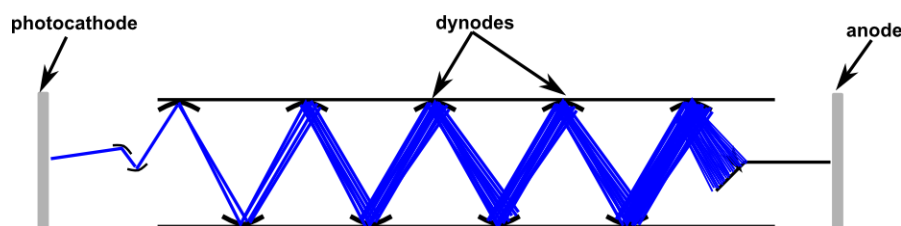


Figure 1-36: Electron amplifier through a serie of dynodes

The Esquire 6000 has some additional performance features. These include

- the ability of fast polarity switching (approx. 400ms)
- automatic control of the amount of ions restrained in the trap with the aim to avoid space charge effects that reduce resolution and sensitivity
- automatic transfer and storage
- various scan modes to meet different requirements

Scan mode	Peak width FWHM/(m/z)	Mass range (m/z)	Scan rate (m/z)/s
Standard	0.6	50-3000	13000
Enhanced	0.45	50-3000	5500
Max. Resolution	0.35	50-3000	1650
Extended	2-4	200-6000	27000

- MS<sup>n</sup> ability up to MS<sup>11</sup> in all scan modes

### 1.4.2 maXis (BRUKER DALTONICS)

Additional ESI studies were conducted with a high resolution Time-of-Flight mass spectrometer (maXis 3G, Bruker Daltonics). The increased resolving power of the maXis allows for an exact establishment of the elemental composition, confirming assignments made when using the ion trap. Furthermore, CID experiments providing complementary data to those performed with the ion trap became possible. The scheme of the maXis is shown in Figure 1-37.

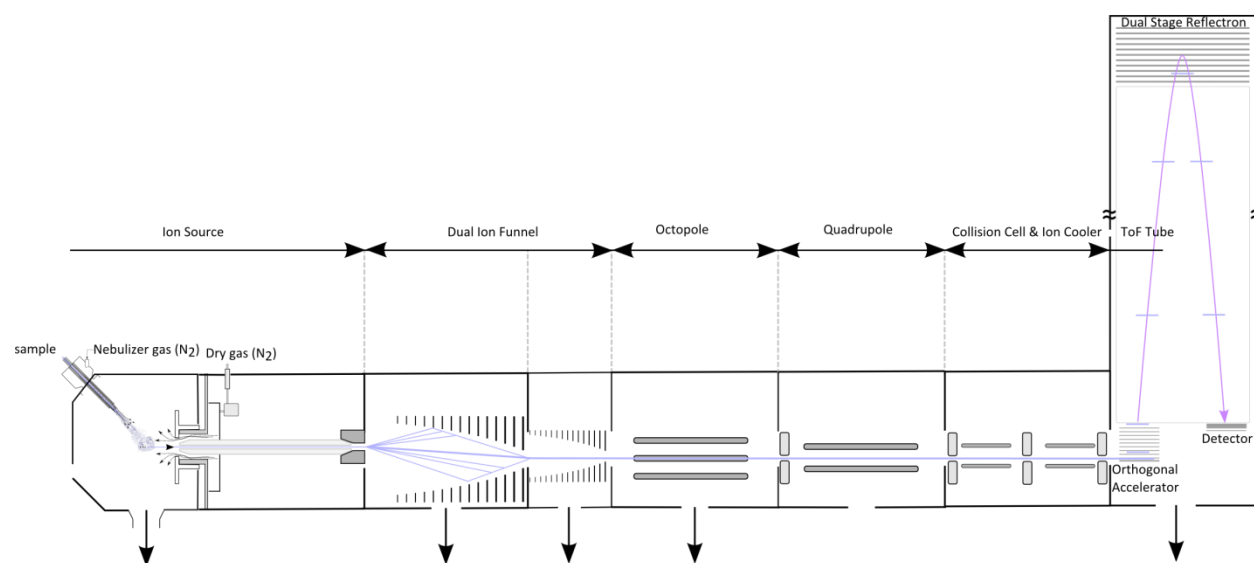


Figure 1-37: Scheme of the maXis

The ESI ion source of the maXis is very similar to the one discussed for the Esquire6000. The sample solution is introduced by a nebulizer supported by the nebulizer gas (Nitrogen in both cases). As outlined above, the electrospray generates small, charged droplets which eventually develop into solvent-free ions of the analyte. Ions enter the analyser through a glass capillary due to an electrostatic gradient from the tip of the nebulizer to the end plate. Ions are further transferred by a dual ion funnel stage, with successive reduction of pressure. A RF voltage is applied inside the funnel to confine the ion beam and two DC voltages direct the ion beam through the funnel. The newly applied dual funnel transmission concept is a highly sensitive and soft process as the widely open funnel collects almost all the ions with a high transmission efficiency, and at the same time uncharged particles are pumped away through the gaps between the funnel plates. The funnel axis is offset from the axis of the capillary in order to eliminate possible contamination. By increasing the DC potentials of the funnel one can accelerate ions into the second funnel. This feature can be employed to activate in-source collision-induced dissociation (ISCID)<sup>[109-115]</sup> which allows to conduct an MS<sup>3</sup>-type experiment with the maXis. Subsequently, a multipole stage is utilized to transport and focus ions under a further reduced pressure of  $3 \times 10^{-4}$  mbar. The following analytical quadrupole is the first analyser in the maXis which allows one to store and isolate ions of interest and additionally the quadrupole functions as an ion guide. A collision cell is located behind the quadrupole to dissociate selected parent ions by colliding them with neutral collision gas typically nitrogen or argon at about  $10^{-2}$  mbar. This process is called collision-induced dissociation (CID). Thereafter, ions are guided into a cooling cell which is an extra pressure stage before ions flow into the MS analyzer. The time of flight analyzer in maXis is composed of three main components, which are the orthogonal acceleration device,

the reflectron and the detector. Packages of ions are accelerated by the orthogonal acceleration device via a pulsed mode. Possible differences in ion final kinetic energy are adjusted by the dual stage reflectron. Eventually, ions are reflected towards the detector and thus detected. During this process, the ion signal is converted to an electrical signal by the detector. In the maXis, the electrical signal is transmitted to a digitizer card which is mounted at the computer for data acquisition.

The following performance features are valid for instrument with a 4GHz digitizer card:

- Mass range
  - 5-20,000 m/z (the full scan range is restricted by the size of digitizer card)
- Mass resolution
  - 40,000-60,000 FWHM
- Mass accuracy
  - 600-800 ppb
- Signal to noise ratio
  - $\geq 50 : 1$
- Scan speed
  - 20 full spectra per second

---

### 1.4.3 AXIMA CONFIDENCE (SHIMADZU)

---

Matrix-assisted laser desorption/ionisation (MALDI) measurements were conducted with a Shimadzu Axima (model Confidence) time-of-flight (ToF) instrument. The components of the Shimadzu Confidence are presented in Figure 1-38 and the corresponding steps of performance are described below.

1. A pulsed laser beam ( $N_2$ , 50 Hz,  $\lambda = 337$  nm) is directed to the sample plate
2. When there is no matrix presents (LDI), the laser light is directly absorb by the sample, which is desorped and ionised. In MALDI, energy is absorbed by the matrix, by which the sample is protected from direct laser exposure. The sample is now ionised by energy transfer from excited matrix molecules.
3. Ions are accelerated at the extraction plates, where a high voltage is applied, and driven towards the flight tube.
4. The ion beam is focussed by the ion lenses.
5. Deflector plates direct the ion beam towards the linear detector at the end of the flight tube.
6. An ion gate is placed here allowing the deflection of unnecessary low mass ions and the selection of an ion of interest.
7. Additional deflector plates correct the ion beam deviating from the path towards the detector.
8. Ions are detected at the linear detector at the end of the instrument.
9. The ion beam is directed into a reflectron with a curved high-voltage electric field applied, which provides energy selectivity and produces a better resolution, and then reflected towards the reflectron mode detector.
10. Ions are detected by the reflectron mode detector.

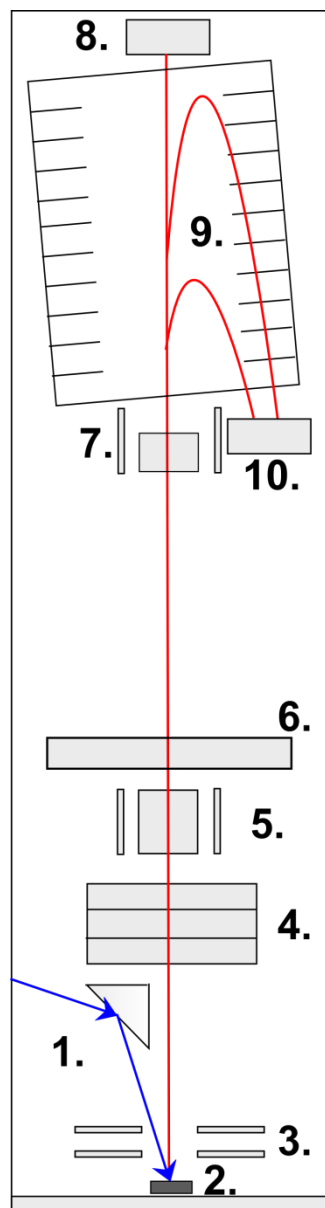


Figure 1-38: Diagram of the MALDI-ToF instrument from Shimadzu AXIMA Confidence

The instrument is characterised by the following performance features:

- Mass range:
    - linear: 1-500 kDa
    - reflectron: 1-80 kDa
  - Mass resolution:
    - linear: >5,000 FWHM over peak of ACTH 18-39, ((M+H) + 2,465 Da)
    - reflectron: >14,000 FWHM over peak of ACTH 7-38, ((M+H) + 3,660 Da)
    - MS/MS: isotopic resolution of fragments
  - Mass accuracy:
    - linear: <30 ppm with internal calibration  
<200 ppm with external calibration\*
    - reflectron: <10 ppm with internal calibration  
<100 ppm with external calibration\*
- \* Nearest neighbour external calibration on 384-well sample target, within 30 minutes.
- Precursor resolution: >200 FWHM at 1000 Da
  - Sensitivity:
    - linear: 250 fmol - bovine serum albumin (loaded)  
250 amol - Glu-1-Fibropeptide B (loaded)
    - reflectron: 500 amol - Glu-1-Fibropeptide B (loaded)
    - MS/MS: 25 fmol - Glu-1-Fibropeptide B (loaded)

(FWHM = Full Width at Half Maximum, as shown in Figure 1-3 in previous section)

## MALDI SAMPLE PREPARATION

A stainless steel plate is designed as sample carrier for the (MA)LDI measurements. The target plate offers a 16 × 24 spot array, which has a 3 mm spot diameter. The plate measurements are 84 × 128 mm<sup>2</sup>. The plate is shown in below in Figure 1-39.

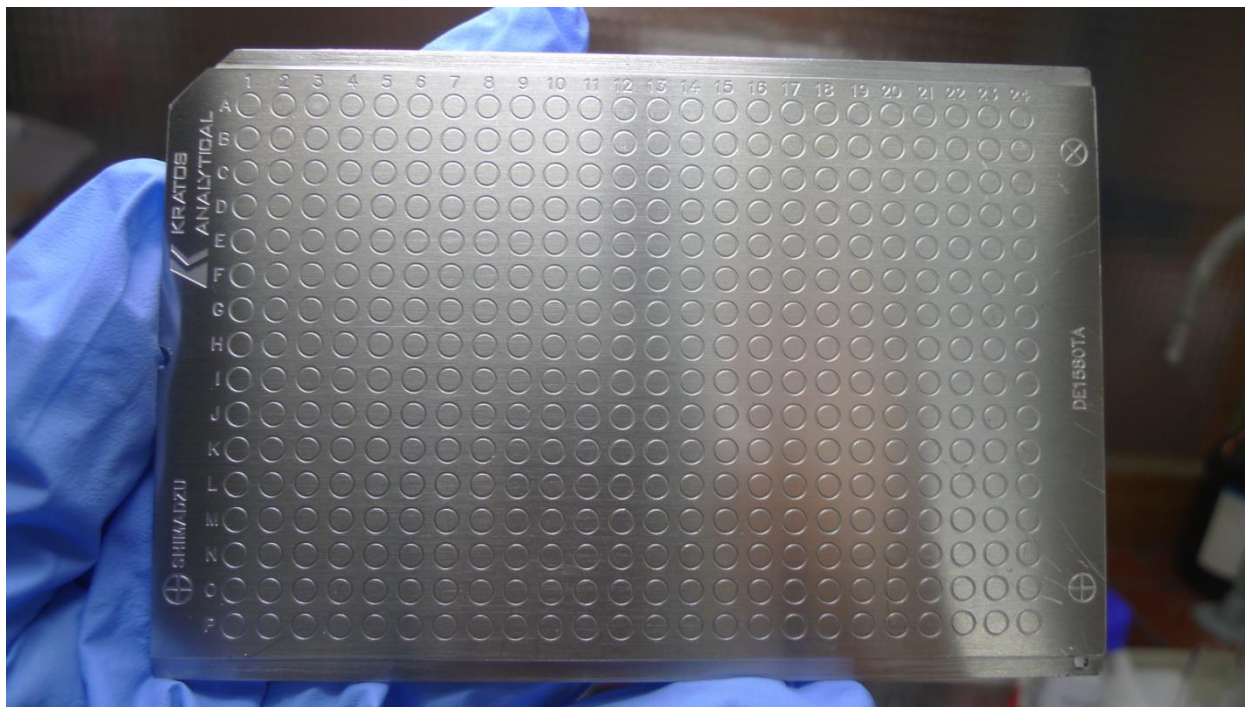


Figure 1-39: Photo of a MALDI sample plate from Shimadzu

Samples were prepared at a concentration of 1mg/mL in toluene or DCM for LDI/MALDI experiments. For MALDI analysis, the matrix 2-[(2E)-3-(4-tert-butylphenyl)-2-methylprop-2-enylidene]malononitrile (DCTB), at a concentration of 1mg/mL, was generally applied. The analyte and DCTB were mixed at a molar ratio (analyte: DCTB) of 1:50 just before performing the experiment. This ratio was found in earlier experiments as suitable for the MALDI analysis of most fullerene derivatives. The dried-droplet method<sup>[97]</sup> is generally applied in which crystallization of analyte and matrix occur as the solvent evaporates. Typically 10-20  $\mu$ L of sample solution was deposited onto each spot on the target plate and the droplets shrank as the solvent evaporated leaving the sample on the target spot. Another method, (ultra) thin layer method<sup>[116]</sup>, is also applied in which matrix and samples are applied to the target plate layer by layer, alternately. Samples can also be measured in a solid state by being adhered to the target plate with double-sided glue tape. This solvent-free method is employed to overcome adverse solvent related effects, such as insolubility or degradation.<sup>[117-129]</sup>

The choice of matrix can be ultimately determined by the method of ionisation needed for the analytes; however, the wavelength of the applied laser is also an important factor.

## INSTRUMENTAL CALIBRATION

The instrument needed calibration in both linear and reflectron mode. In general, fullerenes were employed for calibration using the masses of C<sub>60</sub> (m/z 720), C<sub>70</sub> (m/z 840) and C<sub>84</sub> (m/z 1008). For higher masses a peptide mixture (Bruker) was used.

## 2 REFERENCE

---

- [1] K. Duerr, J. Olah, R. Davydov, M. Kleimann, J. Li, N. Lang, R. Puchta, E. Hubner, T. Drewello, J. N. Harvey, N. Jux, I. Ivanović-Burmazović, *Dalton Trans.* **2010**, 39, 2049-2056.
- [2] K. Duerr, O. Troeppner, J. Olah, J. Li, A. Zahl, T. Drewello, N. Jux, J. N. Harvey, I. Ivanović-Burmazović, *Dalton Trans.* **2012**, 41, 546-557.
- [3] J. Li, W. Wei, L. C. Nye, P. S. Schulz, P. Wasserscheid, I. Ivanovic-Burmazovic, T. Drewello, *Phys. Chem. Chem. Phys.* **2012**, 14, 5115-5121.
- [4] I. Niedermaier, C. Kolbeck, N. Taccardi, P. S. Schulz, J. Li, T. Drewello, P. Wasserscheid, H. P. Steinrück, F. Maier, *ChemPhysChem* **2012**, 13, 1725-1735.
- [5] Y. Xia, S. A. McLuckey, *J. Am. Soc. Mass Spectrom.* **2008**, 19, 173-189.
- [6] A. K. Vrkic, T. Taverner, P. F. James, R. A. O'Hair, *Dalton Trans.* **2004**, 197-208.
- [7] C. E. C. A. Hop, D. A. Saulys, D. F. Gaines, *J. Am. Soc. Mass Spectrom.* **1995**, 6, 860-865.
- [8] G. J. van Berkel, F. M. Zhou, *Anal. Chem.* **1995**, 67, 3958-3964.
- [9] X. P. Li, J. A. Stone, *Can. J. Chem.* **1987**, 65, 2454-2460.
- [10] A. P. Bateman, M. L. Walser, Y. Desyaterik, J. Laskin, A. Laskin, S. A. Nizkorodov, *Environ. Sci. Technol.* **2008**, 42, 7341-7346.
- [11] J. r. H. Gross, *Mass spectrometry a textbook*, Springer, Berlin u.a., **2004**.
- [12] P. Debievre, P. D. P. Taylor, *Int. J. Mass Spectrom. Ion Processes* **1993**, 123, 149-166.
- [13] N. M. M. Nibbering, *4. Fundamentals of and Applications to Organic (and Organometallic) Compounds, Vol. 4*, 1. ed., Elsevier, Amsterdam, **2005**.
- [14] M. Yamashita, J. B. Fenn, *J. Phys. Chem.* **1984**, 88, 4451-4459.
- [15] M. L. Alexandrov, L. N. Gall, N. V. Krasnov, V. I. Nikolaev, V. A. Pavlenko, V. A. Shkurov, *Dokl Akad Nauk Sssr+* **1984**, 277, 379-383.
- [16] M. Dole, H. L. Cox, J. Gieniec, *Adv. Chem. Ser.* **1973**, 73-84.
- [17] M. Dole, H. L. Cox, J. Gieniec, *Abstr. Pap. Am. Chem. Soc.* **1971**, 44-47.
- [18] M. N. Eberlin, *Eur. J. Mass Spectrom.* **2007**, 13, 19-28.
- [19] K. Schug, P. Frycak, N. M. Maier, W. Lindner, *Anal. Chem.* **2005**, 77, 3660-3670.
- [20] K. S. Wang, G. W. Gokel, *J. Org. Chem.* **1996**, 61, 4693-4697.
- [21] P. Kebarle, L. Tang, *Anal. Chem.* **1993**, 65, A972-A986.
- [22] P. Kebarle, U. H. Verkerk, *Mass Spectrom. Rev.* **2009**, 28, 898-917.
- [23] C. N. McEwen, B. S. Larsen, S. Trimpin, *Anal. Chem.* **2010**, 82, 4998-5001.
- [24] L. H. Cohen, A. I. Gusev, *Anal. Bioanal. Chem.* **2002**, 373, 571-586.
- [25] G. McCombie, R. Knochenmuss, *Anal. Chem.* **2004**, 76, 4990-4997.
- [26] R. Knochenmuss, *Anal. Chem.* **2003**, 75, 2199-2207.
- [27] R. Knochenmuss, *Anal. Chem.* **2004**, 76, 3179-3184.
- [28] R. Knochenmuss, A. Stortelder, K. Breuker, R. Zenobi, *J. Mass Spectrom.* **2000**, 35, 1237-1245.
- [29] R. Knochenmuss, R. Zenobi, *Chem. Rev. (Washington, DC, U. S.)* **2003**, 103, 441-452.
- [30] T. Brown, N. L. Clipston, N. Simjee, H. Luftmann, H. Hungerbühler, T. Drewello, *Int. J. Mass Spectrom.* **2001**, 210, 249-263.
- [31] Y. V. Vasil'ev, O. G. Khvostenko, A. V. Streletskii, O. V. Boltalina, S. G. Kotsiris, T. Drewello, *J. Phys. Chem. A* **2006**, 110, 5967-5972.
- [32] L. S. Wang, J. Conceicao, C. M. Jin, R. E. Smalley, *Chem. Phys. Lett.* **1991**, 182, 5-11.
- [33] W. C. Wiley, I. H. McLaren, *J. Mass Spectrom.* **1997**, 32, 4-11.
- [34] R. E. March, *J. Mass Spectrom.* **1997**, 32, 351-369.
- [35] R. E. March, *Int. J. Mass Spectrom.* **2000**, 200, 285-312.
- [36] G. T. Abraham, A. Chatterjee, A. G. Menon, *Int. J. Mass Spectrom.* **2004**, 231, 1-16.

- [37] E. K. G. Subramanyan, A. K. Mohanty, *Int. J. Mass Spectrom.* **2011**, *303*, 31-41.
- [38] J. N. Louris, R. G. Cooks, *Abstr. Pap. Am. Chem. Soc.* **1988**, *196*, 108-ANYL.
- [39] C. Collette, L. Drahos, E. De Pauw, K. Vekey, *Rapid Commun. Mass Spectrom.* **1998**, *12*, 1673-1678.
- [40] X. H. Guo, M. C. Duursma, P. G. Kistemaker, N. M. M. Nibbering, K. Vekey, L. Drahos, R. M. A. Heeren, *J. Mass Spectrom.* **2003**, *38*, 597-606.
- [41] J. Naban-Maillet, D. Lesage, A. Bossee, Y. Gimbert, J. Sztaray, K. Vekey, J. C. Tabet, *J. Mass Spectrom.* **2005**, *40*, 1-8.
- [42] A. Pak, D. Lesage, Y. Gimbert, K. Vekey, J. C. Tabet, *J. Mass Spectrom.* **2008**, *43*, 447-455.
- [43] D. Rondeau, N. Galland, E. L. Zins, C. Pepe, L. Drahos, K. Vekey, *J. Mass Spectrom.* **2011**, *46*, 100-111.
- [44] K. Vekey, *J. Mass Spectrom.* **1996**, *31*, 445-463.
- [45] K. Vekey, A. Somogyi, V. H. Wysocki, *J. Mass Spectrom.* **1995**, *30*, 212-217.
- [46] W. H. H. G. A. Muccini, R. Barker, *J. Phys. Chem.* **1964**, *68*, 261-264.
- [47] R. Kaufmann, P. Chaurand, D. Kirsch, B. Spengler, *Rapid Commun. Mass Spectrom.* **1996**, *10*, 1199-1208.
- [48] D. J. Kenny, J. M. Brown, M. E. Palmer, M. F. Snel, R. H. Bateman, *J. Am. Soc. Mass Spectrom.* **2006**, *17*, 60-66.
- [49] B. A. Mamyrin, *Int. J. Mass Spectrom.* **2001**, *206*, 251-266.
- [50] T. J. Cornish, R. J. Cotter, *Rapid Commun. Mass Spectrom.* **1994**, *8*, 781-785.
- [51] T. J. Cornish, R. J. Cotter, *Rapid Commun. Mass Spectrom.* **1993**, *7*, 1037-1040.
- [52] R. J. Cotter, B. D. Gardner, S. Iltchenko, R. D. English, *Anal. Chem.* **2004**, *76*, 1976-1981.
- [53] R. J. Cotter, B. D. Gardner, S. Iltchenko, D. X. Wang, R. Gundry, *Abstr. Pap. Am. Chem. Soc.* **2004**, *227*, U272-U272.
- [54] R. J. Cotter, W. Griffith, C. Jelinek, *J. Chromatogr., B: Anal. Technol. Biomed. Life Sci.* **2007**, *855*, 2-13.
- [55] A. K. Shukla, J. H. Futrell, *J. Mass Spectrom.* **2000**, *35*, 1069-1090.
- [56] H. W. Kroto, J. R. Heath, S. C. O'Brien, R. F. Curl, R. E. Smalley, *Nature* **1985**, *318*, 162-163.
- [57] W. Kratschmer, L. D. Lamb, K. Fostiropoulos, D. R. Huffman, *Nature* **1990**, *347*, 354-358.
- [58] V. Parasuk, J. Almlöf, *Chem. Phys. Lett.* **1991**, *184*, 187-190.
- [59] T. Tomiyama, S. Uchiyama, H. Shinohara, *Chem. Phys. Lett.* **1997**, *264*, 143-148.
- [60] M. S. Dresselhaus, G. Dresselhaus, P. C. Eklund, *Science of fullerenes and carbon nanotubes*, Academic Press, San Diego, **1996**.
- [61] P. W. Stephens, L. Mihaly, P. L. Lee, R. L. Whetten, S. M. Huang, R. Kaner, F. Deiderich, K. Holczer, *Nature* **1991**, *351*, 632-634.
- [62] H. Tanaka, K. Takeuchi, *Appl Phys a-Mater* **2005**, *80*, 759-761.
- [63] R. F. Curl, H. W. Kroto, R. E. Smalley, *S Afr J Chem-S-Afr T* **1997**, *50*, 102-105.
- [64] G. B. M. Vaughan, P. A. Heiney, J. E. Fischer, D. E. Luzzi, D. A. Rickettsfoot, A. R. Mcghee, Y. W. Hui, A. L. Smith, D. E. Cox, W. J. Romanow, B. H. Allen, N. Coustel, J. P. McCauley, A. B. Smith, *Science* **1991**, *254*, 1350-1353.
- [65] M. A. Verheijen, H. Meekes, G. Meijer, P. Bennema, J. L. Deboer, S. Vansmaalen, G. Vantendeloo, S. Amelinckx, S. Muto, J. Vanlanduyt, *Chem. Phys.* **1992**, *166*, 287-297.
- [66] W. I. F. David, R. M. Ibberson, J. C. Matthewman, K. Prassides, T. J. S. Dennis, J. P. Hare, H. W. Kroto, R. Taylor, D. R. M. Walton, *Nature* **1991**, *353*, 147-149.
- [67] R. D. Beck, P. Weis, A. Hirsch, I. Lamparth, *J. Phys. Chem.* **1994**, *98*, 9683-9687.
- [68] M. D. Tzirakis, M. Orfanopoulos, *Angew. Chem., Int. Ed.* **2010**, *49*, 5891-5893.
- [69] O. V. Boltalina, L. N. Sidorov, V. F. Bagryantsev, V. A. Seredenko, A. S. Zapolskii, J. M. Street, R. Taylor, *J Chem Soc Perk T 2* **1996**, 2275-2278.



- [70] K. Komatsu, M. Murata, Y. Murata, *Science* **2005**, *307*, 238-240.
- [71] M. Murata, Y. Murata, K. Komatsu, *J. Am. Chem. Soc.* **2006**, *128*, 8024-8033.
- [72] Y. Murata, S. Maeda, M. Murata, K. Komatsu, *J. Am. Chem. Soc.* **2008**, *130*, 6702-6703.
- [73] Y. Murata, M. Murata, K. Komatsu, *J. Am. Chem. Soc.* **2003**, *125*, 7152-7153.
- [74] Y. Murata, M. Murata, K. Komatsu, *Chemistry* **2003**, *9*, 1600-1609.
- [75] S. Stevenson, G. Rice, T. Glass, K. Harich, F. Cromer, M. R. Jordan, J. Craft, E. Hadju, R. Bible, M. M. Olmstead, K. Maitra, A. J. Fisher, A. L. Balch, H. C. Dorn, *Nature* **1999**, *401*, 55-57.
- [76] M. Krause, H. Kuzmany, P. Georgi, L. Dunsch, K. Vietze, G. Seifert, *J. Chem. Phys.* **2001**, *115*, 6596-6605.
- [77] M. Saunders, H. A. Jimenezvazquez, R. J. Cross, S. Mroczkowski, D. I. Freedberg, F. A. L. Anet, *Nature* **1994**, *367*, 256-258.
- [78] M. Freemantle, C. Royal Society of, *An introduction to ionic liquids*, RSC Pub., Cambridge, **2010**.
- [79] S. Zhang, *Ionic liquids physicochemical properties*, 1. ed., Elsevier, Amsterdam u.a., **2009**.
- [80] C. J. Hogan, Jr., J. Fernandez de la Mora, *J. Am. Soc. Mass Spectrom.* **2010**, *21*, 1382-1386.
- [81] T. Singh, A. Kumar, *J. Phys. Chem. B* **2007**, *111*, 7843-7851.
- [82] A. M. Fernandes, M. A. Rocha, M. G. Freire, I. M. Marrucho, J. A. Coutinho, L. M. Santos, *J. Phys. Chem. B* **2011**, *115*, 4033-4041.
- [83] G. P. Jackson, D. C. Duckworth, *Chem. Commun.* **2004**, 522-523.
- [84] P. J. Dyson, J. S. McIndoe, D. Zhao, *Chem Commun (Camb)* **2003**, 508-509.
- [85] P. J. Dyson, I. Khalaila, S. Luetzgen, J. S. McIndoe, D. Zhao, *Chem Commun (Camb)* **2004**, 2204-2205.
- [86] Z. B. Alfassi, R. E. Huie, B. L. Milman, P. Neta, *Anal. Bioanal. Chem.* **2003**, *377*, 159-164.
- [87] F. C. Gozzo, L. S. Santos, R. Augusti, C. S. Consorti, J. Dupont, M. N. Eberlin, *Chem-Eur J* **2004**, *10*, 6187-6193.
- [88] M. A. Henderson, J. S. McIndoe, *Chem. Commun.* **2006**, 2872-2874.
- [89] A. Deyko, K. R. J. Lovelock, P. Licence, R. G. Jones, *Phys. Chem. Chem. Phys.* **2011**, *13*, 16841-16850.
- [90] D. F. Kennedy, C. J. Drummond, *J. Phys. Chem. B* **2009**, *113*, 5690-5693.
- [91] Y. Fujiwara, N. Saito, H. Nonaka, T. Nakanaga, S. Ichimura, *Nucl. Instrum. Methods Phys. Res., Sect. B* **2010**, *268*, 1938-1941.
- [92] I. Nakurte, P. Mekss, K. Klavins, A. Zicmanis, G. Vavilina, S. Dubrovina, *Eur. J. Mass Spectrom.* **2009**, *15*, 471-478.
- [93] E. J. H. Yoo, L. Feketeova, G. N. Khairallah, R. A. J. O'Hair, *J. Phys. Chem. A* **2011**, *115*, 4179-4185.
- [94] S. R. Kass, *J. Am. Chem. Soc.* **2005**, *127*, 13098-13099.
- [95] J. S. McIndoe, M. A. Henderson, *Abstr. Pap. Am. Chem. Soc.* **2008**, 236.
- [96] D. W. Armstrong, L. K. Zhang, L. He, M. L. Gross, *Anal. Chem.* **2001**, *73*, 3679-3686.
- [97] M. Karas, F. Hillenkamp, *Anal. Chem.* **1988**, *60*, 2299-2301.
- [98] R. W. Garden, J. V. Sweedler, *Anal. Chem.* **2000**, *72*, 30-36.
- [99] S. Carda-Broch, A. Berthod, D. W. Armstrong, *Rapid Commun. Mass Spectrom.* **2003**, *17*, 553-560.
- [100] Y. L. Li, M. L. Gross, F. F. Hsu, *J. Am. Soc. Mass Spectrom.* **2005**, *16*, 679-682.
- [101] J. J. Jones, S. M. Batoy, C. L. Wilkins, R. Liyanage, J. O. Lay, Jr., *J. Am. Soc. Mass Spectrom.* **2005**, *16*, 2000-2008.
- [102] Y. L. Li, M. L. Gross, *J. Am. Soc. Mass Spectrom.* **2004**, *15*, 1833-1837.
- [103] D. Bungert, S. Bastian, D. M. Heckmann-Pohl, F. Giffhorn, E. Heinzle, A. Tholey, *Biotechnol. Lett.* **2004**, *26*, 1025-1030.
- [104] A. Tholey, E. Heinzle, *Anal. Bioanal. Chem.* **2006**, *386*, 24-37.



- [105] K. Durr, B. P. Macpherson, R. Warratz, F. Hampel, F. Tuczek, M. Helmreich, N. Jux, I. Ivanovic-Burmazovic, *J. Am. Chem. Soc.* **2007**, *129*, 4217-4228.
- [106] P. T. Szabo, Z. Kele, *Rapid Commun. Mass Spectrom.* **2001**, *15*, 2415-2419.
- [107] J. R. Wickens, R. Sleeman, B. J. Keely, *Rapid Commun. Mass Spectrom.* **2007**, *21*, 2491-2496.
- [108] J. F. de la Mora, G. J. Van Berkel, C. G. Enke, R. B. Cole, M. Martinez-Sanchez, J. B. Fenn, *J. Mass Spectrom.* **2000**, *35*, 939-952.
- [109] C. Bure, G. Le Falher, C. Lange, A. Delmas, *J. Mass Spectrom.* **2004**, *39*, 817-823.
- [110] K. C. Crellin, E. Sible, J. van Antwerp, *Int. J. Mass Spectrom.* **2003**, *222*, 281-311.
- [111] C. Kubwabo, N. Vais, F. M. Benoit, *Rapid Commun. Mass Spectrom.* **2005**, *19*, 597-604.
- [112] O. Nunez, E. Moyano, M. T. Galceran, *J. Mass Spectrom.* **2004**, *39*, 873-883.
- [113] C. E. Wujcik, E. P. Kadar, *Rapid Commun. Mass Spectrom.* **2008**, *22*, 3195-3206.
- [114] P. Marquet, N. Venisse, E. Lacassie, G. Lachatre, *Analisis* **2000**, *28*, 925-934A.
- [115] R. Tuytten, F. Lemiere, E. L. Esmans, W. A. Herrebout, B. J. van der Veken, E. Dudley, R. P. Newton, E. Witters, *J. Am. Soc. Mass Spectrom.* **2006**, *17*, 1050-1062.
- [116] D. Fenyo, Q. Wang, J. A. DeGrasse, J. C. Padovan, M. Cadene, B. T. Chait, *J. Vis. Exp.* **2007**, 192.
- [117] S. D. Hanton, T. M. McEvoy, J. R. Stets, *J. Am. Soc. Mass Spectrom.* **2008**, *19*, 874-881.
- [118] S. D. Hanton, D. M. Parees, *J. Am. Soc. Mass Spectrom.* **2005**, *16*, 90-93.
- [119] S. D. Hanton, J. R. Stets, *J. Am. Soc. Mass Spectrom.* **2009**, *20*, 1115-1118.
- [120] A. R. Hortal, P. Hurtado, B. Martinez-Haya, A. Arregui, L. Banares, *J. Phys. Chem. B* **2008**, *112*, 8530-8535.
- [121] L. Hughes, M. F. Wyatt, B. K. Stein, A. G. Brenton, *Anal. Chem.* **2009**, *81*, 543-550.
- [122] S. G. Kotsiris, Y. V. Vasil'ev, A. V. Streletsii, M. Han, L. P. Mark, O. V. Boltalina, N. Chronakis, M. Orfanopoulos, H. Hungerbühler, T. Drewello, *Eur. J. Mass Spectrom.* **2006**, *12*, 397-408.
- [123] I. Kudaka, D. Asakawa, K. Mori, K. Hiraoka, *J. Mass Spectrom.* **2008**, *43*, 436-446.
- [124] H. Pizzala, C. Barrere, M. Mazarin, F. Ziarelli, L. Charles, *J. Am. Soc. Mass Spectrom.* **2009**, *20*, 1906-1911.
- [125] S. M. Puolitaival, K. E. Burnum, D. S. Cornett, R. M. Caprioli, *J. Am. Soc. Mass Spectrom.* **2008**, *19*, 882-886.
- [126] A. Sroka-Bartnicka, W. Ciesielski, J. Libiszowski, A. Duda, M. Sochacki, M. J. Potrzebowski, *Anal. Chem.* **2010**, *82*, 323-328.
- [127] S. Trimpin, *J. Mass Spectrom.* **2010**, *45*, 471-485.
- [128] S. Trimpin, M. L. Deinzer, *J. Am. Soc. Mass Spectrom.* **2007**, *18*, 1533-1543.
- [129] S. Trimpin, A. C. Grimsdale, H. J. Rader, K. Müllen, *Anal. Chem.* **2002**, *74*, 3777-3782.
- [130] J. Schonamsgruber, B. Schade, R. Kirschbaum, J. Li, W. Bauer, C. Bottcher, T. Drewello, A. Hirsch, *Eur. J. Org. Chem.* **2012**, 6179-6186.
- [131] K. M. Kadish, K. M. Smith, R. Guilard, *The porphyrin handbook*, Academic Press, San Diego, Calif.
- [132] E. G. Kovaleva, J. D. Lipscomb, *Science* **2007**, *316*, 453-457.
- [133] A. C. Cole, J. L. Jensen, I. Ntai, K. L. Tran, K. J. Weaver, D. C. Forbes, J. H. Davis, Jr., *J. Am. Chem. Soc.* **2002**, *124*, 5962-5963.
- [134] T. Joseph, S. Sahoo, S. B. Halligudi, *J. Mol. Catal. A: Chem.* **2005**, *234*, 107-110.
- [135] E. J. Angueira, M. G. White, *Abstr. Pap. Am. Chem. Soc.* **2004**, *228*, U769-U769.
- [136] K. Arya, D. S. Rawat, A. Dandia, H. Sasai, *J. Fluorine Chem.* **2012**, *137*, 117-122.
- [137] Z. Y. Duan, Y. L. Gu, Y. Q. Deng, *Catal. Commun.* **2006**, *7*, 651-656.
- [138] M. M. Heravi, N. Tavakoli-Hoseini, F. F. Bamoharram, *Synth. Commun.* **2011**, *41*, 707-714.
- [139] N. Tavakoli-Hoseini, M. M. Heravi, F. F. Bamoharram, *Asian J. Chem.* **2010**, *22*, 7208-7212.
- [140] W. J. Xiao, X. X. Wang, Q. Chen, T. H. Wu, Y. Wu, L. Z. Dai, C. S. Song, *Chem. Lett.* **2010**, *39*, 1112-1113.
- [141] D. Q. Xu, W. L. Yang, S. P. Luo, B. T. Wang, M. Wu, Z. Y. Xu, *Eur. J. Org. Chem.* **2007**, 1007-1012.

### 3 APPENDIX

---

- [P1]. K. Duerr, J. Olah, R. Davydov, M. Kleimann, **J. Li**, N. Lang, R. Puchta, E. Hubner, T. Drewello, J. N. Harvey, N. Jux, I. Ivanović-Burmazović  
*Studies on an iron(III)-peroxo porphyrin. Iron(III)-peroxo or iron(II)-superoxo?*  
*Dalton Trans.* **2010**, 39, 2049-2056.
- [P2]. K. Duerr, O. Troeppner, J. Olah, **J. Li**, A. Zahl, T. Drewello, N. Jux, J. N. Harvey, I. Ivanović-Burmazović<sup>[2]</sup>  
*Solution behavior of iron(III) and iron(II) porphyrins in DMSO and reaction with superoxide. Effect of neighboring positive charge on thermodynamics, kinetics and nature of iron-(su)peroxo product*  
*Dalton Trans.* **2012**, 41, 546-557.
- [P3]. **J. Li**, W. Wei, L. C. Nye, P. S. Schulz, P. Wasserscheid, I. Ivanović-Burmazović, T. Drewello<sup>[3]</sup>  
*Zwitterionic clusters with dianion core produced by electrospray ionisation of Brønsted acidic ionic liquids*  
*Phys. Chem. Chem. Phys.* **2012**, 14, 5115-5121.
- [P4]. I. Niedermaier, C. Kolbeck, N. Taccardi, P. S. Schulz, **J. Li**, T. Drewello, P. Wasserscheid, H. P. Steinrück, F. Maier<sup>[4]</sup>  
*Organic reactions in ionic liquids studied by in situ XPS.*  
*ChemPhysChem* **2012**, 13, 1725-1735.
- [P5]. J. Schönambsgruber, B. Schade, R. Kirschbaum, **J. Li**, W. Bauer, C. Böttcher, T. Drewello, A. Hirsch<sup>[130]</sup>  
*Synthesis and Aggregation Properties of Polycationic Perylenetetracarboxylic Acid Diimides*  
*Eur. J. Org. Chem.* **2012**, 6179-6186.

**Solution behavior of iron(III) and iron(II) porphyrins in DMSO and reaction with superoxide. Effect of neighboring positive charge on thermodynamics, kinetics and nature of iron-(su)peroxo product**

P1

This work represents a continuation of research that is led by I. Ivanović-Burmazović, in close collaboration with N. Jux and their co-workers. The main intention is to enhance the understanding of the different forms that may exist of the heme iron dioxygen adduct, which is a key intermediate in the metalloenzyme-catalyzed dioxygen and hydrogen peroxide activation. It was found in the present study that iron(II)-superoxo species coexist with the commonly accepted form of iron(III)-peroxo species. The product  $\text{Fe}^{\text{II}}$ -superoxo structure has been reported as a reactive intermediate of non-heme extradiol dioxygenase<sup>[131]</sup>. It is known that oxygen is transported and stored by hemoglobin and myoglobin in the human metabolism and both of them contain heme groups. However, the nature of the iron dioxygen adduct is still under debate in spite of many studies. Results from the present work shed new light on the nature of heme iron(III)-peroxo species and provide new insights into the equilibrium between heme iron(III)-peroxo and iron(II)-superoxo species, thus improving the understanding of the appearance of heme iron dioxygen adducts in solution.

IR, EPR, mass spectrometry and Mössbauer spectroscopy were employed in this study and led to complementary findings on the system under investigation. Time-dependent ESI-MS measurements were conducted and provided a comprehensive overview of the whole reaction process. Tandem mass spectrometry ( $\text{MS}^2$ ) was employed and confirmed successfully the iron charge state through the fragmentation of the  $[\text{K} + \text{KFe}(\text{Porph})(\text{O}_2)]^+$  species. In the  $\text{MS}^2$  experiment the  $[\text{K} + \text{KFe}(\text{Porph})(\text{O}_2)]^+$  ion dissociates into  $[\text{K} + \text{Fe}(\text{Porph})]^+$  by loss of the  $\text{KO}_2$  group. It is clear that iron stays in the  $\text{Fe}^{\text{II}}$  form in the  $[\text{K} + \text{Fe}(\text{Porph})]^+$  fragment ion, which strongly supports the characterisation of the species as an intact superoxide adduct of the metal porphyrin and our interpretation of the existence of the low-spin iron(II) species ( $\text{Fe}^{\text{II}}\text{-O}_2^-$ ) in the product solution.

**Studies on an iron(III)-peroxo porphyrin. Iron(III)-peroxo or iron(II)-superoxo?**

Coordination and subsequent redox reaction of iron(II)porphyrin with superoxide ions in the aprotic solvent DMSO is studied in this publication. This study provides insight into activation of molecular oxygen by iron-centered heme-containing enzymes going through the formation of the one-electron reduced form of the iron-dioxygen adduct, which is widely accepted as iron(III)-peroxo species. The same species can be obtained in the reaction between heme iron(II) and superoxide ( $O_2^-$ ). Spectroelectrochemistry, NMR, MS, thermal dynamics and kinetics as well as DFT calculations were employed to study this reaction and it has been our main task to study these processes by ESI-MS.

$Fe^{III}(tBuTPP)Cl$  was studied initially in DMSO, in which  $Fe^{III}(tBuTPP)Cl$  changes into the forms of  $[Fe^{III}(tBuTPP)Cl(DMSO)]$  and  $[Fe^{III}(tBuTPP)(DMSO)_2]^+$ .<sup>[132]</sup> In ESI the ion  $[Fe^{III}(tBuTPP)(DMSO)]^+$  was observed and fragmented into the ion  $[Fe^{III}(tBuTPP)]^+$  by losing the axial ligand. Time-dependent measurements were conducted for the reaction mixture of  $[Fe^{III}(tBuTPP)(DMSO)_2]^+$  and  $KO_2$ , from which dioxygen species were observed and further investigated by tandem mass spectrometry. The same experiments were performed for comparison with an iron(III)porphyrin complex linked to a crown ether (aza-18-crown-6), and with the crown ether added to the solution (i.e. not bound). The effects due to the neighbouring positive charge from the  $K^+$ -crown ether moiety on thermodynamics, kinetics and nature of iron-(su)peroxo product are discussed in great detail.

In summary, this study sheds light on the solution behaviour of iron(III) and iron(II)porphyrins in DMSO and their reaction behaviour with superoxide.

## **Zwitterionic clusters with dianion core produced by electrospray ionisation of Brønsted acidic ionic liquids**

Novel Brønsted acidic ionic liquids (BAILs) are known for their unique dual usage in chemical reactions where they are employed as acidic catalysts as well as solvents.<sup>[133]</sup> BAILs have been widely claimed to be able to provide green, efficient and reusable catalyst system and reaction media for Fischer esterification.<sup>[134-141]</sup> The new types of BAILs that were investigated in this work were synthesized for the same purpose. However, within these BAILs studied here, protons are not only able to be released from the cation as in conventional Brønsted acidic ionic liquids, but also from the designed anion.

This work covers the gas phase behaviour of novel BAILs via electrospray ionisation (ESI) and matrix-assisted laser desorption/ionisation (MALDI) mass spectrometry. BAILs are prepared by treating zwitterions with an alkanedisulfonic acid, therefore, the cation is formed by acidification of the zwitterion and the anion is produced by deprotonation of alkanedisulfonic acid. Compositions of the new BAILs were confirmed by detection of the respective cation and anion in MALDI, whereas identification of the corresponding cation and dianion occurred in ESI. Moreover, in addition to the cation, the ESI spectra revealed aggregation of cation and zwitterions. Similarly, the dianion forms clusters with the zwitterions in negative mode. Collision-induced dissociation (CID) is employed to investigate the fragmentation behaviour of the formed aggregates. Cationic clusters show evaporation of zwitterions until the cation is reached. However, clusters of dianion and zwitterions dissociate by releasing zwitterions until the alkane disulfonate dianion is reached. However, proton transfer is also observed. The adduct of the dianion and one zwitterion fragments into the alkane sulfonic acid and the deprotonated zwitterion with an imidazole-based carbene structure, via coulomb explosion following proton transfer reaction.

**Organic reactions in ionic liquids studied by in situ XPS.**

Organic reactions are followed by XPS (X-ray photoelectron spectroscopy) under ultra high vacuum conditions involving ionic liquids. The attachment of ionic head groups to organic molecules, the reactivity of which is to be studied, reduces their volatility so that they can withstand evaporation in high vacuum to the extent that XPS experiments become possible. The reaction under investigation is an alkylation of a tertiary amine which is attached to an imidazolium or phosphonium cation by 4-chlorobutylsulfonate. In the reaction the amine converts into an ammonium cation and the chlorine atom into a chloride anion.

Our contribution to this study provides unequivocal evidence of the formation of the reaction products by ESI-MS analysis of the methanol washings of the sample holder following ARXPS measurements. The combination of MS<sup>1</sup> and MS<sup>2</sup> experiments allowed the unequivocal assignment of the species involved.

## Synthesis and Aggregation Properties of Polycationic Perylenetetracarboxylic Acid Diimides

The paper reports the first synthesis of polycationic perylenetetracarboxylic acid diimides (PDIs) with 6, 9 and 18 positive charges which are introduced by peripheral pyridinium groups of terminating Newkome dendrons. In the solid, the charges are compensated by bromide anions. In water, the polycationic PDIs are characterized by high solubility which is independent of the pH value. The aggregation behaviour of the PDIs was studied by absorption and fluorescence spectroscopy, as well as by an array of different NMR measurements and by cryo-TEM. Intensive aggregation is found for the smaller first-generation dendrons, which is interpreted as stacking interactions of the perylene moieties, while bulkier second-generation dendrons hamper aggregation.

The ESI-MS analysis of these compounds showed for two sets of compounds intact quasi-molecular ions that were generated by the loss of several of the bromide counter-anions and for the bulkiest and most highly charged dendrons only fragment ions. It is found that the spray conditions to produce these polycations are harsher than those generally applied to biological molecules which are transformed into ions by protonation.

The present investigation prompted further work into related compounds with more detailed studies of the fragmentation mechanism. At least two future publications will follow this first paper. In addition to the molecules studied here, compounds are investigated in which the perylene unit is replaced by the [60]fullerene and 12 pyridinium cations are ligated to the fullerene. In one of these studies, the fragmentation mechanisms are elucidated and in the other, the energetic requirements of the dissociation reactions are considered.

# Studies on an iron(III)-peroxo porphyrin. Iron(III)-peroxo or iron(II)-superoxo?†

Katharina Duerr,<sup>a</sup> Julianna Olah,<sup>b</sup> Roman Davydov,<sup>c</sup> Michael Kleimann,<sup>d</sup> Jing Li,<sup>a</sup> Nina Lang,<sup>a</sup> Ralph Puchta,<sup>a</sup> Eike Hübner,<sup>a</sup> Thomas Drewello,<sup>a</sup> Jeremy N. Harvey,<sup>b</sup> Norbert Jux<sup>a</sup> and Ivana Ivanović-Burmazović<sup>\*a</sup>

Received 29th September 2009, Accepted 30th November 2009

First published as an Advance Article on the web 13th January 2010

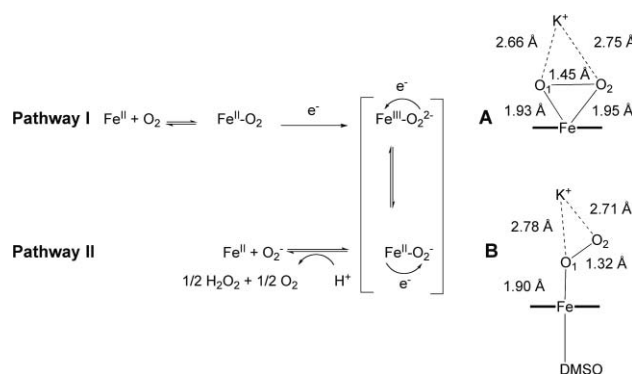
DOI: 10.1039/b920237d

We demonstrate that a one electron reduced product of the heme iron dioxygen adduct exists in solution not only as the commonly accepted iron(III)-peroxo species, but coexists with its isomeric iron(II)-superoxo form. This unusual reduced metal-superoxide adduct  $[M(II)-O_2^-]$  is recently reported as a reactive intermediate in the case of non-heme extradiol dioxygenases and could also be generated by cryoreduction of a heme  $Fe^{II}-O_2$  adduct. The existence of iron(II)-superoxo species in solution is consistent with IR, EPR, mass and Mössbauer spectra. The equilibrium between heme iron(III)-peroxo and iron(II)-superoxo forms is supported by density functional theory and explains our previous finding that upon release of coordinated (su)peroxide a corresponding iron(II) complex remains. These results shed new light on the nature of heme iron(III)-peroxo species that are key intermediates in the metalloenzyme-catalyzed dioxygen and hydrogen peroxide activation.

## Introduction

Heme and non-heme iron centers play an important role in the biochemistry of oxygen and its reduced forms superoxide ( $O_2^-$ ) and peroxide ( $O_2^{2-}$ ). In the human metabolism, oxygen is transported and stored by hemoglobin and myoglobin. Both of them contain heme groups. Despite many studies, the nature of their oxygen adducts  $\{Fe-O_2\}$  is still under debate. It seems that the H-bonding capacity of the protein strengthens the  $Fe^{III}$ -superoxo character of the oxyheme complex.<sup>1</sup> A one electron reduced form of similar iron(II)-dioxygen adducts,  $\{Fe-O_2\}^-$ , (pathway I in Scheme 1) is known as an important intermediate in the catalytic cycle of heme (mono) oxygenases (cytochrome P-450, nitric oxide synthase, cytochrome c oxidases).<sup>2-4</sup> The same type of species can be formed in a direct reaction between an  $Fe^{II}$  center and superoxide (pathway II in Scheme 1), which occurs in the case of the non-heme iron superoxide dismutase (SOD).<sup>5</sup> These enzyme intermediates have been considered as  $Fe^{III}$ -peroxo complexes **A**. Valentine *et al.*<sup>6</sup> investigated the reaction of iron porphyrins with superoxide in aprotic coordinating solvents and the product was also characterized as an unstable  $Fe^{III}$ -peroxo species, in contrary to an earlier ESR study describing this species as  $Fe(II)$ -superoxo **B**.<sup>7</sup>

Recently, an  $Fe^{II}$ -superoxo structure has been considered as a reactive intermediate of non-heme extradiol dioxygenase.<sup>8</sup> Up until now only  $Cu^{II}$ - and  $Ni^{II}$ -superoxo complexes as representa-



**Scheme 1** Reaction pathways leading to iron(II)-superoxo/iron(III)-peroxo species and selected calculated structural data.

tives of unusual reduced metal-superoxide species,  $[M^{II}-O_2^-]$ ,<sup>9</sup> are well characterized.<sup>10-14</sup> For heme/porphyrin systems this type of species has only been generated by cryoreduction of heme  $Fe^{II}-O_2$  adducts.<sup>15-17</sup> Interestingly, they have been named as end-on peroxo, although based on the observed O-O distance<sup>16-18</sup> and quantum chemical calculations they are best interpreted as  $Fe^{II}-O_2^-$ .<sup>8,16</sup> Here, we present some experimental evidence, as well as theoretical background for such an  $Fe^{II}-O_2^-$  **B** species in a porphyrin system, which in solution coexists with its isomeric, commonly accepted  $Fe^{III}-O_2^{2-}$  **A** form.

## Experimental

### Materials

Reagents and solvents were obtained from commercial sources and were of reagent quality unless otherwise stated. DMSO was purchased as extra-dry solvent. All chemicals were used as received without further purification. The preparation of  $H_2Porph$  ( $= 5^2-N-(4-aza-18-crown-6)methyl-5^4,10^4,15^4,20^4-tetra-t-butyl-5^6-methyl-5,10,15,20-tetraphenylporphyrin$ ) and its iron(III) and

<sup>a</sup>Department of Chemistry and Pharmacy, University of Erlangen-Nürnberg, Egerlandstr. 1, 91058 Erlangen, Germany. E-mail: ivana.ivanovic@chemie.uni-erlangen.de; Fax: +49 9131 8527345; Tel: +49 9131 8525428

<sup>b</sup>School of Chemistry and Centre for Computational Chemistry, University of Bristol, Cantock's Close, Bristol, UK BS8 1TS

<sup>c</sup>Department of Chemistry, Northwestern University, 2145 Sheridan Road, Evanston, IL 60208-3113, USA

<sup>d</sup>Mettler Toledo GmbH, Ockerweg 3, 35396 Giessen, Germany

† Electronic supplementary information (ESI) available: Fig. S1–S15 and Tables S1–S3. See DOI: 10.1039/b920237d



zinc(II) complex is described elsewhere.<sup>19,20</sup>  $\text{K}^{18}\text{O}_2$  was synthesized according to the published procedure in our previous paper<sup>19</sup> starting from  $^{18}\text{O}_2$  that was obtained from Aldrich.

An excess of solid  $\text{KO}_2$  was used in order to be able to produce the desired product species. This would not have been possible by stoichiometric addition of  $\text{KO}_2$  since a significant amount of it would have been decomposed by protonation during the solvation process. Using an excess of solid superoxide enables the generation of a steady state concentration of superoxide, since a solvated amount is constantly being used up either within the reaction or by decomposition. Importantly, the iron (su)peroxo species can be generated by applying an excess of superoxide and either the  $\text{Fe}^{\text{III}}$  or  $\text{Fe}^{\text{II}}$  form of a porphyrin complex.<sup>6,19</sup>

### Electrospray ionization (ESI) mass spectrometry of $[\text{Fe}^{\text{III}}(\text{Porph})(\text{O}_2^{2-})]^-$

Samples were prepared by dissolving an excess of either  $\text{KO}_2$ ,  $\text{K}^{18}\text{O}_2$  or  $\text{Na}_2\text{O}_2$  in a  $10^{-4}$  M solution of  $[\text{Fe}^{\text{III}}(\text{Porph})\text{Cl}]$  in dry DMSO under nitrogen. Using a syringe pump at a flow rate of  $240\text{ mL h}^{-1}$ , the DMSO solutions were infused into an orthogonal ESI source of an Esquire 6000 ion trap mass spectrometer (Bruker, Bremen, Germany). Nitrogen was used as the nebulizing gas at a pressure of 10 psi and as the drying gas at a temperature of  $100^\circ\text{C}$  and a flow rate of  $5\text{ L min}^{-1}$ . The source voltages for the positive-ion mode were set as follows: capillary at  $-4.0\text{ kV}$ , end plate offset at  $-500\text{ V}$ , capillary exit at  $188.1\text{ V}$  and lens 2 at  $-60\text{ V}$ . The ion trap was optimized for the respective target mass.

### EPR spectroscopy

Sample preparations were done using either an Ar dry box or Schlenk technique. Samples of  $[\text{NaFe}^{\text{III}}(\text{Porph})\text{OH}]^+$  (2 mM) were prepared by stirring  $[\text{Fe}^{\text{III}}(\text{Porph})\text{Cl}]$  with a saturated solution of NaOH in dry DMSO for 30 min and subsequent filtration. 2 mM solutions of  $[\text{Fe}^{\text{II}}(\text{Porph})(\text{DMSO})_n]$  ( $n = 1$  or  $2$ ) were prepared by stirring  $[\text{Fe}^{\text{III}}(\text{Porph})\text{Cl}]$  with a saturated solution of  $\text{Na}_2\text{S}_2\text{O}_4$  in dry DMSO for 60 min and subsequent filtration. Samples of  $[\text{KFe}^{\text{III}}(\text{Porph})(\text{O}_2^{2-})]$  or  $[\text{NaFe}^{\text{III}}(\text{Porph})(\text{O}_2^{2-})]/[\text{Fe}^{\text{III}}(\text{Porph})(\text{O}_2^{2-})]^-$  were prepared by either the addition of an excess of  $\text{KO}_2$  as a solid or addition of an excess of  $\text{Na}_2\text{O}_2$  as a solid to a 2 mM solution of  $[\text{Fe}^{\text{III}}(\text{Porph})\text{Cl}]$  in dry DMSO, respectively. The suspension was stirred until a color change had occurred. Before taking the spectrum, the solution was filtrated by syringe PTFE filter. In general, after filtration, concentration of free, non-bound superoxide slowly sinks.

The same procedure was used for preparation of  $[\text{NaZn}^{\text{II}}(\text{Porph})(\text{O}_2^{2-})]/[\text{Zn}^{\text{II}}(\text{Porph})(\text{O}_2^{2-})]^-$ . UV/vis properties and further characterization is described elsewhere.<sup>20</sup>

X-Band EPR of  $[\text{Fe}^{\text{II}}(\text{Porph})(\text{DMSO})_n]$  ( $n = 1$  or  $2$ ) was measured at He temperatures. No signal was detected. This is in agreement with the presence of low-spin ( $S = 0$ ) six-coordinate  $[\text{Fe}^{\text{II}}(\text{Porph})(\text{DMSO})_2]$  and EPR silent high-spin ( $S = 2$ ) five-coordinate  $[\text{Fe}^{\text{II}}(\text{Porph})(\text{DMSO})]$  in DMSO solution, as it has previously been confirmed by Mössbauer spectroscopy.<sup>19</sup>

EPR spectra were recorded on a Bruker EPR 300 equipped with Oxford He flow system, and on a JEOL continuous wave spectrometer JES-FA200 equipped with an X-band Gunn oscillator bridge, a cylindrical mode cavity and a Helium cryostat.

### Mössbauer measurements of $[\text{Fe}^{\text{III}}(\text{Porph})(\text{O}_2^{2-})]^-$

Sample preparation was done according to our previous study (complex solution was stirred in a glove box with an excess of solid  $\text{KO}_2$ , generating a steady-state concentration of superoxide, until the color of the solution changed to black-green (*ca.* 30 min), with the typical  $\lambda_{\text{max}} = 440\text{ nm}$  in the UV/vis spectrum), only  $\text{Na}_2\text{O}_2$  was used instead of  $\text{KO}_2$ .<sup>19</sup> Spectra of the  $^{57}\text{Fe}$  enriched samples were recorded on a WissEl Mössbauer spectrometer (MRG-500) at  $77\text{ K}$  in constant acceleration mode.  $^{57}\text{Co}/\text{Rh}$  was used as radiation source. WinNormos for Igor Pro software has been used for the quantitative evaluation of the spectral parameters (least-squares fitting to Lorentzian peaks). The minimum experimental line widths were  $0.20\text{ mm s}^{-1}$ . The temperature of the samples was controlled by an MBBC-HE0106 MÖSSBAUER He/ $\text{N}_2$  cryostat within an accuracy of  $\pm 0.3\text{ K}$ . Isomer shifts were determined relative to  $\alpha$ -iron at  $298\text{ K}$ .

### Time resolved UV/vis spectroscopy of the reaction of $[\text{Fe}^{\text{II}}(\text{Porph})(\text{DMSO})_n]$ ( $n = 1, 2$ ) with superoxide generated from $\text{Na}_2\text{O}_2$

Solution preparations of  $[\text{Fe}^{\text{II}}(\text{Porph})(\text{DMSO})_2]$  and  $[\text{Fe}^{\text{III}}(\text{Porph})(\text{O}_2^{2-})]^-$  in DMSO were done according to our previous study.<sup>19</sup> Saturated solutions of  $\text{Na}_2\text{O}_2$  in DMSO were prepared by stirring solid  $\text{Na}_2\text{O}_2$  pellets in dry solvents either in a Schlenk or in a glovebox. The solution was used after filtration.

Time resolved UV/vis spectra were recorded using a modified  $\mu\text{SFM-20 Bio-Logic}$  stopped-flow module combined with a Huber CC90 cryostat and equipped with a J&M TIDAS high-speed diode array spectrometer with combined deuterium and tungsten lamps (200–1015 nm wavelength range). Isolast O-rings were used for all sealing purposes to enable measurements in DMSO, and solutions were delivered from 10 mL gas-tight Hamilton syringes. The syringes are controlled by separate drives, allowing for variation of the ratio of mixing volumes used in the kinetic runs. Data were analyzed using the integrated Bio-Kine software version 4.23 and also the Specfit/32(tm) program. The stopped-flow instrument was thermostated to the desired temperature  $\pm 0.1^\circ\text{C}$ . Experiments at  $25^\circ\text{C}$  were performed in DMSO solution.

### IR spectroscopy

Sample preparations were done using Schlenk techniques. Samples of  $[\text{Fe}^{\text{III}}(\text{Porph})(\text{O}_2^{2-})]^-$  were prepared by either the addition of an excess of  $\text{K}^{18}\text{O}_2$  or  $\text{K}^{16}\text{O}_2$  as a solid or addition of an excess of  $\text{Na}_2\text{O}_2$  as a solid to a 5 mM solution of  $[\text{Fe}^{\text{III}}(\text{Porph})\text{Cl}]$  in dry DMSO. The suspension was stirred under nitrogen and ReactIR spectra were taken at room temperature. Samples of  $\text{KO}_2$ ,  $\text{K}^{18}\text{O}_2$  or  $\text{Na}_2\text{O}_2$  in dry DMSO were prepared by stirring an excess of the solids in dry DMSO under nitrogen as well.

IR spectra were taken with a ReactIR(tm) 45 m device (Mettler Toledo) utilising a DiComp AgX fibre probe with diamond ATR element and a MCT detector. Spectra were taken every 15 s.

### Computational details

**Geometry optimizations.** Geometry optimizations of the structures were performed with the Jaguar 6.0 program package<sup>21</sup> using the B3PW91 and B3LYP functionals, and a restricted open

shell formalism. Standard DFT and pseudospectral grids were used throughout. The 6-31G(d) basis set was used on all atoms with the exception of the metal ions for which the standard Los Alamos effective core potentials<sup>22</sup> were used with the associated double- $\zeta$ , basis LACVP on potassium and the triplet- $\zeta$  basis LACV3P<sup>23</sup> on iron. This combination is referred to as BSI. The calculated total energies of the optimized structures *in vacuo*, together with the total energy of the dissociated DMSO ligand, were used to compare the stability of the side-on and end-on complexes. Cartesian coordinates and total energies of the optimized structures are given in Tables S1–S3.†

**Mössbauer parameters.** The Orca program package was used to calculate Mössbauer parameters at the geometry obtained with Jaguar 6.0<sup>21</sup> at the B3PW91/BSI level. Parameters were calculated as proposed by Neese *et al.*<sup>24,25</sup> The calculated electron densities at the Fe nucleus ( $\rho(\text{Fe})$ ) can be converted to isomer shift ( $\delta$ ) values using the following equation.

$$\delta = \beta - \alpha * (\rho(\text{Fe}) - C)$$

The values of the fitted  $\alpha$ ,  $\beta$ , and  $C$  constants were obtained from<sup>26</sup>

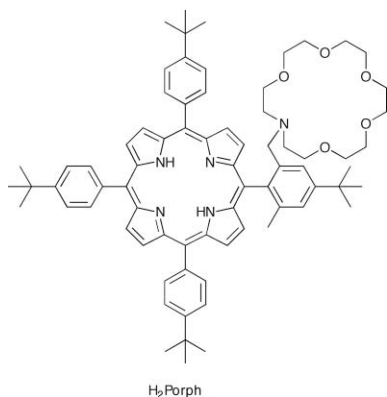
$$\beta = 6.54 \pm 0.61$$

$$\alpha = -0.366 \pm 0.036$$

$$C = 11800.0$$

## Results and discussion

We previously studied the reaction of  $\text{KO}_2$  with an iron complex of a crown ether porphyrin conjugate ( $\text{H}_2\text{Porph}$ , Scheme 2) in DMSO (DMSO = dimethylsulfoxide).<sup>19</sup> Due to the fact that the crown ether moiety stabilizes an iron porphyrin product of superoxide reaction, we were able for the first time to quantify the kinetics and thermodynamics of superoxide binding to a metal center in general, and to an iron center in particular.<sup>19</sup> We have shown that  $\text{O}_2^-$  can react with the  $\text{Fe}^{\text{II}}$  center in a reversible manner (pathway II in Scheme 1) forming a quite stable product, generally characterized as  $\text{Fe}(\text{III})\text{-O}_2^{2-}$  **A** based on its UV/vis and Mössbauer parameters<sup>19</sup> that are analog to those obtained by Valentine *et al.*<sup>6,27</sup> Furthermore, we have demonstrated that this species can release superoxide to form the starting  $\text{Fe}^{\text{II}}$  complex by fine tuning of the proton concentration (pathway II in Scheme 1). This and the reversible nature of the  $\text{O}_2^-$  binding to the  $\text{Fe}^{\text{II}}$  center lead to the assumption that the product can partially have an iron(II)-



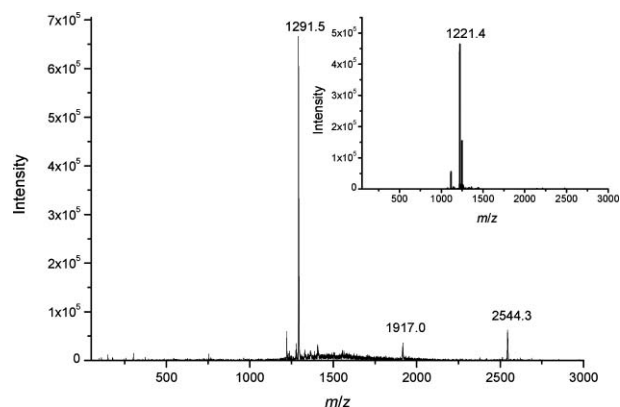
**Scheme 2** Investigated porphyrin ligand.

superoxo resonance character or that a discrete  $\text{Fe}^{\text{II}}\text{-O}_2^-\text{B}$  complex exists either as an intermediate or as a component of a product mixture.

An important clue for elucidating this phenomenon is the fact that in the Mössbauer spectrum of the reaction product between our iron porphyrin and  $\text{O}_2^-$  in DMSO,<sup>19</sup> two species were observed in a 1 : 1 ratio: one high-spin iron(III) ( $\delta = 0.41 \text{ mm s}^{-1}$ ,  $\Delta E_{\text{q}} = 0.51 \text{ mm s}^{-1}$ ), which according to Valentine *et al.*<sup>27</sup> is a typical iron(III)-peroxo complex, and one low-spin iron(II) ( $\delta = 0.36 \text{ mm s}^{-1}$ ,  $\Delta E_{\text{q}} = 1.38 \text{ mm s}^{-1}$ ). In our previous study<sup>19</sup> we did not concentrate on the nature of that low-spin iron(II) species. One possibility would be that it is a residue of the starting low-spin  $\text{Fe}^{\text{II}}$  bis-DMSO complex,  $[\text{Fe}^{\text{II}}(\text{Porph})(\text{DMSO})_2]$ . The starting  $[\text{Fe}^{\text{II}}(\text{Porph})(\text{DMSO})_2]$  complex ( $\delta = 0.44 \text{ mm s}^{-1}$ ,  $\Delta E_{\text{q}} = 1.32 \text{ mm s}^{-1}$ ) and the low-spin  $\text{Fe}^{\text{II}}$  species present in the product solution after reaction with an excess of superoxide have similar Mössbauer parameters, which is in agreement with our DFT calculations (*vide infra*). However, considering the high  $\text{O}_2^-$  binding constant ( $K = (1.7 \pm 0.2) \times 10^5 \text{ M}^{-1}$ )<sup>19</sup> there is no doubt that under the applied experimental conditions (see Experimental) (su)peroxo-complex formation is pushed to completion. Thus, the low-spin iron(II) species which appear in the Mössbauer spectrum together with the high-spin iron(III)-peroxo complex, cannot stand for the unreacted low-spin  $[\text{Fe}^{\text{II}}(\text{Porph})(\text{DMSO})_2]$  but can only represent the low-spin iron(II) form of the product, suggesting a coexistence of **A** and **B** in the product solution.

## Mass spectrometry

The supposition that upon reaction with an excess of  $\text{O}_2^-$  the product solution cannot contain 50% of the starting unreacted  $\text{Fe}^{\text{II}}$  complex was confirmed by ESI mass spectroscopy (Fig. 1). The major peak at  $m/z$  1291.5 corresponds to the intact iron porphyrin, which now incorporates the (su)peroxo ligand and two potassium cations. We can assume that one potassium is directly attached to the (su)peroxo ligand, while the other one resides inside the crown ether. This additional potassium cation is necessary to convert the molecule into a charged species in order to be detectable by mass spectrometry. This ion was mass selected and further activated through collisions with He gas inside the ion trap. The resulting collision-induced dissociation leads *via* loss of  $\text{KO}_2$  to the iron porphyrin with one remaining potassium cation in the

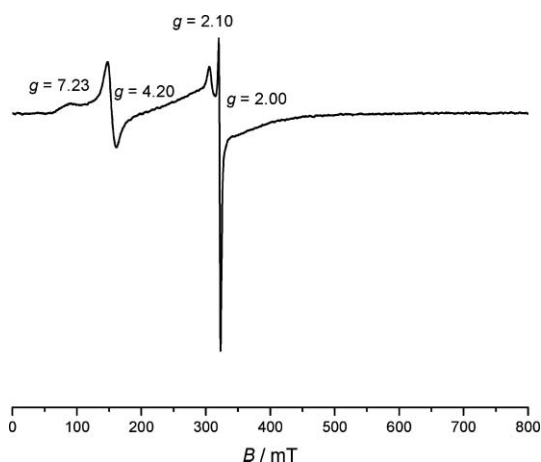


**Fig. 1** Mass spectrum of  $\{\text{K}^+ + \text{KFe}^{\text{III}}(\text{Porph})(\text{O}_2^{2-})\}$ . Inset: MS/MS of  $m/z = 1291.5$ .

crown ether (inset Fig. 1). The fragment is singly charged, which may imply that the iron is in the iron(II) oxidation state after release of su(peroxo) entity. The assumed composition was confirmed in the experiment with  $\text{K}^{18}\text{O}_2$  (ESI, Fig. S1†). The molecular ion is now shifted as expected by 4 mass units to  $m/z$  1295.5 which confirms the assumed composition. The MS/MS of this ion (ESI, inset Fig. S1†) confirms the loss of  $\text{K}^{18}\text{O}_2$ . (There is a formal one mass unit discrepancy between the MS/MS experiment in Fig. 1 and Fig. S1. As the isotopic pattern for both species is the same, the reason is a calibration discrepancy of the instrument.) ESI mass spectrometry was also performed on the starting iron(III) porphyrin in DMSO solution as well as in a saturated solution of KCl in DMSO and only iron(III) species are observed (ESI, Fig. S2 and S3†). Even more, fragmentation of the KCl-adduct of our  $\text{Fe}^{\text{III}}$  complex (ESI, inset Fig. S3†) shows that after the loss of KCl the complex stays in the  $\text{Fe}^{\text{III}}$  form, suggesting that the  $\text{Fe}^{\text{II}}$  form, which remains after the release of  $\text{KO}_2$ , comes from the inherent nature of the studied  $\text{Fe}^{\text{II}}$ -superoxo adduct. Simulations of the isotopic distributions of the measured peaks are given in the ESI (Fig. S4–S7).† These results provide for the first time compelling identification of an intact superoxide adduct of a metal porphyrin in solution and support our interpretation of the low-spin iron(II) species present in the product solution as  $\text{Fe}^{\text{II}}\text{-O}_2^-$  **B**.

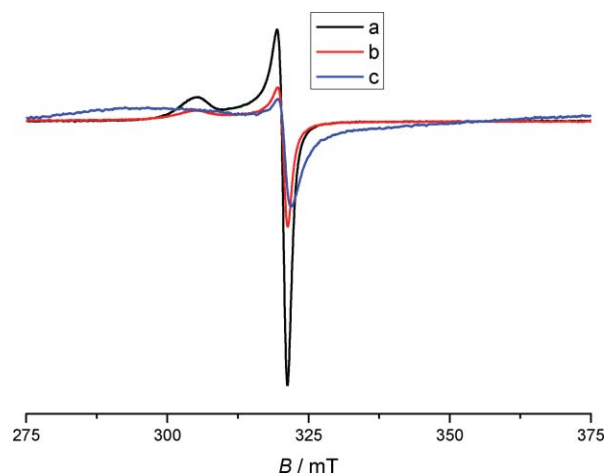
### EPR spectroscopy

X-Band EPR spectra of the reaction product between our iron porphyrin and excess of solid  $\text{KO}_2$  in DMSO at 10 K show the signals of rhombic iron(III) high-spin ( $S = 5/2$ , Fig. 2), which correspond to the side-on peroxo species,<sup>27</sup> as well as the typical axial spectrum of superoxide. Since our iron(II) species are EPR silent, only superoxo  $g$  values (the region of the axial spectrum around  $g = 2$ , with  $g_{\parallel}$  around 2.1 and  $g_{\perp}$  at 2.00)<sup>28</sup> can give evidence for the possible presence of  $\text{Fe}^{\text{II}}\text{-O}_2^-$ . In the following part,  $g_{\perp}$  is not further discussed as it stays the same under the respective conditions. A ferrous heme superoxo species



**Fig. 2** X-Band EPR spectra of  $[\text{Fe}^{\text{III}}(\text{Porph})\text{Cl}]$  with  $\text{KO}_2$  in DMSO at 10 K, microwave frequency was 8.980296 GHz,  $P = 0.5$  mW; mod. width = 0.14 mT, sweep width 800 mT. The signal of a rhombic  $\text{Fe}^{\text{III}}$  high-spin is observed at  $g = 4.20$ , whereas the expected  $g$  values around 9 and 1 are obscured.<sup>35</sup> A weak feature at  $g \sim 9$  expected for the peroxo complex was obscured by the signal at  $g = 7.23$  for  $\text{Fe}^{\text{III}}(\text{Porph})$  impurities,<sup>35</sup> most probably an iron(III)-hydroxo complex (also see ESI, Fig. S8a†).

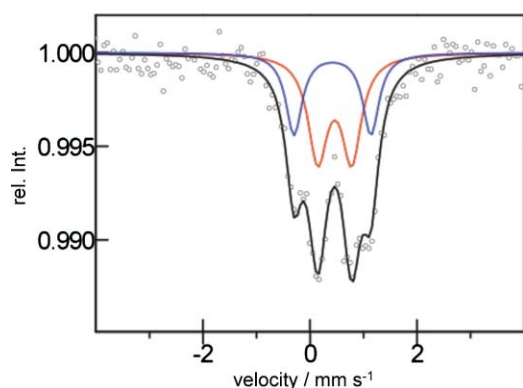
produced at 77 K by cryoreduction by Davydov *et al.* shows  $g_{\parallel} = 2.116$  in DMF and  $g_{\parallel} = 2.11$  in glycerol buffer for a different heme complex.<sup>15</sup> This hints to iron(II)-superoxo species having  $g_{\parallel}$  around 2.1 regardless of solvent and concentration, contrary to free solvated superoxide<sup>29</sup> and ionically coordinated (e.g.  $\text{Na-O}_2^-$  and  $\text{Zn-O}_2^-$ ) superoxide.<sup>30,31</sup> At higher temperatures, the EPR signals of the iron(III) species decrease, enabling us to identify  $g_{\parallel} = 2.10$  (Fig. 3). The much lower intensity of this signal (*i.e.* lower concentration of paramagnetic species) compared to that of free superoxide hints to the signal not being due to free superoxide but to the coordinated  $\text{O}_2^-$  species. Besides,  $g_{\parallel}$  values of free superoxide shift to smaller values with lower concentration,<sup>29</sup> which is not the case here as  $g_{\parallel}$  stays at 2.10. Additionally,  $^{57}\text{Fe}^{\text{III}}(\text{Porph})\text{Cl}$  and  $\text{KO}_2$  were used in order to determine the interaction of bound  $\text{O}_2^-$  with the metal. This is determined by line broadening of  $g_{\parallel}$ . The larger the line broadening, the larger the interaction of the metal with superoxide, as reported by Valentine *et al.* on ZnTPP (TPP = tetraphenylporphyrin).<sup>30</sup> Indeed, in spectra at 77 K, very large line broadening (350 G) is observed (compared to 3–4 G in the case of ZnTPP),<sup>30</sup> as well as shift of  $g_{\parallel}$  to 2.15 (Fig. 3).



**Fig. 3** X-Band EPR spectra in DMSO at 77 K; (a)  $\text{KO}_2$ , microwave frequency was 8.977954 GHz,  $P = 0.2$  mW; mod. width = 0.5 mT, sweep width 100 mT, (b)  $[\text{Fe}^{\text{III}}(\text{Porph})\text{Cl}]$  with excess of  $\text{KO}_2$ , microwave frequency was 8.979592 GHz,  $P = 0.5$  mW; mod. width = 0.5 mT, sweep width 100 mT, (c)  $^{57}\text{Fe}^{\text{III}}(\text{Porph})\text{Cl}$  with  $\text{KO}_2$ , microwave frequency was 8.8984394 GHz,  $P = 1.9$  mW; mod. width = 1.0 mT, sweep width 100 mT.

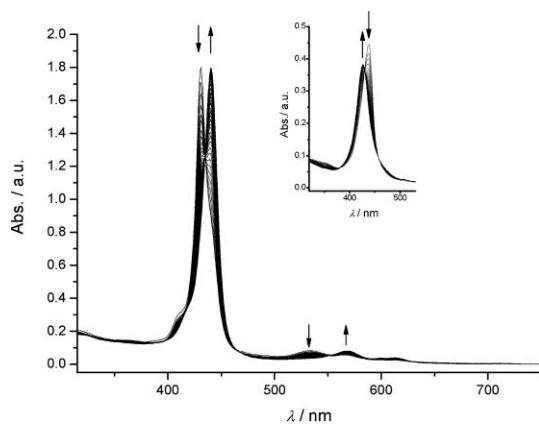
### Reaction with commercially available $\text{Na}_2\text{O}_2$

Knowing that commercially available  $\text{Na}_2\text{O}_2$  contains up to 10% of  $\text{NaO}_2$ , and that “naked” peroxide is not stable in aprotic solution,<sup>28</sup> we used it as another source of superoxide, which is released in solution by stirring of the granules in DMSO. This enables quantitative generation of (su)peroxo species without using a high superoxide excess. That reaction of such  $\text{Na}_2\text{O}_2$  with iron porphyrin in DMSO results in the identical (su)peroxo product  $\{\text{Fe-O}_2\}^-$  as by using  $\text{KO}_2$ , has been confirmed by mass (ESI, Fig. S9† also confirms replacement of the two potassium cations by sodium) and Mössbauer spectroscopy (high-spin species:  $\delta = 0.46$  mm  $\text{s}^{-1}$ ,  $\Delta E_{\text{q}} = 0.63$  mm  $\text{s}^{-1}$ , low-spin species:  $\delta = 0.44$  mm  $\text{s}^{-1}$ ,  $\Delta E_{\text{q}} = 1.44$  mm  $\text{s}^{-1}$ , in Fig. 4). Additionally, we followed the reaction between our  $\text{Fe}^{\text{II}}$  complex and a saturated solution of

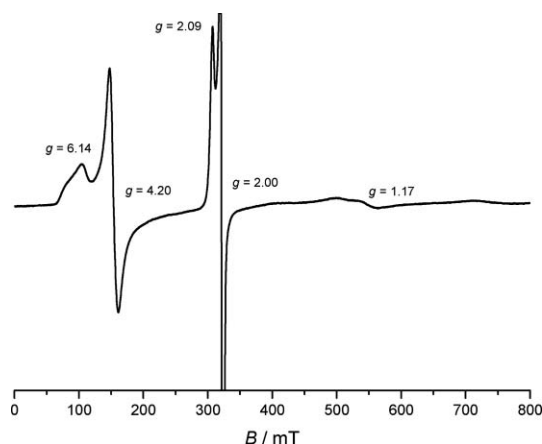


**Fig. 4** Mössbauer spectra of the  $^{57}\text{Fe}$  enriched (su)peroxo adducts prepared with  $\text{Na}_2\text{O}_2$  at 77 K (high-spin species:  $\delta = 0.46 \text{ mm s}^{-1}$ ,  $\Delta E_{\text{q}} = 0.63 \text{ mm s}^{-1}$ , low-spin species:  $\delta = 0.44 \text{ mm s}^{-1}$ ,  $\Delta E_{\text{q}} = 1.44 \text{ mm s}^{-1}$ ).

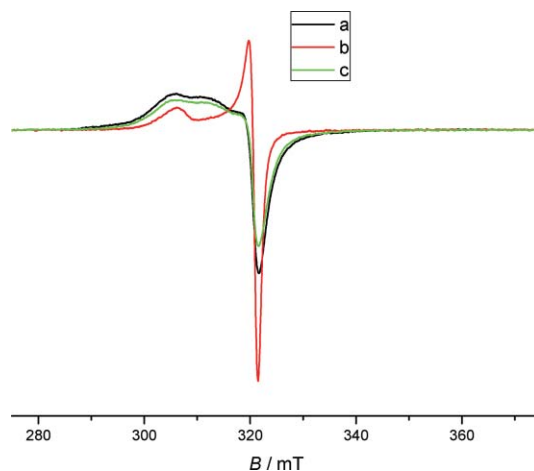
$\text{Na}_2\text{O}_2$  in DMSO by time-resolved UV/vis spectroscopy. The observed spectral changes (Fig. 5) are characteristic for the formation of a su(peroxo) complex.<sup>19</sup> From the observed rate constant,  $k_{\text{obs}} = 1.26 \pm 0.01 \text{ s}^{-1}$  (at  $25^\circ\text{C}$ ), the concentration of superoxide that is present in the saturated DMSO solution of  $\text{Na}_2\text{O}_2$  is estimated to be  $(4 \pm 2) \times 10^{-5} \text{ M}$ , based on the previously determined second order rate constant for superoxide binding ( $k = 36\,500 \pm 500 \text{ s}^{-1} \text{ M}^{-1}$ ).<sup>19</sup> Upon addition of moist DMSO into the product solution, the superoxide release from  $\{\text{Fe-O}_2\}^-$  shifts the reaction equilibrium back to the starting  $\text{Fe}^{\text{II}}$  complex (pathway II in Scheme 1, inset Fig. 5). This confirms that the use of  $\text{Na}_2\text{O}_2$  in DMSO as a source of superoxide does not affect the nature of the product solution as well as the reversible character<sup>19</sup> of the superoxide coordination. Thus, the EPR spectrum at 6 K of such a product solution again shows presence of the peroxo complex ( $g = 4.20$ ) and even the  $g$  value at 1.17 can now be seen (some impurity caused by an iron(III)-hydroxo species is also present in the spectrum, Fig. 6) since there is no excess of superoxide. The most prominent signals are around  $g = 2$ . They show coordinated superoxide at  $g_{\parallel} = 2.09$  (Fig. 6 and Fig. 7). Measurements at 77 K (Fig. 7) with a shorter sweep range confirm this. The spectra are highly reproducible along the whole temperature range from 6 K to 77 K. The shift in  $g_{\parallel}$  compared to free superoxide was shown



**Fig. 5** Time resolved UV/vis spectra of the reaction of a solution of  $[\text{Fe}^{\text{II}}(\text{Porph})(\text{DMSO})_n]$  ( $n = 1, 2$ ) in DMSO ( $5 \times 10^{-6} \text{ M}$ ) with superoxide generated from a saturated solution of  $\text{Na}_2\text{O}_2$  in DMSO at  $25^\circ\text{C}$ . Inset: back reaction after addition of moist DMSO.



**Fig. 6** X-Band EPR spectra of  $[\text{Fe}^{\text{III}}(\text{Porph})\text{Cl}]$  (some impurity caused by an iron(III)-hydroxo species is also present)<sup>35</sup> with  $\text{Na}_2\text{O}_2$  in DMSO at 6 K, microwave frequency was  $8.985163 \text{ GHz}$ ,  $P = 1.0 \text{ mW}$ ; mod. width =  $1.0 \text{ mT}$ , sweep width  $800 \text{ mT}$ . The peroxo complex shows  $g = 4.20$  and even the  $g$  value at 1.17 can now be seen, since there is no excess of superoxide.



**Fig. 7** X-Band EPR spectra in DMSO at 77 K: (a)  $\text{Na}_2\text{O}_2$ , microwave frequency was  $8.978772 \text{ GHz}$ ,  $P = 1.0 \text{ mW}$ ; Mod. width =  $0.35 \text{ mT}$ , sweep width  $80 \text{ mT}$ , (b)  $[\text{Fe}^{\text{III}}(\text{Porph})\text{Cl}]$  with  $\text{Na}_2\text{O}_2$ , microwave frequency was  $8.984580 \text{ GHz}$ ,  $P = 0.5 \text{ mW}$ ; mod. width =  $0.5 \text{ mT}$ , sweep width  $100 \text{ mT}$ , (c)  $[\text{Zn}^{\text{II}}(\text{Porph})]$  with  $\text{Na}_2\text{O}_2$ , microwave frequency was  $8.976918 \text{ GHz}$ ,  $P = 0.2 \text{ mW}$ ; mod. width =  $1.0 \text{ mT}$ , sweep width  $100 \text{ mT}$ .

to be caused by  $\text{O}_2^-$  binding to the metal ion.<sup>30</sup> The shift in  $g_{\parallel}$  can be unambiguously detected, as there is a clear change in the spectrum compared to the spectrum of  $\text{Na}_2\text{O}_2$  in DMSO solution (Fig. 7). The solution of  $\text{Na}_2\text{O}_2$  in DMSO shows two  $g_{\parallel}$  values, one for free  $\text{O}_2^-$  around 2.10 and another around 2.07 for superoxide attached to the sodium ion ( $g_{\parallel} = 2.0841$  in acetonitrile).<sup>31</sup> Spectra of the corresponding  $\text{Zn}^{\text{II}}$ -porphyrin- $\text{O}_2^-$  adduct (also see ESI, Fig. S8b†) show no significant changes compared to the one of  $\text{Na}_2\text{O}_2$  in DMSO, since the signal of an ionic  $\text{Zn}^{\text{II}}$ - $\text{O}_2^-$  adduct is also expected in the same region.<sup>30</sup> However, the reaction product of our iron porphyrin with  $\text{Na}_2\text{O}_2$  in DMSO shows only one  $g_{\parallel}$  value at 2.09, which leads to two conclusions. Interaction of superoxide with iron is not only of electrostatic nature, but the d orbitals are also involved, and secondly, there is no or only a very small amount of free  $\text{O}_2^-$  present in the system due to the stronger binding.

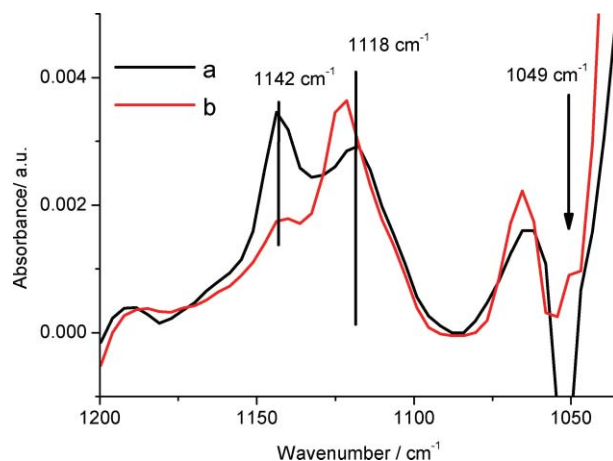
## Effect of cation binding to crown ether moiety

Control experiments were performed to probe the effect of cation coordination alone on the spectral properties of the studied  $\text{Fe}^{\text{III}}$  complex. In order to confirm that coordination of the cation itself in the crown ether moiety of the complex in DMSO does not lead to changes in its UV/vis spectrum, spectroscopic measurements with salts containing coordinating potassium and ammonium, as well as non-coordinating tetrabutylammonium cations were carried out. The anion in each case was non-coordinating hexafluorophosphate. The salt concentration was chosen according to a maximum possible potassium superoxide concentration (4 mM before mixing of solutions). None of these salts produced changes in the UV/vis spectrum (ESI, Fig. S10†). Thus, potassium coordination alone does not influence the spectral properties of the studied  $\text{Fe}^{\text{III}}$  complex. In a control experiment binding of potassium was confirmed by ESI mass spectrometry. The spectrum (ESI, Fig. S11†) of a solution of  $[\text{Fe}^{\text{III}}(\text{Porph})\text{Cl}]$  in DMSO with an excess of the  $\text{KPF}_6$  salt shows three peaks. The one at  $m/z$  1181.5 corresponds to the porphyrin complex without any additional ions  $[\text{Fe}^{\text{III}}(\text{Porph})]^+$ , and two other peaks are due to  $\text{NaCl}$  ( $m/z$  1239.5) and  $\text{KCl}$  ( $m/z$  1255.4) coordination, respectively. (Sodium probably stems from the insides of the instrument.) The coordination of sodium or potassium to the  $\text{Fe}^{\text{II}}$  form of the complex also does not cause any effect on the spectroscopic properties of the complex. That has been confirmed in our previous studies,<sup>19</sup> where the UV/vis spectra of the  $\text{Fe}^{\text{II}}$  form obtained by three different reduction methods, in the presence of  $\text{NBu}_4^+$ ,  $\text{Na}^+$  or  $\text{K}^+$  (electrochemical reductions in the presence of  $\text{NBu}_4\text{PF}_6$ , reduction by  $\text{KO}_2$  and  $\text{Na}_2\text{S}_2\text{O}_4$ ) were completely identical.

## IR spectroscopy in solution

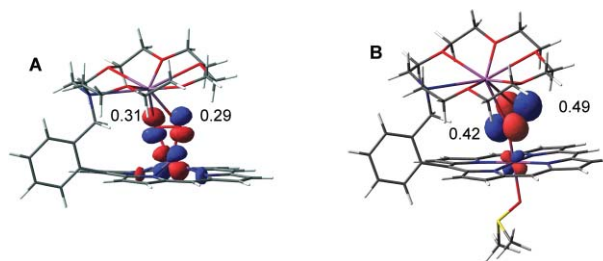
Resonance Raman spectroscopy was not employed, as heme-superoxo species do not exhibit enhancement of the O-O stretching band.<sup>32</sup> Therefore, generation of superoxide by dissolving  $\text{KO}_2$  in DMSO and its reaction products  $[\text{Fe}-\text{O}_2]^-$  was investigated by time resolved IR spectroscopy. In the IR spectrum (ESI, Fig. S12†) of a suspension of  $\text{KO}_2$  in DMSO, (after some minutes of stirring), the band at  $1140\text{ cm}^{-1}$  rises, corresponding to  $\nu_{\text{OO}}$  of solvated superoxide. This is in good agreement with the literature value of  $\nu_{\text{OO}} = 1145\text{ cm}^{-1}$ .<sup>28</sup> Using  $\text{K}^{18}\text{O}_2$ , this band does not appear. A shift of the  $^{18}\text{O}-^{18}\text{O}$  stretching frequency of about  $70\text{ cm}^{-1}$  is expected. Unfortunately, a strong band of DMSO appears in this region making the assignment of bands between  $1070$  and  $1020\text{ cm}^{-1}$  difficult. An observed band at  $1069\text{ cm}^{-1}$  ( $\Delta\nu = 71\text{ cm}^{-1}$ ) would correspond to the  $^{18}\text{O}-^{18}\text{O}$  stretching vibration (ESI, Fig. S13†).

The IR spectra obtained by stirring solid  $\text{KO}_2$  or  $\text{K}^{18}\text{O}_2$  in a porphyrin DMSO solution (Fig. 8) show that the bands of free (at ca.  $1140\text{ cm}^{-1}$ ) and coordinated (at ca.  $1118\text{ cm}^{-1}$ ) unlabelled superoxide overlap with the porphyrin bands of the product complex (at  $1140$  and  $1122\text{ cm}^{-1}$ ). This is obvious in the IR spectrum with  $\text{K}^{18}\text{O}_2$ , since the  $^{18}\text{O}-^{18}\text{O}$  stretching vibrations are now shifted (in the region of the strong DMSO band two weak bands at ca.  $1069$  and  $1049\text{ cm}^{-1}$  appear, which would correspond to free and coordinated  $^{18}\text{O}_2^-$ ). In general these overlaps make a clear assignment of the superoxo bands difficult. However, the band at  $1118\text{ cm}^{-1}$  corresponds to  $\nu_{\text{OO}}$  of end-on coordinated



**Fig. 8** ReactIR spectra of  $[\text{Fe}^{\text{III}}(\text{Porph})\text{Cl}]$  with (a)  $\text{KO}_2$  and (b)  $\text{K}^{18}\text{O}_2$  in DMSO. The spectrum of the complex in DMSO before respective addition of superoxide (not shown) was taken as background.

superoxide to a  $\text{M}^{\text{II}}$  center ( $\nu_{\text{OO}} = 1117$ ,<sup>10</sup>  $1118^{13}$  or  $1121\text{ cm}^{-1}$ <sup>12</sup> for  $\text{Cu}^{\text{II}}-\text{O}_2^-$ , respectively;  $\nu_{\text{OO}} = 1131\text{ cm}^{-1}$ <sup>11</sup> for  $\text{Ni}^{\text{II}}-\text{O}_2^-$ ) and its shift to ca.  $1049\text{ cm}^{-1}$  ( $\Delta\nu = 69\text{ cm}^{-1}$ ) is generally characteristic for both free (*vide supra*) and coordinated  $^{18}\text{O}_2^-$ .<sup>32</sup> In the peroxo region (ESI, Fig. S14†), after addition of  $\text{KO}_2$ , formation of two new bands is observed. The existence of two bands most probably reflects a degree of ion pairing between coordinated  $\text{O}_2^{2-}$  and free or crown-ether chelated  $\text{K}^+$  in solution.<sup>27</sup> The band at  $808\text{ cm}^{-1}$  is in accordance with the side-on coordination of peroxide as reported in the case of  $\text{Fe}^{\text{III}}\text{OEP}(\text{O}_2^{2-})^-$  ( $\text{OEP} = \text{octaethylporphyrin}$ ) by Valentine *et al.*<sup>6</sup> The band at  $853\text{ cm}^{-1}$  is still in the region of high-spin iron(III) side-on peroxo complexes,<sup>5</sup> but has a rather high frequency. This is most probably due to interaction of  $\text{K}^+$  with coordinated  $\text{O}_2^{2-}$ , *i.e.* the  $\eta^1$  coordination of the potassium ion to  $\eta^2$  bound peroxide (in accordance with the DFT calculations, *vide infra*) and consequent electron density withdrawal from the peroxo bond ( $\eta^1$  coordination provides the best overlap of SOMO, see Fig. 9A, and the  $\sigma^*$  orbital on  $\text{K}^+$ ). Using  $\text{K}^{18}\text{O}_2$ , these bands shift to  $795\text{ cm}^{-1}$  ( $\Delta\nu = 58\text{ cm}^{-1}$ ) and  $762\text{ cm}^{-1}$  ( $\Delta\nu = 48\text{ cm}^{-1}$ ). The latter shift is in accordance with the literature value ( $\Delta\nu = 47\text{ cm}^{-1}$ ).<sup>6</sup>



**Fig. 9** DFT calculated spin density of iron(II)-superoxide adduct. Highest-energy SOMO of side-on  $[\text{KFe}^{\text{II}}(\text{por})(\text{O}_2^-)]$  (A in Scheme 1); SOMO of end-on  $[\text{KFe}^{\text{II}}(\text{por})(\text{DMSO})(\text{O}_2^-)]$  (B in Scheme 1).

## DFT calculations

DFT calculations were performed in order to assess the relative energy and electronic structure of two putative forms of the



**Table 1** Relative energies of the end-on doublet and side-on sextet structures of  $\{\text{KFe}^{\text{II}}(\text{por}) + \text{O}_2^-\}$  using the B3PW91 functional (B3LYP results are shown in parentheses)

Species	With coordinated DMSO/kcal mol <sup>-1</sup>	With separated DMSO/kcal mol <sup>-1</sup>
End-on doublet	2.3 (−3.8)	13.0 (8.3)
Side-on sextet	Was not found	0.0 (0.0)

superoxide adduct with Fe<sup>II</sup> porphyrin, *i.e.* the low-spin iron(II)-superoxo and high-spin iron(III)-peroxo species. The optimized geometries of our computational models ( $\{\text{KFe}^{\text{II}}(\text{por})^+ + \text{O}_2^-\}$ ) include the crown ether moiety with coordinated potassium covalently bound on a phenyl group in one *meso* position of the porphyrin core (Scheme 1, ESI, Fig. S14 and Fig. S15†). Several different spin states were considered for each geometry, and we report only the properties for the ground state in each case (Table 1). The end-on species is predicted to be a doublet with a strong interaction between iron and a DMSO ligand. The side-on structure has a sextet ground state, and geometry optimization leads to spontaneous dissociation of DMSO, so the latter was removed from the model. In each case, the potassium ion coordinates more strongly to one of the two O atoms of the superoxo or peroxo ligand. The two species are predicted to be close in energy, with the side-on complex lower by 2.3 kcal mol<sup>-1</sup> with B3PW91, and the end-on species lower by 3.8 kcal mol<sup>-1</sup> with B3LYP, respectively (Table 1). Given the different bonding pattern and spin-state of the two species, this is well within the expected error margin of DFT for complex transition metal systems,<sup>33</sup> even considering that dissociation of DMSO to provide the side-on species is entropically favored. Hence calculations support the suggestion that end-on and side-on complexes could exist in equilibrium. The computed O-O bond lengths (Scheme 1 and Table 2) in the end-on and side-on structure are typical for the superoxide<sup>18,28</sup> and peroxide entities, respectively. The O-O distance of the superoxo species is in the same region as those of the cryoradiolytically generated ones.<sup>16,17</sup> This is also supported by the spin densities on the oxygen atoms (Fig. 9).

The calculated Mössbauer parameters for the unusual low-spin Fe<sup>II</sup>-superoxo species ( $\delta = 0.53$  mm s<sup>-1</sup> and  $\Delta E_{\text{q}} = 1.37$  mm s<sup>-1</sup>) are also in good agreement with the experimental data obtained for the Fe<sup>II</sup> species that is present in the Mössbauer spectrum of the reaction product between our complex and either KO<sub>2</sub> or Na<sub>2</sub>O<sub>2</sub> (Fig. 4).

Inspection of molecular orbitals also supports the assigned character of the two species. The five singly occupied orbitals in the side-on complex are largely metal-based, with only the highest

orbital having significant O2  $\pi^*$  character (A in Fig. 9), whereas in the low-spin end-on complex (B in Fig. 9), the SOMO is essentially a pure superoxo  $\pi^*$  MO, with limited metal d orbital character.

## Conclusion

In conclusion, our Mössbauer, mass, EPR and IR spectra, as well as DFT calculations shed new light on the superoxide adduct of heme-Fe<sup>II</sup> species,  $\{\text{Fe}-\text{O}_2\}^-$ , suggesting that in coordinating DMSO solvent,  $\{\text{Fe}-\text{O}_2\}^-$  exists in both isomeric forms, Fe<sup>III</sup>-peroxo and Fe<sup>II</sup>-superoxo. Importantly, they are not resonance structures, but two discrete isomers. The existence of heme-Fe<sup>II</sup>-superoxo species explains our previous finding<sup>19</sup> that upon release of coordinated (su)peroxide from  $\{\text{Fe}-\text{O}_2\}^-$  a corresponding iron(II) complex remains in solution (pathway II in Scheme 1). Interestingly, Valentine *et al.* have also observed that in DMSO solution iron(III)-peroxo species can lead to corresponding Fe<sup>II</sup> complexes upon addition of coordinating pyridine, which was not further studied.<sup>6</sup> Now it is obvious that the obtained Fe<sup>II</sup> species results from the substitution reaction on an Fe<sup>II</sup>-O<sub>2</sub><sup>-</sup> isomer, which shifts the equilibrium from Fe<sup>III</sup>-peroxo back to its starting Fe<sup>II</sup> form (similar to pathway II). This finding is not only of general chemical importance but also helps in perceiving a nature of key intermediates  $\{\text{Fe}-\text{O}_2\}^-$  involved in dioxygen and hydrogen peroxide activation by hemoproteins,<sup>2</sup> which are commonly defined as Fe(III)-peroxo species. These complexes, as well as enzyme intermediates that incorporate such species, exhibit diverse types of reactivity that cannot always be explained by their iron(III)-peroxo character.<sup>34</sup> The existence of heme-Fe(II)-superoxo species may also have implications for some reaction mechanisms in which these types of intermediates are involved, questioning the nature of the active species in, for example, nucleophilic epoxidation reactions: is it a peroxo or a superoxo form which nucleophilically attacks an organic substrate? As proposed by Valentine *et al.*,<sup>34</sup> it seems that the end-on form of Fe<sup>III</sup>-peroxo species, favored by coordination of an axial ligand, is a promoter of nucleophilic attack. Here we suggest that such an end-on form has actually Fe<sup>II</sup>-superoxo character, which explains the nature of its catalytic action. It is indicative that after nucleophilic epoxidation reactions, *i.e.* oxygen transfer from Fe<sup>III</sup>-peroxo studied by Valentine *et al.*,<sup>34</sup> the complexes remain in the corresponding Fe<sup>II</sup> form.

The existence of the two isomeric forms of the  $\{\text{Fe}-\text{O}_2\}^-$  species speaks much better for its reactivity towards versatile substrates within catalytic cycles of corresponding heme enzymes. The results reported here should promote further consideration of heme-Fe(II)-superoxo species as possible reactive intermediates (not metastable intermediates or transition states) in biological and chemical systems.

**Table 2** Selected geometrical parameters of the optimized structures of end-on  $\{\text{KFe}^{\text{II}}(\text{por})(\text{DMSO}) + \text{O}_2^-\}$  and side-on  $\{\text{KFe}^{\text{II}}(\text{por}) + \text{O}_2^-\}$ , spin densities on the iron atom and on the oxygen atoms of the superoxide ligand in the complexes

Species	Bond lengths/Å						Bond angle/°	Spin densities		
	O1O2	FeO1	FeO2	FeO <sub>DMSO</sub>	K <sup>+</sup> O1	K <sup>+</sup> O2	FeOO	Fe	O1	O2
End-on $\{\text{KFe}^{\text{II}}(\text{por})(\text{DMSO}) + \text{O}_2^-\}$	1.322	1.897	2.798	2.115	2.782	2.705	119.7	0.067	0.424	0.488
Side-on $\{\text{KFe}^{\text{II}}(\text{por}) + \text{O}_2^-\}$	1.448	1.925	1.945	—	2.656	2.746	68.7	4.064	0.308	0.293

## Acknowledgements

The authors gratefully acknowledge financial support from the Deutsche Forschungsgemeinschaft through SFB 583 "Redox-active metal complexes" (K. D.; N. L.; N. J. and I. I.-B.). J. O. acknowledges receipt of an EU Marie Curie Fellowship (Project "Modelling CYPs").

## Notes and references

- 1 H. Chen, M. Ikeda-Saito and S. Shaik, *J. Am. Chem. Soc.*, 2008, **130**, 14778–14790.
- 2 M. Sono, M. P. Roach, E. D. Coulter and J. H. Dawson, *Chem. Rev. (Washington, D. C.)*, 1996, **96**, 2841–2887.
- 3 I. Schlichting, J. Berendzen, K. Chu, A. M. Stock, S. A. Maves, D. E. Benson, R. M. Sweet, D. Ringe, G. A. Petsko and S. G. Sligar, *Science*, 2000, **287**, 1615–1622.
- 4 E. Kim, E. E. Chufan, K. Kamaraj and K. D. Karlin, *Chem. Rev. (Washington, DC, U. S.)*, 2004, **104**, 1077–1133.
- 5 C. Mathe, T. A. Mattioli, O. Horner, M. Lombard, J.-M. Latour, M. Fontecave and V. Nivière, *J. Am. Chem. Soc.*, 2002, **124**, 4966–4967.
- 6 E. McCandlish, A. R. Miksztal, M. Nappa, A. Q. Sprenger, J. S. Valentine, J. D. Stong and T. G. Spiro, *J. Am. Chem. Soc.*, 1980, **102**, 4268–4271.
- 7 V. K. Kol'tover, O. I. Koifman, A. M. Khenkin and A. A. Shteinman, *Izv. Akad. Nauk SSSR, Ser. Khim.*, 1978, 1690–1691.
- 8 E. G. Kovaleva and J. D. Lipscomb, *Science*, 2007, **316**, 453–457.
- 9 J. P. Emerson, E. G. Kovaleva, E. R. Farquhar, J. D. Lipscomb, L. Que and Jr, *Proc. Natl. Acad. Sci. U. S. A.*, 2008, **105**, 7347–7352.
- 10 M. Schatz, V. Raab, S. P. Foxon, G. Brehm, S. Schneider, M. Reiher, M. C. Holthausen, J. Sundermeyer and S. Schindler, *Angew. Chem., Int. Ed.*, 2004, **43**, 4360–4363.
- 11 M. T. Kieber-Emmons, J. Annaraj, M. S. Seo, K. M. Van Heuvelen, T. Tosha, T. Kitagawa, T. C. Brunold, W. Nam and C. G. Riordan, *J. Am. Chem. Soc.*, 2006, **128**, 14230–14231.
- 12 D. Maiti, H. C. Fry, J. S. Woertink, M. A. Vance, E. I. Solomon and K. D. Karlin, *J. Am. Chem. Soc.*, 2007, **129**, 264–265.
- 13 D. Maiti, D.-H. Lee, K. Gaoutchenova, C. Wuertele, M. C. Holthausen, A. A. Narducci Sarjeant, J. Sundermeyer, S. Schindler and K. D. Karlin, *Angew. Chem., Int. Ed.*, 2008, **47**, 82–85.
- 14 S. Yao, E. Bill, C. Milsmann, K. Wieghardt and M. Driess, *Angew. Chem., Int. Ed.*, 2008, **47**, 7110–7113.
- 15 R. Davydov, J. D. Satterlee, H. Fujii, A. Sauer-Masarwa, D. H. Busch and B. M. Hoffman, *J. Am. Chem. Soc.*, 2003, **125**, 16340–16346.
- 16 H.-P. Hersleth, Y.-W. Hsiao, U. Ryde, C. H. Goerbitz and K. K. Andersson, *Biochem. J.*, 2008, **412**, 257–264.
- 17 M. Unno, H. Chen, S. Kusama, S. Shaik and M. Ikeda-Saito, *J. Am. Chem. Soc.*, 2007, **129**, 13394–13395.
- 18 M. Pedio, Z. Y. Wu, M. Benfatto, A. Mascaraque, E. Michel, C. Ottaviani, C. Crotti, M. Peloi, M. Zacchigna and C. Comicioli, *Phys. Rev. B: Condens. Matter Mater. Phys.*, 2002, **66**, 144109.
- 19 K. Duerr, B. P. Macpherson, R. Warratz, F. Hampel, F. Tuzek, M. Helmreich, N. Jux and I. Ivanovic-Burmazovic, *J. Am. Chem. Soc.*, 2007, **129**, 4217–4228.
- 20 M. Helmreich, *PhD*, University of Erlangen-Nuernberg, 2005.
- 21 *Jaguar 6.0*, Schrödinger, LLC, New York, 2005.
- 22 P. J. Hay and W. R. Wadt, *J. Chem. Phys.*, 1985, **82**, 299–310.
- 23 The LACV3P basis set is a triple-zeta contraction of the LACVP basis set developed and tested at Schrödinger, Inc.
- 24 S. Sinnecker, L. D. Slep, E. Bill and F. Neese, *Inorg. Chem.*, 2005, **44**, 2245–2254.
- 25 In accordance with<sup>24</sup> the CP(PPP) basis set was used on Fe, and the TZVP basis set on nitrogen and oxygen atoms, and the SV(P) basis set on the rest of the atoms.
- 26 M. J. Frisch, G. W. Trucks, H. B. Schlegel, G. E. Scuseria, M. A. Robb, J. R. Cheeseman, J. J. A. Montgomery, T. Vreven, K. N. Kudin, J. C. Burant, J. M. Millam, S. S. Iyengar, J. Tomasi, V. Barone, B. Mennucci, M. Cossi, G. Scalmani, N. Rega, G. A. Petersson, H. Nakatsuji, M. Hada, M. Ehara, K. Toyota, R. Fukuda, J. Hasegawa, M. Ishida, T. Nakajima, Y. Honda, O. Kitao, H. Nakai, M. Klene, X. Li, J. E. Knox, H. P. Hratchian, J. B. Cross, V. Bakken, C. Adamo, J. Jaramillo, R. Gomperts, R. E. Stratmann, O. Yazyev, A. J. Austin, R. Cammi, C. Pomelli, J. W. Ochterski, P. Y. Ayala, K. Morokuma, G. A. Voth, P. Salvador, J. J. Dannenberg, V. G. Zakrzewski, S. Dapprich, A. D. Daniels, M. C. Strain, O. Farkas, D. K. Malick, A. D. Rabuck, K. Raghavachari, J. B. Foresman, J. V. Ortiz, Q. Cui, A. G. Baboul, S. Clifford, J. Cioslowski, B. B. Stefanov, G. Liu, A. Liashenko, P. Piskorz, I. Komaromi, R. L. Martin, D. J. Fox, T. Keith, M. A. Al-Laham, C. Y. Peng, A. Nanayakkara, M. Challacombe, P. M. W. Gill, B. Johnson, W. Chen, M. W. Wong, C. Gonzalez and J. A. Pople *Gaussian 03, Revision C.02*, Gaussian, Inc., Wallingford CT, 2004.
- 27 J. N. Burstyn, J. A. Roe, A. R. Miksztal, B. A. Shaevitz, G. Lang and J. S. Valentine, *J. Am. Chem. Soc.*, 1988, **110**, 1382–1388.
- 28 D. T. Sawyer and J. S. Valentine, *Acc. Chem. Res.*, 1981, **14**, 393–400.
- 29 D. T. Sawyer, T. S. Calderwood, K. Yamaguchi and C. T. Angelis, *Inorg. Chem.*, 1983, **22**, 2577–2583.
- 30 J. S. Valentine, Y. Tatsuno and M. Nappa, *J. Am. Chem. Soc.*, 1977, **99**, 3522–3523.
- 31 S. Fukuzumi and K. Ohkubo, *Chem.-Eur. J.*, 2000, **6**, 4532–4535.
- 32 J. P. Collman, C. J. Sunderland, K. E. Berg, M. A. Vance and E. I. Solomon, *J. Am. Chem. Soc.*, 2003, **125**, 6648–6649.
- 33 J. N. Harvey, *Annu. Rep. Prog. Chem., Sect. C*, 2006, **102**, 203–226.
- 34 M. Selke and J. S. Valentine, *J. Am. Chem. Soc.*, 1998, **120**, 2652–2653.
- 35 E. E. Chufan and K. D. Karlin, *J. Am. Chem. Soc.*, 2003, **125**, 16160–16161.

## Solution behavior of iron(III) and iron(II) porphyrins in DMSO and reaction with superoxide. Effect of neighboring positive charge on thermodynamics, kinetics and nature of iron-(su)peroxo product†

K. Duerr,<sup>a</sup> O. Troeppner,<sup>a</sup> J. Olah,<sup>‡b</sup> J. Li,<sup>a</sup> A. Zahl,<sup>a</sup> T. Drewello,<sup>a</sup> N. Jux,<sup>a</sup> J. N. Harvey<sup>b</sup> and I. Ivanović-Burmazović<sup>\*a</sup>

Received 12th August 2011, Accepted 26th September 2011

DOI: 10.1039/c1dt11521a

The solution behavior of iron(III) and iron(II) complexes of 5<sup>4</sup>,10<sup>4</sup>,15<sup>4</sup>,20<sup>4</sup>-tetra-*tert*-butyl-5,10,15,20-tetraphenylporphyrin (H<sub>2</sub>tBuTPP) and the reaction with superoxide (KO<sub>2</sub>) in DMSO have been studied in detail. Applying temperature and pressure dependent NMR studies, the thermodynamics of the low-spin/high-spin equilibrium between bis- and mono-DMSO Fe<sup>II</sup> forms have been quantified ( $K_{\text{DMSO}} = 0.082 \pm 0.002$  at 298.2 K,  $\Delta H^\circ = +36 \pm 1$  kJ mol<sup>-1</sup>,  $\Delta S^\circ = +101 \pm 4$  J K<sup>-1</sup> mol<sup>-1</sup>,  $\Delta V^\circ = +16 \pm 2$  cm<sup>3</sup> mol<sup>-1</sup>). This is a key activation step for substitution and inner-sphere electron transfer. The superoxide binding constant to the iron(II) form of the studied porphyrin complex was found to be  $(9 \pm 0.5) \times 10^3$  M<sup>-1</sup>, and does not change significantly in the presence of the externally added crown ether in DMSO  $(11 \pm 4) \times 10^3$  M<sup>-1</sup>. The rate constants for the superoxide binding ( $k_{\text{on}} = (1.30 \pm 0.01) \times 10^5$  M<sup>-1</sup> s<sup>-1</sup>) and release ( $k_{\text{off}} = 11.6 \pm 0.7$  s<sup>-1</sup>) are not affected by the presence of the external crown ether in solution. The resulting iron(II)-superoxide adduct has been characterized (mass spectrometry, EPR, high-pressure UV/Vis spectroscopy) and upon controlled addition of a proton source it regenerates the starting iron(II) complex. Based on DFT calculations, the reaction product without neighboring positive charge has iron(II)-superoxo character in both high-spin side-on and low-spin end-on forms. The results are compared to those obtained for the analogous complex with covalently attached crown ether, and more general conclusions regarding the spin-state equilibrium of iron(II) porphyrins, their reaction with superoxide and the electronic structure of the product species are drawn.

### Introduction

Activation of molecular oxygen by an iron(II) center within heme-containing enzymes (cytochrome P450, NO synthase, cytochrome oxidase)<sup>1</sup> proceeds through the formation of the one-electron reduced form of the iron(II)-dioxygen adduct, {Fe–O<sub>2</sub>}<sup>-</sup>, which is widely accepted as an iron(III)-peroxo species.<sup>2</sup> The same species can be obtained in the reaction between heme iron(II) and superoxide (O<sub>2</sub><sup>-</sup>). Due to its transient character and inherent low

stability, its characterization could only be achieved at subzero temperatures, both in enzymatic and porphyrin model systems.<sup>2,3</sup> Even more difficult is the trapping and characterization of a monoprotonated iron(III)-hydroperoxo form, which is a short-lived intermediate on a way to an iron(IV)-oxo species, which results from O–O bond cleavage assisted by a second protonation step involving the same (distal) oxygen atom. Preparation of the iron(III)-hydroperoxo complex has been recently reported by using a porphyrin system with covalently linked axial imidazole (Im).<sup>4</sup> The axial imidazole ligation seems to be important for the formation of a metastable hydroperoxo species, because in a concerted fashion with the proton transfer it assists in the spin state and binding mode switch, from high-spin side-on to a low-spin end-on configuration (pathway (a), Scheme 1).<sup>4</sup>

We have also observed that the axial ligation influences the nature of a heme iron-dioxygen species and controls the mechanism of its formation.<sup>5</sup> These findings were obtained by studying the reaction of superoxide in DMSO with an iron complex of a crown ether-porphyrin conjugate (H<sub>2</sub>Porph), which is also able to chelate the potassium cation.<sup>5</sup> There we have shown that axial coordination of DMSO alone causes not only a spin-state and

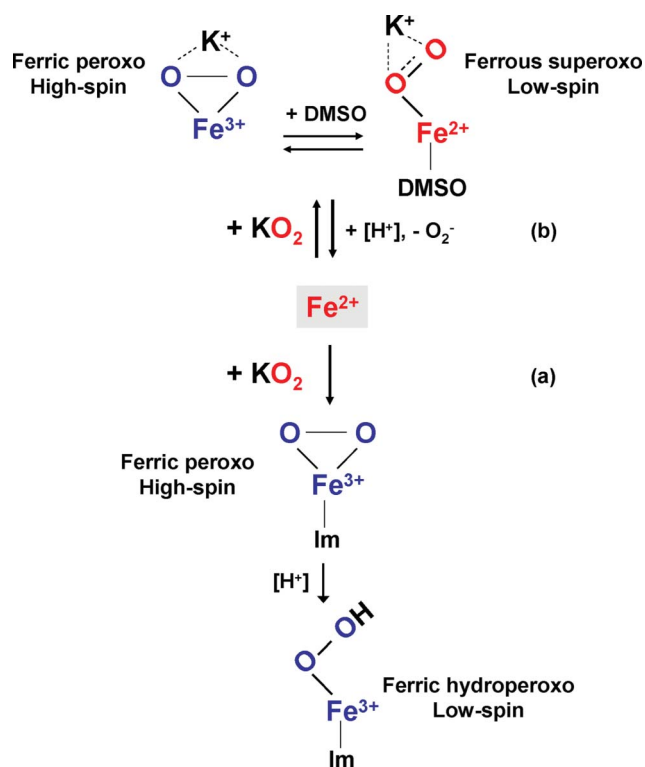
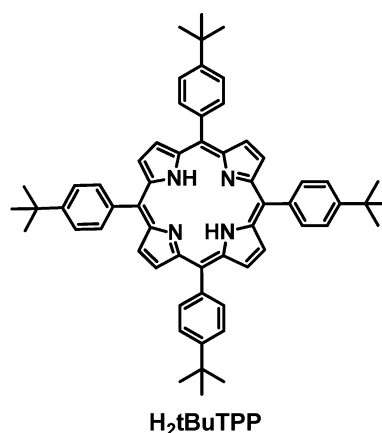
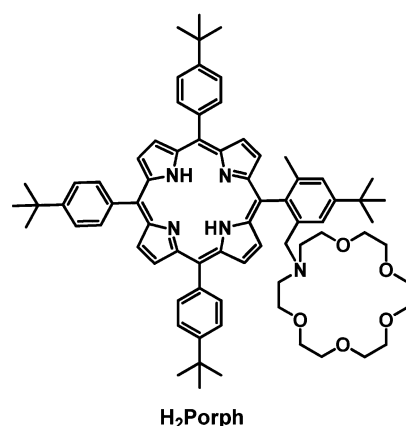
<sup>a</sup>Department of Chemistry and Pharmacy, University of Erlangen-Nürnberg, Egerlandstr. 1, 91058, Erlangen, Germany. E-mail: ivana.ivanovic@chemie.uni-erlangen.de

<sup>b</sup>School of Chemistry and Centre for Computational Chemistry, University of Bristol, Cantock's Close, Bristol, UK, BS8 1TS

† Electronic supplementary information (ESI) available: Spectroelectrochemistry, effect of temperature and pressure on the equilibrium constant  $K_{\text{DMSO}}$ , ESI mass spectrometry, EPR spectroscopy kinetics and thermodynamics of superoxide binding, high-pressure UV/vis measurements, DFT calculations. See DOI: 10.1039/c1dt11521a

‡ Present address: Department of Inorganic and Analytical Chemistry and Materials Structure and Modeling Research Group of the Hungarian Academy of Sciences, Budapest University of Technology and Economics, P.O. Box 91, 1521 Budapest, Hungary.





**Scheme 1** Products of the superoxide reaction with heme Fe(II) and subsequent fine tuned protonation: (a) heme species with the covalently linked axial imidazole ligand,<sup>4</sup> (b) heme species with the covalently linked potassium cation moiety.<sup>5</sup>

binding-mode switch of heme peroxide but also a redox-state switch, resulting in the co-existence of two isomeric forms in equilibrium, *viz.* Fe(II)-superoxo and Fe(III)-peroxo (pathway (b), Scheme 1).<sup>5b,c</sup> The presence of nearby K<sup>+</sup> seemed to be crucial for the remarkably high stability of the iron-(su)peroxo complex that was stable even at room temperature. Aided by its stability we have been able to demonstrate that binding of superoxide to the iron(II) center is a reversible process and we could quantify the kinetics and thermodynamics of O<sub>2</sub><sup>-</sup> binding.<sup>5a,c</sup> Interestingly, addition of a controlled amount of proton sources to the reaction mixture has not resulted in either formation of Fe(III)-hydroperoxo or O–O bond cleavage and formation of a high-valent oxo-iron species. Instead, it pulled the reaction equilibrium back to the iron(II)

form by decomposing the excess of superoxide present in solution (pathway (b), Scheme 1).

The arising question is whether findings such as reversible superoxide binding, high stability of the obtained iron-(su)peroxo porphyrin, the equilibrium between Fe(II)-superoxo and Fe(III)-peroxo species and generation of the Fe(II) form upon proton addition are unique features of this particular complex, caused by the presence of the nearby positive charge from the K<sup>+</sup>-crown ether moiety. To answer this question the current study investigates the iron complex of the corresponding porphyrin without covalently attached crown ether moiety (H<sub>2</sub>tBuTPP) and the reaction of the Fe(II) form with superoxide (KO<sub>2</sub>) in DMSO. The reaction has also been studied in the presence of externally added crown ether (18-crown-6) in order to compare its effects with those of covalently attached crown ether. To obtain insight into the influence of the positively charged surrounding on the nature of the product heme iron-(su)peroxo species, computational DFT studies have been performed as well.

## Experimental

### Materials and general considerations

Reagents and solvents were obtained from commercial sources and were of reagent quality unless otherwise stated. DMSO and acetonitrile were purchased as extra-dry solvents. All chemicals were used as received without further purification. K<sup>18</sup>O<sub>2</sub> was prepared according to a published method;<sup>6</sup> <sup>18</sup>O<sub>2</sub> was obtained from Aldrich.

### H<sub>2</sub>tBuTPP

The H<sub>2</sub>tBuTPP (5<sup>4</sup>,10<sup>4</sup>,15<sup>4</sup>,20<sup>4</sup>-tetra-*tert*-butyl-5,10,15,20-tetraphenylporphyrin) ligand was obtained as a side product in the synthesis of a precursor of H<sub>2</sub>Porph (5<sup>2</sup>-*N*-(4-aza-18-crown-6)methyl-5<sup>4</sup>,10<sup>4</sup>,15<sup>4</sup>,20<sup>4</sup>-tetra-*tert*-butyl-5<sup>6</sup>-methyl-5,10,15,20-tetraphenylporphyrin).<sup>5a</sup>

### [Fe<sup>III</sup>(tBuTPP)Cl]

H<sub>2</sub>tBuTPP (300 mg, 0.357 mmol) was dissolved in 30 mL of CHCl<sub>3</sub>. An FeCl<sub>2</sub> solution (67.0 mg, 0.524 mmol) in 30 mL of ethanol was added. Two drops of 2,6-lutidine were added and the solution refluxed for 2 h. Completion of the reaction was

followed by thin layer chromatography on  $\text{Al}_2\text{O}_3$  plates, which is indicated by disappearance of the fluorescence of the free base porphyrin. After that, the mixture was filtered and worked up by shaking with water and half concentrated HCl. The organic layer was dried over anhydrous  $\text{MgSO}_4$  and the solvent removed. The product is a brown powder in 84% yield.  $^1\text{H}$  NMR (400 MHz,  $\text{CDCl}_3$ , 25° C):  $\delta$  [ppm] 80.9 (br s, 8H,  $\beta$ -pyrr.), 13.7 (s, 4H,  $m$ -ArH), 12.5 (s, 4H,  $m$ -ArH), 7.50 (s, 4H,  $o$ -ArH), 2.51 (s, 36H, Ar- $t$ -Bu).  $^{13}\text{C}$  NMR (100 MHz,  $\text{CDCl}_3$ , 25° C):  $\delta$  [ppm] 145.0 (4C,  $m$ -ArCH), 140.7 (4C,  $m$ -ArCH), 37.7 (4C,  $t$ -BuC $^q$ ), 29.6 (12C,  $t$ -Bu-CH $_3$ ). FAB-MS:  $m/z$  892 ( $\text{M}^+ - \text{Cl}$ ). UV/Vis ( $\text{CH}_2\text{Cl}_2$ ):  $\lambda$  [nm] ( $\epsilon$  [ $\text{L cm}^{-1} \text{mol}^{-1}$ ]) 381 (54100), 419 (114000), 512 (12400), 585 (2470), 615 (5640). IR (KBr):  $\tilde{\nu}$  [ $\text{cm}^{-1}$ ] 2960, 2926, 2866, 1495, 1461, 1395, 1363, 1333, 1267, 1202, 1109, 1069, 998, 805, 721. Elemental analysis for  $\text{C}_{60}\text{H}_{60}\text{ClFeN}_4\cdot 3\text{H}_2\text{O}$ . Calc.: C, 73.35; H, 6.77; N, 5.70. Found: C, 73.30; H, 6.95; N, 5.40%.

### $[\text{Fe}^{\text{III}}(\text{tBuTPP})_2]\text{O}$

The  $\mu$ -oxo-dimer was prepared by shaking a solution of  $[\text{Fe}^{\text{III}}(\text{tBuTPP})\text{Cl}]$  (100.0 mg, 0.119 mmol) in  $\text{CH}_2\text{Cl}_2$  (20 mL) with a 2 M solution of aqueous NaOH (20 mL). The organic layer was separated and dried over anhydrous  $\text{MgSO}_4$ , and the solvent was evaporated. A brown solid was obtained in 79% yield.  $^1\text{H}$  NMR (400 MHz,  $\text{CDCl}_3$ , 25° C):  $\delta$  [ppm] 13.3 (s, 16H,  $\beta$ -pyrr.), 7.76 (s, 8H,  $m$ -ArH), 7.65 (s, 8H,  $o$ -ArH), 1.67 (s, 72H, Ar- $t$ -Bu).  $^{13}\text{C}$  NMR (100 MHz,  $\text{CDCl}_3$ , 25° C):  $\delta$  [ppm] 150.3 (8C,  $p$ -ArC $^q$ ), 144.2 (16C,  $\alpha$ -pyrr.), 142.1 (8C, ArC $^q$ ), 134.3 (16C,  $o$ -ArCH), 131.7 (16C,  $\beta$ -pyrr.), 123.3 (16C,  $m$ -ArCH), 119.9 (8C, *meso*-C), 34.5 (8C,  $t$ -BuC $^q$ ), 31.8 (24C,  $t$ -Bu-CH $_3$ ). FAB-MS:  $m/z$  1802 ( $\text{M}^+$ ) 892 ( $\text{M}^+ - \text{O} - \text{Fe}(\text{tBuTPP})$ ). UV/Vis ( $\text{CH}_2\text{Cl}_2$ ):  $\lambda$  [nm] ( $\epsilon$  [ $\text{L cm}^{-1} \text{mol}^{-1}$ ]) 418 (194000), 513 (11800), 575 (2980). UV/Vis (DMSO):  $\lambda$  [nm] 417, 560 sh, 574, 613. IR (KBr):  $\tilde{\nu}$  [ $\text{cm}^{-1}$ ] 2962, 2926, 2867, 1496, 1461, 1396, 1363, 1340, 1267, 1203, 1109, 1070, 999, 895, 876, 812, 799, 719.

### $[\text{Fe}^{\text{III}}(\text{tBuTPP})(\text{DMSO})_2]^+$

A solution of  $[\text{Fe}^{\text{III}}(\text{tBuTPP})\text{Cl}]$  in DMSO yields the bis-DMSO complex of the iron porphyrin. UV/Vis (DMSO):  $\lambda$  [nm] ( $\epsilon$  [ $\text{L mol}^{-1} \text{cm}^{-1}$ ]) 404sh (15400), 419 (17600), 496sh (3850), 535 (4000), 719 (2095).

### $[\text{Fe}^{\text{III}}(\text{tBuTPP})\text{OH}]$

Addition of water or NaOH to a solution of  $[\text{Fe}^{\text{III}}(\text{tBuTPP})(\text{DMSO})_2]^+$  yields the hydroxo complex  $[\text{Fe}^{\text{III}}(\text{tBuTPP})\text{OH}]$ . UV/Vis (DMSO):  $\lambda$  [nm] ( $\epsilon$  [ $\text{L mol}^{-1} \text{cm}^{-1}$ ]) 416sh (14900), 438 (30600), 540 (3100), 573 (1400).

### $[\text{Fe}^{\text{II}}(\text{tBuTPP})(\text{DMSO})_{1,2}]$

The reduced form of  $[\text{Fe}^{\text{III}}(\text{tBuTPP})\text{Cl}]$  could be obtained by chemical reduction or bulk electrolysis. Chemical reduction in dry DMSO was achieved by using sodium dithionite (saturated solution) as reductant. UV/Vis (DMSO):  $\lambda$  [nm] ( $\epsilon$  [ $\text{L mol}^{-1} \text{cm}^{-1}$ ]) 411sh (12500), 430 (69750), 533 (3100).  $^1\text{H}$  NMR (reduction with sodium dithionite, 300 MHz,  $\text{DMSO}-d_6$ , 25° C):  $\delta$  [ppm] 13.0 (br s, mono-DMSO pyrr.), 9.90 (s, bis-DMSO pyrr.), 8.13 (s, bis-DMSO

$o$ -phenyl), 7.86 (s, bis-DMSO  $m$ -phenyl), 3.34 (s, bis-DMSO  $t$ -Bu), 1.60 (s, mono-DMSO  $t$ -Bu).

### $\text{K}[\text{Fe}^{\text{III}}(\text{tBuTPP})(\text{O}_2^{2-})]$

$\text{KO}_2$  was suspended in a solution of  $[\text{Fe}^{\text{III}}(\text{tBuTPP})\text{Cl}]$  in dry DMSO. The solution was stirred until the color changed to green and was filtered under argon atmosphere. UV/Vis (DMSO):  $\lambda$  [nm] ( $\epsilon$  [ $\text{L mol}^{-1} \text{cm}^{-1}$ ]) 422sh (36100), 439 (148000), 568sh (6900), 612 (3710).

### Equipment

Elemental analysis was carried out on a HERAEUS CHN-Mikroautomat, a Euro EA 3000 (Euro Vector) and an EA 1108 (Carlo Erba) instrument. L-SIMS ( $\text{Cs}^+$ ) mass spectra were recorded with a Micromass ZABSpec mass spectrometer employing  $m$ -NBA as the matrix. Standard  $^1\text{H}$  and  $^{13}\text{C}$  NMR spectra were measured on a Bruker Avance 300 spectrometer. Standard IR spectra (KBr) were measured on a FT-IR IFS 88 spectrometer (Bruker Analytische Messtechnik GmbH).

### Spectroelectrochemistry

Electrochemical reduction was performed under nitrogen at a Pt mesh working electrode with an Ag wire pseudo-reference electrode and a platinated Ti auxiliary electrode separated from the working electrode compartment by a glass frit. The experiment was stopped when no further change in the UV/Vis spectra was observed. Time-resolved UV/Vis spectra were taken by a UV/Vis immersion probe (Hellma 661.502-QX quartz suprasil). It was attached *via* optical cables to a 150 W Xe lamp. Recording of the spectra was done by a multi-wavelength J & M detector. An Autolab instrument with a PGSTAT 30 was used as potentiostat.

### $^1\text{H}$ NMR investigation of $[\text{Fe}^{\text{II}}(\text{tBuTPP})(\text{DMSO})_n]$ ( $n = 1, 2$ )

Sample preparations were done in an Ar MBraun glovebox. A sample of  $[\text{Fe}^{\text{II}}(\text{tBuTPP})(\text{DMSO})_n]$  ( $n = 1, 2$ ) was prepared by addition of an excess of  $\text{Na}_2\text{S}_2\text{O}_4$  to a 2 mM solution of  $[\text{Fe}^{\text{III}}(\text{tBuTPP})(\text{DMSO})_n]$  ( $n = 1, 2$ ) in dry  $\text{DMSO}-d_6$ . The suspension was stirred for 30 min.  $^1\text{H}$  NMR spectra were taken after filtration.

Temperature-dependent NMR spectra in  $\text{DMSO}-d_6$  were measured on a Bruker Avance 300 or Bruker AVANCE DRX 400WB instrument. All spectra were recorded in 5 mm o.d. NMR tubes, and chemical shifts were reported as  $\delta$  (ppm) values calibrated to natural abundance deuterium solvent peaks (ppm).

A homemade high-pressure probe described in the literature was used for the variable-pressure experiments.<sup>7</sup> Pressure-dependent measurements were performed in a standard 5 mm NMR tube cut to a length of 50 mm. To enable pressure transmittance to the solution, the NMR tube was closed with a moveable KEL-S piston. The advantage of this method is that oxygen-sensitive samples can be easily placed in the NMR tube and sealed with the KEL-S piston under argon atmosphere. A safe subsequent transfer to the high-pressure probe is assured. The pressure was applied to the high-pressure probe *via* a perfluorinated hydrocarbon pressure medium (hexafluoropropylene oxide, Hostinert 175, Hoechst) and measured by a VDO gauge with an accuracy of 1%. The

temperature was adjusted with circulating, thermostated water (Colora thermostat WK 16) to 0.1 K of the desired value and monitored before each measurement with an internal Pt-resistance thermometer with an accuracy of 0.2 K.<sup>8</sup> The temperature was chosen to be 320 K and kept constant, since at lower temperatures DMSO can freeze upon increasing the pressure.

### ESI and cryospray mass spectrometry

Using a syringe pump at a flow rate of 240 mL h<sup>-1</sup>, the DMSO solutions were infused into an orthogonal ESI source of an Esquire 6000 ion trap mass spectrometer (Bruker, Bremen, Germany). Nitrogen was used as the nebulizing gas at a pressure of 10 psi and as the drying gas at a temperature of 300 °C and a flow rate of 5 L min<sup>-1</sup>. The ion trap was optimized for the respective target mass of the ions under investigation. The source voltages varied with this optimization. All experiments were carried out in the positive-ion mode. The sample of the starting complex [Fe<sup>III</sup>(tBuTPP)Cl] was prepared by making a 5 × 10<sup>-4</sup> M suspension in dry DMSO (stirred overnight) under nitrogen and subsequent filtration. Other samples were prepared by dissolving excess of either KO<sub>2</sub> or K<sup>18</sup>O<sub>2</sub> in an overnight-prepared 5 × 10<sup>-4</sup> M suspension of [Fe<sup>III</sup>(tBuTPP)Cl] in dry DMSO under nitrogen and subsequent filtration. High mass accuracy ESI spectra were recorded on an ultra high-resolution ESI-Time-Of-Flight MS, a Bruker Daltoniks (Bremen, Germany) Maxis, which also was coupled to the Bruker cryospray. For the cryospray measurements samples were dissolved in a MeCN–DMSO (70 : 30) mixture.

### Thermodynamics and kinetics

Solution preparations of KO<sub>2</sub>, [Fe<sup>II</sup>(tBuTPP)(DMSO)<sub>n</sub>] (*n* = 1, 2) and [Fe<sup>III</sup>(tBuTPP)(O<sub>2</sub><sup>2-</sup>)]<sup>-</sup> in DMSO without 18-crown-6 were done according to our previous study.<sup>5</sup> Solutions of [Fe<sup>III</sup>(tBuTPP)(O<sub>2</sub><sup>2-</sup>)]<sup>-</sup> in DMSO with 18-crown-6 were prepared by addition of a ten-fold excess of 18-crown-6 (relative to the porphyrin concentration) to a freshly prepared solution of [Fe<sup>II</sup>(tBuTPP)(DMSO)<sub>n</sub>] (*n* = 1, 2).

A Hewlett-Packard 8452A spectrophotometer was used for qualitative UV/Vis measurements and measurement of the binding constant of superoxide to [Fe<sup>II</sup>(tBuTPP)(DMSO)<sub>n</sub>] (*n* = 1, 2) without and with added 18-crown-6 (10 times the concentration of the porphyrin complex).

A spectrophotometric study of the binding of superoxide to [Fe<sup>II</sup>(tBuTPP)(DMSO)<sub>n</sub>] (*n* = 1, 2) was performed in a 1-cm path length cuvette with a 25 mL reservoir under nitrogen. The 1.3 × 10<sup>-5</sup> M solution (5 mL) of electrochemically generated [Fe<sup>II</sup>(tBuTPP)(DMSO)<sub>n</sub>] (*n* = 1, 2) was titrated with aliquots of a saturated KO<sub>2</sub> solution in DMSO added from a Hamilton microsyringe. The same experiment was performed with the Fe(II) complex and added 18-crown-6 (1.3 × 10<sup>-5</sup> M and 1.3 × 10<sup>-4</sup> M, respectively). Data were fitted according to following equation (*A*<sub>0</sub> and *A*<sub>∞</sub> represent the absorbance at 0 and 100% of the product formation, respectively, *A*<sub>x</sub> represents the absorbance at the respective measured superoxide concentration):<sup>9</sup>

$$A_x = A_0 + (A_\infty - A_0)K[\text{O}_2^{\cdot-}]/(1 + K[\text{O}_2^{\cdot-}])$$

Kinetic data were obtained by recording time-resolved UV/Vis spectra using a modified μSFM-20 Bio-Logic stopped-flow module combined with a Huber CC90 cryostat or a Biologic SFM-400 four syringes stopped-flow system (using only the first three syringes) and a high density mixer to minimize mixing effects in DMSO solutions. The stopped-flow set-ups were equipped with a J&M TIDAS high-speed diode array spectrometer with combined deuterium and tungsten lamps (200–1015 nm wavelength range). Isolast O-rings were used for all sealing purposes to enable measurements in DMSO, and solutions were delivered from 10 mL gas-tight Hamilton syringes. The syringes were controlled by separate drives, allowing for variation of the ratio of mixing volumes used in the kinetic runs. Data were analyzed using the integrated Bio-Kine software version 4.23 and also the Specfit/32™ program. At least five kinetic runs were recorded under all conditions, and the reported rate constants represent the mean values. The stopped-flow instrument was thermostated to the desired temperature ±0.1 °C. Experiments at 25 °C were performed in DMSO solution. All kinetic measurements were carried out under pseudo-first-order conditions; *i.e.* superoxide concentration was in large excess (complex concentration was usually 5 × 10<sup>-6</sup> M). The reactions were studied at an ionic strength of 0.1 M (Bu<sub>4</sub>NPF<sub>6</sub>).

For the rapid kinetic measurements, the Bio-Logic stopped-flow module was upgraded to a submillisecond mixing stopped-flow configuration by combining it with a microcuvette accessory (with an optical pathlength of 0.8 mm) and a monochromator to minimize the dead time of the instrument.<sup>10</sup>

### High-pressure UV/Vis measurements

Sample preparation was carried out in an Ar MBraun glovebox. A sample of [Fe<sup>III</sup>(tBuTPP)(O<sub>2</sub><sup>2-</sup>)]<sup>-</sup> was prepared by addition of an excess of KO<sub>2</sub> to a 10<sup>-5</sup> M solution of [Fe<sup>III</sup>(tBuTPP)Cl] in a dry DMSO solution of 0.1 M TBAP. The suspension was stirred for 30 min. High pressure UV/Vis spectra were recorded after filtration.

Spectral measurements at elevated pressure were performed in a pill-box cuvette on a Shimadzu UV-2101-PC spectrophotometer using a home-made high-pressure cell.<sup>11</sup> The high-pressure pump was purchased from NOVA SWISS (Nova Werke AG, CH-8307 Effretikon, Vogelsangstrasse); it allows measurements up to 150 MPa.

### DFT calculations

Geometry optimizations of the structures were performed with the Jaguar 6.0 program package<sup>12</sup> using the B3PW91 and B3LYP functionals, and a restricted open shell formalism (ROKS). The 6-31G(d) basis set was used on all atoms with the exception of the metal ions for which the standard Los Alamos effective core potentials<sup>13</sup> were used with the associated double-ζ, basis LACVP on potassium and the triplet-ζ basis LACV3P<sup>14</sup> on iron. The calculated total energies of the optimized structures *in vacuo*, together with the total energy of the dissociated DMSO ligand, were used to compare the stability of the side-on and end-on complexes.

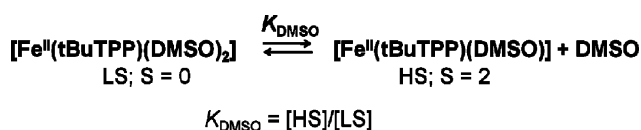
### Results and discussion

In a DMSO solution Fe(III) porphyrins exist as bis-DMSO species.<sup>15</sup> Similar to the [Fe<sup>III</sup>(Porph)(DMSO)<sub>2</sub>]<sup>+</sup> complex

with the covalently attached crown ether moiety,<sup>5</sup> the  $[\text{Fe}^{\text{III}}(\text{tBuTPP})(\text{DMSO})_2]^+$  complex reacts with an excess of  $\text{KO}_2$  resulting in an adduct commonly described as  $[\text{Fe}^{\text{III}}(\text{tBuTPP})(\text{O}_2^{2-})]^-$ .<sup>2</sup> The reaction proceeds in two steps. In the first step  $\text{Fe}(\text{III})$  is reduced to  $\text{Fe}(\text{II})$ , which in the second step binds superoxide yielding  $[\text{Fe}^{\text{III}}(\text{tBuTPP})(\text{O}_2^{2-})]^-$ .<sup>2,5</sup> In this study we used the electrochemically generated  $\text{Fe}(\text{II})$  form of the complex as the reactant, *i.e.* we concentrated on the second reaction step. As previously reported,<sup>5a</sup> the first reaction step, reduction of the  $\text{Fe}^{\text{III}}$  to the  $\text{Fe}^{\text{II}}$  porphyrin complex by  $\text{KO}_2$ , could not be quantitatively studied in detail because of interference of the  $\text{Fe}(\text{III})$ -hydroxo species formation by  $\text{KOH}$ , which is inevitably present in commercial  $\text{KO}_2$ . Details on the spectroelectrochemical measurements and UV/vis characterization of different  $\text{Fe}(\text{III})$  forms of the studied complex are given in ESI† (Fig. S1–S4, Table S1 and Scheme S1)

### $^1\text{H}$ NMR investigation of $[\text{Fe}^{\text{II}}(\text{tBuTPP})(\text{DMSO})_n]$ ( $n = 1, 2$ )

Solvation of iron(II) tetraphenylporphyrins in DMSO leads to an equilibrium between mono- and bis-DMSO complexes (Scheme 2).<sup>5,16</sup> In order to investigate the thermodynamics of such equilibrium in the case of  $[\text{Fe}^{\text{II}}(\text{tBuTPP})(\text{DMSO})_n]$ , temperature- and pressure-dependent  $^1\text{H}$  NMR studies were performed.



Scheme 2

Literature data on NMR of  $[\text{Fe}^{\text{II}}(\text{tpp})]$  in DMSO reveal the coexistence of high-spin and low-spin species<sup>16</sup> with a moderately broad paramagnetic signal of the pyrrole protons at around 12 ppm. This finding corresponds to the NMR spectra of investigated  $[\text{Fe}^{\text{II}}(\text{tBuTPP})(\text{DMSO})_n]$  ( $n = 1, 2$ ) (Fig. S5, ESI†). In the region from 0 to 10 ppm, there are signals with only minor line broadening which correspond to the signals of the diamagnetic  $[\text{Fe}^{\text{II}}(\text{tBuTPP})(\text{DMSO})_2]$  species. The broad signal at around 13 ppm belongs to the resonances of the pyrrole protons of the paramagnetic  $[\text{Fe}^{\text{II}}(\text{tBuTPP})(\text{DMSO})]$  species. The remaining paramagnetic resonances cannot be observed as they are merged with the diamagnetic ones (Fig. S5, ESI†). The position and line broadening of the pyrrole protons of a porphyrin system are generally used in order to determine the spin state of the central metal.<sup>17</sup>

Upon increase of temperature the paramagnetic signal shifts strongly to lower field (Fig. S6, ESI†). The remainder of the spectrum remains almost unchanged. Line broadening increases only moderately. After letting the sample cool down, the starting spectrum is retrieved. This supports the existence of the high-spin/low-spin equilibrium, with the share of the high spin species increasing with the temperature increase.

Since the low-spin/high-spin equilibrium constant ( $K_{\text{DMSO}}$ , Scheme 2) should also be pressure sensitive, we performed pressure-dependent  $^1\text{H}$  NMR measurements. A pressure increase shows a shift of the equilibrium to the diamagnetic low-spin species (Fig. 1). This is expected, since a higher pressure favors the

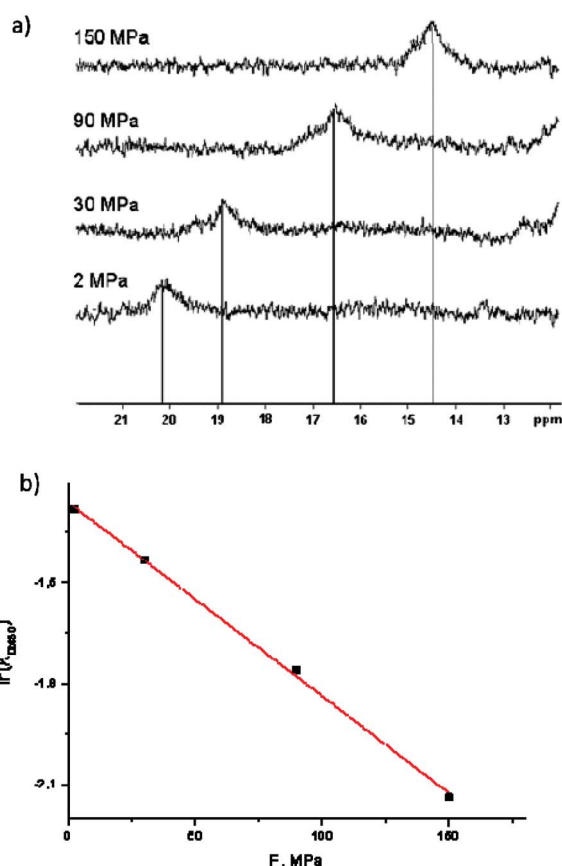


Fig. 1 (a)  $^1\text{H}$  NMR spectrum of  $[\text{Fe}^{\text{II}}(\text{tBuTPP})(\text{DMSO})_n]$  ( $n = 1, 2$ ) at 325.2 K and different pressures; (b) plot of  $\ln(K_{\text{DMSO}})$  vs. pressure.

coordination of the second DMSO molecule. Decrease of pressure after the experiment shows again a larger share of the high-spin species and confirms the reversibility of the observed pressure dependent process.

The temperature- and pressure-dependent measurements enable the quantification of the thermodynamic parameters for the equilibrium  $K_{\text{DMSO}}$  in Scheme 2 (HS = high-spin mono-DMSO complex; LS = low-spin bis-DMSO complex; the activity of solvent is considered to be 1). The parameters are summarized in Table 1 (for details see Supplementary Information and Table S2, ESI†).

The temperature dependence plot of  $\ln(K_{\text{DMSO}})$  (Fig. S7, ESI†) was found to be linear and resulted in significantly positive values for the thermodynamic parameters  $\Delta H^\circ$  and  $\Delta S^\circ$  (Table 1). They are in agreement with the endothermic and dissociative character of the underlying low-spin to high-spin transition. Interestingly, the spin-state equilibrium in the case of ferric cytochrome P450 is characterized within the corresponding temperature range by similar thermodynamic parameters ( $\Delta H^\circ = +42 \text{ kJ mol}^{-1}$  and

Table 1 Thermodynamic parameters for the equilibrium constant  $K_{\text{DMSO}}$

$K_{\text{DMSO}}$ at 298.2 K	$0.082 \pm 0.002$
$\Delta H^\circ/\text{kJ mol}^{-1}$	$+36 \pm 1$
$\Delta S^\circ/\text{J K}^{-1} \text{mol}^{-1}$	$+101 \pm 4$
$\Delta G^\circ/\text{kJ mol}^{-1}$ at 298.2 K	$6 \pm 1$
$\Delta V^\circ/\text{cm}^3 \text{mol}^{-1}$ at 325.2 K	$+16 \pm 2$

$\Delta S^\circ = +152 \text{ J K}^{-1} \text{ mol}^{-1}$ ).<sup>18</sup> A typical entropy change that is considered to drive the spin transition from low- to high-spin state is approximately  $50 \text{ J K}^{-1} \text{ mol}^{-1}$ , and in the case of an Fe(II) spin-crossover compound is found to be  $60 \text{ J K}^{-1} \text{ mol}^{-1}$ .<sup>19</sup> The observed entropy change of  $\sim 101 \text{ J K}^{-1} \text{ mol}^{-1}$  (Table 1) is significantly larger than that associated with the simple spin transition indicating that the covalent bond breaking and an increase in translational and rotational degrees of freedom as a consequence of a dissociative process have significant contribution. By way of comparison, in the opposite associative process accompanied by high-spin to low-spin transition upon CO rebinding to the five-coordinate (L)Fe<sup>II</sup>4SP complexes (4SP = tetrakis(4-sulfonatophenyl)porphyrin, L = H<sub>2</sub>O or 2-methylimidazole) the reaction entropy were found to be  $-117 \text{ J K}^{-1} \text{ mol}^{-1}$ .<sup>20</sup>

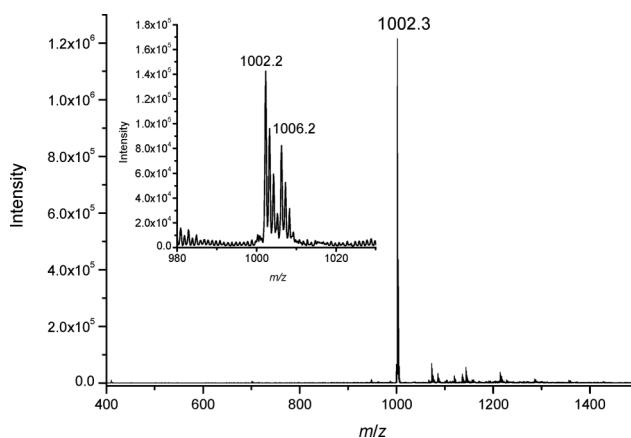
The values of  $K_{\text{DMSO}}$  and the corresponding distribution of species (see Table S2, ESI†) show that in DMSO solution mostly the low-spin bis-DMSO complex exists (92% at 298 K and 0.1 MPa). The pressure dependence of  $\ln(K_{\text{DMSO}})$  also gave a straight line (Fig. 1b) and resulted in  $\Delta V^\circ = +16 \pm 2 \text{ cm}^3 \text{ mol}^{-1}$ . The high positive reaction volume is a result of DMSO dissociation that accompanies the spin-state change on the Fe center. The reaction volume changes for spin transitions in Fe(II) complexes have been reported to range between 5 and  $19 \text{ cm}^3 \text{ mol}^{-1}$ ,<sup>19,21</sup> whereas the covalent bond breaking contributes to a volume change with roughly  $5\text{--}10 \text{ cm}^3 \text{ mol}^{-1}$ .<sup>22</sup> This implies that the change in coordination number on the iron center coupled to a spin-state transformation is characterised by volume changes of  $10\text{--}30 \text{ cm}^3 \text{ mol}^{-1}$ . For example, CO photodissociation accompanied by low-spin to high-spin change is coupled to volume expansions of  $\sim 17$  and  $\sim 12 \text{ cm}^3 \text{ mol}^{-1}$  for the above mentioned (L)Fe<sup>II</sup>4SP complex and Fe<sup>II</sup>MP-11 (MP-11 = microperoxidase-11), respectively.<sup>20</sup> Similar processes of other heme model complexes exhibit an reaction volume of  $\sim 30 \text{ cm}^3 \text{ mol}^{-1}$ .<sup>23</sup> On the other hand measurements of spin equilibria and ligand binding/release in the case of heme proteins typically yield volume changes of  $10\text{--}50 \text{ cm}^3 \text{ mol}^{-1}$ .<sup>24</sup> However, the case of proteins may differ from model complexes in that the spin-state transition caused by ligand binding/release can be coupled with additional changes of the protein structure and prominent solvent reorganisation due to (de)hydration of regions outside the active site, resulting in very large volume changes (larger than  $200 \text{ cm}^3 \text{ mol}^{-1}$ ).<sup>24b</sup> Interestingly, our recent studies on the spin state equilibrium (analogue to that in Scheme 2) of the iron(II) complex of the crown ether-porphyrin conjugate,<sup>5c</sup> [Fe<sup>II</sup>(Porph)(DMSO)<sub>n</sub>] ( $n = 1, 2$ ), have shown that the presence of the crown ether moiety slightly shifts the  $K_{\text{DMSO}}$  equilibrium into the direction of the low-spin bis-DMSO species ( $K_{\text{DMSO}} = 0.030 \pm 0.001$ , 97% of the low-spin component at 298 K and 0.1 MPa). This strongly suggests that the covalently attached crown ether makes dissociation of the sixth ligand somewhat less favorable.<sup>5c</sup> The corresponding reaction enthalpy ( $\Delta H^\circ = +48 \pm 1 \text{ kJ mol}^{-1}$ ) is more positive than that for [Fe<sup>II</sup>(tBuTPP)(DMSO)<sub>n</sub>], supporting the fact that the crown ether makes DMSO dissociation more endothermic. Furthermore, the significantly larger reaction volume ( $\Delta V^\circ = +26 \pm 2 \text{ cm}^3 \text{ mol}^{-1}$ )<sup>5c</sup> in the case of [Fe<sup>II</sup>(Porph)(DMSO)<sub>n</sub>] implies that DMSO release causes additional structural changes on the resulting mono-DMSO species, which involves a new orientation between the covalently attached crown ether and porphyrin plane (creating a more “open” structure) accompanied by additional solvent perturbations.

## ESI mass spectrometry in DMSO

The best correlation of mass spectra with the solution chemistry of the corresponding coordination compounds is currently achieved by soft electrospray ionization (ESI). Therefore, we have used ESI for the characterization of the reactant and product species in solution.

The mass spectrum of the starting Fe(III) complex (Fig. S8, ESI†), [Fe<sup>III</sup>(tBuTPP)(DMSO)<sub>2</sub>]<sup>+</sup>, shows a single peak at  $m/z$  970.3, corresponding to [Fe<sup>III</sup>(tBuTPP)(DMSO)]<sup>+</sup>. The isotopic distribution (Fig. S9, ESI†) confirms this assignment. A collision experiment with He gas (MS/MS or tandem mass spectrometry) yields the porphyrin complex [Fe<sup>III</sup>(tBuTPP)]<sup>+</sup> without axial ligands at  $m/z$  892.4 (inset in Fig. S8, ESI†).

The reaction mixture of [Fe<sup>III</sup>(tBuTPP)(DMSO)<sub>2</sub>]<sup>+</sup> and KO<sub>2</sub> was investigated. The ESI mass spectrum of the reaction product shows the main ion peak at  $m/z$  1002.3 corresponding to {K<sup>+</sup> + K[Fe<sup>III</sup>(tBuTPP)(O<sub>2</sub><sup>2-</sup>)]} (Fig. 2). In order to confirm the peak at  $m/z$  1002.3 as the superoxo {K<sup>+</sup> + K[Fe<sup>III</sup>(tBuTPP)(O<sub>2</sub><sup>2-</sup>)]} adduct, the same experiment was repeated with a mixture of K<sup>16</sup>O<sub>2</sub> and K<sup>18</sup>O<sub>2</sub> (1 : 1) (inset in Fig. 2). The mass spectrum shows again the peak at  $m/z$  1002.3 with a new one at  $m/z$  1006.3, shifted by 4 mass units as expected for the <sup>18</sup>O<sub>2</sub><sup>-</sup> adduct, and its elemental composition is also confirmed by the corresponding isotopic distributions (Fig. S10, ESI†).



**Fig. 2** Mass spectrum of {K<sup>+</sup> + K[Fe<sup>III</sup>(tBuTPP)(O<sub>2</sub><sup>2-</sup>)]}. Inset: Mass spectrum of {K<sup>+</sup> + K[Fe<sup>III</sup>(tBuTPP)(<sup>16</sup>O<sub>2</sub><sup>2-</sup>)]} and {K<sup>+</sup> + K[Fe<sup>III</sup>(tBuTPP)(<sup>18</sup>O<sub>2</sub><sup>2-</sup>)]}.

The corresponding crown ether containing species, {K<sup>+</sup> + K[Fe<sup>III</sup>(Porph)(O<sub>2</sub><sup>2-</sup>)]}, was observed previously using the crown ether attached porphyrin complex.<sup>5b</sup> Both these ions show a distinctly different dissociation behavior in MS/MS experiments, which indicates different structural motifs. Upon collision with He gas, {K<sup>+</sup> + K[Fe<sup>III</sup>(Porph)(O<sub>2</sub><sup>2-</sup>)]} shows the fragmentation into intact K[Fe<sup>II</sup>(Porph)]<sup>+</sup> by the straightforward loss of KO<sub>2</sub>. Obviously, one K<sup>+</sup> cation is coordinated with the O<sub>2</sub> moiety while the other K<sup>+</sup> cation resides with the crown ether. The covalently attached crown ether stabilizes the porphyrin complex as a potassium chelating agent. The MS/MS experiment of {K<sup>+</sup> + K[Fe<sup>III</sup>(tBuTPP)(O<sub>2</sub><sup>2-</sup>)]} shows a more complex dissociation behavior which clearly also involves the decomposition of the porphyrin. Fragment ions are observed at  $m/z$  984.1, 958.1, 946.2 and 825.1 (inset in Fig. S11, ESI†). These fragment ions are shifted

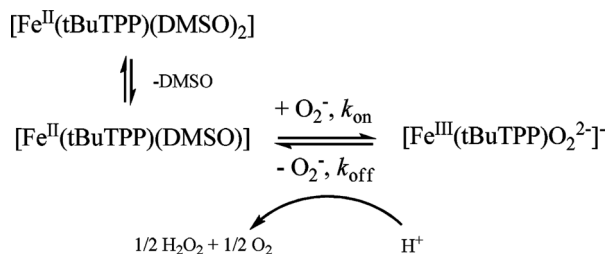
by two mass units to higher masses when the  $^{18}\text{O}_2$ -labeled  $\{\text{K}^+ + \text{K}[\text{Fe}^{\text{III}}(\text{tBuTPP})(^{18}\text{O}_2^{2-})]\}$  precursor is studied as the parent ion. Therefore, each fragment ion has lost one oxygen atom in the dissociation. A tentative assignment of the fragment ions would be  $\text{H}_2\text{O}$  loss ( $m/z$  984.1), followed by loss of CN or  $\text{C}_2\text{H}_2$  ( $m/z$  958.1), followed by the loss of a *tert*-butylphenyl radical ( $m/z$  825.1). An  $\text{MS}^3$  experiment confirmed the sequence:  $m/z$  1002 dissociates *via*  $m/z$  958 into  $m/z$  825. The fragment ion at  $m/z$  946.2 could correspond to the loss of KOH. In summary, the dissociations of  $\{\text{K}^+ + \text{K}[\text{Fe}^{\text{III}}(\text{tBuTPP})(\text{O}_2^{2-})]\}$  show both incorporation of one oxygen atom and fragmentation of the porphyrin moiety.

We also used a cryospray mass spectrometric technique<sup>25</sup> coupled to the ultra-high-resolution time-of-flight detector to allow efficient transfer of the intact species from solution-state into the gas phase. Operation on low temperatures (at  $-30\text{ }^{\circ}\text{C}$  in the MeCN–DMSO (70 : 30) solvent mixture)<sup>5a</sup> reduces possible decomposition processes and dissociation of weakly bound ligands to a minimum. Also under these conditions, in the MS spectrum of the starting Fe(III) complex,  $[\text{Fe}^{\text{III}}(\text{tBuTPP})(\text{DMSO})]^+$  (peak at  $m/z$  970.4287) appears as a main species (Fig. S12, ESI<sup>†</sup>), whereas the spectrum of the reaction product clearly shows existence of the  $\{\text{K}^+ + \text{K}[\text{Fe}^{\text{III}}(\text{tBuTPP})(\text{O}_2^{2-})]\}$  adduct (peak at  $m/z$  1002.3337) (Fig. S13, ESI<sup>†</sup>). This suggests that DMSO as the sixth ligand is quite labile, at least under the conditions of MS experiments.

## Kinetics and thermodynamics

We have previously studied the kinetics and thermodynamics of the superoxide binding to the  $[\text{Fe}^{\text{II}}(\text{Porph})(\text{DMSO})_n]$  porphyrin complex with covalently attached crown ether.<sup>5a</sup> In order to understand the influence of a crown ether moiety on the thermodynamics and kinetics of the iron porphyrins interaction with superoxide in DMSO, a comparative thermodynamic and kinetic study on the porphyrin without a covalently attached crown ether moiety, was carried out. Two different sets of experiments were performed: one without any crown ether and another with a ten-fold excess of deliberately added 8-crown-6 present in solution.

As mentioned above, the reaction between the iron(II) form of the complex with  $\text{KO}_2$  was studied, which results in  $[\text{Fe}^{\text{III}}(\text{tBuTPP})(\text{O}_2^{2-})]^-$ . Qualitative experiments on the stability of  $[\text{Fe}^{\text{III}}(\text{tBuTPP})(\text{O}_2^{2-})]^-$  ( $\lambda_{\text{max}} = 439 \text{ nm}$ ) were done by bubbling moist air through the complex solution in presence of excess superoxide. In analogy to the iron porphyrin complex with the covalently attached crown ether,<sup>5a</sup> the iron(II) complex ( $\lambda_{\text{max}} = 430 \text{ nm}$ ) is formed (Fig. S14, ESI†) due to the superoxide decomposition and shift of the equilibrium to the starting complex (Scheme 3). This shows that reversible binding of superoxide to an iron(II) porphyrin is a general feature independent of the presence of

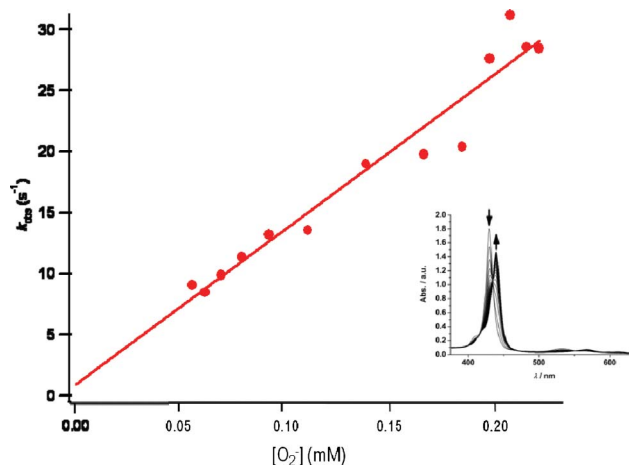


### Scheme 3

the covalently attached crown in the complex structure. The reaction and its reversibility were further thermodynamically and kinetically quantified.

The superoxide binding constant was determined by titration experiments in analogy to the previous study (Fig. S15, ESI†).<sup>5a</sup> The experimentally obtained value ( $K = (9 \pm 0.5) \times 10^3 \text{ M}^{-1}$ ) for the binding of superoxide to  $[\text{Fe}^{\text{II}}(\text{tBuTPP})(\text{DMSO})_n]$  is approximately one order of magnitude lower than the corresponding value in the case of  $[\text{Fe}^{\text{II}}(\text{Porph})(\text{DMSO})_n]$  ( $K = (1.7 \pm 0.2) \times 10^5 \text{ M}^{-1}$ ).<sup>5a</sup> This corresponds to our qualitative observations of  $[\text{Fe}^{\text{III}}(\text{tBuTPP})(\text{O}_2^{2-})]$  being less stable than its analogue with covalently attached crown ether moiety. The same experiment was done with addition of a ten-fold excess of 18-crown-6 related over the porphyrin concentration (Fig. S16, ESI†). The binding constant of  $K = (11 \pm 4) \times 10^3 \text{ M}^{-1}$  is obtained and it is the same (within experimental error) as in the case with no external crown ether present in solution. This shows that the presence of external crown ether in the solution does not exhibit a beneficial stabilizing effect. In that way, a stabilizing effect of covalently attached crown ether on the peroxo complex could be quantified.

UV/Vis stopped-flow measurements of the reaction of  $[\text{Fe}^{\text{II}}(\text{tBuTPP})(\text{DMSO})_n]$  ( $n = 1, 2$ ) with saturated  $\text{KO}_2$  solution in DMSO were performed. The experiment was carried out according to our previous study.<sup>5a,25</sup> Superoxide concentrations were varied by using saturated  $\text{KO}_2$  solution in DMSO and varying the mixing volume ratios. The time-resolved spectra were fitted to a single-exponential function to give values for the observed rate constants  $k_{\text{obs}}$  (Fig. 3). The corresponding second-order rate constant  $k_{\text{on}} = (1.30 \pm 0.01) \times 10^5 \text{ M}^{-1} \text{ s}^{-1}$  is approximately one order of magnitude higher than in the case of the complex with covalently attached crown ether ( $k_{\text{on}} = (3.65 \pm 0.05) \times 10^4 \text{ M}^{-1} \text{ s}^{-1}$ ).<sup>5a</sup> Such kinetic effect is most probably due to steric reasons. Considering the binding constants and the values for  $k_{\text{on}}$  for both complexes, it can be concluded that  $k_{\text{off}}$  ( $k_{\text{off}} = k_{\text{on}}/K$ ) is approximately two orders of magnitude slower for  $[\text{Fe}^{\text{III}}(\text{Porph})(\text{O}_2^-)]^-$  ( $k_{\text{off}} = 0.21 \pm 0.01 \text{ s}^{-1}$ )<sup>5a</sup> than for  $[\text{Fe}^{\text{III}}(\text{tBuTPP})(\text{O}_2^-)]^-$  ( $k_{\text{off}} = 14.4 \pm 0.1 \text{ s}^{-1}$ ). By slowing down the superoxide dissociation from the metal center the crown ether moiety with coordinated  $\text{K}^+$  stabilizes



**Fig. 3** Plot of  $k_{\text{obs}}$  vs. superoxide concentration for the reaction of  $1 \times 10^{-5}$  M  $[\text{Fe}^{\text{II}}(\text{tBuTTP})(\text{DMSO})_n]$  ( $n = 1, 2$ ) and  $\text{KO}_2$  at  $25^\circ\text{C}$  using different mixing volume ratios ( $I = 0.1$  M  $\text{Bu}_4\text{NPF}_6$ ). Inset: Time resolved UV/Vis spectra of the reaction of complex with  $0.1 \times 10^{-3}$  M of  $\text{KO}_2$ .



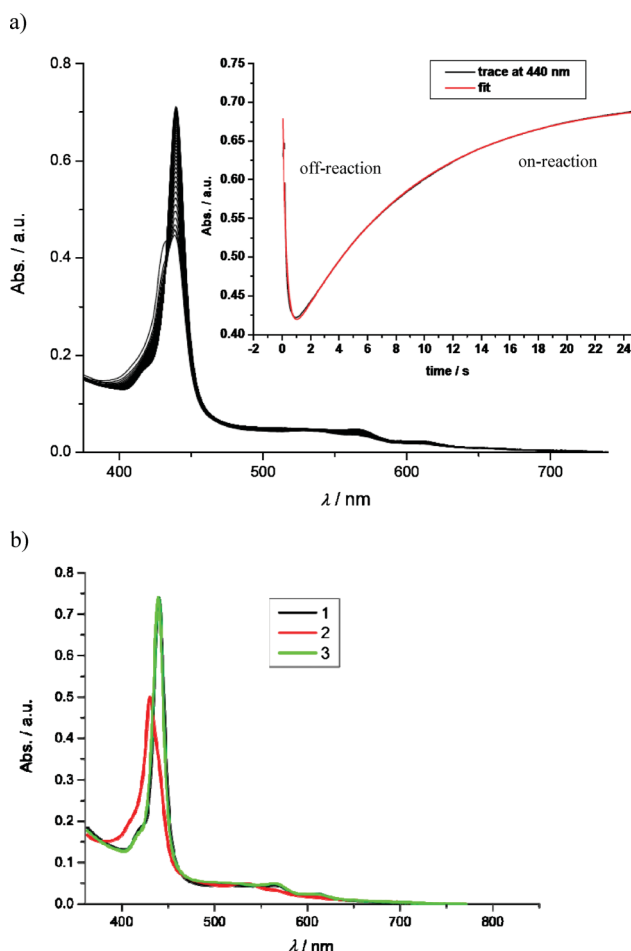
the superoxide adduct. The assumption that the crown ether side chain prevents to some extent dissociation of the axial ligand is in agreement with somewhat higher amount of bis-DMSO species present in the  $K_{\text{DMSO}}$  equilibrium mixture (Scheme 2) in the case of  $[\text{Fe}^{\text{II}}(\text{Porph})(\text{DMSO})_n]$  (97%;  $n = 1$  or 2) than in the case of the  $[\text{Fe}^{\text{II}}(\text{tBuTPP})(\text{DMSO})_n]$  system (92%; *vide supra*).

The  $k_{\text{off}}$  value have been also directly determined by adding controlled amount of a proton source (HOTf acid) into the  $[\text{Fe}^{\text{III}}(\text{tBuTPP})(\text{O}_2^-)]^-$  product solution, where an excess of  $\text{KO}_2$  was also present. HOTf was chosen since it is known that strong acids react with superoxide in aprotic solvents extremely rapidly ( $k' > 1 \times 10^7 \text{ M}^{-1} \text{ s}^{-1}$ )<sup>26</sup> which makes them very efficient  $\text{O}_2^-$  scavengers even at low concentrations. As shown in Scheme 3, rapid decomposition of superoxide shifts the equilibrium back to the Fe(II) form. Upon subsequent addition of superoxide to this solution the product  $[\text{Fe}^{\text{III}}(\text{tBuTPP})(\text{O}_2^-)]^-$  is fully recovered. To better visualize this process we performed experiments by using two-mixer stopped-flow system. The  $[\text{Fe}^{\text{III}}(\text{tBuTPP})(\text{O}_2^-)]^-$  complex ( $5 \times 10^{-6} \text{ M}$ ) with excess of  $\text{KO}_2$  (0.1–1 mM) was in the first syringe and mixed with the solution of HOTf (0.1–2 mM) from the second syringe (off-reaction). To the obtained product solution (after 1 s delay) additional superoxide (from the third syringe) was introduced in the second mixer (on-reaction). The corresponding time-resolved spectra, kinetic trace and speciation spectra are shown in Fig. 4. Such experiments have revealed that independent on the applied acid concentration or excess of  $\text{KO}_2$  the formation of the Fe(II) complex proceeds in one step, without formation of any intermediate Fe(III) specie, with the corresponding first order rate constant  $k_{\text{obs}} = k_{\text{off}} = 11.6 \pm 0.7 \text{ s}^{-1}$ . This value is in excellent agreement with that obtained based on  $k_{\text{on}}$  and the binding constant ( $k_{\text{off}} = k_{\text{on}}/K$ , *vide supra*).

The kinetic studies were also performed for the reaction of  $[\text{Fe}^{\text{II}}(\text{tBuTPP})(\text{DMSO})_n]$  ( $n = 1, 2$ ) in the presence of a ten-fold excess of 18-crown-6 in solution. The obtained second-order rate constant (Fig. S17, Table S3, ESI†) for the formation of the peroxo complex was  $k_{\text{on}} = (1.6 \pm 0.2) \times 10^5 \text{ M}^{-1} \text{ s}^{-1}$ , which corresponds to the one obtained without added crown ether ( $k_{\text{on}} = (1.30 \pm 0.01) \times 10^5 \text{ M}^{-1} \text{ s}^{-1}$ ). Having  $k_{\text{on}}$  and  $k_{\text{off}}$  ( $11.1 \pm 0.5 \text{ s}^{-1}$ ) for the reactions in the presence of external crown-ether, the reaction equilibrium constant can be calculated  $K = k_{\text{on}}/k_{\text{off}} = (14 \pm 3) \times 10^3 \text{ M}^{-1}$ . The obtained value is in excellent agreement with the thermodynamically estimated one ( $K = (11 \pm 5) \times 10^3 \text{ M}^{-1}$ , *vide supra*) and with that obtained without added crown ether present in solution.

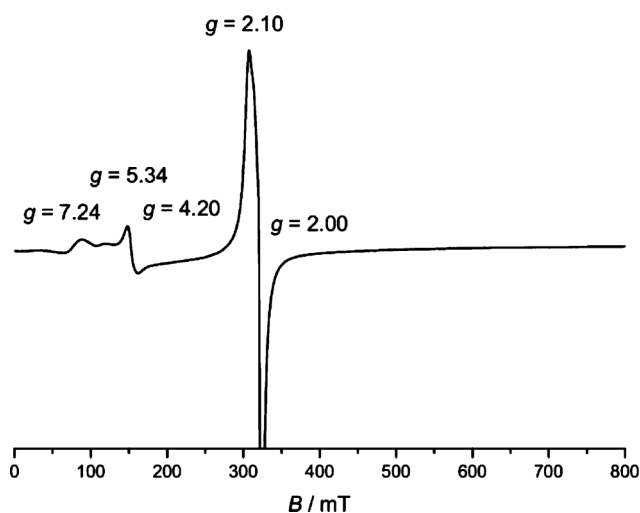
## EPR

In order to shed light on the electronic nature of our  $\text{Fe}^{\text{II}}$  porphyrin superoxide adduct we performed X-band EPR measurements. However, in contrast to our previous investigations on the crown ether porphyrin system ( $[\text{Fe}(\text{Porph})\text{Cl}]$ ),<sup>5b</sup> due to the very low solubility of the studied  $[\text{Fe}(\text{tBuTPP})\text{Cl}]$  complex in DMSO we were not able to obtain detailed information from those measurements. Usually the iron signals were near the detection limit and superoxide signals dominated. Moreover, due to the lower stability of the superoxo adduct of the complex without covalently attached crown ether, signals of the reaction side products, such as hydroxo and  $\mu$ -oxo complexes (*vide infra*), interfered significantly.



**Fig. 4** (a) Time resolved UV/Vis spectra (from the experiment in the two-mixer stopped-flow) of the reaction of  $5 \times 10^{-6} \text{ M}$   $[\text{Fe}^{\text{III}}(\text{tBuTPP})(\text{O}_2^-)]^-$  (in the presence of  $10^{-3} \text{ M}$   $\text{KO}_2$ ) with 1 mM HOTf (in the first mixer) and subsequently with  $\text{KO}_2$  (in the second mixer after 1 s delay; in DMSO,  $I = 0.1 \text{ M}$   $\text{Bu}_4\text{NPF}_6$ ); inset: kinetic trace at 440 nm and a two-exponential fit. (b) Spectra of the species observed along the reaction path: 1  $[\text{Fe}^{\text{III}}(\text{tBuTPP})\text{O}_2^{2-}]^-$ , 2  $[\text{Fe}^{\text{II}}(\text{tBuTPP})(\text{DMSO})_n]$  ( $n = 1, 2$ ), 3  $[\text{Fe}^{\text{III}}(\text{tBuTPP})\text{O}_2^{2-}]^-$ .

As commercially available  $\text{Na}_2\text{O}_2$  contains up to 10% of  $\text{NaO}_2$ , and since “naked” peroxide is not stable in aprotic solution,<sup>27</sup> we used it as a source of superoxide, which is released in solution by stirring of the granules in DMSO. This enables quantitative generation of iron (su)peroxo species without using a high superoxide excess (the concentration of superoxide that is present in the saturated DMSO solution of  $\text{Na}_2\text{O}_2$  is estimated to be  $(4 \pm 2) \times 10^{-5} \text{ M}$ ).<sup>5b</sup> The EPR spectrum at 12 K of the reaction product between the studied iron porphyrin and  $\text{Na}_2\text{O}_2$  in DMSO (Fig. 5) shows only a weak signal of rhombic high-spin  $\text{Fe}^{\text{III}}$  at  $g = 4.20$ , characteristic for the side-on peroxo species.<sup>2b,5b</sup> Signals of a byproduct  $\text{Fe}^{\text{III}}$  hydroxo species ( $g = 7.24$  and  $g = 5.34$ ) are also present in the spectrum, similar to what has been observed in the case of  $[\text{Fe}^{\text{III}}(\text{Porph})]^{5b}$  and other porphyrin systems.<sup>28</sup> The signals of the free solvated superoxide and superoxide bound to the  $\text{Na}^+$  cation ( $g = 2.10$ ,  $g = 2.00$ )<sup>5b</sup> are much more intense than the signals of the iron species. Thus, although the EPR spectra demonstrated the presence of both  $\text{Fe}^{\text{II}}\text{--O}_2^-$  and  $\text{Fe}^{\text{III}}\text{--O}_2^{2-}$  species of the crown ether porphyrin conjugate,<sup>5b</sup> evidence for the possible



**Fig. 5** X-Band EPR spectra of  $[\text{Fe}^{\text{III}}(\text{tBuTPP})\text{Cl}]$  with  $\text{Na}_2\text{O}_2$  in DMSO at 12 K, microwave frequency was 8.989384 GHz,  $P = 1$  mW; modulation width = 1.0 mT, sweep width 800 mT.

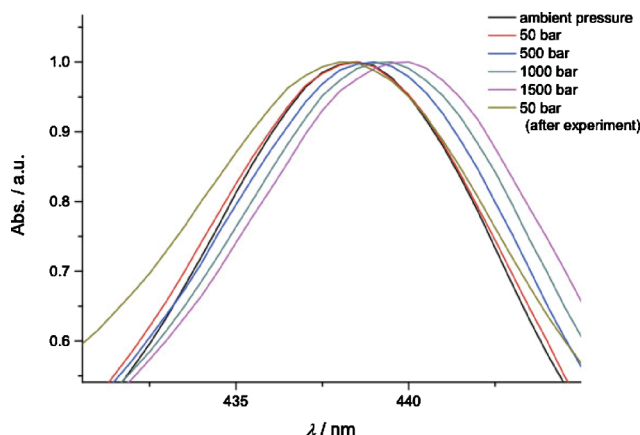
superoxide coordination to iron,  $\text{Fe}^{\text{II}}\text{-O}_2^-$ , could not be found in the case of the  $[\text{Fe}(\text{tBuTPP})]$  system. At 77 K iron signals could not be observed at all, whereas the superoxo signals showed no change in  $g$  values with temperature increase.

When  $\text{KO}_2$  was used, higher concentrations of superoxide and hydroxide were present in solution compared to the  $\text{Na}_2\text{O}_2$  experiment. The corresponding EPR spectrum of  $[\text{Fe}^{\text{III}}(\text{tBuTPP})\text{Cl}]$  with  $\text{KO}_2$  in DMSO at 12 K (Fig. S18, ESI†), besides the signals of rhombic iron(III)-peroxo ( $g = 4.20$ ) and hydroxo species ( $g = 5.46$ ,  $g = 7.32$ ), showed a large paramagnetic signal around  $g = 1.99$  mixed with the signal of free superoxide. It has the nature of a system with one unpaired electron.<sup>29</sup> It should be mentioned that  $\mu$ -oxo species of iron(III) are EPR silent due to antiferromagnetic coupling.<sup>29,30</sup> The observed signal could be related to the formation of an iron(II)–iron(III)  $\mu$ -oxo porphyrin dimer,  $[[\text{Fe}^{\text{II}}(\text{tBuTPP})]\text{-O-}[\text{Fe}^{\text{III}}(\text{tBuTPP})]]$ , upon decomposition of the (su)peroxo species.<sup>30</sup> As expected for an iron species, it is only observed at temperatures below 77 K.<sup>30</sup> Kadish *et al.*<sup>30</sup> proposed an analogous species with the TPP system and described it as a  $\mu$ -oxo complex with a single electron added. The EPR spectrum of this species is very similar to the one we observe, showing one asymmetric line with  $g = 1.95$ . One can just speculate whether this species might be a hint for the existence of both iron(III)-peroxo and iron(II)-superoxo forms in solution. In the case of the complex with the covalently attached crown ether such species have not been observed, in agreement with the fact that the crown ether sterically hinders the formation of dimer complexes. At 77 K only a signal of free superoxide is observed and the other signals have vanished due to their low concentration (inset in Fig. S18, ESI†).

By using a ten-fold excess of 18-crown-6 over  $[\text{Fe}^{\text{III}}(\text{tBuTPP})\text{-}(\text{DMSO})_2]^+$  a huge signal at  $g = 2$  is observed (Fig. S19, ESI†), which upon temperature variation changes only its intensity but not the shape. The signal corresponds to superoxide bound to the potassium cation inside the crown ether and is influenced by moisture in solution.<sup>31</sup> In the case of iron signals only the general rhombic signal of the peroxo species around  $g = 4.2$  can be observed (Fig. S19, ESI†).

## High-pressure UV/Vis spectroscopy

Since based on the EPR spectra we were not able to get information about the possible co-existence of two isomeric forms in product solution, *viz.*  $\text{Fe}(\text{II})$ -superoxo and  $\text{Fe}(\text{III})$ -peroxo, we performed pressure-dependent UV/Vis measurements to probe the existence of an equilibrium state. (Due to the low complex solubility, which limited the quality of the EPR spectral data, the Mössbauer spectra of the required resolution could not be obtained as well.) The high-spin/low-spin equilibria are usually pressure sensitive and as expected the increasing pressure in the DMSO solution of the product (su)peroxide adduct causes a small but significant red-shift of the Soret absorption band (Fig. 6), indicating a shift of the equilibrium towards the low-spin six-coordinate component of the product mixture. This is in agreement with observations made when studying the temperature dependent spectra of liver microsomal cytochrome P450 in the presence of different substrates.<sup>32</sup> On releasing pressure the starting spectrum was obtained, which demonstrates the reversibility of the pressure-induced changes on the equilibrium. The presence of the externally added crown ether in solution, did not affect this pressure-dependent behaviour (Fig. S20, ESI†). The same behaviour we observed in the case of the complex with the covalently attached crown ether moiety, where we were able to demonstrate the existence of the equilibrium between the low-spin  $\text{K}[\text{Fe}^{\text{II}}(\text{Porph})(\text{DMSO})(\text{O}_2^-)]$  and high-spin  $\text{K}[\text{Fe}^{\text{III}}(\text{Porph})(\text{O}_2^{2-})]$  species by means of different methods (Mössbauer, EPR, IR spectroscopy, ESI mass spectrometry, high-pressure kinetic measurements, DFT calculations).<sup>5b,c</sup> The quantification of such equilibrium constant is not possible to achieve since the spectra of the pure iron(II)-superoxo or pure iron(III)-peroxo forms are yet unknown, and there is no corresponding data available in the literature. Therefore, future studies will be required to tune this equilibrium such that it can be pushed completely in any of the two directions in order to independently characterize these two species.



**Fig. 6** UV/Vis spectra of  $\text{K}[\text{Fe}^{\text{III}}(\text{tBuTPP})(\text{O}_2^{2-})]$  at different pressures in the presence of 0.1 M TBAP.

## DFT calculations and correlations with experiments

To understand the possible influence of a nearby positive charge on the molecular and electronic structure of heme iron (su)peroxide adducts we performed DFT studies. The same B3LYP and

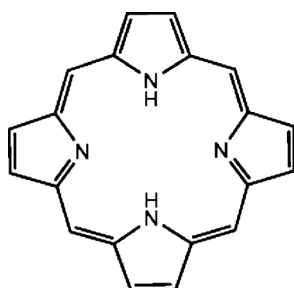


**Table 2** Calculated B3PW91 (and B3LYP) relative energies (in kcal mol<sup>-1</sup>) for end-on and side-on {Fe<sup>II</sup>(porphyrin)O<sub>2</sub><sup>-</sup>} and {Fe<sup>II</sup>(porphyrin)O<sub>2</sub><sup>-</sup>·DMSO}

	Multiplicity	{Fe <sup>II</sup> (porphyrin)O <sub>2</sub> <sup>-</sup> }	{Fe <sup>II</sup> (porphyrin)O <sub>2</sub> <sup>-</sup> ·DMSO}
End-on	2	12.6 (8.2)	8.9 (3.5) <sup>a</sup>
	4	16.7 (14.0)	17.8 <sup>a</sup>
	6	13.7 (13.9)	<sup>b</sup>
Side-on	2	21.9 (18.5)	<sup>b</sup>
	4	11.8 (12.9)	<sup>b</sup>
	6	0.0 (0.0)	<sup>b</sup>

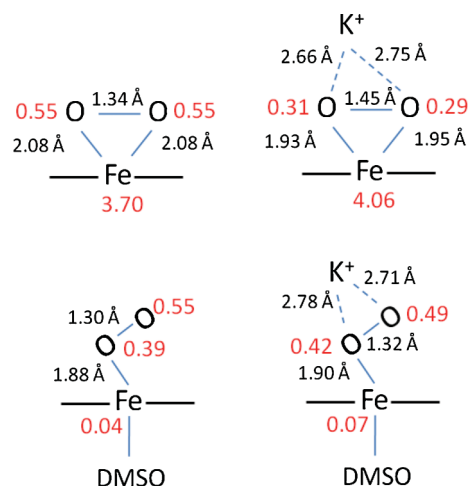
<sup>a</sup> Compared to the energy of the free side-on sextet structure and a free DMSO ligand. <sup>b</sup> No complex with DMSO bound to the axial position was found on the PES.

B3PW91 levels of theory were used as in our previous study of the species with the crown ether moiety,<sup>5b</sup> for consistency. The optimized geometries of our computational models include the iron porphyrin core structure without the phenyl groups in *meso* positions, and the structures with and without coordinated DMSO are considered. Several different spin states (doublet, quartet and sextet) were considered for each structure (Table 2). Only the doublet and quartet states of the end-on structure bind DMSO with the doublet end-on structure being lowest in energy.



Porphyrin

As in the previous study, the lowest energy structure found is the sextet high-spin side-on structure, in which the coordination site at the other side of the heme ring is vacant. The calculations suggest considerable superoxo character, as shown by the large spin densities on the both oxygen atoms (0.55, Scheme 4). The calculated O–O distance is 1.34 Å and the oxygen–oxygen bond lies above one of the N–N diagonals of the porphyrin ring. This is a typical superoxo O–O distance,<sup>33</sup> consistent with the calculated spin densities, though most experimental data on superoxide adducts of iron porphyrins strongly suggest that they have peroxo character<sup>2</sup> (an exception is an earlier ESR study describing such a species as Fe(II)-superoxo<sup>34</sup>). The Fe–O bond is somewhat elongated (Scheme 4), and the calculated structure of this side-on form can be understood in terms of weakly coordinated superoxide to high-spin Fe<sup>II</sup>. Our previous DFT studies on the model system with the covalently attached crown ether including the chelated K<sup>+</sup> cation<sup>5b</sup> showed a larger peroxo character of the side-on sextet structure, with decreased spin-density on the oxygen atoms, longer O–O bond and shorter Fe–O bonds (Scheme 4). It seems that the nearby positive charge has a significant influence on the electronic structure of the side-on adduct. Indeed, a calculation on the simple model used here, but with an added ‘naked’ K<sup>+</sup> ion (no crown ether moiety) leads to results more similar to those in the previous



**Scheme 4** Comparison of selected atomic distances and spin densities (red) for the calculated DMSO free sextet side-on porphyrin and the DMSO bound doublet end-on species of porphyrin (this work) and the model system with the covalently attached K<sup>+</sup>-crown-ether moiety.<sup>5b</sup> Results were obtained at the B3PW91/BSI level of theory.

study<sup>5b</sup> (reduced spin-density on the oxygen atoms 0.30, larger O–O bond distance 1.45 Å). Our thermodynamic and kinetic studies which show the greater stability of the (su)peroxo adduct in the case of the complex with the K<sup>+</sup>-crown ether moiety are in agreement with the shortening of the Fe–O bonds caused by nearby positive charge. Additional stabilizing effect comes from the fact that the dissociation of axial ligands is to some extent sterically hindered by the bulkiness of the covalently linked crown ether (*vide supra*). It should be mentioned that based on our experiments, cations that are present in solution when KO<sub>2</sub> or Na<sub>2</sub>O<sub>2</sub> are used as source of superoxide do not contribute to the product stability like the covalently attached cation moiety, which due to the steric proximity directly interacts with bound (su)peroxide inducing a stronger effect.

The end-on structure, which binds DMSO, is higher in energy than the side-on structure by 8.9 kcal mol<sup>-1</sup> with B3PW91 or by 3.5 kcal mol<sup>-1</sup> with B3LYP (Table 2). It has a doublet low-spin ground state with superoxo character. The spin density on the O atom nearer to Fe is 0.39 while on the distal one it is 0.55. The shortest Fe–O distance is 1.88 Å, and the O–O distance is 1.30 Å, similar to the distance of free superoxide.<sup>27,33a</sup> The Fe–O bond is significantly shorter than in the case of side-on structure (Scheme 4). The effect of the K<sup>+</sup>-crown ether side chain on this end-on form

is negligible and does not influence its electronic structure, which remains to have low-spin Fe(II)-superoxo character (Scheme 4).

The energy difference between the side-on and end-on species suggests that the side-on structure is more favorable, but does not exclude the existence of equilibrium between them (3.5 kcal mol<sup>-1</sup> energy difference obtained with B3LYP, Table 2). In the case of the model complex with covalently attached K<sup>+</sup>-crown ether there was a smaller energy difference between these two isomeric forms.<sup>5b</sup> Our high-pressure experiments have shown the existence of the equilibrium in the product solution (*vide supra*). We should consider that the presence of the K<sup>+</sup> cations under experimental conditions in solution (from KO<sub>2</sub>) lowers the energy difference between two forms, although not to that extent as in the case of the system with covalently attached K<sup>+</sup>-crown ether side chain, but still favors their coexistence.

Collectively, the DFT data suggest that without nearby positive charge the reaction product has a character of a Fe<sup>II</sup>-superoxo species in both side-on high-spin as well as end-on low-spin forms. The presence of the positive charge stabilizes the side-on high-spin adduct and changes its character into the Fe<sup>III</sup>-peroxo species, whereas the Fe<sup>II</sup>-superoxo character of the end-on low-spin isomer remains unchanged. One can speculate that if superoxide adduct would be produced in an experimental setup with no cations available in solution it would predominantly exhibit superoxo character (increased spin-density on the oxygen atoms, stronger O–O bond), but at the same time significantly decreased stability (weaker Fe–O bond). Such experimental conditions can be achieved by *in situ* radiolytic cryoreduction of heme Fe<sup>II</sup>–O<sub>2</sub> adducts.<sup>3</sup> Interestingly, such {Fe–O<sub>2</sub>}<sup>-</sup> products have usually been described as end-on peroxo species, although based on the observed O–O distance<sup>3b,c</sup> and quantum chemical calculations they are best interpreted as Fe<sup>II</sup>–O<sub>2</sub><sup>-</sup>.<sup>33a,35</sup> Only Davydov *et al.* clearly classified the primary reduction product of monomeric oxy-hemoglobin (oxy-GMH3) from *Glycera dibranchiata* as Fe<sup>II</sup>-superoxo based on EPR/ENDOR experiments.<sup>3a</sup> They also suggest that the internal redox transition to peroxo/hydroperoxo-ferric intermediates is driven by H-bonding/proton donation by the environment,<sup>3a</sup> which, based on our findings, can be interpreted as peroxo form stabilization by adjacent positive charge.

## Conclusion

Based on our investigations of the superoxide reactions with Fe<sup>II</sup> porphyrins with and without covalently attached crown ether moiety and with deliberately added crown ether we can conclude the following: (a) superoxide binds reversibly to Fe<sup>II</sup> porphyrins in DMSO independently on the general existence of crown ether, (b) in DMSO solution with an excess of superoxide, the product (su)peroxo species generates the starting Fe<sup>II</sup> complex upon controlled addition of a proton source, also independent on the presence of the crown ether moiety, (c) to a certain extent, the crown ether side chain favors the low-spin six-coordinate form of the Fe<sup>II</sup> porphyrin in the solution, (d) since generation of the high-spin five-coordinate Fe<sup>II</sup> species is the actual activation step towards substitution and subsequent inner-sphere electron transfer, the superoxide binding ( $k_{\text{on}}$ ) is approximately one order of magnitude slower when crown ether is covalently attached to porphyrin, whereas externally added crown ether does not influence the rate determining step, (e) by preventing the axial

ligand dissociation covalently attached crown ether slows down the superoxide release from the product (su)peroxo species (resulting in a decrease of  $k_{\text{off}}$  by two orders of magnitude), (f) the more prominent effect of attached crown ether on the superoxide dissociation ( $k_{\text{off}}$ ) than on the DMSO dissociation ( $k_{\text{on}}$ ) suggests that the positive charge of chelated K<sup>+</sup> additionally prevents the superoxide release, (g) these effects of the crown ether side chain on  $k_{\text{on}}$  and  $k_{\text{off}}$  result in the ten times larger superoxide binding constant and make the product (su)peroxo complex significantly more stable, whereas external addition of crown ether does not bring any stabilization, (h) due to this higher stability, detailed spectroscopic studies on the (su)peroxo complex with the crown ether side chain could be performed, demonstrating the existence of the redox tautomerism between the end-on Fe<sup>II</sup>-superoxo and side-on Fe<sup>III</sup>-peroxo forms, which is supported by DFT calculations, (i) the lower solubility and stability of the (su)peroxo complex without crown ether moiety did not allow detailed spectroscopic characterization of its nature, however, DFT calculations demonstrate that without nearby positive charge the reaction product has the Fe<sup>II</sup>-superoxo character in both side-on high-spin as well as end-on low-spin forms. These findings are important for understanding the real nature of the corresponding biologically relevant (su)peroxo intermediaries of heme-containing enzymes involved in activation of molecular oxygen and hydrogen peroxide, because they show that the nature and electronic structure of these intermediates can be tuned not only by axial ligand coordination but also by the charge of a surrounding of an iron heme center in the active site of an enzyme. Our kinetic and thermodynamic studies quantify the effect of semi-confined environment around iron center, caused by the covalently attached crown-ether, on its reactivity toward axial ligands in general, and superoxide in particular. The results obtained in this investigation represent a motivating foundation for future studies towards the understanding of the effects that might be caused by the solvent, a *trans* ligand, and possible involvement of coordinated (su)peroxide in hydrogen bonding or electrostatic interactions, on the structure and electronic properties of the heme iron-superoxide adducts and their reactivity towards different organic substrates of biological and synthetic importance.

## Acknowledgements

This work was supported by the Deutsche Forschungsgemeinschaft through SFB 583 “Redox-active metal complexes” (K. D., A. Z., N. J., I. I. B.). J. O. acknowledges receipt of an EU Marie Curie Fellowship (Project “Modelling CYPs”).

## References

- (a) I. Schlichting, J. Berendzen, K. Chu, A. M. Stock, S. A. Maves, D. E. Benson, R. M. Sweet, D. Ringe, G. A. Petsko and S. G. Sligar, *Science*, 2000, **287**, 1615; (b) D. L. Wertz and J. S. Valentine, *Struct. Bonding*, 2000, **97**, 37; (c) E. Kim, E. E. Chufan, K. Kamaraj and K. D. Karlin, *Chem. Rev.*, 2004, **104**, 1077.
- (a) E. McCandlish, A. R. Miksztal, M. Nappa, A. Q. Sprenger, J. S. Valentine, J. D. Stong and T. G. Spiro, *J. Am. Chem. Soc.*, 1980, **102**, 4268; (b) J. N. Burstyn, J. A. Roe, A. R. Miksztal, B. A. Shaevitz, G. Lang and J. S. Valentine, *J. Am. Chem. Soc.*, 1988, **110**, 1382; (c) E. E. Chufan and K. D. Karlin, *J. Am. Chem. Soc.*, 2003, **125**, 16160; (d) M. Selke, M. F. Sisemore and J. S. Valentine, *J. Am. Chem. Soc.*, 1996, **118**, 11692.

- 3 (a) R. Davydov, J. D. Satterlee, H. Fujii, A. Sauer-Masarwa, D. H. Busch and B. M. Hoffman, *J. Am. Chem. Soc.*, 2003, **125**, 16340; (b) H.-P. Hersleth, Y.-W. Hsiao, U. Ryde, C. H. Goerbitz and K. K. Andersson, *Biochem. J.*, 2008, **412**, 257; (c) M. Unno, H. Chen, S. Kusama, S. Shaik and M. Ikeda-Saito, *J. Am. Chem. Soc.*, 2007, **129**, 13394.
- 4 J.-G. Liu, T. Ohta, S. Yamaguchi, T. Ogura, S. Sakamoto, Y. Maeda and Y. Naruta, *Angew. Chem., Int. Ed.*, 2009, **48**, 9262.
- 5 (a) K. Duerr, B. P. Macpherson, R. Warratz, F. Hampel, F. Tuczek, M. Helmreich, N. Jux and I. Ivanović-Burmazović, *J. Am. Chem. Soc.*, 2007, **129**, 4217; (b) K. Duerr, J. Olah, R. Davydov, M. Kleimann, J. Li, N. Lang, R. Puchta, E. Huebner, T. Drewello, J. N. Harvey, N. Jux and I. Ivanović-Burmazović, *Dalton Trans.*, 2010, **39**, 2049; (c) K. Duerr, N. Jux, A. Zahl, R. van Eldik and I. Ivanović-Burmazović, *Inorg. Chem.*, 2010, **49**, 11254.
- 6 I. Rosenthal, *J. Labelled Compd. Radiopharm.*, 1976, **12**, 317.
- 7 A. Zahl, A. Neubrand, S. Aygen and R. van Eldik, *Rev. Sci. Instrum.*, 1994, **65**, 882.
- 8 J. Maigut, R. Meier, A. Zahl and R. van Eldik, *Inorg. Chem.*, 2007, **46**, 5361.
- 9 I. Ivanović-Burmazović, M. S. A. Hamza and R. van Eldik, *Inorg. Chem.*, 2006, **45**, 1575.
- 10 (a) G.-F. Liu, M. Filipović, F. W. Heinemann and I. Ivanović-Burmazović, *Inorg. Chem.*, 2007, **46**, 8825; (b) G.-F. Liu, M. Filipović, I. Ivanović-Burmazović, F. Beuerle, P. Witte and A. Hirsch, *Angew. Chem., Int. Ed.*, 2008, **47**, 3991.
- 11 (a) M. Spitzer, F. Gartig and R. van Eldik, *Rev. Sci. Instrum.*, 1988, **59**, 2092; (b) K. F. Fleischmann, G. E. Conze, R. D. Stranks and H. Kelm, *Rev. Sci. Instrum.*, 1974, **45**, 1427.
- 12 Jaguar, version 6.0, Schrödinger, LLC, New York, NY, 2005.
- 13 J. P. Hay and W. R. Wadt, *J. Chem. Phys.*, 1985, **82**, 299.
- 14 The LACV3P basis set is a triple-zeta contraction of the LACVP basis set developed and tested at Schrödinger, Inc.
- 15 J. K. M. Sanders, N. Bampos, Z. Clyde-Watson, S. L. Darling, J. C. Hawley, H.-J. Kim, C. C. Mak and S. J. Webb, in *The Porphyrin Handbook*, ed. K. Kadish, K. Smith and R. Guilard, Academic Press, New York, 2003, vol. 3.
- 16 (a) R. C. Parmely and H. M. Goff, *J. Inorg. Biochem.*, 1980, **12**, 269; (b) A. Shirazi and H. M. Goff, *J. Am. Chem. Soc.*, 1982, **104**, 6318.
- 17 F. A. Walker, *The Porphyrin Handbook*, Academic Press, New York, 2003, vol. 5.
- 18 R. Lange, C. Larroque and P. Anzenbacher, *Eur. J. Biochem.*, 1992, **207**, 69.
- 19 B. Li, R.-J. Wei, J. Tao, R.-B. Huang and L.-S. Zheng, *Inorg. Chem.*, 2010, **49**, 745, and references therein.
- 20 J. Mikškovská, J. Norstrom and R. W. Larsen, *Inorg. Chem.*, 2005, **44**, 1006.
- 21 K. Hereman, in *High-pressure Chemistry and Biochemistry*, ed. R. van Eldik and J. Jonas, D. Reidel Publishing Co., Dordrecht, Holland, 1987.
- 22 (a) R. van Eldik, T. Asano and W. le Noble, *Chem. Rev.*, 1989, **89**, 549; (b) R. R. Hung and J. J. Grabowski, *J. Am. Chem. Soc.*, 1992, **114**, 351.
- 23 A. Franke, N. Hessenauer-Ilicheva, D. Meyer, G. Stochel, W. D. Woggon and R. van Eldik, *J. Am. Chem. Soc.*, 2006, **128**, 13611.
- 24 (a) G. Hui Bon Hoa and M. C. Marden, *Eur. J. Biochem.*, 1982, **124**, 311; (b) D. R. Davydov, G. Hui Bon Hoa and J. A. Peterson, *Biochemistry*, 1999, **38**, 751.
- 25 H. N. Miras, E. F. Wilson and L. Cronin, *Chem. Commun.*, 2009, 1297, and references therein.
- 26 D.-H. Chin, G. Jr. Chiericato, E. J. Jr. Nanni and D. T. Sawyer, *J. Am. Chem. Soc.*, 1982, **104**, 1296.
- 27 D. T. Sawyer and J. S. Valentine, *Acc. Chem. Res.*, 1981, **14**, 393.
- 28 E. E. Chufan and K. D. Karlin, *J. Am. Chem. Soc.*, 2003, **125**, 16160.
- 29 G. Palmer in *Physical Methods in Bioinorganic Chemistry*, ed. L. Que, Jr., University Science Books, Sausalito, CA, 2000.
- 30 K. M. Kadish, G. Larson, D. Lexa and M. Momenteau, *J. Am. Chem. Soc.*, 1975, **97**, 282.
- 31 M. C. R. Symons, G. W. Eastland and L. R. Denny, *J. Chem. Soc., Faraday Trans. 1*, 1980, **76**, 1868.
- 32 H. Rein, O. Ristau, J. Friedrich, G.-R. Jänig and K. Ruckpaul, *FEBS Lett.*, 1977, **75**, 19.
- 33 (a) M. Pedio, Z. Y. Wu, M. Benfatto, A. Mascaraque, E. Michel, C. Ottaviani, C. Crotti, M. Peloi, M. Zacchigna and C. Comicioli, *Phys. Rev. B: Condens. Matter*, 2002, **66**, 144109/144101/144104; (b) C. J. Cramer, W. B. Tolman, K. H. Theopold and A. L. Rheingold, *Proc. Natl. Acad. Sci. U. S. A.*, 2003, **100**, 3635.
- 34 V. K. Kol'tover, O. I. Koifman, A. M. Khenkin and A. A. Shteinman, *Izv. Akad. Nauk SSSR, Ser. Khim.*, 1978, 1690.
- 35 E. G. Kovaleva and J. D. Lipscomb, *Science*, 2007, **316**, 453.

## Zwitterionic clusters with dianion core produced by electrospray ionisation of Brønsted acidic ionic liquids

Jing Li,<sup>a</sup> Wei Wei,<sup>b</sup> Leanne C. Nye,<sup>c</sup> Peter S. Schulz,<sup>b</sup> Peter Wasserscheid,<sup>\*b</sup>  
Ivana Ivanović-Burmazović<sup>c</sup> and Thomas Drewello<sup>\*a</sup>

Received 21st December 2011, Accepted 5th March 2012

DOI: 10.1039/c2cp24071h

New Brønsted acidic ionic liquids (BAILs) are prepared by treating zwitterions, which are composed of an imidazolium cation and a sulfonate anion, with an alkanedisulfonic acid. Acidification of the zwitterions produces the cation and deprotonation of the alkanedisulfonic acid forms the anion of the new BAILs. Direct laser desorption/ionisation (LDI), matrix-assisted LDI (MALDI) and electrospray ionisation (ESI) are employed to transfer ions into the gas-phase for detection by mass spectrometry and for dissociation studies by tandem mass spectrometry. The components of the BAILs are confirmed by LDI and MALDI by the detection of the respective cation and anion and by ESI by the observation of the cation and the dianion. A prominent feature of ESI is the formation of aggregates (cluster ions). Positively charged cluster ions are formally composed of multiple zwitterions plus one additional proton. In the negative-ion mode the clusters also incorporate the zwitterions which are, however, linked with the alkanedisulfonate dianion. In collision-induced dissociations (CID), the cationic aggregates show the evaporation of zwitterions until the protonated zwitterion is reached. Similarly, the cluster dianions release zwitterions until the free alkane disulfonate dianion is reached. However, the 1 : 1 adduct of dianion and zwitterion also displays proton transfer and Coulomb explosion into the mono-protonated disulfonic mono-anion and an imidazole-based carbene with sulfonate mono-anion.

### Introduction

Mass spectrometry has been a vital tool for the characterisation of ionic liquids (ILs).<sup>1–10,12–33</sup> The fact that cation and anion – as the essential components of the IL – are already preformed in such compounds, requires just their transfer into the gas-phase for detection. The ionisation step which often induces unwanted dissociations has become redundant. The most frequently used modern ionisation methods, such as electrospray ionisation (ESI)<sup>1,22</sup> and matrix-assisted (MALDI)<sup>4</sup> or direct laser desorption/ionisation (LDI),<sup>4,5</sup> are almost ideally suited for the analysis of ILs. The straightforward analysis in each ion mode would normally reveal the composition of the ion pair. If the ion pair was evaporated as an intact moiety, the “ionisation

step” is still required as a means to activate and separate the ion pair to allow the detection of the free cation.<sup>6,9–11</sup> Besides its use as an analytical tool, mass spectrometry-based investigations have focused on several other issues connected with IL at the interface of liquid and gas-phases. These include the appearance of IL vapour in the gas-phase,<sup>5–14</sup> the formation of aggregates<sup>2,15–21</sup> and their decay,<sup>18–24</sup> the interaction of and the bond strength between cation and anion,<sup>18–23</sup> and the application of ILs to modify ionisation methods.<sup>4,25–30</sup>

Despite the enormous variety within the materials that show IL behaviour, some basic statements can be made regarding their gas-phase behaviour. The vapour of aprotic ILs is in general composed of the ion pair that includes the cation and anion of the IL.<sup>5–14</sup> The transfer of protic ILs into the gas-phase is accompanied by proton transfer.<sup>9,10</sup> MALDI and the related harsher direct LDI allows, for species that are stable enough, the transfer of the intact cation and anion into the gas-phase.<sup>4,5</sup> A particular prominent feature when ILs are electrosprayed (ESI)<sup>1,2</sup> is the occurrence of cluster ions of the general type  $\text{Cat}(\text{CatAn})_n^+$  and  $\text{An}(\text{CatAn})_n^-$  in the respective ion mode, whereby Cat = cation, An = anion and CatAn = ion pair. The occurrence of such clusters is not restricted to ESI and is observed also with other ionisation methods.<sup>31–33</sup> Also, this type of cluster ion is not unique to the ILs, it is in fact

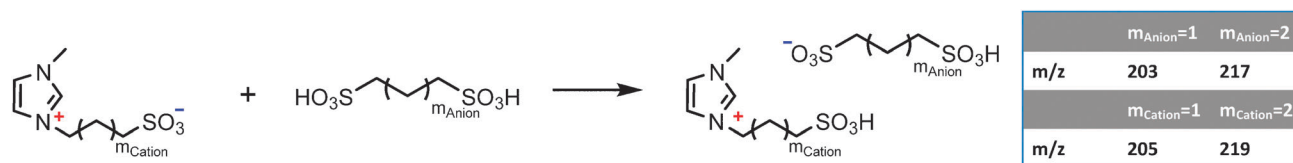
<sup>a</sup> Physical Chemistry I, Department of Chemistry and Pharmacy, University of Erlangen-Nuremberg, Egerlandstrasse 3, 91058 Erlangen, Germany.

E-mail: thomas.drewello@chemie.uni-erlangen.de

<sup>b</sup> Chemical Reaction Engineering (CRT), Department of Chemical and Bioengineering, University of Erlangen-Nuremberg, Egerlandstrasse 3, 91058 Erlangen, Germany.

E-mail: wasserscheid@crt.cbi.uni-erlangen.de

<sup>c</sup> Bioinorganic Chemistry, Department of Chemistry and Pharmacy, University of Erlangen-Nuremberg, Egerlandstrasse 1, 91058 Erlangen, Germany



**Fig. 1** The synthetic route to the BAILs: alkane disulfonic acid protonates the zwitterion leading to the acidified zwitterion and mono-deprotonated alkane disulfonic acid. The  $m/z$  values of the cations and anions of the BAILs ion pairs are provided.

commonly observed for ionic, salt-like species and there have been earlier studies by this group on non-IL cluster ions of this type.<sup>34–36</sup> In tandem mass spectrometry experiments a cluster ion of choice is separated from others and allowed to dissociate. All cluster ions of ILs of this type studied thus far show the release of the intact ion pair (CatAn) from the cluster ion including multiples thereof,<sup>18–24</sup> which may also involve the loss of intact moieties ((CatAn)<sub>m</sub>).<sup>21</sup> The smallest cluster ion can be produced as a heterodimer of the type Cat'AnCat''<sup>+</sup> (or An'CatAn''<sup>–</sup>) and constitutes an ion that now can dissociate in two ways, whereby the ion pair with the bigger affinity between cation and anion will now be lost preferably as the neutral. The analysis of such competing dissociations for a variety of different cations and anions allows the evaluation of the bond strengths between them.<sup>18–22</sup> This method is commonly referred to as Cooks' kinetic method.<sup>37</sup> ILs have also been used to modify the performance of existing ionisation methods. In MALDI "ionic liquid matrix" materials have been successfully introduced,<sup>4,25,26</sup> employing an equimolar mixture of a conventional matrix and an organic base. The addition of particular ILs to the ESI process has improved the detection of certain analytes.<sup>27,28,30</sup>

The present investigation focuses on Brønsted acidic ionic liquids (BAILs). Strong Brønsted acids are widely used in industrial processes. As nonvolatile materials, solid acids are more widely applied than traditional liquid acids which can cause severe reactor corrosion and have isolation and recycling difficulties. However, solid acids have shortcomings as well, such as rapid deactivation and lower activity. To overcome the disadvantages of liquid and solid acids, a new type of Brønsted acids based on ionic liquids has been proposed, combining solid-like non-volatility with motility, greater effective surface area, and potential activity of the liquid phase. The first BAILs bearing HO<sub>3</sub>S-functionalised cations were synthesized by Cole and coworkers.<sup>38</sup> These BAILs demonstrated excellent performances in terms of reaction rates, selectivity as well as recycling ability in Fisher esterification, alcohol dehydrodimerization and the pinacol rearrangement. Other BAILs based on imidazolium, ammonium, phosphonium, pyridinium cations and even dicationic imidazolium with carboxylic and alkane sulfonic acid covalently tethered to the cation were intensively investigated in a broad range of typical acid catalyzed reactions.<sup>39–45</sup> Most of the publications demonstrated high yields and high reaction rates under mild reaction conditions compared to those of traditional acids. BAILs with HO<sub>3</sub>S-functionalized cations were mostly synthesized by the protonation of the corresponding zwitterion with strong acids. The potential problem for those ionic liquids is the reversible process of protonation. The acidity might therefore come from the mixture composed of ionic liquid, zwitterion and corrosive liquid acid.

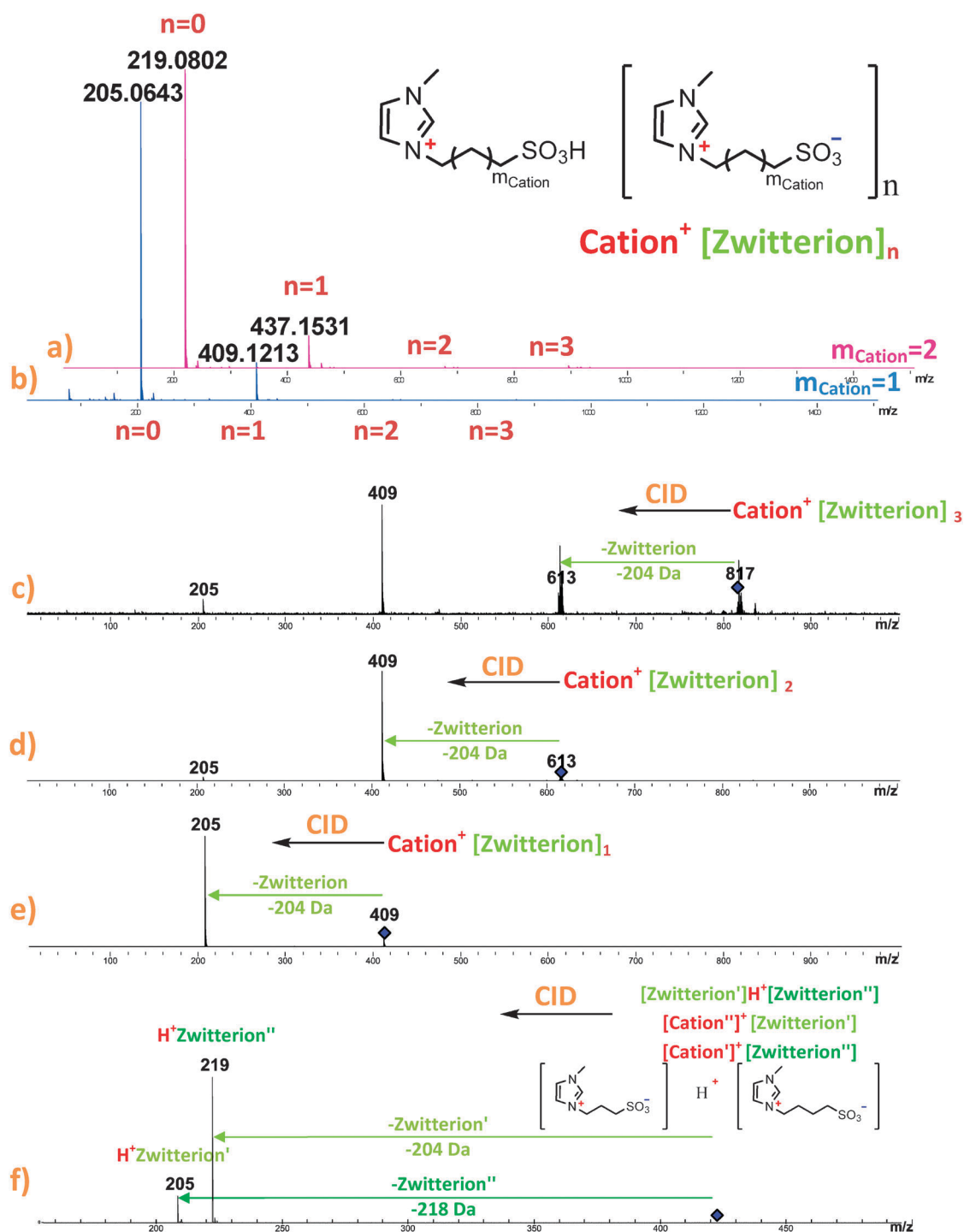
In the present investigation, (MA)LDI and ESI are applied to the gas-phase transfer of a new representative of this type of IL. Fig. 1 displays the formation of the BAILs under investigation. The preparation is based on the concept of acidification of the anionic part of a zwitterionic precursor by a stronger acid,<sup>38</sup> leading to a BAIL with the protonated zwitterion as the new cation and the deprotonated acid as the new anion. The zwitterion is composed of an imidazolium cation with a pendant sulfonate group and an alkanedisulfonic acid which functions as the donor acid.

## Experimental

The new BAILs were prepared as follows: the zwitterionic reactants were synthesized by nucleophilic addition of methyl-imidazol to 1,3-propane- and 1,4-butane sultone.<sup>38</sup> The alkane disulfonic acids were obtained by ring-opening of 1,3-propane- and 1,4-butane sultone with sodium sulphite followed by sodium/proton ion exchange using amberlite ion exchange resin. Finally, the alkane disulfonic acid compound and the zwitterions were reacted in an acid–base reaction to form the BAIL.

LDI and MALDI mass spectra were recorded with a curved-field reflectron time-of-flight mass spectrometer (Axima Confidence, Shimadzu). A nitrogen laser was employed for the target activation. The target was prepared by deposition of the BAIL onto a stainless steel target holder. For MALDI the matrix material was applied on top of a dried 1 mg mL<sup>–1</sup> sample solution (1 : 1 of CH<sub>3</sub>CN : H<sub>2</sub>O) and dried. A second layer of IL and matrix was applied on top before insertion into the ion source. DCTB (*trans*-2-[3-(4-*tert*-butyl-phenyl)-2-methyl-2-propenylidene]malononitrile, 1 mg mL<sup>–1</sup> in CH<sub>2</sub>Cl<sub>2</sub>) was used as the matrix material.<sup>46,47</sup> The ions were isotopically resolved (resolution was below 5000) and identified by their nominal  $m/z$  values.

ESI experiments were conducted with a large-scale high resolution/high mass accuracy quadrupole time-of-flight (qToF) mass spectrometer (maXis, Bruker). The mass resolution was typically in the range of 40 000–60 000 FWHM and the ions were identified with a mass accuracy of 1–5 ppm. The BAILs were electrosprayed from water solutions at a concentration of 0.2 mg mL<sup>–1</sup> using direct syringe pump infusion at a flow rate of 180 μL h<sup>–1</sup>. The nebulizer pressure was at 0.4 bar and the nitrogen dry gas was heated to 180 °C at a flow rate of 4.0 L min<sup>–1</sup>. Collision-induced dissociations (CID, MS<sup>2</sup>) were conducted in a collision cell located between q and ToF, following mass selection and preceding the high resolution daughter ion analysis in the ToF analyser. Nitrogen (N<sub>2</sub>) was used as the collision gas. The laboratory collision energy was varied between 5–15 eV, which translates to a centre-of-mass collision energy range of 0.3–1.2 eV.



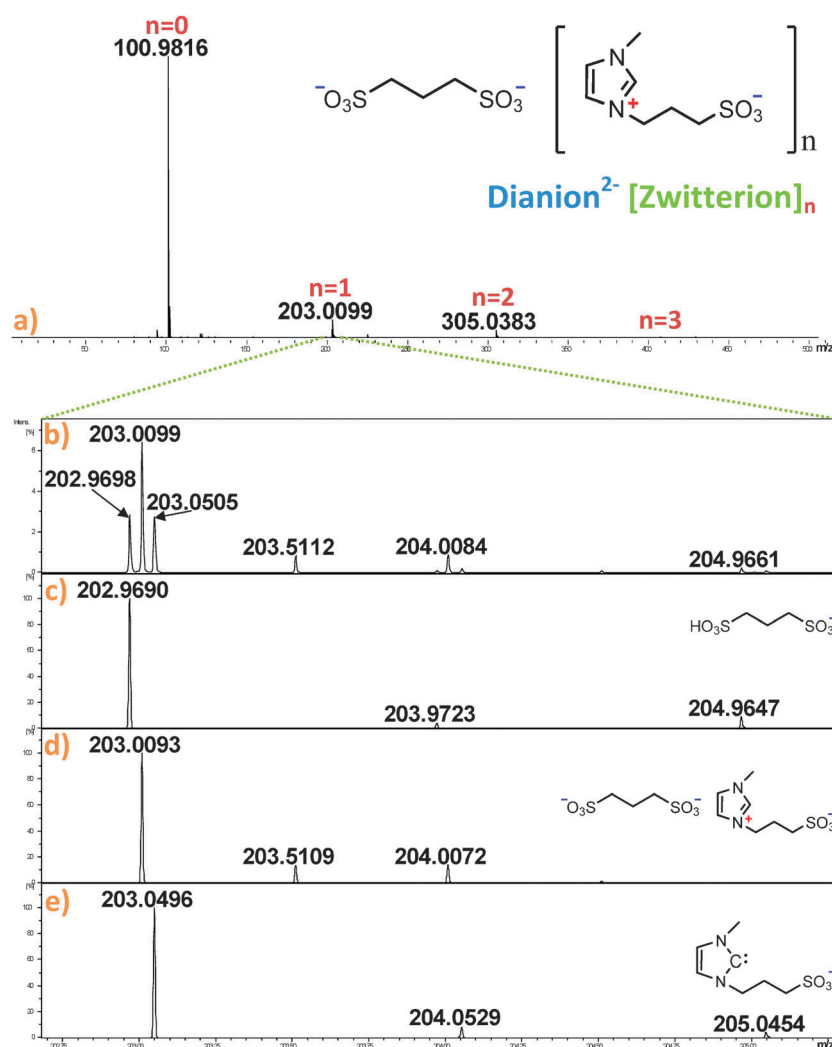
**Fig. 2** The positive-ion ESI mass spectra of (a) the BAIL with  $m_{\text{Cation}} = 2$  ( $m_{\text{Anion}} = 2$ ) and (b)  $m_{\text{Cation}} = 1$  ( $m_{\text{Anion}} = 2$ ). The cluster ions composed of  $\text{cation}[\text{zwitterion}]_n^+$  formed from the BAIL with  $m_{\text{Cation}} = 1$  ( $m_{\text{Anion}} = 1$ ) were studied by CID. The CID spectra are shown for (c)  $n = 3$ , (d)  $n = 2$  and (e)  $n = 1$ , showing the evaporation of the zwitterion from the cluster ions. (f) Competing dissociation of the proton-bound mixed zwitterion dimer with  $m_{\text{Cation}} = 1$  and  $m_{\text{Cation}} = 2$ .

## Results and discussion

The new BAILs (Fig. 1) showed thermal stability up to 320 °C and when left at  $10^{-2}$  mbar and 80 °C for 48 h no mass loss could be observed. Fig. 1 also provides the  $m/z$  values of the cations and anions of the BAILs under study. The  $m/z$  values of all the other major protagonists (deprotonated species,

aggregates and doubly charged ions) can be obtained from the table. The ionic liquids were first investigated by direct LDI and the corresponding cations and anions of which the BAILs are composed were readily observed in the respective ion modes. Thus, the protonated zwitterion (referred to below as the imidazolium ion) was observed as cation and the mono-deprotonated alkanedisulfonic acid as the anion. MALDI



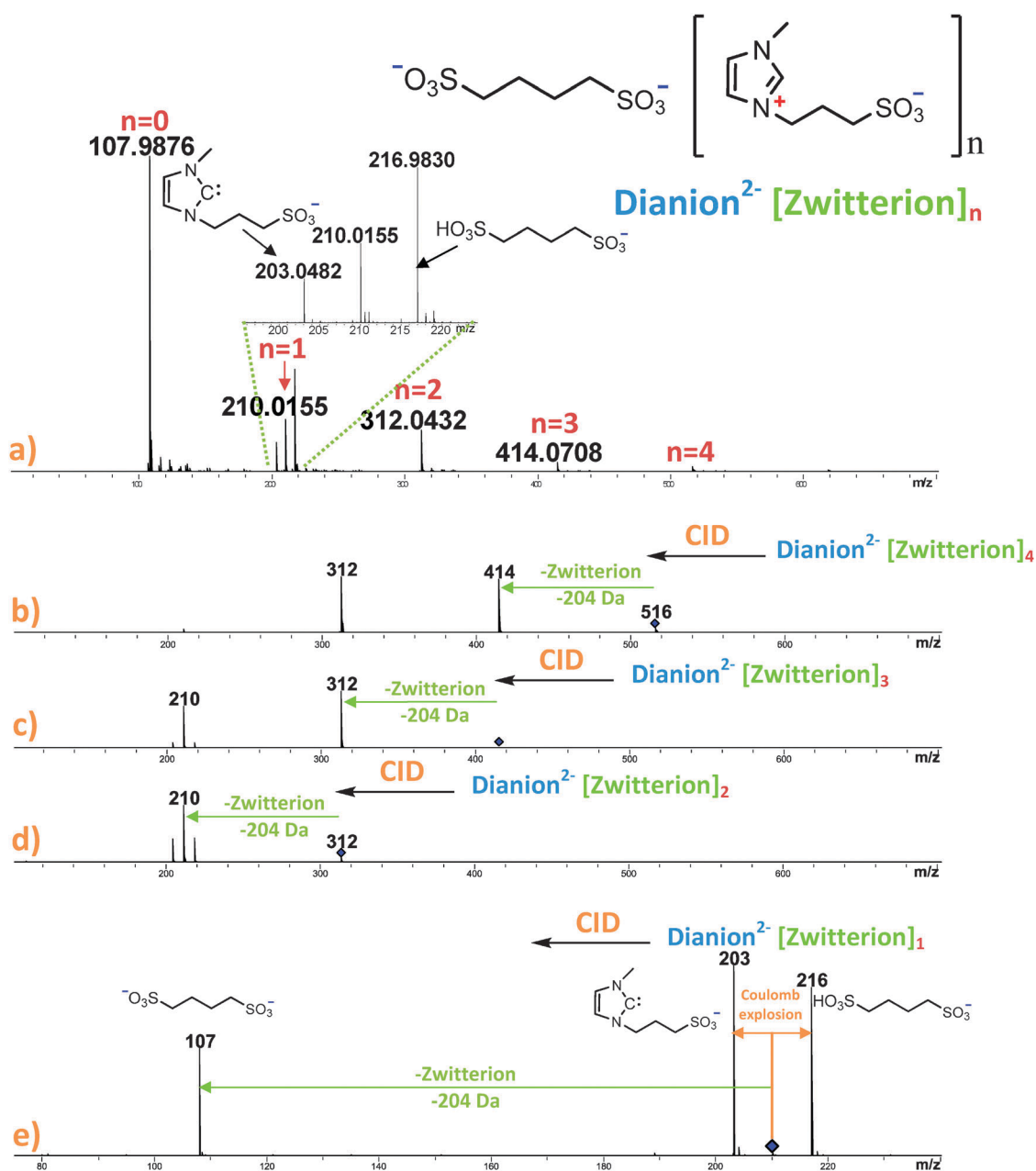


**Fig. 3** (a) The negative-ion ESI mass spectrum of the BAIL with  $m_{\text{Cation}} = 1$  and  $m_{\text{Anion}} = 1$ . Cluster ions of the type dianion[zwitterion] $_n^{2-}$  with  $n = 0-3$  are observed. (b) Enlargement of the measured spectrum. High resolution/high mass accuracy reveals the composite nature of the signal at  $m/z$  203. Assignment of the contributions to  $m/z$  203 by calculated patterns as: (c) mono-protonated alkane disulfonate, (d) dianion[zwitterion] $_n^{2-}$  with  $n = 1$  ( $m_{\text{Cation}} = 1$  and  $m_{\text{Anion}} = 1$ ) and (e) deprotonated zwitterion (carbene-anion).

employs the laser activation of a composite target of sample and matrix material and was also performed, using DCTB as the matrix. This matrix normally requires only very low laser fluencies for the desorption and has been successfully applied before with non-biological compounds.<sup>46,47</sup> Earlier work compared LDI and MALDI with other matrix materials.<sup>4</sup> The matrix is usually in excess and has the function of protecting the sample from direct exposure to laser light, while being activated itself. The activation leads to material desorption and also ion formation, the latter being unnecessary in the present case as the sample contains the ions already preformed. In the present experiments, MALDI led to the same results as obtained by direct LDI, but the overall quality of the spectra was not as good as with LDI. Cluster ions were not observed with both approaches. As a result, both LDI and MALDI lead to the detection of those ions that are preformed in the ionic liquid and confirm the composition of it.

When the ionic liquid is electrosprayed as an aqueous solution in the positive-ion mode the spectra shown in Fig. 2 are obtained. Fig. 2(a) ( $m_{\text{Cation}} = 2$ ) and (b) ( $m_{\text{Cation}} = 1$ ) show typical mass spectra as obtained for both cations. These

are independent of the respective anion of the starting ionic liquid. The spectra are dominated by the imidazolium ion, followed by an aggregate ion composed of imidazolium and zwitterion. This ion is the first cluster of a series with the general formula cation(zwitterion) $_n^+$ . Higher members of this series are, however, so low in abundance that their signals would not be visible within the scale used for Fig. 2(a) and (b). Nevertheless, it was possible to obtain MS/MS spectra of such cluster ions up to the ion with  $n = 3$  and the corresponding CID spectra are shown as Fig. 2(c)–(e). Evidently, all cluster ions decompose by the loss of one or more zwitterionic moieties. The same MS and MS<sup>2</sup> behaviour was recently obtained when a pure zwitterionic liquid (no alkanedisulfonate treatment) with similar structure was electrosprayed. Note that in this work,<sup>48</sup> a typographical error identifies the cluster ion cation(zwitterion) $_3^+$  as cation<sub>2</sub>(zwitterion) $_2^+$ , while its identity as the former is very evident. Also when electrospraying BAILS based on imidazolium/carboxylic-zwitterions, aggregates of the type cation(zwitterion) $_n^+$  could be observed.<sup>39</sup> In summary, the disulfonic moiety of the initial ionic liquid is not contributing to the positive-ion ESI mass spectrum. This finding is understandable



**Fig. 4** The negative-ion ESI mass spectrum of the BAIL with  $m_{\text{Cation}} = 1$  and  $m_{\text{Anion}} = 2$ . Cluster ions of the type dianion[zwitterion]<sub>n</sub><sup>2-</sup> with  $n = 0-4$  are observed. The corresponding ions of  $m/z$  203 in Fig. 3(a) are now separated by seven mass units. CID spectra of the cluster ions are shown for dianion[zwitterion]<sub>n</sub><sup>2-</sup> with (b)  $n = 4$ , (c)  $n = 3$ , (d)  $n = 2$  and (e)  $n = 1$ .

as the disulfonic moiety could only interact either as neutral or as a negatively charged species with cationic imidazolium. Apparently, the interaction of the imidazolium cation with one or – to a lesser extent – with more zwitterions is more attractive than involving the disulfonic moiety into the aggregates. The electrospray process clearly creates conditions for proton transfer, allowing the re-generation of the zwitterions which are incorporated as building blocks into larger aggregates. The assignment of the aggregates as cation(zwitterion)<sub>n</sub><sup>+</sup> is a formalism that assumes the proton being firmly located at one zwitterion converting it to the cation. The alternative notation of (zwitterion)<sub>n+1</sub>H<sup>+</sup> implies that the proton may not be located at a particular zwitterion. To illustrate the competition of different zwitterions for the proton, a mixed

proton-bound dimer of the two zwitterions (*i.e.* with  $m_{\text{Cation}} = 1$  and  $m_{\text{Anion}} = 2$ ) was formed, selected and dissociated. Fig. 2(f) displays the resulting daughter ion spectrum, illustrating that the zwitterion with the slightly longer alkyl chain possesses the larger proton affinity, as its (zwitterion)H<sup>+</sup> daughter ion (the “cation”) is several times more abundantly formed in the dissociation. The protonated zwitterion with  $m_{\text{Cation}} = 1$  is thus the stronger acid. The gas phase relative acidities of sulfonic acids have been established<sup>49</sup> by the same experimental approach.<sup>37</sup>

The negative-ion mass spectra are of peculiar appearance, as clustering occurs with a disulfonate dianion to which a number of zwitterions are attached. Fig. 3(a) displays the negative-ion mass spectrum obtained for the BAIL with  $m_{\text{Cation}} = m_{\text{Anion}} = 1$ . The



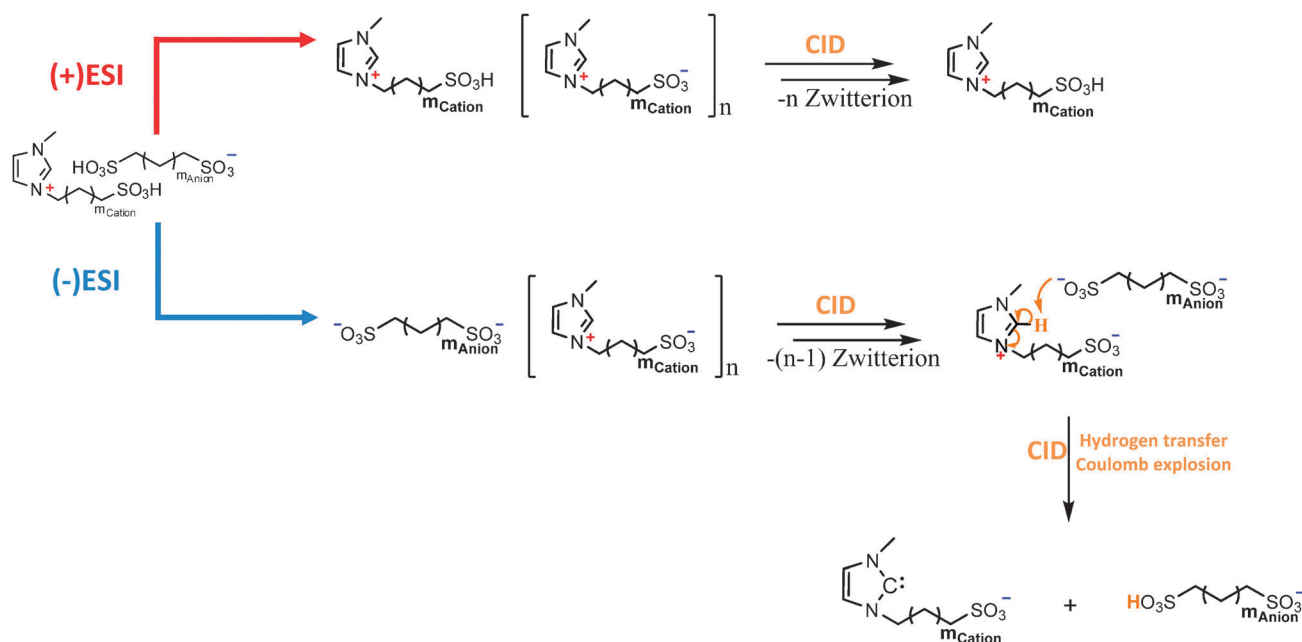


Fig. 5 Formation (ESI) and dissociation (CID) schemes of the cluster ions derived from the BAILs under investigation.

most abundant ion is the “free” disulfonate dianion, followed by an array of signals with declining intensities of the composition: dianion(zwitterion) $_n^{2-}$  with  $n = 1, 2$  and  $3$ . The identity of the dianions is undoubtedly established through their isotope pattern, showing the characteristic spacing of  $0.5$  Da, which indicates two charges ( $m/z$  with  $z = 2$ ). Moreover, all ions are characterised by measuring their accurate masses. The high resolution and high mass accuracy capabilities also reveal that three ions contribute to the signal at  $m/z$  203. These were identified as the deprotonated disulfonic acid monoanion ( $\text{HO}_3\text{S}(\text{CH}_2)_3\text{SO}_3^-$ ), the first representative of the aggregates (dianion(zwitterion) $_1^{2-}$ ) and interestingly a monoanion that would result from deprotonation of the zwitterion. The resulting carbene/sulfonate anion is a representative of an imidazol-2-ylidene carbene, which was first synthesized by Wanzlick and co-workers by deprotonation of an imidazolium salt.<sup>50</sup> In the present case, the deprotonation “neutralises” the positive charge on the nitrogen while turning the central carbon into a carbene. As the proton loss eliminates one effective charge, it is in fact the presence of the additional anion from the initial zwitterion which makes the observation of this species possible. In a recent gas-phase experiment,<sup>51</sup> an imidazole-centred carbene was produced by collision-induced HCl loss from an imidazolium chloride which was linked to an imidazolium cation. Pure zwitterions with a methylated imidazolium ring in the 2-position also showed deprotonation when electrosprayed in the negative-ion mode.<sup>52</sup>

The structural identity of the dianion(zwitterion) $_n^{2-}$  clusters has been established in CID experiments, which are illustrated in Fig. 4. The three isobaric species with the nominal  $m/z$  203 (Fig. 3) make it impossible to select only the dianionic component for CID with the instrumentation used. Therefore, the experiments were conducted with the disulfonium dianion with  $m_{\text{Anion}} = 2$  and the zwitterion with  $m_{\text{Cation}} = 1$ . As Fig. 4(a) shows, this combination allows to separate the three species that were formerly at  $m/z$  203 by seven mass units from each other, so that the dianionic species could now be separated straightforwardly from the other ions. For the

dianion(zwitterion) $_n^{2-}$  clusters with  $n > 1$ , the loss of one or more zwitterions occurs in  $\text{MS}^2$  experiments. This in turn establishes that the zwitterion and dianion are intact entities within the cluster. A scenario whereby the dianion and the zwitterion might have turned into two monoanions within the cluster can be ruled out on the basis of the zwitterion loss as the sole reaction of these clusters. However, the situation changes when the smallest cluster composed of one dianion and one zwitterion is reached ( $n = 1$ ). The loss of the zwitterion leading to the free dianion is only one of two pathways. In addition, a proton abstraction from the zwitterion by the dianion takes place whereby two mono-anions result which consequently undergo a dissociation driven by the Coulombic repulsion of the two charges which are now located on two separate entities. The two resulting mono-anions are in fact identical with the above discussed protonated disulfonic acid and the carbene/sulfonate ion. Interestingly, these are also the only mono-anions observed in the normal mass spectrum, which may strongly suggest the same mechanistic pathway for their formation, although for the electrospray conditions leading to the normal mass spectrum other pathways may equally be feasible. We note that already the aggregate which binds two zwitterions to the dianion does not undergo hydrogen abstraction from the zwitterion. This strongly suggests that the two zwitterions block the disulfonium dianion with their positively charged sites, so that the hydrogen abstraction is hindered. The “free” disulfonic acid dianions dissociate by Coulomb explosion into  $\text{SO}_3^-$  and alkyl-sulfonate anion. This behaviour is in line with the recently described reactions of gaseous dianionic naphthalenedisulfonates.<sup>53</sup> Fig. 5 summarizes the main findings.

## Conclusion

It becomes evident that the conditions by which the ions are desorbed from liquid to the gas-phase are most influential on the nature and distribution of the ions that are eventually observed.

Despite the frequent notion that soft-ionisation methods would literally transfer solution species into the gas-phase without alteration, this cannot be taken for granted. In the present case the (MA)LDI treatment does lead exactly to those ions that are expected from the composition of the BAILS. However, the observed ions are also a reflection of preferred stabilities of the ionic species under the applied conditions. Like (MA)LDI, ESI also confirms the components of the BAILS by detection of the cation, however, electrospray favours the formation of the dianion over the mono-anion. ESI also features several ionic species that are not initially expected to represent a prominent part of the BAIL. These include in the positive-ion mode proton-bound zwitterion clusters and in the negative-ion mode mono-anions with imidazole-based carbenes and zwitterion clusters with dianionic centre. The formation of cluster ions with dianionic core is unusual<sup>54</sup> and emphasizes the uniqueness of the combination of electrospray occurring at atmospheric pressure and the ion detection in the dilute gas-phase. In the cluster, the dianion interacts with the cationic part of the zwitterions, to which further zwitterions may aggregate to form larger clusters. Only the 1:1 adduct of dianion and zwitterion is able to undergo Coulomb explosion following the proton abstraction by the free sulfonate branch of the dianion. Finally, it would be interesting to study the behaviour of the BAILS by complementary approaches involving first evaporation followed by ionisation.<sup>6,9–11</sup>

## References

- Z. B. Alfassi, R. E. Huie, B. L. Milman and P. Neta, *Anal. Bioanal. Chem.*, 2003, **377**, 159–164.
- B. K. Ku and J. Fernandez de la Mora, *J. Phys. Chem. B*, 2004, **108**, 14915–14923.
- P. J. Dyson, I. Khalaila, S. Luetzgen, J. S. McIndoe and D. Zhao, *Chem. Commun.*, 2004, (19), 2204–2205.
- M. Zabet-Moghaddam, R. Krüger, E. Heinze and A. Tholey, *J. Mass Spectrom.*, 2004, **39**, 1494–1505.
- Y. Dessiaterik, T. Baer and R. E. Miller, *J. Phys. Chem. A*, 2006, **110**, 1500–1505.
- J. P. Armstrong, C. Hurst, R. G. Jones, P. Licence, K. R. J. Lovelock, C. J. Satterley and I. J. Villar-Garcia, *Phys. Chem. Chem. Phys.*, 2007, **9**, 982–990.
- V. N. Emel'yanenko, S. P. Verevkin, A. Heintz, J.-A. Corfield, A. Deyko, K. R. J. Lovelock, P. Licence and R. G. Jones, *J. Phys. Chem. B*, 2008, **112**, 11734–11742.
- A. Deyko, K. R. J. Lovelock, P. Licence and R. G. Jones, *Phys. Chem. Chem. Phys.*, 2011, **13**, 16841–16850.
- J. P. Leal, J. M. S. S. Esperança, M. E. Minas da Piedade, J. N. C. Lopes, L. P. N. Rebelo and K. R. Seddon, *J. Phys. Chem. A*, 2007, **111**, 6176–6182.
- J. Vitorino, J. P. Leal, M. E. Minas da Piedade, J. N. Canongia Lopes, J. M. S. S. Esperança and L. P. N. Rebelo, *J. Phys. Chem. B*, 2010, **114**, 8905–8909.
- D. Strasser, F. Goulay, M. S. Kelkar, E. J. Maginn and S. R. Leone, *J. Phys. Chem. A*, 2007, **111**, 3191–3195.
- B. A. D. Neto, L. S. Santos, F. M. Nachtigall, M. N. Eberlin and J. Dupont, *Angew. Chem., Int. Ed.*, 2006, **45**, 7251–7254.
- S. D. Chambreau, J. A. Boatz, G. L. Vaghjiani, J. F. Friedman, N. Eyt and A. A. Viggiano, *J. Phys. Chem. Lett.*, 2011, **2**, 874–879.
- J. H. Gross, *J. Am. Soc. Mass Spectrom.*, 2008, **19**, 1347–1352.
- S. Dorbritz, W. Ruth and U. Kragl, *Adv. Synth. Catal.*, 2005, **347**, 1273–1279.
- H. Chen, Z. Ouyang and R. G. Cooks, *Angew. Chem., Int. Ed.*, 2006, **45**, 3656–3660.
- D. F. Kennedy and C. J. Drummond, *J. Phys. Chem. C*, 2009, **113**, 5690–5693.
- F. C. Gozzo, L. S. Santos, R. Augusti, C. S. Consorti, J. Dupont and M. N. Eberlin, *Chem.-Eur. J.*, 2004, **10**, 6187–6193.
- R. Bini, O. Bortolini, C. Chiappe, D. Pieraccini and T. Siciliano, *J. Phys. Chem. B*, 2007, **111**, 598–604.
- A. M. Fernandes, J. A. P. Coutinho and I. M. Marrucho, *J. Mass Spectrom.*, 2009, **44**, 144–150.
- R. Lopes da Silva, I. M. Marrucho, J. A. P. Coutinho and A. M. Fernandes, *Molten salts and ionic liquids: never the twain?*, ed. M. Gaune-Escard and K. R. Seddon, John Wiley & Sons, Inc., 2010, p. 49.
- A. M. Fernandes, M. A. A. Rocha, M. G. Freire, I. M. Marrucho, J. A. P. Coutinho and L. M. N. B. F. Santos, *J. Phys. Chem. B*, 2011, **115**, 4033–4041.
- S. Kitaoka, K. Nobuoka, Y. Ishikawa and A. Wakisaka, *Anal. Sci.*, 2008, **24**, 1311.
- C. J. Hogan and J. Fernandez de la Mora, *J. Am. Soc. Mass Spectrom.*, 2010, **21**, 1382–6.
- D. W. Armstrong, L.-K. Zhang, L. He and M. L. Gross, *Anal. Chem.*, 2001, **73**, 3679–3686.
- A. Tholey and E. Heinze, *Anal. Bioanal. Chem.*, 2006, **386**, 24–37.
- P. J. Dyson, J. S. McIndoe and D. Zhao, *Chem. Commun.*, 2003, (4), 508–509.
- M. A. Henderson and J. S. McIndoe, *Chem. Commun.*, 2006, (27), 2872–2874.
- Y. Fujiwara, N. Saito, H. Nonaka, T. Nakanaga and S. Ichimura, *Nucl. Instrum. Methods Phys. Res., Sect. B*, 2010, **268**, 1938–1941.
- Y.-L. Chang, Y.-C. Lee, W.-B. Yang and C.-H. Chen, *J. Mass Spectrom.*, 2011, **46**, 367–375.
- J. H. Gross, *J. Am. Soc. Mass Spectrom.*, 2007, **18**, 2254–2262.
- M. Holzweber and H. Hutter, *Surf. Interface Anal.*, 2010, **42**, 1025–1029.
- M. Holzweber, E. Pittenauer and H. Hutter, *J. Mass Spectrom.*, 2010, **45**, 1104–1110.
- R. Cozzolino, R. T. Gallagher and T. Drewello, *Eur. J. Mass Spectrom.*, 2006, **12**, 31–35.
- R. Herzsuh and T. Drewello, *Int. J. Mass Spectrom.*, 2004, **233**, 355–359.
- T. Drewello, R. Herzsuh and J. Stach, *Z. Phys. D: At., Mol. Clusters*, 1993, **28**, 339–343.
- R. G. Cooks, J. S. Patrick, T. Kotiaho and S. A. McLuckey, *Mass Spectrom. Rev.*, 1994, **13**, 287–339.
- A. C. Cole, J. L. Jensen, I. Ntai, K. L. T. Tran, K. J. Weaver, D. C. Forbes and J. H. Davis, *J. Am. Chem. Soc.*, 2002, **124**, 5962–5963.
- Z. Fei, D. Zhao, T. J. Geldbach, R. Scopelliti and P. J. Dyson, *Chem.-Eur. J.*, 2004, **10**, 4886–4893.
- X. Liu, L. Xiao, H. Wu, J. Chen and C. Xia, *Helv. Chim. Acta*, 2009, **92**, 1014.
- X. Liu, J. Zhou, X. Guo, M. Liu, X. Ma, C. Song and C. Wang, *Ind. Eng. Chem. Res.*, 2008, **47**, 5298.
- D. Fang, H. B. Zhang and Z. L. Liu, *J. Heterocycl. Chem.*, 2010, **11**, 1057.
- H. Xing, T. Wang, Z. Zhou and Y. Dai, *Ind. Eng. Chem. Res.*, 2005, **44**, 4147.
- M. Yoshizawa, M. Hirao, K. Ito-Akita and H. Ohno, *J. Mater. Chem.*, 2001, **11**, 1057.
- J. Gui, X. Cong, D. Liu, X. Zhang, Z. Hu and Z. Sun, *Catal. Commun.*, 2004, **5**, 473.
- L. Ulmer, J. Mattay, H. G. Torres-Garcia and H. Luftmann, *Eur. J. Mass Spectrom.*, 2000, **6**, 49–52.
- Y. V. Vasil'ev, O. G. Khvostenko, A. V. Streletskii, O. V. Boltalina, S. G. Kotsiris and T. Drewello, *J. Phys. Chem. A*, 2006, **110**, 5967–5672.
- I. Nakurte, P. Mekss, K. Klavins, A. Zicmanis, G. Vavilina and S. Dubrovina, *Eur. J. Mass Spectrom.*, 2009, **15**, 471–478.
- J. D. Smith, R. A. J. O'Hair and T. D. Williams, *Phosphorus, Sulfur Silicon Relat. Elem.*, 1996, **1**, 49–59.
- H.-J. Schönherr and H.-W. Wanzlick, *Justus Liebigs Ann. Chem.*, 1970, **731**, 176–179.
- M. C. A. Kuhn, A. A. M. Lapis, G. Machado, T. Roisnel, J.-F. Carpentier, B. A. D. Neto and O. L. Casagrande, *Inorg. Chim. Acta*, 2011, **370**, 505–512.
- A. Podjava, P. Mekss and A. Zicmanis, *Eur. J. Mass Spectrom.*, 2011, **17**, 377–383.
- S. Ard, N. Mirsaleh-Kohan, J. D. Steill, J. Oomens, S. B. Nielsen and R. N. Compton, *J. Chem. Phys.*, 2010, **132**, 094301.
- T. B. Arthur, M. Peschke and P. Kebarle, *Int. J. Mass Spectrom.*, 2003, **228**, 1017–1034.

# Organic Reactions in Ionic Liquids Studied by in Situ XPS

Inga Niedermaier,<sup>[a]</sup> Claudia Kolbeck,<sup>[a]</sup> Nicola Taccardi,<sup>[b]</sup> Peter S. Schulz,<sup>[b]</sup> Jing Li,<sup>[c]</sup> Thomas Drewello,<sup>[c]</sup> Peter Wasserscheid,<sup>[b]</sup> Hans-Peter Steinrück,<sup>[a]</sup> and Florian Maier<sup>\*[a]</sup>

We demonstrate the application of in situ X-ray photoelectron spectroscopy (XPS) to monitor organic, liquid-phase reactions. By covalently attaching ionic head groups to the reacting organic molecules, their volatility can be reduced such that they withstand ultra high vacuum conditions. The applied method, which is new for the investigation of organic reactions, allows for following the fate of all elements present in the reaction mixture—except for hydrogen—in a quantitative and oxida-

tion-state-sensitive manner in one experiment. This concept is demonstrated for the alkylation of a tertiary amine attached to an imidazolium or phosphonium moiety by the anion 4-chlorobutylsulfonate ( $[\text{ClC}_4\text{H}_8\text{SO}_3]^-$ ). In the course of the reaction, the covalently bound chlorine is converted to chloride and the amine to ammonium as reflected by the distinct shifts in the N 1s and Cl 2p binding energies.

## 1. Introduction

Commonly, X-ray photoelectron spectroscopy (XPS) is considered a powerful surface-sensitive method for the detailed study of solid surfaces and of processes occurring at solid surfaces under ultra-high vacuum (UHV) conditions. The fact that most liquids simply evaporate in UHV, due to their comparably high vapor pressures, renders them unsuitable for conventional XPS setups. Only by using sophisticated and advanced experimental methods, such as vacuum–liquid microjets combined with synchrotron-radiation,<sup>[1]</sup> normal liquid surfaces have become accessible to some extent by means of XPS.

Due to their extremely low vapor pressure, ionic liquids (ILs) present an exception to this restriction.<sup>[2]</sup> ILs are defined as salts with a melting point below 100 °C. They have received increasing attention during the last two decades because of their unique physico-chemical characteristics and their potential for many applications.<sup>[2]</sup> Particularly, this interest also concerns studies of IL surfaces under UHV conditions. In the field of ionic liquid surface science, conventional XPS has very recently developed into one of the most powerful methods.<sup>[3,4]</sup> The strongly increasing number of UHV-based studies has not only increased our knowledge on surface and also bulk properties of ILs, but also provides additional information concerning the atomistic understanding of surface properties of liquids in general.

Apart from a steady-state analysis of the chemical composition of the near-surface region of ILs, XPS investigations have even been extended towards the monitoring of reactions or other time-dependent processes (denoted “in situ XPS” in the following) within IL systems. The number of such studies is, however, very limited. The Licence group investigated the adsorption, dissolution, and desorption of water on  $[\text{C}_8\text{C}_1\text{Im}][\text{BF}_4]$  by temperature-programmed XPS,<sup>[5]</sup> and the electrochemical generation of a  $\text{Cu}^+$  species in a picolinium-based IL,<sup>[6]</sup> as well as the electrochemical reduction of a haloferrate(III) IL dissolved in  $[\text{C}_2\text{C}_1\text{Im}][\text{EtOSO}_3]$  to a haloferrate(II) compound.<sup>[7]</sup> The electrodeposition of potassium metal from a pyrrolidinium-

based IL was studied by Compton et al.,<sup>[8]</sup> whereas Kötze et al. addressed the influence of the applied potential on the binding energy and stability of  $[\text{C}_2\text{C}_1\text{Im}][\text{BF}_4]$  with in situ electrochemical XPS.<sup>[9]</sup> Using IR and in situ XP spectroscopy, Sobota et al. investigated the replacement of CO molecules pre-adsorbed at Pd-nanoparticles on an  $\text{Al}_2\text{O}_3/\text{NiAl}(110)$  support by  $[\text{C}_4\text{C}_1\text{Im}][\text{Tf}_2\text{N}]$ .<sup>[10]</sup> All these studies were performed using non-functionalized ILs, and addressed either the reaction at an interface or an electrochemical reaction.

Very recently, we demonstrated that such in situ studies can be extended to the monitoring of liquid-phase organic reactions.<sup>[11]</sup> Building on this communication, we herein demonstrate that this concept can be generalized to more complex reactions. Conceptually, the reacting groups are linked to ionic head groups in order to drastically lower the vapor pressures of the reactants. The feasibility of this approach is shown for several nucleophilic substitution reactions. In each case reported here, an alkyl amine and a chloroalkyl moiety are attached to cationic and anionic IL headgroups, respectively. The advantage of in situ XPS, as compared to common analytical

[a] I. Niedermaier, C. Kolbeck, Prof. H.-P. Steinrück, Dr. F. Maier  
Lehrstuhl für Physikalische Chemie II  
Universität Erlangen-Nürnberg  
Egerlandstraße 3  
91058 Erlangen (Germany)  
E-mail: florian.maier@chemie.uni-erlangen.de

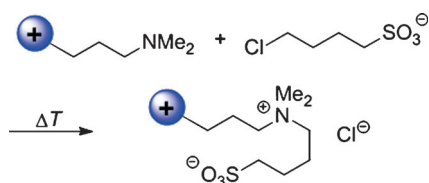
[b] Dr. N. Taccardi, Dr. P. S. Schulz, Prof. P. Wasserscheid  
Lehrstuhl für Chemische Reaktionstechnik  
Universität Erlangen-Nürnberg  
Egerlandstraße 3  
91058 Erlangen (Germany)

[c] J. Li, Prof. T. Drewello  
Lehrstuhl für Physikalische Chemie I  
Universität Erlangen-Nürnberg  
Egerlandstraße 3  
91058 Erlangen (Germany)

Supporting information for this article is available on the WWW under <http://dx.doi.org/10.1002/cphc.201100965>.

methods, such as NMR, is that all elements (apart from hydrogen and helium) can be quantified and analyzed with respect to their chemical state (e.g. oxidation state) within one experiment. In contrast to bulk methods, XPS focuses on the near-surface region of a solid or liquid sample. Its inherent surface sensitivity is due to the small inelastic mean free path of photoelectrons in matter.<sup>[12]</sup> For ILs, a typical information depth below 9 nm is obtained under normal emission (i.e. an electron emission angle of 0°).<sup>[13]</sup> By increasing the emission angle [angle resolved XPS (ARXPS)], the information depth can be reduced, for example, down to ~1.5 nm at 80°. Consequently, the variation of the emission angle provides information on orientation and/or enrichment of molecules at the surface. An increase of a particular core level with increasing detection angle indicates a higher concentration of this element in the topmost layers as compared to the bulk, and vice versa.

In this *in situ* ARXPS study, we monitored the reaction between a dimethylpropylamine substituent ( $\text{Me}_2\text{NC}_3\text{H}_6$ ) attached to the cation of **IL1** and the chloroalkyl moiety of the 4-chlorobutylsulfonate ( $[\text{ClC}_4\text{H}_8\text{SO}_3]^-$ ) anion of **IL2**. The anticipated alkylation reaction is depicted in Scheme 1, whereby the



**Scheme 1.** Alkylation of the 3-dimethylaminepropyl substituent at the cation with the 4-chlorobutyl substituent at the anion forming a zwitterionic compound.

nucleophilic amine functionality is alkylated by the  $[\text{ClC}_4\text{H}_8\text{SO}_3]^-$  electrophile to form a new zwitterionic compound. The resulting changes in electronic state (the amine is transformed into an ammonium and the covalently bound chlorine into a free chloride) give rise to distinct binding energy shifts in both the N 1s and Cl 2p signals, making the monitoring by XPS possible.

The alkylation reaction was carried out by mixing both functionalized ILs in a molar 1:1 ratio. As the reaction occurs only slowly at room temperature, we first examined the surface composition of the unreacted, binary IL mixtures thoroughly by ARXPS, and thereafter initiated the alkylation reaction by heating the sample *in situ* to 100 °C. In addition, the primary ILs were measured separately at room temperature and at elevated temperatures ( $T > 70$  °C) to analyze surface orientation effects and thermal stability.

The full characterization of the individual reactants and of the mixture at room temperature and at elevated temperatures was carried out for three different IL pairs (pairs **a–c**). In each case, the **IL1** cation was amine-functionalized and the **IL2** anion contained the chloroalkyl moiety. The three investigated IL pairs are listed in Table 1 together with their structures and abbreviations. The cations of **IL1 a** and **IL1 b** are imidazolium-based, while in the cation of **IL1 c** the identical amine group is attached to phosphonium. For the three ILs **IL2 a–c**, the chloroalkyl function is part of the  $[\text{ClC}_4\text{H}_8\text{SO}_3]^-$  anion. The remaining non-functionalized ions in the reaction mixtures, that is, the **IL1 a–c** anions and the **IL2 a–c** cations are inert under the applied reaction conditions. The **IL1** anions are  $[\text{TfO}]^-$ ,  $[\text{Tf}_2\text{N}]^-$ , and  $[\text{FAP}]^-$  for **IL1 a**, **IL1 b**, and **IL1 c**, respectively. Both the **IL2 a** and **IL2 b** cation are imidazolium-based with different alkyl chain lengths, whereas **IL2 c** is a phosphonium cation.

## 2. Results and Discussion

UHV conditions and exposure to X-rays are unavoidable when performing XPS. Both factors, alone and in combination with elevated temperatures, could affect the stability of primary ILs. To evaluate stability issues and potential side reactions, XPS measurements of the neat ILs were conducted at elevated temperatures ( $\geq 70$  °C); the corresponding results are discussed first before considering the reactive mixtures.

### 2.1. Primary Ionic Liquids

From ARXPS, surface-active impurities, such as polysiloxane<sup>[14]</sup> and hydrocarbons,<sup>[15]</sup> which are not observable with NMR or

**Table 1.** Summary of investigated mixtures.

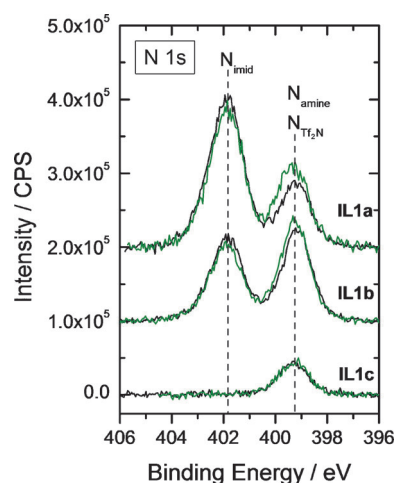
Abbr.	Short Name	Structure		IUPAC Name
<b>IL1 a</b>	$[(\text{Me}_2\text{NC}_3\text{H}_6)\text{C}_1\text{Im}]$ [TfO]		$\text{F}_3\text{C}-\text{SO}_3^-$	1-methyl-3-(3'-dimethylaminopropyl)imidazolium trifluoromethylsulfonate
<b>IL2 a</b>	$[\text{C}_2\text{C}_1\text{Im}]$ [ $\text{ClC}_4\text{H}_8\text{SO}_3$ ]		$\text{Cl}-\text{C}_4\text{H}_8-\text{SO}_3^-$	1-ethyl-3-methylimidazolium 4-chlorobutylsulfonate
<b>IL1 b</b>	$[(\text{Me}_2\text{NC}_3\text{H}_6)\text{C}_1\text{Im}]$ [ $\text{Tf}_2\text{N}$ ]		$\text{F}_3\text{C}-\text{S}^+(\text{O})_2-\text{N}^-(\text{CF}_3)_2$	1-methyl-3-(3'-dimethylaminopropyl)imidazolium bis[(trifluoromethyl)sulfonyl]imide
<b>IL2 b</b>	$[\text{C}_8\text{C}_1\text{Im}]$ [ $\text{ClC}_4\text{H}_8\text{SO}_3$ ]		$\text{Cl}-\text{C}_4\text{H}_8-\text{SO}_3^-$	1-methyl-3-octylimidazolium 4-chlorobutylsulfonate
<b>IL1 c</b>	$[(\text{Me}_2\text{NC}_3\text{H}_6)\text{PBu}_3]$ [FAP]		$\text{C}_2\text{F}_5-\text{P}^+(\text{F})(\text{C}_2\text{F}_5)_3$	(3'-dimethylaminopropyl)tributylphosphonium tris(pentafluoroethyl)trifluorophosphate
<b>IL2 c</b>	[PBu <sub>4</sub> ] [ $\text{ClC}_4\text{H}_8\text{SO}_3$ ]		$\text{Cl}-\text{C}_4\text{H}_8-\text{SO}_3^-$	tetrabutylphosphonium 4-chlorobutylsulfonate



other bulk sensitive measurements due to their low concentration, were excluded for most of the studied ILs. Only **IL2c** contained a surface-active impurity, comprised of phosphorous, oxygen and sodium, which is probably caused by the poor quality of the starting material used for its synthesis.

## 2.2. Amine-Functionalized ILs (**IL1a–c**)

Apart from determining purity, ARXPS measurements also permit conclusions about the preferential orientation of the ions at the surface. Hereto, the N 1s spectra of **IL1a–c**, measured at room temperature, are depicted in Figure 1 for emission angles of 0° (black) and 80° (green). **IL1c** only contains



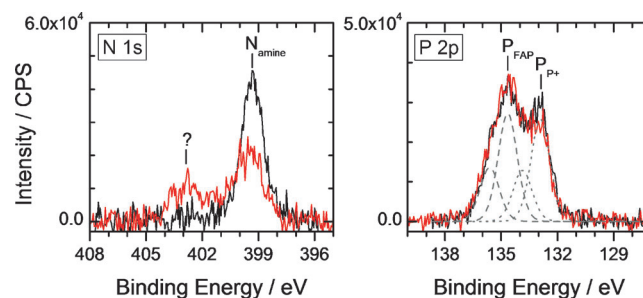
**Figure 1.** N 1s spectra in 0° (black) and 80° emission (green), measured at room temperature for **IL1a** (top), **IL1b** (middle) and **IL1c** (bottom). The spectra are offset for better clarity.

one nitrogen species from the amine group ( $N_{\text{amine}}$ ), therefore, the N 1s signal at 399.3 eV can unambiguously be attributed to this nitrogen. **IL1a** shows a second signal at 401.9 eV, originating from the two imidazolium nitrogens ( $N_{\text{imid}}$ ). **IL1b** contains a third nitrogen species in its anion  $[\text{Tf}_2\text{N}]^-$  ( $N_{\text{Tf}_2\text{N}}$ ), whose signal superimposes the  $N_{\text{amine}}$  signal, resulting in an overall 1:1 ratio of the two peaks at 399.3 and 401.9 eV.

By changing the sensitivity from bulk (0°, black) to more surface sensitive (80°, green), a slight increase in the  $N_{\text{amine}}$  signal and a concomitant slight decrease in the  $N_{\text{imid}}$  signal is observed for the imidazolium-based ILs **IL1a** and **IL1b**, indicating a preference for the amine containing chain to stick out into the vacuum, while the imidazolium groups are preferentially pointing towards the bulk. In **IL1b** this effect could also be attributed to a preferential orientation of  $[\text{Tf}_2\text{N}]^-$  towards the vacuum. However, the intensities of the F 1s, O 1s, and the S 2p signals of the  $[\text{Tf}_2\text{N}]^-$  anion are insensitive to the different emission angles (spectra not shown). Thus, the observed increase of the N 1s signal at 399.2 eV can unambiguously be assigned to  $N_{\text{amine}}$ . In contrast to the imidazolium-based ILs, the phosphonium IL **IL1c** shows no changes in intensity when

going from 0° to 80° emission, indicating an isotropic arrangement of its ions at the surface.

The thermal stabilities of the amine-functionalized ILs in UHV were tested by ARXPS measurements after heating the sample in situ to 100 °C for several hours. For the imidazolium-based ILs **IL1a** and **IL1b**, no changes were observed after heating for 2 h and 5 h, respectively, proving the stability of both ILs under the conditions used for the reactive mixture. However, **IL1c** exhibited signs of decomposition upon heating: The N 1s and P 2p 0° spectra of **IL1c** before (black) and after (red) heating for 4 h to 100 °C are depicted in Figure 2. In the

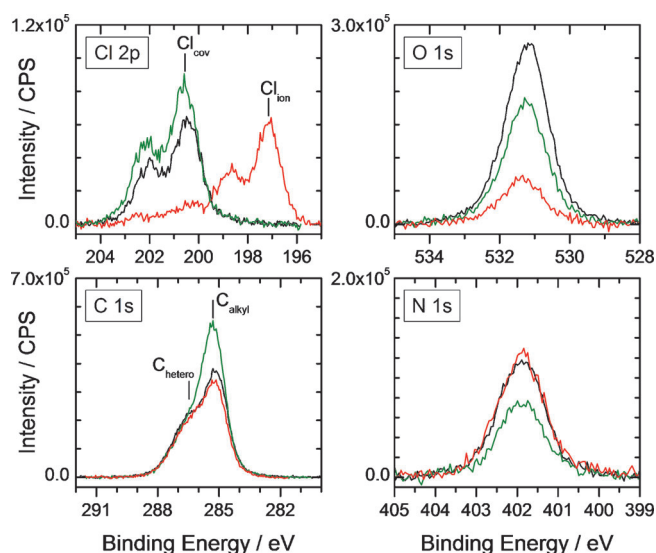


**Figure 2.** N 1s and P 2p spectra of **IL1c** at 0° emission before heating (black; taken at room temperature) and after heating to 100 °C for 4 h (red; taken at 100 °C).

N 1s region, a substantial decrease in the  $N_{\text{amine}}$  intensity is observed, while a second peak arises at a higher binding energy of 402.7 eV. This binding energy is in the range of the  $N_{\text{imid}}$  signal, suggesting a conversion into an ammonium species. Concerning the P 2p region, two P 2p signals are expected, one for the phosphonium cation ( $P_{\text{P}^+}$ ) and one for the  $[\text{FAP}]^-$  anion ( $P_{\text{FAP}}$ ). Due to spin-orbit coupling, 2p signals generally split into the two peaks  $2p_{1/2}$  and  $2p_{3/2}$  with an 1:2 intensity ratio. By fitting the 0° emission spectrum with two doublets (gray dashed and dotted lines in Figure 2), binding energies of 132.9 and 134.7 eV are found for the P  $2p_{3/2}$  peaks of  $P_{\text{P}^+}$  and  $P_{\text{FAP}}$  respectively. After heating **IL1c** in situ for 4 h to 100 °C, the  $P_{\text{P}^+}$  signal loses intensity, while the  $P_{\text{FAP}}$  signal remains constant, suggesting a degradation of the phosphonium cation. The decomposition products either diffuse into the bulk or evaporate. An independent in situ XPS measurement of the IL  $[(\text{Me}_2\text{NC}_3\text{H}_6)\text{C}_1\text{Im}][\text{FAP}]$ , that differs from **IL1c** by having the amine moiety attached to an imidazolium cation, showed the same degradation of the amine functionality upon heating to 100 °C for 4 h. This observation indicates a limited thermal stability of the  $[\text{FAP}]^-$ -containing ILs in general. However, the decomposition pathway is unknown yet.

## 2.3. 4-Chlorobutylsulfonate ILs (**IL2a–c**)

Information about the surface orientation of the 4-chlorobutylsulfonate anion can be derived by ARXPS measurements of **IL2a** and **IL2b**. In Figure 3, the Cl 2p, O 1s, C 1s, and N 1s spectra are shown for **IL2b**. In the Cl 2p region, the signal of covalently bound chlorine,  $\text{Cl}_{\text{cov}}$ , (Cl  $2p_{3/2}$  at 200.5 eV) increases



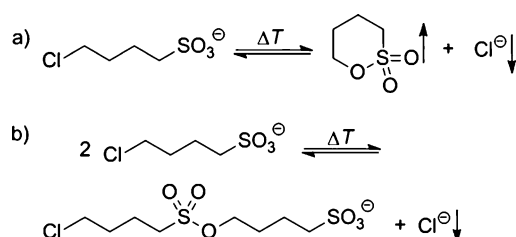
**Figure 3.** Cl 2p, O 1s, C 1s, and N 1s spectra of **IL2b** in  $0^\circ$  (black) and  $80^\circ$  (green) emission before heating and in  $0^\circ$  emission after heating to  $70^\circ\text{C}$  for 6 h (red). All spectra were measured at room temperature.

when changing from the bulk-sensitive ( $0^\circ$ , black) to the surface-sensitive ( $80^\circ$ , green) geometry, whereas the O 1s and S 2p peaks (not shown) are concomitantly decreasing. These ARXPS characteristics reveal a pronounced preferential orientation of the 4-chlorobutylsulfonate anion with its chlorobutyl chain sticking out towards the vacuum side, while its sulfonate group points towards the bulk. The imidazolium N 1s signal (401.9 eV) of the cation, and also the O 1s (531.2 eV) and S 2p (not shown) signals of the  $\text{SO}_3^-$  group of the anion are concomitantly decreasing, when changing from  $0^\circ$  to  $80^\circ$ . From this behavior, it is concluded that in the first molecular layer of **IL2b** both charged headgroups (consisting of the imidazolium rings of the cation and the sulfonate groups of the anion) are located at the same distance below the outer surface that preferentially consists of the chlorobutyl chains of the anion and the octyl chains of the cation (see below). Note that the same orientation behavior within the surface layer was also observed for **IL2a**.<sup>[11]</sup>

The detailed analysis of the two discernible C 1s peaks ( $\text{C}_{\text{hetero}}$  and  $\text{C}_{\text{alkyl}}$  at 286.4 and 285.1 eV, respectively) in Figure 3, as described for example, in ref. [16], is not possible for **IL2b**. The contributions originating from the carbon atoms of the cation and of the anion are superimposed. Nevertheless, due to the abundance of the seven alkyl carbons in the octyl chain versus the two alkyl carbons in the 4-chlorobutylsulfonate anion, the strongly increased  $\text{C}_{\text{alkyl}}$  peak at  $80^\circ$  can only be explained by a surface enrichment of the octyl chain. The preferential surface orientation of  $[\text{C}_8\text{C}_1\text{Im}]^+$  cations pointing the octyl chains towards the vacuum has also been observed for many other  $[\text{C}_8\text{C}_1\text{Im}]$ -ILs by our group,<sup>[17]</sup> supporting the proposed composition for the outer surface layer of **IL2b** described above.

Concerning the thermal stability of **IL2a–c**, all three ILs exhibited degradation of the 4-chlorobutylsulfonate anion at elevated temperatures ( $T \geq 70^\circ\text{C}$ ). The  $0^\circ$  emission spectra of **IL2b**

after heating to  $70^\circ\text{C}$  for 6 h are included in Figure 3 (red lines). Upon heating, the signal of covalently bound chlorine,  $\text{Cl}_{\text{cov}}$ , ( $\text{Cl } 2p_{3/2}$  at 200.5 eV) decreases, while a second Cl 2p doublet at lower binding energy ( $\text{Cl } 2p_{3/2}$  at 197.2 eV) arises. By comparison with XPS measurements of  $[\text{C}_8\text{C}_1\text{Im}]\text{Cl}$ ,<sup>[17]</sup> the new Cl species is identified as chloride ( $\text{Cl}_{\text{ion}}$ ). Simultaneous to the transformation of covalent chlorine to chloride a decrease in the O 1s (Figure 3) and S 2p (not shown) intensity is observed. Both observations indicate that upon heating the IL in vacuo, the ring opening reaction of the sultone employed to prepare **IL2a–c** is reversed (Scheme 2a). The thereby formed 1,4-butane sultone evaporates in UHV, explaining the high gas



**Scheme 2.** Degradation of **IL 2a–c** anions by two different reaction pathways: a) formation of volatile 1,4-butane sultone (intramolecular reaction), b) formation of 4-chlorobutylsulfonate ester (intermolecular reaction). For both pathways, released chloride is preferentially depleted from the near-surface region in case of the reacted binary mixtures (for details, see text), according to ref. [11].

evolution observed (pressure increase from  $10^{-8}$  mbar to  $10^{-6}$  mbar) upon heating the samples. In situ mass spectroscopy of the gas phase supports this assumption, as the fragment pattern of 1,4-butane sultone was observed indeed. For **IL2a**, thermal gravimetric analysis (TGA) showed decomposition of the anion to 1,4-butane sultone and chloride at  $214.9^\circ\text{C}$  under standard pressure.<sup>[18]</sup> However, at UHV conditions decomposition occurs at much lower temperature, as the volatile sultone in the near-surface region is continuously removed from the equilibrium.

If sultone formation would be the only reaction occurring upon heating, the relative signal intensity loss for the  $\text{Cl}_{\text{cov}}$  and O 1s signals should be identical. However, the decrease in O 1s intensity is significantly smaller than in  $\text{Cl}_{\text{cov}}$  intensity. For **IL2b**, the O 1s signal decreases only to 25% of its former intensity, while the signal of  $\text{Cl}_{\text{cov}}$  decreases to 18%. The corresponding values for **IL2a** are 58 and 45%, respectively.<sup>[11]</sup> Therefore, at least one additional side reaction next to formation of sultone has to be taken into account. The formation of a sulfonic acid ester by an intermolecular reaction of the 4-chlorobutylsulfonate (Scheme 2b) is a possibility. The formed ester, due to its anionic nature, would not evaporate but contribute to the observed O 1s signal.

Summarizing this section, all three ILs **IL1a,b** (and to some extent **IL1c**) are stable under reaction conditions in UHV at  $100^\circ\text{C}$ . However, the sulfonate anions of **IL2a–c** exhibit a fast thermal degradation process already at  $70^\circ\text{C}$  by the formation of free chloride anions and either neutral (and thus volatile)

sultones or anionic esters in form of dimers (and perhaps small amounts of higher oligomers).

## 2.4. Reactive binary 1:1 mixtures

After having addressed the stability of the primary ILs at elevated temperatures in UHV, we now turn to the reactive mixtures **IL1 a/IL2 a**, **IL1 b/IL2 b**, and **IL1 c/IL2 c**. The results for **IL1 a/IL2 a** have been partly reported in a very recent communication.<sup>[11]</sup> They are expanded here together with the results of the two other examples, in order to illustrate the potential of XPS for in situ monitoring of organic liquid-phase reactions for a range of different structures.

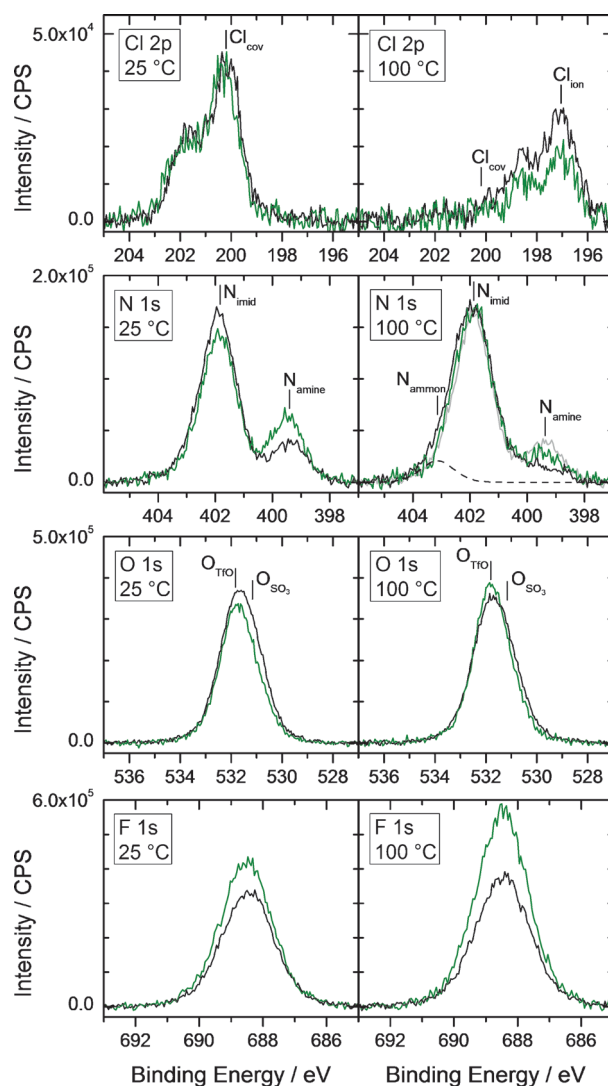
It turned out that storage of a 1:1 colorless mixture of **IL1 b** and **IL2 b** at ambient conditions for one week led to a slow macroscopic change in appearance, turning finally into a whitish, gel-like suspension. Thus, to rule out any slow reactions at room temperature, all binary 1:1 mixtures were always freshly mixed immediately before they were introduced into the spectrometer (within a maximum time delay of 10 min). To trigger the reaction (Scheme 1) the mixtures were heated to 100 °C, while XPS measurements were conducted.

## 2.5. Mixture a—IL1a/IL2a

$[(\text{Me}_2\text{NC}_3\text{H}_6)\text{C}_1\text{Im}][\text{TfO}]/[\text{C}_2\text{C}_1\text{Im}][\text{CIC}_4\text{H}_8\text{SO}_3]$

To confirm the occurrence of the alkylation process proposed in Scheme 1, the reaction was first carried out under standard laboratory conditions whereby a 1:1 mixture of **IL1 a** and **IL2 a** was heated to 100 °C for 90 min. To analyze the product mixture, <sup>1</sup>H NMR and electro-spray ionization-mass spectroscopy (ESI-MS) were applied. With <sup>1</sup>H NMR only minor changes ( $\delta \leq 0.1$  ppm) were observed in comparison to the unreacted mixture suggesting that <sup>1</sup>H NMR is not applicable for monitoring this reaction. The ESI-MS analysis (see Figure S1 in the Supporting Information), however, showed a species with  $m/z=304.2$  which unambiguously can be attributed to the formed product cation.

In Figure 4, the XP spectra of the Cl 2p, N 1s, O 1s, and F 1s regions are depicted at 0° (black) and 80° (green) emission before (left side) and after (right side) in situ heating of the **IL1 a/IL2 a** mixture to 100 °C for 2 h.<sup>[11]</sup> For the unreacted mixture, the signals of  $\text{N}_{\text{amine}}$  and F 1s at 80° reveal a distinct increase in signal intensity compared to 0° emission, whereas the  $\text{N}_{\text{imid}}$  and O 1s signals concomitantly decrease in intensity. These opposing changes in intensity with emission angle for the N 1s region are much more pronounced for the mixture than for pure **IL1 a** (compare Figure 1 and 4). Moreover, the change in F 1s intensity (related to the  $\text{CF}_3$ -group of the **IL1 a** anion) with emission angle in the mixture was not detected for the pure **IL1 a**. As a consequence, the 80° intensities of the mixture cannot be explained by a surface molecular layer with a **IL1 a** : **IL2 a** = 1:1 composition, taking the orientation effects observed for the pure ILs into account. Hence, the composition of the surface layer of the mixture deviates significantly from the bulk 1:1 stoichiometry. The strong increase of the  $\text{N}_{\text{amine}}$  signal indicates that  $[(\text{Me}_2\text{NC}_3\text{H}_6)\text{C}_1\text{Im}]^+$  is enriched at the sur-



**Figure 4.** Cl 2p, N 1s, O 1s, and F 1s spectra of the binary mixture **IL1 a/IL2 a** at 0° (black) and 80° (green) emission, before (left side) and after (right side) heating in situ to 100 °C for 2 h and cooling down to 60 °C for the XPS measurement.<sup>[11]</sup> Note that the 0° room temperature N 1s spectrum is superimposed in the 100 °C N 1s spectrum in grey for visual comparison.

face at the expense of  $[\text{C}_2\text{C}_1\text{Im}]^+$ , resulting in a 2.6:1 ratio for  $\text{N}_{\text{imid}}$  :  $\text{N}_{\text{amine}}$  at 80° instead of the nominal 4:1. The higher intensity of F 1s at 80° compared to 0° suggests an enrichment of  $[\text{TfO}]^-$  at the surface at the expense of  $[\text{CIC}_4\text{H}_8\text{SO}_3]^-$ . The preferential orientation of the  $[\text{CIC}_4\text{H}_8\text{SO}_3]^-$  anion at the surface (chlorobutyl chain pointing towards the vacuum) is still observable, as can be seen in the O 1s and Cl 2p regions: Both anions contain a sulfonate group. Despite the resemblance in chemical nature of the  $\text{SO}_3^-$  groups, their oxygen binding energy values as measured for pure **IL1 a** and **IL2 a** differ by 0.7 eV, that is 531.8 eV for  $[\text{TfO}]^-$  ( $\text{O}_{\text{TfO}}$ ) and 531.1 eV for  $[\text{CIC}_4\text{H}_8\text{SO}_3]^-$  ( $\text{O}_{\text{SO}_3}$ ). By changing from 0° to 80°, an intensity loss at the lower binding energy side of the O 1s signal is observed, resulting in an asymmetric peak shape (fit data not shown in Figure 4) which confirms the surface enrichment of  $[\text{TfO}]^-$  as already deduced from the F 1s spectra. In contrast to the intensity loss of the  $\text{O}_{\text{SO}_3}$  signal, the  $\text{Cl}_{\text{cov}}$  peak does not decrease

with emission angle, indicating an orientation of the 4-chlorobutylsulfonate anions of **IL2a** with their terminal chlorine atoms preferentially pointing towards vacuum and their charged  $\text{SO}_3^-$  head groups towards the bulk, similar as in the pure IL.

Upon heating the binary mixture to 100 °C, the alkylation of the amine functionality of **IL1a** by the 4-chlorobutylsulfonate of **IL2a** is initiated.<sup>[11]</sup> It is important to note that the maximum background pressure in our UHV system is considerably lower ( $\sim 5 \times 10^{-8}$  mbar) for the mixture at 100 °C than for the primary **IL2a** alone at 70 °C ( $\sim 2 \times 10^{-6}$  mbar), indicating that the formation of volatile sultones is considerably reduced for the mixture. The most obvious changes in the XP spectra are expected to occur in the Cl 2p and N 1s regions, due to changes in the chemical state, particularly electronic changes (in the course of the reaction, covalently bound chlorine is transformed into chloride and the amine-functionality is alkylated to form an ammonium). The measured XP spectra after heating to 100 °C for 2 h are depicted on the right hand side of Figure 4 for 0° (black) and 80° (green) emission. At this stage, prolonged heating time does not lead to significant spectral changes. Focusing first on the N 1s region, an intensity decrease of the  $N_{\text{amine}}$  signal to 44% of its former intensity in 0° emission is observed after heating, suggesting a 56% conversion of **IL1a** to the alkylated product. Simultaneously, a new peak,  $N_{\text{ammon}}$ , emerges at higher binding energy, thereby broadening the  $N_{\text{imid}}$  signal (for better comparison, the 0° emission spectrum before heating is added in gray in Figure 4). The loss in  $N_{\text{amine}}$  intensity and the intensity of the new peak are balanced, suggesting that this new peak stems from the ammonium group in the zwitterionic reaction product (Scheme 1). Fitting the data yields a binding energy of  $403.1 \pm 0.2$  eV for this ammonium group  $N_{\text{ammon}}$  (dashed line in Figure 4), which fits well to values of ammonium containing ILs measured in our group.<sup>[19]</sup>

In contrast to the N 1s spectra indicating a  $\sim 56\%$  conversion of **IL1a** in the near-surface region the Cl 2p core-level spectra show an intensity shift from covalently bound chlorine ( $\text{Cl}_{\text{cov}}$ ; Cl 2p<sub>3/2</sub> at 200.2 eV) to free chloride ( $\text{Cl}_{\text{ion}}$ ; 197.0 eV) by  $\sim 91\%$  upon heating. This suggests that parallel to the alkylation (i.e. zwitterion formation), sultone formation and 4-chlorobutylsulfonate ester formation has also taken place. The remaining 9% of the  $\text{Cl}_{\text{cov}}$  signal indicates that 18% of the **IL2a** anion have formed a dimerized ester (Scheme 2b, two  $\text{Cl}_{\text{cov}}$  yield one  $\text{Cl}_{\text{cov}}$  and one  $\text{Cl}_{\text{ion}}$ ). The residual **IL2a** anions ( $100\% - 56\% - 18\% = 26\%$ ) react to volatile sultones. From the fact that **IL1a** and **IL2a** both contain one  $\text{SO}_3$  group, one expects an overall intensity decrease of the O 1s peaks (Figure 4) and S 2p peaks (not shown) by 13% upon heating. However, only changes smaller than 5% are observed. Simultaneously, in the 0° spectra in Figure 4 the F 1s intensity increases by 18% and the total Cl 2p signals decrease by 20% upon heating. These observations indicate that chloride is depleted from the IL surface, while at the same time the  $[\text{TfO}]^-$  anion enriches due to its higher surface activity. The surface enrichment of the  $\text{SO}_3$  containing  $[\text{TfO}]^-$  anions roughly compensates for the expected intensity losses in O 1s and S 2p signals due to the evaporating 1,4-butane sultone molecules.

The enrichment of  $[\text{TfO}]^-$  and the depletion of  $\text{Cl}_{\text{ion}}$  is more pronounced in the 80° measurements, as is deduced from the increase of the F 1s signal and the decrease of the  $\text{Cl}_{\text{ion}}$  signal, respectively, when going from 0° to 80° emission. Furthermore, the depletion of the cation of the alkylation product and the associated enrichment of the unreacted  $[(\text{Me}_2\text{NC}_3\text{H}_6)\text{C}_1\text{Im}]^+$  cation of **IL1a** can be seen in the 80° spectrum of the N 1s region: Here, the  $N_{\text{amine}}$  signal clearly gains intensity compared to the 0° spectrum, while the  $N_{\text{ammon}}$  signal is not observable anymore.

Subsequent to these ARXPS measurements, the sample holder of the spectrometer was washed with methanol. The collected washings were analyzed by ESI-MS which, independent from the XPS measurements, unequivocally demonstrated the formation of the reaction product. The spectra showed a species with  $m/z = 304.2$ , corresponding to the mass of the zwitterionic compound (Scheme 1) obtained by reacting **IL1a** and **IL2a**. The MS fragmentation pattern of the 304.2 species, which was isolated from the gas phase by a first MS and analyzed in a consecutive MS, showed a signal at  $m/z = 168.3$  that was attributed to the **IL1a** cation, confirming the expected product structure. (The corresponding spectra are shown in Figure S2 of the Supporting Information.)

## 2.6. Mixture b—IL1b/IL2b

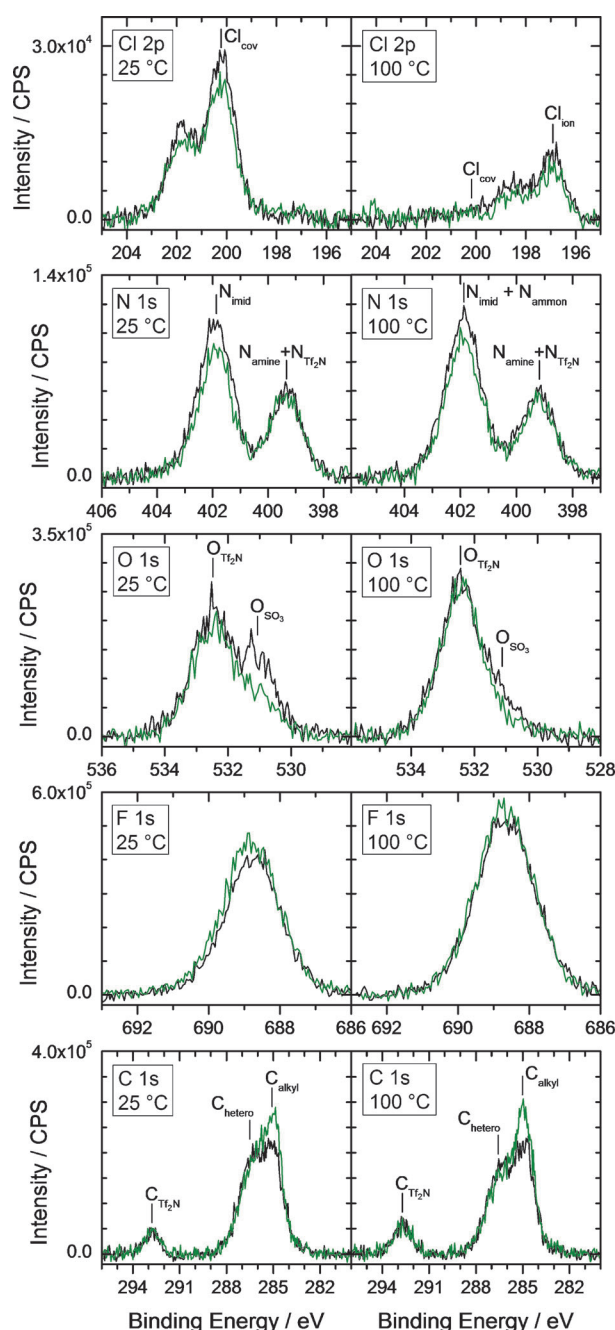
$[(\text{Me}_2\text{NC}_3\text{H}_6)\text{C}_1\text{Im}][\text{Tf}_2\text{N}]/[\text{C}_8\text{C}_1\text{Im}][\text{ClC}_4\text{H}_8\text{SO}_3]$

The reaction monitoring of the binary mixture **IL1b/IL2b** by XPS is more complex than for the **IL1a/IL2a** mixture as **IL1b** contains  $[\text{Tf}_2\text{N}]^-$  and the corresponding  $N_{\text{Tf}_2\text{N}}$  signal superimposes the  $N_{\text{amine}}$  signal, as is evident in the N 1s spectra of the primary **IL1b** in Figure 1.

In Figure 5 the Cl 2p, N 1s, O 1s, F 1s, and C 1s spectra of the binary mixture **IL1b/IL2b** are depicted at 0° (black) and 80° (green) emission, before (left side) and after (right side) heating in situ to 100 °C for 6 h. Before heating, the unreacted mixture shows the same preferential surface orientation of the  $[\text{C}_8\text{C}_1\text{Im}]^+$  cation as the primary IL, with its octyl chain pointing towards the vacuum and its imidazolium moiety pointing towards the bulk. This behavior is deduced from the increase in  $\text{C}_{\text{alkyl}}$  signal and the decrease in  $N_{\text{imid}}$  signal intensity at 80° compared to 0° emission. The identical ( $N_{\text{amine}} + N_{\text{Tf}_2\text{N}}$ ) intensity for both emission angles indicates that there is no enrichment of the  $[(\text{Me}_2\text{NC}_3\text{H}_6)\text{C}_1\text{Im}]^+$  cation in the unreacted **IL1b/IL2b** mixture, in contrast to the **IL1a/IL2a** mixture (see above). This difference in surface activity could be related to the presence of  $[\text{C}_8\text{C}_1\text{Im}]^+$  instead of  $[\text{C}_2\text{C}_1\text{Im}]^+$  in the **IL1a/IL2a** mixture. It has been shown for pure ILs that the  $[\text{C}_8\text{C}_1\text{Im}]^+$  cation of **IL1a** exhibits a preferential orientation at the surface, while the  $[\text{C}_2\text{C}_1\text{Im}]^+$  cation of **IL2a** exhibits a more isotropic behavior.<sup>[16]</sup>

The slight increase in F 1s intensity and the slight decrease in Cl 2p intensity when going from 0° to 80° emission suggests a moderate enrichment of  $[\text{Tf}_2\text{N}]^-$  at the expense of  $[\text{ClC}_4\text{H}_8\text{SO}_3]^-$ , analogous to the **IL1a/IL2a** mixture. Also, the preferential orientation of the  $[\text{ClC}_4\text{H}_8\text{SO}_3]^-$  anion of the pure **IL2a-c** ILs is still present in the **IL1b/IL2b** mixture. The O 1s region exhibits two peaks at 532.6 and 531.1 eV, which are at-





**Figure 5.** Cl 2p, N 1s, O 1s, F 1s, and C 1s spectra of the binary mixture IL1 b/IL2 b at 0° (black) and 80° (green) emission, measured before (left side; at room temperature) and after (right side; at 100 °C) heating the mixture to 100 °C for 6 h.

tributed to the four oxygen atoms of the  $[\text{Tf}_2\text{N}]^-$  sulfonyl groups ( $\text{O}_{\text{Tf}_2\text{N}}$ ) and to the three oxygen atoms of the  $[\text{ClC}_4\text{H}_8\text{SO}_3]^-$  sulfonate group ( $\text{O}_{\text{SO}_3}$ ), respectively. With increasing surface sensitivity, a distinct decrease in  $\text{O}_{\text{SO}_3}$  signal intensity and only a slight decrease in Cl 2p signal intensity is observed, suggesting that chlorine lies closer to the outer surface than the sulfonate group.

After heating the binary mixture to 100 °C for 6 h (see right half of Figure 5), an almost complete transformation of  $\text{Cl}_{\text{cov}}$  to  $\text{Cl}_{\text{ion}}$  (binding energy shift from 200.2 to 197.2 eV) is observed,

similar to the IL1 a/IL2 a mixture (see above). Again, the  $\text{Cl}_{\text{cov}}$  signal is ~9% of its original intensity, suggesting that 18% of  $[\text{ClC}_4\text{H}_8\text{SO}_3]^-$  is converted to the 4-chlorobutylsulfonate ester (see Scheme 2b) whereas 82% are subject to the alkylation or the sultone formation. Moreover, an absolute decrease (58%) in overall Cl intensity is observed, which is more pronounced than seen for the IL1 a/IL2 a mixture. Concomitantly to the Cl 2p signal, the  $\text{O}_{\text{SO}_3}$  signal of the IL1 b/IL2 b mixture also exhibits an absolute loss in intensity to 38% of its former value (note that both intensity losses are more pronounced at 80°). In addition to sultone formation (which leads to a decrease in the  $\text{SO}_3^-$  signals similar to the IL1 a/IL2 a mixture), we show in the following that precipitation of the zwitterionic product as solid chloride salt (and its removal from the near-surface region) also plays a major role. Note that an ex situ reaction of a large amount of the IL1 b/IL2 b mixture leads to a white precipitate covered by a transparent liquid. The latter consist mainly of  $[\text{C}_8\text{C}_1\text{Im}][\text{Tf}_2\text{N}]$  as solvent, proven by XPS. The reason why the reaction product precipitates in case of the IL1 b/IL2 b mixture and not in case of IL1 a/IL2 a is likely to be related to the presence of the accompanying  $[\text{C}_8\text{C}_1\text{Im}]^+$  and  $[\text{Tf}_2\text{N}]^-$  ions in IL1 b/IL2 b, which are less polar than  $[\text{C}_2\text{C}_1\text{Im}]^+$  and  $[\text{TfO}]^-$  in IL1 a/IL2 a.<sup>[20]</sup>

Due to the precipitation of the reaction product, the composition changes during the reaction, and, after heating, mainly  $[\text{C}_8\text{C}_1\text{Im}]^+$  cations and  $[\text{Tf}_2\text{N}]^-$  anions are detected. The increase in  $[\text{Tf}_2\text{N}]^-$  intensity is obvious from the increase in the signals of F 1s, O 1s ( $\text{O}_{\text{Tf}_2\text{N}}$  at 532.6 eV), S 2p (168.9 eV, not shown), and C 1s ( $\text{C}_{\text{Tf}_2\text{N}}$  at 292.8 eV) at 0° emission upon heating (compare left and right side of Figure 5). For the C 1s and N 1s intensities of the  $[\text{C}_8\text{C}_1\text{Im}]^+$  cation the interpretation is not as straightforward, since the signals of educts and products are superimposed. In the C 1s spectra before and after heating, the  $\text{C}_{\text{hetero}}$  peak at 286.4 eV is attributed to carbon atoms with neighboring hetero atoms (nitrogen, sulfur, chlorine), whereas the  $\text{C}_{\text{alkyl}}$  peak at 284.9 eV is assigned to carbon atoms bound solely to carbon and hydrogen. As both  $\text{C}_{\text{hetero}}$  and  $\text{C}_{\text{alkyl}}$  are part of the  $[\text{C}_8\text{C}_1\text{Im}]^+$  cation, but also of the reaction product, the expected increase in the  $[\text{C}_8\text{C}_1\text{Im}]^+$  signals in the 0° spectra after heating is compensated (for  $\text{C}_{\text{alkyl}}$ ) or overcompensated (for  $\text{C}_{\text{hetero}}$ ) by a loss of the corresponding signals of the reaction product due to precipitation.

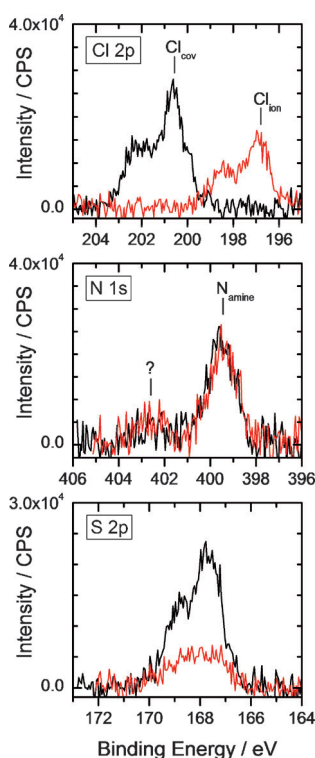
The same explanation is valid for the N 1s region, where virtually no changes are observed at 0° upon heating, in contrast to our first expectations. Before the reaction, the signal of the amine is superimposed by the  $[\text{Tf}_2\text{N}]^-$  signal at 399.3 eV. Upon heating, the neutral amine group is transformed into a positively charged ammonium, which exhibits a higher binding energy close to that of an imidazolium nitrogen at 401.9 eV (Section 2.5., IL1 a/IL2 a mixture). Therefore, the expected increases in the  $\text{N}_{\text{imid}} + \text{N}_{\text{ammon}}$  signals and decreases in the  $\text{N}_{\text{amine}} + \text{N}_{\text{Tf}_2\text{N}}$  signals during the reaction are obscured by the precipitation of the zwitterionic chloride salt (which leads to a loss of  $\text{N}_{\text{imid}}$  and  $\text{N}_{\text{ammon}}$  in XPS) and by the enrichment of  $[\text{Tf}_2\text{N}]^-$  anions, respectively.

## 2.7. Mixture c—IL1c/IL2c

$[(\text{Me}_2\text{NC}_3\text{H}_6)\text{PBu}_3][\text{FAP}]/[\text{PBu}_4][\text{ClC}_4\text{H}_8\text{SO}_3]$

To avoid the superimposition of N 1s signals of different species and to enable an unambiguous monitoring of the alkylation, the imidazolium head groups were exchanged in the IL1c/IL2c mixture by phosphonium, and as counterion for the amine-functionalized IL1c, the nitrogen-free [FAP]<sup>−</sup> anion was used.

Despite the instabilities of both phosphonium ILs at the chosen reaction conditions (Figure 2), the binary IL1c/IL2c mixture was tested for the alkylation reaction by in situ XPS. The corresponding 0° emission XP spectra of the N 1s, Cl 2p, and S 2p regions are depicted in Figure 6, before (black) and



**Figure 6.** Cl 2p, N 1s, and S 2p spectra of the binary IL1c/IL2c mixture in 0° emission before (black; taken at room temperature) and after (red; taken at 100 °C) heating the mixture to 100 °C for 1.5 h.

after (red) heating to 100 °C for 1.5 h. 80° emission spectra cannot be used as a statement about surface enrichment or orientation effects because of the presence of surface-active contaminations in IL2c. As can be seen from the Cl 2p region, covalent chlorine was converted completely to chloride upon heating (binding energy shift from 200.6 eV to 196.9 eV), indicating alkylation and/or sultone formation. The absence of Cl<sub>cov</sub> signals rules out the formation of dimerized esters according to Scheme 2b as a significant reaction pathway. In the N 1s region, two signals are visible already from the very beginning, although only the amine nitrogen peak at 399.5 eV should be present in the mixture (Figure 1). The second peak at 402.3 eV has already been observed after heating the primary IL1c to

100 °C (N 1s region in Figure 2), and reflects the thermal decomposition of the cation to an ammonium species without a present electrophile. We propose that similar decomposition reactions start right after mixing IL1c with IL2c at room temperature at a non-negligible rate. Upon heating the binary mixture for 1.5 h, no further changes are observed in the N 1s region. Thus, neither thermal decomposition nor alkylation reactions take place during this heating time. We do not have an explanation for the enhanced thermal stability of the IL1c in the mixture yet. The decrease in Cl<sub>cov</sub> and SO<sub>3</sub><sup>−</sup>-signals while the N<sub>amine</sub> intensity remains virtually unchanged indicates that the dominant reaction is the ring closing of [ClC<sub>4</sub>H<sub>8</sub>SO<sub>3</sub>]<sup>−</sup>, forming volatile 1,4-butane sultone, whereas alkylation is at least one order of magnitude slower in this mixture. Note that the pressure increase for this mixture during heating was at least ten times higher than for the first two mixtures, which is in line with the enhanced formation of volatile sultone. Possibly, the attack of the electrophile (i.e. the electron-deficient carbon bound to chlorine in IL2c) on the amine group is sterically hindered by the neighboring butyl chains of the phosphonium cation.

## 3. Conclusions

We demonstrated that XPS is an efficient tool to monitor organic liquid-phase reactions. It enables the simultaneous observation of changes for all elements (except hydrogen) in a quantitative and chemical-state sensitive manner. In order to lower the volatility of the reagents, the reacting groups were covalently linked to ionic head groups of the cation or anion of ILs. Herein, we concentrated on the alkylation of a dimethylpropylamine substituent attached to a cationic head group by the anion [ClC<sub>4</sub>H<sub>8</sub>SO<sub>3</sub>]<sup>−</sup>. In the course of this reaction, the covalent chlorine was expected to be substituted by the amine group at elevated temperature, resulting in an ammonium group and a chloride counter-ion. These changes in the electronic state induce distinct binding energy shifts in the N 1s and Cl 2p spectra which, along with the changes of all other core-level signals, allow for the identification of the targeted reaction as well as unintended side reactions.

The present study follows and expands a recent short communication, which focused on the binary mixture  $[(\text{Me}_2\text{NC}_3\text{H}_6)\text{C}_1\text{Im}][\text{TfO}]/[\text{C}_2\text{C}_1\text{Im}][\text{ClC}_4\text{H}_8\text{SO}_3]$ .<sup>[11]</sup> Altogether, three different IL mixtures were investigated. In all cases the dimethylpropylamine substituent was attached to the cation of IL1 and 4-chlorobutylsulfonate salts represented IL2. To rule out any slow reactions at room temperature, all binary 1:1 mixtures were freshly mixed immediately before the measurements, and then heated to 100 °C to trigger the reaction.

For  $[(\text{Me}_2\text{NC}_3\text{H}_6)\text{C}_1\text{Im}][\text{TfO}]/[\text{C}_2\text{C}_1\text{Im}][\text{ClC}_4\text{H}_8\text{SO}_3]$ , denoted as (IL1a/IL2a), alkylation was observed indeed. In addition, two parallel reactions took place. From a decrease in O 1s and S 2p intensity upon heating, the formation of 1,4-butane sultone as a concurrent reaction was deduced. This sultone formation was also seen in the primary ILs [C<sub>2</sub>C<sub>1</sub>Im][ClC<sub>4</sub>H<sub>8</sub>SO<sub>3</sub>] (IL2a), [C<sub>8</sub>C<sub>1</sub>Im][ClC<sub>4</sub>H<sub>8</sub>SO<sub>3</sub>] (IL2b), and [PBu<sub>4</sub>][ClC<sub>4</sub>H<sub>8</sub>SO<sub>3</sub>] (IL2c) at elevated temperatures, and was ascribed to an intramolecular

ring-closing reaction of  $[\text{ClC}_4\text{H}_8\text{SO}_3]^-$ . The second concurrent reaction was the formation of an anionic sulfonate ester by dimerization of  $[\text{ClC}_4\text{H}_8\text{SO}_3]^-$ . Quantification of the three parallel reactions showed that ~56% of  $[\text{ClC}_4\text{H}_8\text{SO}_3]^-$  reacted within the desired alkylation process, ~26% were converted into 1,4-butane sultone, and the residual ~18% formed the sulfonate ester.

The analysis of reaction of the binary mixture  $[(\text{Me}_2\text{NC}_3\text{H}_6)\text{C}_1\text{Im}][\text{Tf}_2\text{N}]/[\text{C}_8\text{C}_1\text{Im}][\text{ClC}_4\text{H}_8\text{SO}_3]$  (**IL1 b/IL2 b**) was more challenging due to the superimposition of the N 1s signal of the  $[\text{Tf}_2\text{N}]^-$  anion. This fact hampered the unequivocal analysis of the conversion of amine to ammonium upon heating in the N 1s spectra. Upon heating, the formation of the zwitterionic alkylation product as precipitating chloride salt was observed by visual inspection and by reduced XPS intensities of the precipitate related core levels. The alkylation was again accompanied by the same two side reactions, namely sultone formation and sulfonate ester formation.

To completely avoid the superimposition of the N 1s signals of different species and therefore to enable an unambiguous monitoring of the alkylation in the binary mixture, the imidazolium head groups were exchanged by phosphonium, and as counterion for the amine-functionalized **IL1 c**, the nitrogen-free  $[\text{FAP}]^-$  anion was used. The corresponding binary mixture was  $[(\text{Me}_2\text{NC}_3\text{H}_6)\text{PBu}_3][\text{FAP}]/[\text{PBu}_4][\text{ClC}_4\text{H}_8\text{SO}_3]$  (**IL1 c/IL2 c**). For this mixture, however, the alkylation process was not observed, most likely due to steric hindrance. As there was also no indication for ester formation, a complete conversion of  $[\text{ClC}_4\text{H}_8\text{SO}_3]^-$  into 1,4-butane sultone occurred as the only reaction channel.

The detailed analysis of the ARXPS measurements of the primary ILs and the binary IL mixtures provide additional information about the orientation and/or enrichment of ions at the surface. Regarding the anions, the chlorine of  $[\text{ClC}_4\text{H}_8\text{SO}_3]^-$  pointed towards the vacuum at the surface, while the sulfonate group pointed bulkwards. This orientation was maintained in the binary mixtures. In addition,  $[\text{ClC}_4\text{H}_8\text{SO}_3]^-$  as well as formed chloride were depleted, while  $[\text{TfO}]^-$  or  $[\text{Tf}_2\text{N}]^-$  were enriched at the surface. For the functionalized cations,  $[(\text{Me}_2\text{NC}_3\text{H}_6)\text{PBu}_3]^+$  displayed an isotropic behavior, while  $[(\text{Me}_2\text{NC}_3\text{H}_6)\text{C}_1\text{Im}]^+$  showed a preferential orientation, with the amine-functionalized chain pointing towards the vacuum at the surface. In the binary **IL1 a/IL2 a** mixture, the  $[(\text{Me}_2\text{NC}_3\text{H}_6)\text{C}_1\text{Im}]^+$  cation is enriched at the surface at the expense of  $[\text{C}_2\text{C}_1\text{Im}]^+$ , while in the **IL1 b/IL2 b** mixture, a homogeneous distribution of  $[(\text{Me}_2\text{NC}_3\text{H}_6)\text{C}_1\text{Im}]^+$  and  $[\text{C}_8\text{C}_1\text{Im}]^+$  was found.

After demonstrating the principal feasibility of using XPS to monitor organic liquid-phase reactions, even in the presence of concurrent processes, one can now envisage to perform detailed studies of the here presented and other reactions, in order to derive atom-specific, electronic-state-specific and surface-selective information, including kinetic parameters, such as activation energies and prefactors. For that purpose one has to follow the evolution of the reaction with time *in situ* by isothermal angle resolved XPS measurements of one or more relevant core levels.<sup>[21]</sup> This requires short data collection times,

which can be reduced either by concentrating on one core level or by using high-intensity synchrotron radiation.<sup>[21]</sup>

## Experimental Section

### Synthesis

All reagents were commercial and used as received. NMR spectra were recorded on a JEOL ECX 400 MHz spectrometer at 25 °C. The ionic liquids used in the present study were synthesized as follows:

**1-Methyl-3-(3'-dimethylaminopropyl)imidazolium trifluoromethylsulfonate IL1 a:** Tetrabutylammonium trifluoromethanesulfonate (20.53 g, 0.05 mol) was added to a solution of **IL1 b** (25.23 g, 0.05 mol) in methylene chloride (150 mL). The solution was stirred until it became homogeneous and then extracted with distilled water (100 mL). The aqueous extract was evaporated leaving 15.21 g (96% yield) of a colorless viscous liquid.  $^1\text{H}$  NMR ( $[\text{D}_6]\text{DMSO}$ ):  $\delta$  = 1.9 (quint,  $J$  = 7 Hz, 2,  $\text{CH}_2$ ); 2.2 (s, 6,  $\text{NCH}_3$ ); 3.3 (broad s, 2,  $\text{NCH}_2$ ); 3.8 (s, 3,  $\text{NCH}_3$ ); 4.4 (t,  $J$  = 7 Hz, 2,  $\text{NCH}_2$ ); 7.6 (s, 1, CH); 7.7 (s, 1, CH); 9.0 ppm (s, 1, CH).  $^{13}\text{C}$ - $\{^1\text{H}\}$ :  $\delta$  = 137.2; 124.0; 122.8; 121.2 (q,  $J_{\text{C-F}}$  = 21 Hz;  $\text{CF}_3$ ); 56.4; 47.4; 45.2; 36.2; 27.4 ppm.

**1-Methyl-3-(3'-dimethylaminopropyl)imidazolium bis[(trifluoromethyl)sulfonyl]imide IL1 b:** A solution of 3-chloropropyldimethylammonium chloride (15.83 g, 0.10 mol) and methylimidazole (21.6 g, 0.26 mol, 2.6 eq) in 50 mL distilled water was refluxed for 48 h. The resulting solution was decolorized with active charcoal, filtered and the solvent was evaporated by means of a rotary evaporator. The white residue was washed with acetonitrile (3 × 25 mL) and diethyl ether (3 × 25 mL). The resulting solid was dissolved in distilled water and LiOH (4.2 g) and  $\text{Li}[\text{Tf}_2\text{N}]$  (29.5 g) were added. The mixture was vigorously stirred for 1 h and then extracted with methylene chloride (50 mL). The organic phase was washed with distilled water until the washings were negative to the  $\text{AgNO}_3$  test for chloride. The solvent was evaporated by means of a rotary evaporator, yielding 25.23 g (53%, based on 3-chloropropyldimethylammonium hydrochloride) of a colorless liquid.  $^1\text{H}$  NMR ( $[\text{D}_6]\text{DMSO}$ ):  $\delta$  = 1.9 (quint,  $J$  = 7 Hz, 2,  $\text{CH}_2$ ); 2.1 (s, 6,  $\text{NCH}_3$ ); 3.3 (broad s, 2,  $\text{NCH}_2$ ); 3.8 (s, 3,  $\text{NCH}_3$ ); 4.2 (t,  $J$  = 7 Hz, 2,  $\text{NCH}_2$ ); 7.6 (s, 1, CH); 7.7 (s, 1, CH); 9.0 ppm (s, 1, CH).  $^{13}\text{C}$ - $\{^1\text{H}\}$ :  $\delta$  = 137.3; 124.0; 122.8; 120.0 (q,  $J_{\text{C-F}}$  = 321 Hz;  $\text{CF}_3$ ); 55.6; 47.5; 45.3; 36.2; 27.7 ppm.

**(3'-Dimethylaminopropyl)tributylphosphonium tris(pentafluoroethyl)-trifluorophosphate IL1 c:** A solution of 3-chloropropyldimethylammonium chloride (6.02 g, 0.04 mol) and tributylphosphine (9.92 g, 0.05 mol, 1.3 eq) in 100 mL dry isopropanol was refluxed under argon. The reaction was monitored by means of  $^{31}\text{P}$  NMR. When the reaction was complete, the resulting solution was cooled and the solvent was evaporated by means of a rotary evaporator. The white, waxy residue was washed with acetonitrile (3 × 25 mL) and diethyl ether (3 × 25 mL). The resulting solid was dissolved in distilled water (150 mL) and KOH (2.82 g) and potassium tris(pentafluoroethyl)-trifluorophosphate (21.00 g) were added. The mixture was vigorously stirred for 1 h and then extracted with methylene chloride (50 mL). The organic phase was washed with distilled water until the washings were negative to the  $\text{AgNO}_3$  test for chloride. The solvent was evaporated by means of a rotary evaporator, yielding 26.03 g (87%, based on 3-chloropropyldimethylammonium chloride) of a colorless viscous liquid.  $^1\text{H}$  NMR ( $[\text{D}_6]\text{DMSO}$ ):  $\delta$  = 0.9 (t,  $J$  = 7 Hz, 9,  $\text{CH}_3$ ); 1.4 (broad mult, 12,  $\text{CH}_2$ ); 1.6 (broad mult, 2,  $\text{CH}_2$ ); 2.1 (s, 6,  $\text{NCH}_3$ ); 2.2 (broad mult, 6,  $\text{CH}_2$ ); 2.3 ppm (t,  $J$  = 7 Hz, 2,  $\text{NCH}_2$ ).  $^{13}\text{C}$ - $\{^1\text{H}\}$ :  $\delta$  = 120.5 (qmult,  $J_{\text{CF}}$  = 284 Hz); 59.2 (d,  $J_{\text{CP}}$  =



15 Hz); 45.2; 23.8 (d,  $J_{CP}$  = 16 Hz); 23.1 (d,  $J_{CP}$  = 4 Hz); 19.3 (d,  $J_{CP}$  = 3 Hz); 18.3 (d,  $J_{CP}$  = 48 Hz); 16.0 (d,  $J_{CP}$  = 50 Hz), 13.4 ppm.  $^{19}\text{F}$ :  $\delta$  = -44.2 (dmult,  $J_{PF}$  = 902 Hz); -79.6 (mult,  $J_{PF}$  = 8 Hz); -81.2; -87.4 (dmult,  $J_{PF}$  = 902 Hz); -115.5 (dmult,  $J_{PF}$  = 81 Hz); -116.1 ppm (dmult,  $J_{PF}$  = 91 Hz).  $^{31}\text{P}$ -{ $^1\text{H}$ }:  $\delta$  = 34.8; -147.5 ppm (dmult,  $J_{PF}$  = 820 Hz).

**1-Ethyl-3-methylimidazolium 4-chlorobutylsulfonate IL2a:** A solution of 1,4-butane sultone (11.3657 g, 83.6 mmol, 1.2 eq) and 1-ethyl-3-methylimidazolium chloride (9.7061 g, 71.1 mmol) in 50 mL acetonitrile was refluxed for 12 h under argon atmosphere. The solvent was evaporated by means of a rotary evaporator. The oily residue was taken up in water (100 mL) and the solution washed with diethyl ether (3×50 mL). The aqueous phase was evaporated, yielding 19.1821 g (98%) of a pale yellow viscous liquid.  $^1\text{H}$  NMR ( $[\text{D}_6]\text{DMSO}$ ):  $\delta$  = 1.4 (t,  $J$  = 7 Hz, 3,  $\text{CH}_3$ ); 1.7 (mult, 4,  $\text{CH}_2\text{CH}_2$ ); 2.4 (t,  $J$  = 8 Hz, 2,  $\text{CH}_2\text{SO}_3$ ); 3.6 (t,  $J$  = 6 Hz, 2,  $\text{ClCH}_2$ ); 3.8 (s, 3,  $\text{CH}_3$ ); 4.2 (t,  $J$  = 7 Hz, 2,  $\text{NCH}_2$ ); 7.6 (t,  $J$  = 2 Hz, 1, CH); 7.7 (t,  $J$  = 2 Hz, 1, CH); 9.0 ppm (s, 1, CH).  $^{13}\text{C}$ -{ $^1\text{H}$ }:  $\delta$  = 137.0; 124.0; 122.5; 51.1; 45.9; 44.6; 36.1; 31.8; 23.0; 15.7 ppm.

**1-Methyl-3-octylimidazolium 4-chlorobutylsulfonate IL2b:** A solution of 1,4-butane sultone (2.97 g, 22 mmol, 1.1 eq) and 1-methyl-3-octylimidazolium chloride (4.575 g, 20 mmol) in 50 mL acetonitrile was refluxed for 12 h under argon atmosphere. The solvent was evaporated by means of a rotary evaporator. The oily residue was taken up in water (100 mL) and the solution washed with diethyl ether (3×50 mL). The aqueous phase was evaporated, yielding 7.18 g (98%) of a pale yellow liquid.  $^1\text{H}$  NMR ( $[\text{D}_6]\text{DMSO}$ ):  $\delta$  = 0.8 (t,  $J$  = 7 Hz, 3,  $\text{CH}_3$ ); 1.2 (mult, 12,  $\text{CH}_2\text{CH}_2$ ); 1.7 (mult, 6,  $\text{CH}_2\text{CH}_2$ ); 2.4 (t,  $J$  = 8 Hz, 2,  $\text{CH}_2\text{SO}_3$ ); 3.6 (t,  $J$  = 6 Hz, 2,  $\text{ClCH}_2$ ); 3.8 (s, 3,  $\text{CH}_3$ ); 4.1 (t,  $J$  = 7 Hz, 2,  $\text{NCH}_2$ ); 7.6 (t,  $J$  = 2 Hz, 1, CH); 7.8 (t,  $J$  = 2 Hz, 1, CH); 9.2 ppm (s, 1, CH).  $^{13}\text{C}$ -{ $^1\text{H}$ }:  $\delta$  = 137.2; 124.1; 122.8; 51.1; 49.2; 45.9; 36.2; 31.9; 31.7; 30.0; 29.1; 28.9; 26.1; 23.2; 22.6; 14.5 ppm.

**Tetrabutylphosphonium 4-chlorobutylsulfonate IL2c:** A solution of 1,4-butanedisulfone (4.79 g, 36 mmol, 1.05 eq) and tetrabutylphosphonium chloride (9.87 g, 34 mmol) in 50 mL acetonitrile was refluxed for 12 h under argon atmosphere. The solvent was evaporated by means of a rotary evaporator. The oily residue was taken up in water (100 mL) and the solution washed with diethyl ether (3×50 mL). The aqueous phase was evaporated, yielding 13.78 g (94%) of a viscous colorless liquid.  $^1\text{H}$  NMR ( $\text{D}_2\text{O}$ ):  $\delta$  = 0.9 (t,  $J$  = 7 Hz, 12,  $\text{CH}_3$ ); 1.4 (mult, 18,  $\text{CH}_2\text{CH}_2$ ); 1.8 (mult, 4,  $\text{CH}_2\text{CH}_2$ ); 2.1 (mult, 6,  $\text{CH}_2\text{CH}_2$ ); 2.8 (t,  $J$  = 7 Hz, 2,  $\text{CH}_2\text{SO}_3$ ); 3.6 ppm (t,  $J$  = 6 Hz, 2,  $\text{ClCH}_2$ ).  $^{13}\text{C}$ -{ $^1\text{H}$ }:  $\delta$  = 50.5; 45.4; 31.2; 23.5 (d,  $J_{CP}$  = 15 Hz); 23.0; 22.1 ppm (d,  $J_{CP}$  = 48 Hz).  $^{31}\text{P}$ -{ $^1\text{H}$ }:  $\delta$  = 33.9 ppm.

## ARXPS

The ARXP spectra of **IL1a**, **IL1c**, **IL2a**, **IL2c**, and their respective binary mixtures were measured with the SPECS XR 50 X-ray source using non-monochromatized  $\text{Al K}_{\alpha}$  radiation ( $h\nu$  = 1486.6 eV) at a power of 250 W ( $U$  = 12.5 kV,  $I$  = 20 mA) and a VG Scienta R3000 electron analyzer. **IL1b**, **IL2b**, and the binary **IL1b/IL2b** mixture were measured with the same analyzer but as X-ray source the X-ray gun of the VG ESCALAB 200 was utilized. Hereby, a non-monochromatized  $\text{Al K}_{\alpha}$  radiation was used at a power of 150 W ( $U$  = 15 kV,  $I$  = 10 mA) but with a smaller distance to the sample resulting in an intensity decrease of 9%, in comparison to the SPECS XR 50 X-ray source. During X-ray irradiation ILs have been shown to charge; therefore, binding energies were referenced to the N 1s signal of the imidazolium nitrogen at 401.9 eV for **IL1a**, **IL1b**, **IL2a**, **IL2b** and their respective binary mixtures, and to the

P 2p signal of the phosphonium cation at 132.9 eV for **IL1c**, **IL2c** and their binary mixture. Core-level spectra were recorded with a pass energy of 100 eV, resulting in an overall resolution of ~0.9 eV. Because of the inelastic mean free path of about 3 nm of photoelectrons in organic compounds<sup>[22]</sup> at the kinetic energies used (~800–1300 eV), measurements at 0° emission with respect to the surface normal average over several layers of the near-surface region (information depth,  $\text{ID}$  = 7–9 nm, depending on the kinetic energy), while measurements at 80° emission only probe the top-most layers ( $\text{ID}$  = 1–1.5 nm). All spectra recorded at 80° were multiplied by an empirical factor to allow for direct visual comparison with the 0° spectra (for details, see ref. [16]).

The XP spectra were analyzed using the CasaXPS software (version 2.3.16Dev6). For the majority of the spectra a two-point linear background subtraction was applied. Only for the C 1s spectra of perfluoroalkyl-containing systems a three-point linear background subtraction was used. All peaks were fitted using a Gaussian–Lorentz profile with 30% Lorentz contribution. Using the areas under the fitted peaks and taking into account the sensitivity factors for the different elements, quantitative information was obtained on the stoichiometry of the near-surface region analyzed. The atomic sensitivity factors (ASFs) used, were calibrated for our specific experimental setup by the process reported by Kolbeck et al.<sup>[15]</sup> By this procedure,  $\pm 5\%$  accuracy for atomic concentration values given in the text was reached.

The thin IL (mixture) films were prepared by deposition of the corresponding IL (mixture) onto a planar Au foil (20 mm×15 mm×0.1 mm). These samples were then introduced into the UHV system through a loadlock. To ensure a good mixing of both target-specific ILs the 1:1 mixtures were prepared in acetonitrile. With a time delay of ~10 min the mixtures were introduced into the UHV chamber where the acetonitrile vaporized.

The in situ heating of the ILs (mixtures) was done by heating from the backside of the samples. A thermocouple attached near the sample resulted in a temperature reading with an error of  $\pm 5^\circ\text{C}$ .

## ESI-MS

ESI-MS data were obtained with a Bruker Esquire 6000 operated in positive mode using methanol as solvent.

## Acknowledgements

This work has been supported by the DFG through SPP 1191, grants STE 620/7-2 and WA 1615/8-2 and by the Excellence Cluster "Engineering of Advanced Materials" granted to the University of Erlangen-Nuremberg. C.K. acknowledges also support by the Max-Buchner-Stiftung.

**Keywords:** reaction monitoring • surface science • ionic liquids • X-ray photoelectron spectroscopy • zwitterions

- [1] B. Winter, *Nucl. Instrum. Methods Phys. Res. Sect. A* **2009**, 601, 139.
- [2] P. Wasserscheid, T. Welton, *Ionic Liquids in Synthesis*, 2nd ed., Wiley-VCH, Weinheim, **2008**.
- [3] K. R. J. Lovelock, I. J. Villar-Garcia, F. Maier, H. P. Steinrück, P. Licence, *Chem. Rev.* **2010**, 110, 5158.
- [4] H.-P. Steinrück, *Surf. Sci.* **2010**, 604, 481.
- [5] K. R. J. Lovelock, E. F. Smith, A. Deyko, I. J. Villar-Garcia, P. Licence, R. G. Jones, *Chem. Commun.* **2007**, 4866.

- [6] F. L. Qiu, A. W. Taylor, S. Men, I. J. Villar-Garcia, P. Licence, *Phys. Chem. Chem. Phys.* **2010**, *12*, 1982.
- [7] A. W. Taylor, F. L. Qiu, I. J. Villar-Garcia, P. Licence, *Chem. Commun.* **2009**, 5817.
- [8] R. G. Compton, R. Wibowo, L. Aldous, R. M. J. Jacobs, N. S. A. Manan, *Chem. Phys. Lett.* **2011**, *509*, 72.
- [9] R. Kötz, D. Weingarth, A. Foelske-Schmitz, A. Wokaun, *Electrochem. Commun.* **2011**, *13*, 619.
- [10] M. Sobota, M. Schmid, M. Happel, M. Amende, F. Maier, H. P. Steinrück, N. Paape, P. Wasserscheid, M. Laurin, J. M. Gottfried, J. Libuda, *Phys. Chem. Chem. Phys.* **2010**, *12*, 10610.
- [11] C. Kolbeck, I. Niedermaier, N. Taccardi, P. S. Schulz, F. Maier, P. Wasserscheid, H. P. Steinrück, *Angew. Chem. Int. Ed.*, DOI: 10.1002/anie.201107402.
- [12] M. P. Seah, W. A. Dench, *Surf. Interface Anal.* **1979**, *1*, 2.
- [13] F. Maier, T. Cremer, C. Kolbeck, K. R. J. Lovelock, N. Paape, P. S. Schulz, P. Wasserscheid, H.-P. Steinrück, *Phys. Chem. Chem. Phys.* **2010**, *12*, 1905.
- [14] J. M. Gottfried, F. Maier, J. Rossa, D. Gerhard, P. S. Schulz, P. Wasserscheid, H. P. Steinrück, *Z. Phys. Chem. (Muenchen Ger.)* **2006**, *220*, 1439.
- [15] C. Kolbeck, M. Killian, F. Maier, N. Paape, P. Wasserscheid, H. P. Steinrück, *Langmuir* **2008**, *24*, 9500.
- [16] K. R. J. Lovelock, C. Kolbeck, T. Cremer, N. Paape, P. S. Schulz, P. Wasserscheid, F. Maier, H. P. Steinrück, *J. Phys. Chem. B* **2009**, *113*, 2854.
- [17] C. Kolbeck, T. Cremer, K. R. J. Lovelock, N. Paape, P. S. Schulz, P. Wasserscheid, F. Maier, H.-P. Steinrück, *J. Phys. Chem. B* **2009**, *113*, 8682.
- [18] N. Paape, W. Wei, A. Bosmann, C. Kolbeck, F. Maier, H. P. Steinrück, P. Wasserscheid, P. S. Schulz, *Chem. Commun.* **2008**, *33*, 3867.
- [19] C. Kolbeck, J. Lehmann, K. R. J. Lovelock, T. Cremer, N. Paape, P. Wasserscheid, A. P. Fröba, F. Maier, H.-P. Steinrück, *J. Phys. Chem. B* **2010**, *114*, 17025.
- [20] R. Lungwitz, V. Strehmel, S. Spange, *New J. Chem.* **2010**, *34*, 1135.
- [21] R. Streber, C. Papp, M. P. A. Lorenz, A. Bayer, R. Denecke, H. P. Steinrück, *Angew. Chem.* **2009**, *121*, 9925; *Angew. Chem. Int. Ed.* **2009**, *48*, 9743.
- [22] R. F. Roberts, D. L. Allara, C. A. Pryde, D. N. E. Buchanan, N. D. Hobbins, *Surf. Interface Anal.* **1980**, *2*, 5.

Received: December 5, 2011

Published online on March 1, 2012

# Synthesis and Aggregation Properties of Polycationic Perylenetetracarboxylic Acid Diimides

Jörg Schönambsgruber,<sup>[a]</sup> Boris Schade,<sup>[b]</sup> Rolf Kirschbaum,<sup>[c]</sup> Jing Li,<sup>[c]</sup> Walter Bauer,<sup>[a]</sup>
  
 Christoph Böttcher,<sup>[b]</sup> Thomas Drewello,<sup>[c]</sup> and Andreas Hirsch\*<sup>[a]</sup>

**Keywords:** Dendrimers / Amphiphiles / Micelles / Aggregation /  $\pi$  interactions

The synthesis and structural characterization of a first family of dendronized polycationic perylenetetracarboxylic acid diimides (PDIs) **7**, **8**, and **10** is reported. They were obtained by amide coupling reactions of pyridinium salt head groups with terminal carboxylic groups of Newkome-dendron-type functionalized PDIs. Resulting pyridinium-terminated PDIs **7**, **8**, and **10** are highly water-soluble, independent of the pH value. This is due to 6, 18, and 9 permanent positive charges, respectively. PDIs **7** containing the smaller first-generation

dendrons exhibit a pronounced aggregation behavior in water. This was studied by absorption and fluorescence spectroscopy, by pulsed-gradient spin-echo (PGSE, DOSY) NMR measurements, and by cryo-transmission electron microscopy (cryo-TEM). The counterparts containing the bulkier second-generation dendrons hamper aggregation, and as a consequence intermolecular  $\pi$ - $\pi$  stacking interactions between the perylene cores is suppressed.

## Introduction

In recent years, perylene-3,4,9,10-tetracarboxylic acid diimides (peryene diimides, PDIs) have received considerable interest as a versatile family of dye molecules that can easily be functionalized both at the bay and imide positions (Figure 1). This development was pioneered to a large extend by Würthner and co-workers.<sup>[1]</sup> PDI derivatives have been investigated as organic field-effect transistors (OFET),<sup>[2,3]</sup> organic light-emitting diodes (OLED),<sup>[4]</sup> dyes, sensitizers in organic solar cells,<sup>[5]</sup> liquid crystals,<sup>[6]</sup> and in the context of supramolecular self-organization as amphiphilic building blocks.<sup>[7]</sup>

Upon chemical derivatization, PDIs can be adapted to specific functions.<sup>[4]</sup> For instance, the nature of the substituents in the imide positions can tune the solubility in various media. Furthermore, by altering the steric bulk of the substituents, the aggregation behavior based on  $\pi$ - $\pi$  stacking can be controlled or even suppressed. Optical and electronic

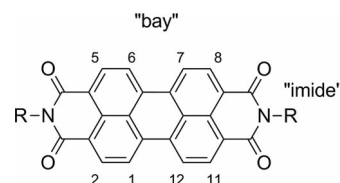


Figure 1. General structure of PDIs. Numbering and the “bay” and “imide” positions are marked.

properties are influenced only to a minor extend by the substituents located in the imide positions. In contrast, substituents in the 1, 6, 7, or 12 “bay” positions (Figure 1) cause a much more pronounced modification of the electronic properties due to twisting of the conjugated  $\pi$  system, and depending on the size of the bay substituents might even prevent aggregation via  $\pi$ - $\pi$  stacking. Recently, substituents in the so called “ortho-position” (2-,5-,8-,11-positions) have been introduced as well.<sup>[8]</sup>

Our group has recently started investigating highly water-soluble PDIs.<sup>[9]</sup> For this purpose, we have integrated Newkome-type polycarboxylate dendrons<sup>[10]</sup> of various generations in the imide position (Figure 2). Negatively charged carboxylates can be easily generated in buffer solution at pH 7.2, causing very pronounced water solubility. Aggregation through  $\pi$ - $\pi$  stacking can be observed with some of the compounds. These water-soluble PDIs were also used in our group for the solubilization and fractioning of single-walled carbon nanotubes (SWCNT) and the exfoliation of graphene.<sup>[11]</sup>

Here we report for the first time on the synthesis of water-soluble PDIs containing dendritic pyridinium substit-

[a] Department of Chemistry and Pharmacy, Friedrich-Alexander Universität Erlangen-Nürnberg, Institut für Organische Chemie, Henkestraße 42, 91054 Erlangen, Germany  
 Fax: +49-9131-8526864  
 E-mail: andreas.hirsch@chemie.uni-erlangen.de  
 Homepage: <http://www.chemie.uni-erlangen.de/hirsch/index.html>

[b] Research Center of Electron Microscopy, Institute for Chemistry and Biochemistry, Freie Universität Berlin, Fabeckstraße 36a, 14195 Berlin, Germany

[c] Department of Chemistry and Pharmacy, Friedrich-Alexander Universität Erlangen-Nürnberg, Institut für Physikalische Chemie, Egerlandstraße 3, 91058 Erlangen, Germany

Supporting information for this article is available on the WWW under <http://dx.doi.org/10.1002/ejoc.201201062>.

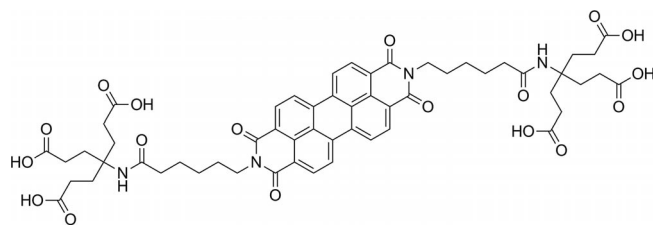
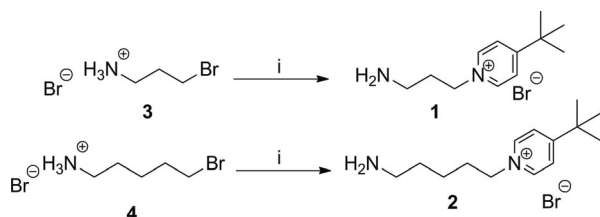


Figure 2. Example for PDI with polycarboxylate dendrons.

uents in the imide positions by introducing positive charges at the periphery of these architectures. In contrast to the corresponding anionic polycarboxylates that we developed previously the number of charges and the water solubility itself is independent of a buffered system.

## Results and Discussion

As a general building block for the oligopyridinium substituents in the target molecules, 1-(3-aminopropyl)-4-(*tert*-butyl)pyridinium bromide (**1**) and 1-(3-aminopentyl)-4-(*tert*-butyl)pyridinium bromide (**2**) were synthesized by solvent-free electrophilic substitution of 4-*tert*-butylpyridine with the corresponding  $\omega$ -bromoalkylamine hydrobromides **3** and **4** (Scheme 1). For the isolation of the free amines of **1** and **2**, final treatment with sodium hydroxide was required.



Scheme 1. Synthesis of cationic pyridinium building blocks **1** and **2**. Reagents and conditions: (i) 1. 4-*tert*-butylpyridine (2 equiv.), 100 °C, 3 h; 2. NaOH in H<sub>2</sub>O.

Bromides **1** and **2** are suitable building blocks for amide coupling reactions with carboxylic acids promoted by *N,N'*-dicyclohexylcarbodiimide (DCC) and hydroxybenzotriazole (HOBt) as coupling agents. Indeed, the amide coupling reactions allowed for the transformation of PDI polyacids<sup>[9a]</sup> into highly water-soluble PDIs **7** and **8** with 6 and 18 positive charges, respectively (Scheme 2). For the preparation of the four dumbbell-shaped perylene derivatives with 6 (for **7a** and **7b**) and 18 positive charges (for **8a** and **8b**), symmetrically substituted PDIs containing two first- (for **5**) or second-generation dendrons (for **6**) were converted with 4-(*tert*-butyl)-1-( $\omega$ -aminoalkyl)pyridinium compounds **1** or **2**, respectively. The carboxylic groups of the PDI polyacids were activated with DCC to form the HOBt esters. These activated species readily underwent reaction with prepared cationic amines **1** and **2**. As a result of the increased polarity and charge of the PDIs, the products could be purified by repeated precipitation.

In addition, amphiphilic PDI **9**, with a dodecyl chain as the apolar part of the molecule, was used to synthesize two asymmetric perylene derivatives **10** with 9 positive charges (Scheme 3).

The polycationic PDIs were investigated by mass spectrometry by using electrospray ionization in combination with a quadrupole ion trap (ESI-QIT). For PDIs **8a** and **8b**, only fragments of the dendrimer were observed, containing the pyridinium terminus. Their identity was confirmed by collision-induced dissociations in MS<sup>2</sup> experiments (MS<sup>2</sup>-CID). However, compounds **7a,b** and **10a,b** provided intact quasimolecular ions in the form of  $[M - nBr]^n+$  ions through loss of the bromide anions. Thus, the completion of the conversion of all carboxylic acid groups into the corresponding pyridinium termini was evidenced by the appearance of signals according to the ions  $[M - 2Br]^2+$ ,  $[M - 3Br]^3+$ ,  $[M - 4Br]^4+$ ,  $[M - 5Br]^5+$ , etc.<sup>[12]</sup> Furthermore, ions developed from an exchange of Br<sup>-</sup> to <sup>-</sup>OBt (out of reaction) were obtained.

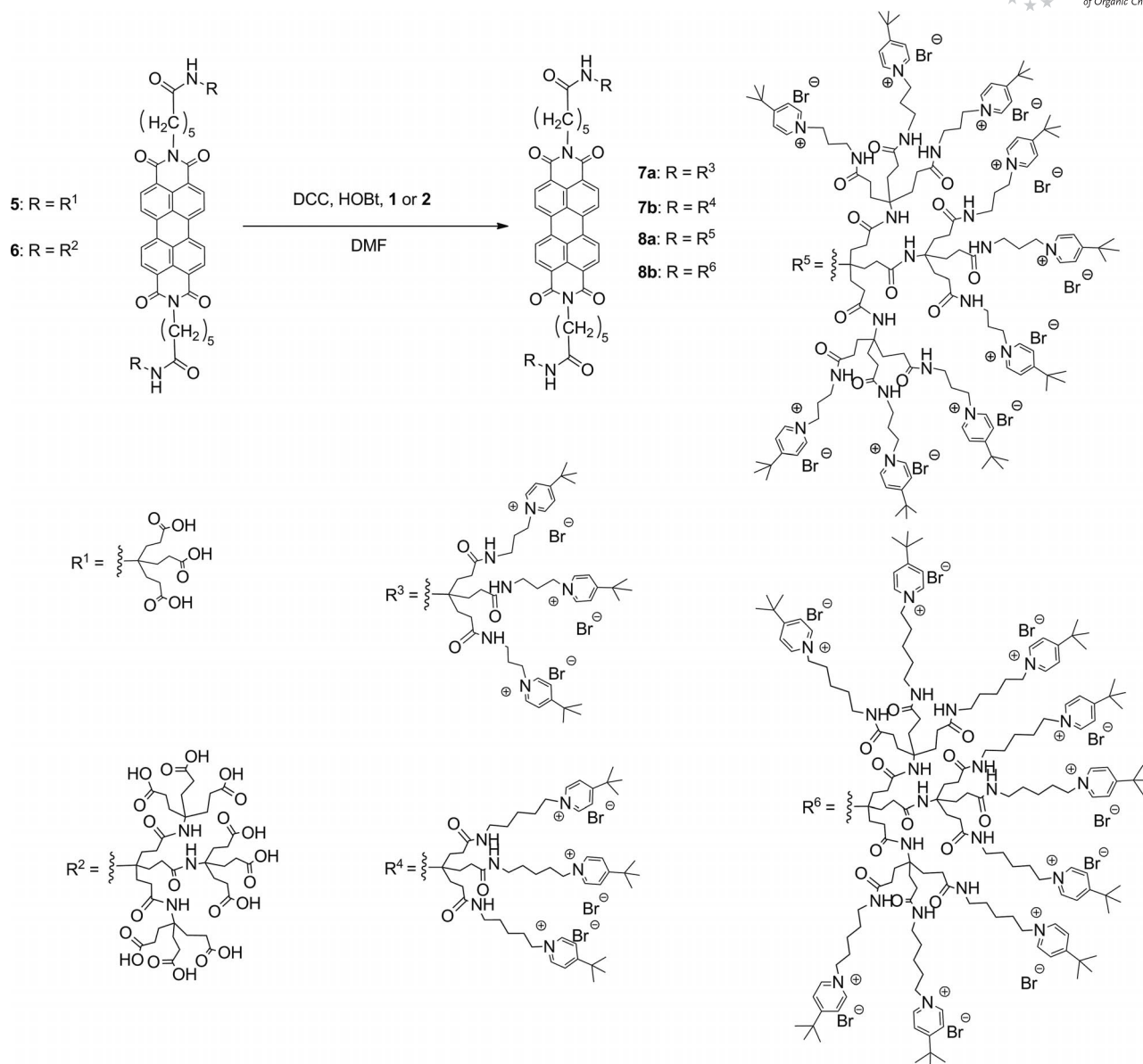
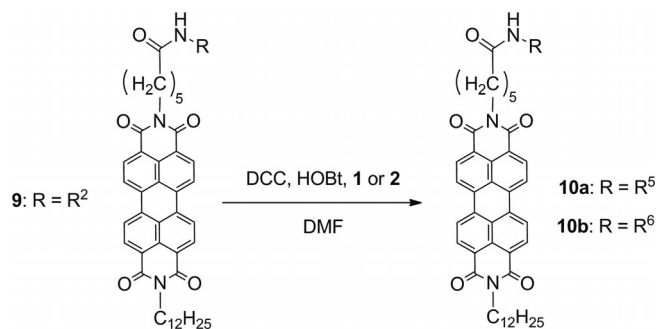
All synthesized perylenes are soluble in water. However, whereas highly charged PDIs **8a** and **8b** could be only dissolved in pure water, all other compounds are also partly soluble in methanol and DMF or in mixtures thereof with water.

Figure 3 displays the absorption and fluorescence spectra of PDIs **7b**, **8b**, and **10b** in water. The spectra of the analogues with the shorter 1-(3-aminopropyl)-4-(*tert*-butyl)pyridinium group (for **7a**, **8a** and **10a**) are qualitatively comparable (see Supporting Information). All PDIs carrying the second-generation dendrons show absorption bands at 467, 498, and 533 nm that are characteristic for non-aggregated PDIs. The observed bands can be assigned to the vibronic fine structures (0  $\rightarrow$  2, 0  $\rightarrow$  1, 0  $\rightarrow$  0) of the S<sub>0</sub> to S<sub>1</sub> transition of perylene.<sup>[13]</sup> The intensities of these bands follow the order 0  $\rightarrow$  2 < 0  $\rightarrow$  1 < 0  $\rightarrow$  0 for **8b** and **10b**. However, for **7b** we observed the same bands but in contrast to the aforementioned in a different intensity order. The bands for 0  $\rightarrow$  1 and 0  $\rightarrow$  2 are enhanced against the 0  $\rightarrow$  0 band. The Frank–Condon factors now favor the higher (0  $\rightarrow$  1) excited vibronic state, which indicates the formation of  $\pi$ – $\pi$  stacking towards H-type aggregates.<sup>[9,14,15]</sup>

The fluorescence spectra show emission bands at 547, 588, and 630 nm. The formation of H-aggregates can also be estimated from a comparison of the fluorescence quantum yield ( $\Phi_F$ ) of all compounds. Calculation of  $\Phi_F$  results in values between 0.63 and 0.79 for the second-generation systems (for **8a**, **8b**, **10a**, and **10b**), whereas the fluorescence of first-generation analogues **7a** and **7b** is clearly quenched. Here, low  $\Phi_F$  values of 0.07 and 0.11 evidence a radiation-free decay from the excited state due to the close proximity of aggregated molecules. Concentration-dependent UV/Vis absorption and fluorescence spectra of 10<sup>-3</sup> to 10<sup>-8</sup> mol L<sup>-1</sup> indicated no change in the aggregation behavior even at very low concentration levels.

To gain more information about the self-organization behavior, we analyzed the interaction of aggregated PDI **7b** with three different (standard) detergents: nonionic [Brij58<sup>®</sup>, critical micelle concentration (cmc) =



Scheme 2. Synthesis of symmetrically substituted cationic perylenebisimides **7a**, **7b**, **8a**, and **8b**.Scheme 3. Synthesis of unsymmetrically substituted cationic perylenes **10a** and **10b**.

$6 \times 10^{-6} \text{ mol L}^{-1}$ ], a cationic CTAB (hexadecyltrimethylammonium bromide,  $\text{cmc} = 1 \times 10^{-3} \text{ mol L}^{-1}$ ), and anionic SDS (sodium dodecyl sulfate,  $\text{cmc} =$

$8.2 \times 10^{-3} \text{ mol L}^{-1}$ ). Thereby, the concentration of **7b** was held constant at  $10^{-5} \text{ mmol mL}^{-1}$ , while the concentration of the detergents was increased from  $10^{-5}$  up to  $10^{-2} \text{ mol L}^{-1}$ . The absorption spectra of the aqueous solutions of the PDI with differing spectra of the three detergents are shown in Figure 4. The spectrum of aggregated **7b** did not change at any concentration of Brij58® (Figure 4, top). Again, with increasing concentrations of CTAB the spectrum remained unchanged for low concentrations of the detergent. The intensities of the absorption bands ( $0 \rightarrow 0 > 0 \rightarrow 1$ ) changed abruptly only above the cmc of CTAB, and it was at this point that the monomer spectrum of non-aggregated PDI appeared (Figure 4, middle). Finally, the spectra of PDI with the detergent were altered with the initial addition of SDS (Figure 4, bottom). From these results, we conclude that the nonionic Brij58® did not interact with the positively charged PDI,



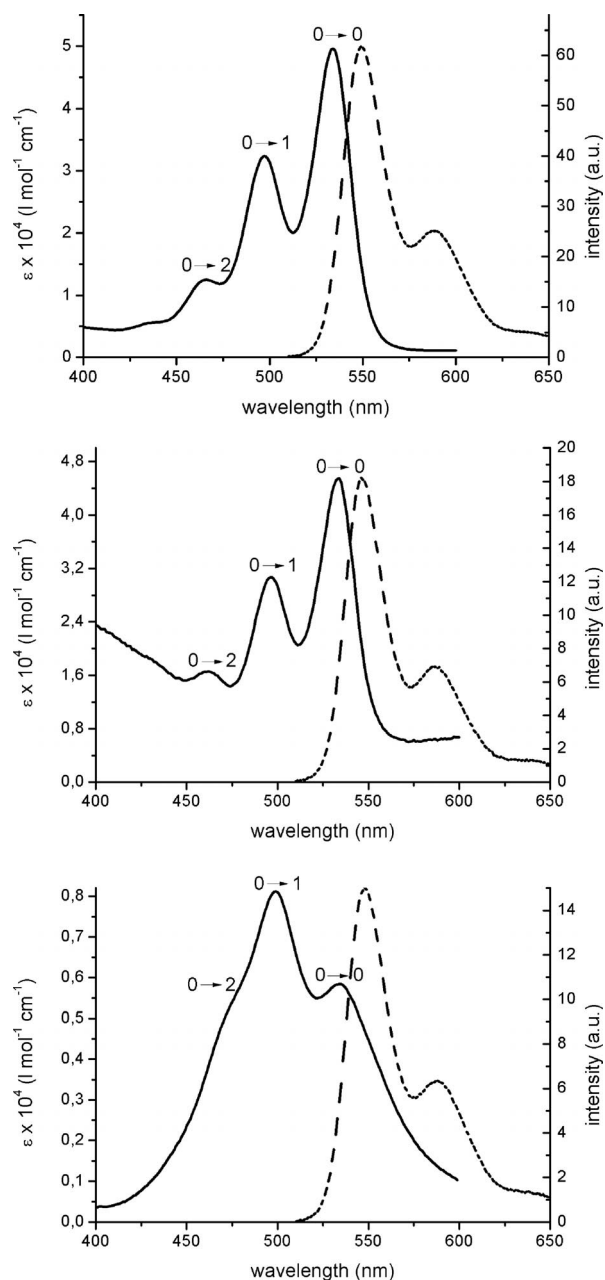


Figure 3. Absorption (solid lines) and fluorescence spectra (dashed lines) of **8b** (top), **10b** (middle), and **7b** (bottom) with a concentration of  $10^{-5}$  mmol mL $^{-1}$  in water.

whereas a sharp alteration of the absorption indicates complete dissolution of the PDI molecules within the CTAB and SDS micelles.

Furthermore, the aggregation behavior was investigated by pulsed-gradient spin-echo (PGSE, DOSY) NMR spectroscopy. Spectra were measured for all six compounds at a concentration of  $10^{-6}$  mol L $^{-1}$  in water. The NMR spectra obtained from the DOSY experiments were put together in a stacked plot with increasing gradient strength  $G$ . This leads to an exponential decay of the signals with increasing  $G$ . Plotting  $\ln(I/I_0)$  vs.  $G^2$  yields a straight line, whose slope is proportional to the diffusion constant  $D$ . The calculated results for  $D$  are listed in Table 1.

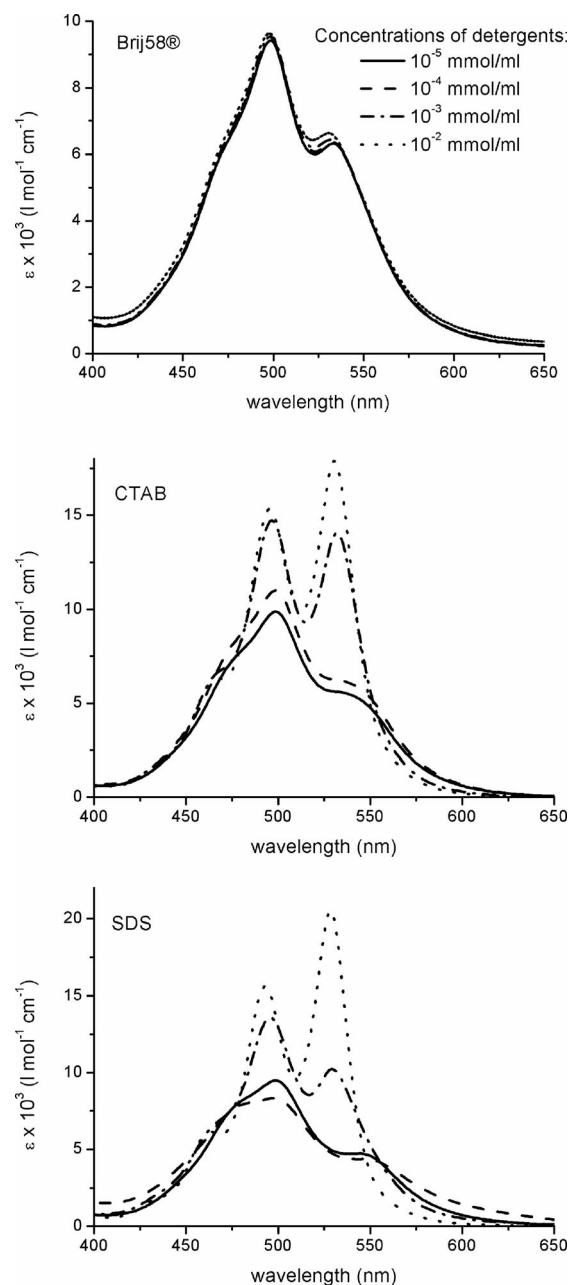


Figure 4. Absorption spectra of **7b** in the presence of different concentrations of detergents Brij58® (top), CTAB (middle), and SDS (bottom). For compound **7a**, see the Supporting Information.

Table 1. DOSY NMR results for cationic perylene compounds at 303 K in water with a concentration of  $10^{-6}$  mol L $^{-1}$ .

Compound	Charges	Propyl/pentyl-pyridinium	$D$ (m $^2$ s $^{-1}$ )
<b>7a</b>	6	propyl	$2.51 \times 10^{-10}$
<b>10a</b>	9	propyl	$1.07 \times 10^{-9}$
<b>8a</b>	18	propyl	$1.04 \times 10^{-9}$
<b>7b</b>	6	pentyl	$2.08 \times 10^{-10}$
<b>10b</b>	9	pentyl	$9.08 \times 10^{-10}$
<b>8b</b>	18	pentyl	$7.93 \times 10^{-10}$

Comparing the resulting  $D$  values allows for an evaluation of the size and the aggregation behavior of these cationic PDIs. It can be shown that the pentylpyridinium cations (i.e., **7b**, **8b**, and **10b**) have smaller diffusion constants than their analogs with propylpyridinium head groups (i.e., **7a**, **8a**, and **10a**). Moreover, the determined  $D$  values of the compounds with first-generation dendrons **7a** and **7b** are more than four times smaller than those for the PDIs with second-generation dendrons **8a** and **8b**. The tremendous reduction in the molecular mobility clearly refers to  $\pi$ - $\pi$  stacking aggregation. For those PDIs bearing larger dendrons, steric hindrance hampers the perylene stacking and thus aggregation.

Applying the calculated  $D$  value to the Stokes–Einstein equation, the hydrodynamic radius  $R_0$  could be calculated for those compounds (PDIs bearing second-generation dendrons) where a spherical geometry can be assumed. The value of  $R_0$  was determined to be in the range of 2.5–3.5 nm. The  $R_0$  values of the aggregating species were not calculated due to their non-spherical geometry (see next paragraph).

To investigate structural aspects of the aggregating first-generation dendron-substituted bola-amphiphilic PDIs **7a** and **7b** in water, cryogenic electron microscopy (cryo-TEM) was carried out at different perylene concentrations. Micrographs of 1-mM solutions of **7a** revealed a dense packing of elongated entities of varying length and uniform diameter, which create a lamellar pattern of constant periodicity in different in-plane rotational orientations. Figure 5 (left) shows an illustrative example of this behavior at an even lower concentration of 0.2 mM.

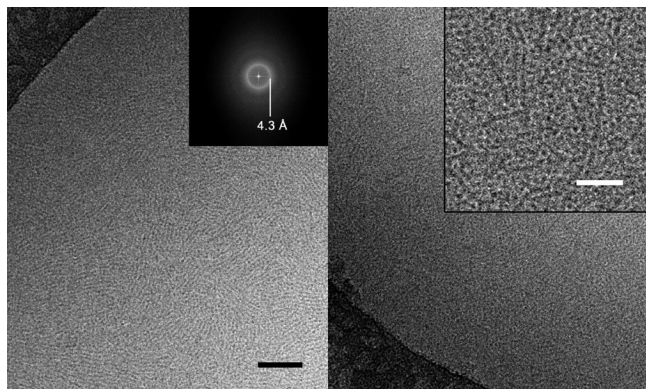


Figure 5. Cryo-TEM images of **7a** in water. Left: The 0.2 mM sample shows lamellar-like periodic patterns. FTs of these patterns (inset) show diffraction rings corresponding to a mean distance in real space of about  $4.3 \pm 0.5$  nm. Right: Only in 0.05 mM solutions can individual threads and spherical particles (inset) be detected, though the aggregate density is always very high at the concentration used. Bar corresponds to 50 nm; inset bar (right) corresponds to 25 nm.

Fourier transforms (FTs) of the ordered areas provide diffraction rings indicating a constant spacing in real space of  $4.3 \pm 0.5$  nm for **7a** and of  $4.5 \pm 0.5$  nm for **7b**. These values can roughly be attributed to the diameters of the mostly thread-like aggregates, as the uniform reciprocal pattern oc-

curs because of the dense side-by-side packing of the assemblies. By lowering the concentration further to 0.05 mM, the aggregate packing density decreases, and individual thread-like micelles of up to several tens of nanometers in length and diameters in the same order of magnitude derived from the more concentrated solutions become evident (Figure 5, right). Moreover, even individual spherical micellar assemblies can be detected, which show similar radii as observed with the threads.

Determination of the dimensions of small ( $< 5$ – $7$  nm) micellar assemblies from individual aggregates is always somewhat inaccurate due to the uncertainty of the exact edge of the structures. Owing to the periodicity of the structures found in the more concentrated solutions ( $> 0.2$  mM), values are more reliable due to the inherent statistics.

From these structural investigations, it seems reasonable that  $\pi$ - $\pi$  stacking of the perylene cores accounts for the formation of the thread-like micelles. This packing model is consistent with the formation of H-aggregates indicated by UV and fluorescence spectroscopy (s.a.). Nonetheless, it remains open to what extent linear stacking is realized in spherical particles as was detected in the 0.05 mM solutions.

## Conclusions

We have presented the first synthesis of polycationic PDIs **7**, **8**, and **10** with 6, 18, and 9 positive charges, respectively. The pH-independent positive charges stem from peripheral pyridinium groups of terminating Newkome dendrons bound in the imide positions of the PDIs. These cationic architectures are very soluble in water. Their aggregation properties have been determined by optical and PGSE NMR spectroscopy and have been visualized by cryo-TEM measurements. PDIs **7a** and **7b** bearing smaller first-generation dendrons exhibit pronounced aggregation behavior due to  $\pi$ - $\pi$  stacking interactions. The investigation of these and other polycationic PDIs with respect to exfoliation of carbon nanotubes and graphene as well as their supramolecular interactions with related polyanionic PDIs is currently underway in our laboratory.

## Experimental Section

**Materials and Methods:** 5-Bromopentylamine hydrobromide was synthesized by the method of Brown and Schmid.<sup>[18]</sup> Precursor molecules **5**, **6**, and **9** were prepared according to literature procedures.<sup>[9a]</sup> HPLC-grade DMF was used. Additional solvents were freshly distilled. Other chemicals were purchased from Acros Organics or Aldrich and used as received. NMR spectra were recorded with a Bruker Avance 300 (300 MHz), Avance 400 (400 MHz), and a Jeol EX 400 (400 MHz). Chemical shifts are given in ppm at room temperature. IR spectra were recorded with a Bruker Tensor 27 (ATR) spectrometer. A Varian Cary 5000 was used for UV/Vis measurements. Fluorescence spectra were obtained from a Shimadzu RF-5301 PC. Fluorescence quantum yields ( $\Phi_F$ ) were determined in water against a cross-reference system with rhodamine B and fluorescein. Mass spectrometry was car-

ried out with a Shimadzu AXIMA Confidence (MALDI-TOF, matrices: sinapinic acid SIN, 2,5-dihydroxybenzoic acid DHB) and a Bruker Esquire 6000 (ESI-QIT).

**<sup>1</sup>H Pulsed-Gradient Spin-Echo PGSE (DOSY) NMR:** Experiments were obtained with a Jeol Alpha500 spectrometer with a sample concentration of 10<sup>-6</sup> mol L<sup>-1</sup> in water. Spectra were recorded with a maximum gradient strength of 180 G cm<sup>-1</sup> and a diffusion delay of 100 ms at a temperature of 303 K.

**Cryo-Electron Microscopy:** All samples were prepared from 1.0 to 0.02 mM aqueous solutions of the corresponding compounds according to our standard protocol. By this, carbon-covered porous (1-μm hole diameter) supporting films on 200 mesh copper grids [R1/4 batch of Quantifoil (MicroTools GmbH, Jena, Germany)] were hydrophilized by a 60-s plasma treatment with a BALTEC MED 020 device at 8 W before use. Then, 5 μL droplets of the sample solutions were applied and the excess amount of fluid was removed with a filter paper until an ultrathin layer spanning the holes of the carbon film was obtained. Immediately thereafter, the samples were vitrified by propelling the grids with a guillotine-like plunging device into liquid ethane at its freezing point (90 K). The specimens were stored under liquid nitrogen until use. Cryo-microscopy was carried out at a sample temperature of 94 K with a Philips CM12 transmission electron microscope (FEI, Oregon) employing a Gatan (Gatan, Inc., California) cryoholder and stage (model 626) and using the microscopes low-dose protocol at a primary magnification of ×58,300, an accelerating voltage of 100 kV (LaB6-illumination), and the defocus set to -1.2 μm in all cases.

**1-(3-Aminopropyl)-4-(tert-butyl)pyridinium Bromide (1):** A mixture of 3-bromopropylamine hydrobromide (5.00 g, 22.8 mmol) was suspended in 4-*tert*-butylpyridine (6.17 g, 45.6 mmol) and heated at 100 °C for 3 h. First, the solution became clear, then it became more viscous, and finally, it solidified in a glass-like manner. The resulting solid was dissolved in water (50 mL) and extracted with ethyl ether (2 × 50 mL). Solid sodium hydroxide was added slowly to the aqueous mixture until pH 9.4 was reached. The solvent was evaporated under reduced pressure leaving a white solid. After extraction of the solid with acetonitrile (3 × 50 mL), the solvent of the combined extracts was distilled off at reduced pressure to afford a viscous hygroscopic oil that was dried in vacuo to yield **1** (5.98 g, 21.9 mmol, 96%). <sup>1</sup>H NMR (400 MHz, [D<sub>6</sub>]DMSO, r.t.): δ = 1.35 (s, 9 H, CH<sub>3</sub>), 2.01 (m, 2 H, CH<sub>2</sub>), 2.58 (t, *J* = 6.7 Hz, 2 H, CH<sub>2</sub>), 4.68 (t, *J* = 7.2 Hz, 2 H, CH<sub>2</sub>), 8.19 (d, *J* = 7.1 Hz, 2 H, CH), 9.07 ppm (d, *J* = 7.1 Hz, 2 H, CH). <sup>13</sup>C NMR (100.5 MHz, [D<sub>6</sub>]DMSO, r.t.): δ = 29.6 (CH<sub>3</sub>), 30.2 (CH<sub>2</sub>), 33.3 (C), 36.3, 57.0 (CH<sub>2</sub>), 125.2, 144.2 (CH), 169.9 ppm (C). IR (ATR): ν̄ = 665, 688, 762, 851, 929, 1027, 1054, 1114, 1187, 1228, 1275, 1321, 1273, 1463, 1514, 1562, 1598, 1638, 2033, 2360, 2868, 2963, 3008, 3409 cm<sup>-1</sup>. MS (MALDI-TOF, SIN): *m/z* = 193 [M - Br]<sup>+</sup>.

**1-(3-Aminopentyl)-4-(tert-butyl)pyridinium Bromide (2):** A mixture of 5-bromopentylamine hydrobromide (5.00 g, 20.2 mmol) was suspended in 4-*tert*-butylpyridine (5.46 g, 40.4 mmol) and heated at 100 °C for 3 h. Further preparation was the same as that outlined above for **1**. Product **2** was obtained as a hygroscopic solid (5.78 g, 19.2 mmol, 95%). <sup>1</sup>H NMR (400 MHz, [D<sub>4</sub>]methanol, r.t.): δ = 1.43 (m, 2 H, CH<sub>2</sub>), 1.46 (s, 9 H, CH<sub>3</sub>), 1.55 (m, 2 H, CH<sub>2</sub>), 2.04 (m, 2 H, CH<sub>2</sub>), 2.65 (t, *J* = 6.9 Hz, 2 H, CH<sub>2</sub>), 4.62 (t, *J* = 7.3 Hz, 2 H, CH<sub>2</sub>), 8.15 (d, *J* = 5.3 Hz, 2 H, CH), 8.91 ppm (d, *J* = 7.1 Hz, 2 H, CH). <sup>13</sup>C NMR (100.5 MHz, [D<sub>4</sub>]methanol, r.t.): δ = 24.6 (CH<sub>3</sub>), 30.4 (CH<sub>2</sub>), 32.3 (C), 33.2, 37.7, 42.3, 62.1 (CH<sub>2</sub>), 126.7, 145.4 (CH), 172.7 ppm (C). IR (ATR): ν̄ = 665, 687, 732, 750, 851, 864, 914, 977, 1030, 1077, 1116, 1187, 1211, 1235, 1276, 1352, 1365, 1375, 1463, 1516, 1561, 1601, 1637, 1981, 2163, 2860,

2933, 3083, 3264, 3350 cm<sup>-1</sup>. MS (MALDI-TOF, DHB): *m/z* = 221 [M - Br]<sup>+</sup>.

**6-Fold Charged *N,N'*-Substituted Perylene-3,4,9,10-tetracarboxdiimide (7a):** In a round-bottomed flask, **5** (50 mg, 0.046 mmol) and HOBt (75 mg, 0.557 mmol) were dissolved in DMF (3 mL) under a N<sub>2</sub> atmosphere and cooled to 0 °C. A solution of DCC (115 mg, 0.557 mmol) in DMF (1 mL) was added, and stirring was continued for 15 min at 0 °C. Compound **1** (152 mg, 0.557 mmol) in DMF (1 mL) was added dropwise, and the mixture was stirred for 48 h at room temperature. After filtering, the residue was dissolved in methanol/water (1:1). The solvent was removed under reduced pressure, and a red solid was precipitated by the addition of a large quantity of acetone. The suspension was centrifuged, and the precipitation procedure was repeated two more times. After drying in vacuo, **7a** was obtained as a dark red solid (69 mg, 0.026 mmol, 57%). <sup>1</sup>H NMR (300 MHz, [D<sub>4</sub>]methanol/D<sub>2</sub>O, r.t.): δ = 1.45 (s, 54 H, CH<sub>3</sub>), 1.66 (m, 12 H, CH<sub>2</sub>), 2.08 (m, 12 H, CH<sub>2</sub>), 2.30 (m, 28 H, CH<sub>2</sub>), 3.33 (m, 12 H, CH<sub>2</sub>), 4.74 (m, 12 H, CH<sub>2</sub>), 8.20 (d, *J* = 6.2 Hz, 12 H, CH), 9.06 ppm (d, *J* = 6.2 Hz, 12 H, CH). <sup>13</sup>C NMR (100.5 MHz, D<sub>2</sub>O, r.t.): δ = 25.8, 26.7, 27.4 (CH<sub>2</sub>), 29.5 (CH<sub>3</sub>), 30.8 (C), 31.3, 32.1, 36.4, 37.0, 41.0, 58.6 (CH<sub>2</sub>), 121.3, 124.1 (C), 125.3 (CH), 125.8, 127.5, 131.0, 133.2 (C), 149.9 (CH), 164.0 (CON), 172.3 (C), 176.6, 183.3 ppm (COOR). IR (ATR): ν̄ = 627, 746, 794, 809, 850, 971, 1115, 1160, 1184, 1249, 1344, 1402, 1440, 1460, 1541, 1594, 1641, 1691, 1980, 2049, 2163, 2870, 2961, 3045, 3247 cm<sup>-1</sup>. UV/Vis (H<sub>2</sub>O): λ (log ε) = 499 (4.44), 533 (2.90) nm; fluorescence (H<sub>2</sub>O, λ<sub>exc.</sub> = 499 nm): λ = 548, 588, 640 nm; Φ<sub>F</sub> = 0.07 (aggregated species). MS (ESI-QIT, acetonitrile): *m/z* = 441.9 [M - 5Br]<sup>5+</sup>, 572.4 [M - 4Br]<sup>4+</sup>, 789.5 [M - 3Br]<sup>3+</sup>, 1224.1 [M - 2Br]<sup>2+</sup>.

**6-Fold Charged *N,N'*-Substituted Perylene-3,4,9,10-tetracarboxdiimide (7b):** A procedure similar to that outlined for **7a** was used but with amine **2** instead of **1**. Dark red solid. Yield: 76 mg (59%). <sup>1</sup>H NMR (300 MHz, D<sub>2</sub>O, r.t.): δ = 1.32 (m, 54 H, CH<sub>3</sub>), 1.47 (m, 24 H, CH<sub>2</sub>), 1.67 (m, 12 H, CH<sub>2</sub>), 1.92 (m, 6 H, CH<sub>2</sub>), 2.00 (m, 12 H, CH<sub>2</sub>), 2.13 (m, 14 H, CH<sub>2</sub>), 3.07 (m, 12 H, CH<sub>2</sub>), 4.49 (t, *J* = 7.1 Hz, 12 H, CH<sub>2</sub>), 8.01 (m, 12 H, CH), 8.68 ppm (m, 12 H, CH). <sup>13</sup>C NMR (100.5 MHz, D<sub>2</sub>O, r.t.): δ = 23.1, 25.6, 26.6, 28.3 (CH<sub>2</sub>), 29.5 (CH<sub>3</sub>), 29.7 (C), 30.5, 30.7, 31.0, 36.5, 36.9, 39.6, 58.3, 61.1 (CH<sub>2</sub>), 120.0–135.0 (broad signals, C), 125.3 (CH), 144.0 (CH), 162.8 (CON), 172.0 (C), 175.9, 181.3 ppm (COOR). IR (ATR): ν̄ = 615, 629, 746, 794, 809, 850, 930, 1026, 1114, 1184, 1250, 1344, 1402, 1440, 1459, 1541, 1594, 1640, 1691, 2048, 2163, 2864, 2934, 3046, 3248 cm<sup>-1</sup>. UV/Vis (H<sub>2</sub>O): λ (log ε) = 498 (4.01), 544 (3.70) nm; fluorescence (H<sub>2</sub>O): λ = 548, 588, 630 nm; Φ<sub>F</sub> = 0.11 (aggregated species). MS (ESI-TOF, methanol): *m/z* = 382.9 [M - 6Br]<sup>6+</sup>, 475.4 [M - 5Br]<sup>5+</sup>, 614.4 [M - 4Br]<sup>4+</sup>, 845.9 [M - 3Br]<sup>3+</sup>, 1308.2 [M - 2Br]<sup>2+</sup>.

**18-Fold Charged *N,N'*-Substituted Perylene-3,4,9,10-tetracarboxdiimide (8a):** In a round-bottomed flask, **5** (150 mg, 0.06 mmol) and HOBt (291 mg, 2.16 mmol) were dissolved in DMF (3 mL) under a N<sub>2</sub> atmosphere and cooled to 0 °C. A solution of DCC (444 mg, 2.16 mmol) in DMF (1 mL) was added, and stirring was continued for 15 min at 0 °C. Compound **1** (590 mg, 2.16 mmol) in DMF (1 mL) was added dropwise, and the mixture was stirred for 48 h at room temperature. After filtering, the residue was dissolved in water. The solvent was removed under reduced pressure, and a red solid was precipitated by the addition of a large quantity of acetone. The suspension was centrifuged, and the precipitation procedure was repeated two more times. After drying in vacuo, **8a** was obtained as a dark red solid (120 mg, 0.017 mmol, 43%). <sup>1</sup>H NMR (300 MHz, D<sub>2</sub>O, r.t.): δ = 1.28 (m, 166 H, CH<sub>3</sub> + CH<sub>2</sub>), 1.85 (m,



56 H, CH<sub>2</sub>), 2.10 (m, 52 H, CH<sub>2</sub>), 2.32 (m, 36 H, CH<sub>2</sub>), 3.05 (m, 36 H, CH<sub>2</sub>), 4.59 (m, 36 H, CH<sub>2</sub>), 8.00 (m, 36 H, CH), 8.68 ppm (m, 36 H, CH). <sup>13</sup>C NMR (100.5 MHz, D<sub>2</sub>O, r.t.):  $\delta$  = 23.6, 24.0, 25.9, 27.5 (CH<sub>2</sub>), 29.4 (CH<sub>3</sub>), 30.2, 36.3 (CH<sub>2</sub>), 36.8 (C), 37.1, 45.0, 57.8, 58.0 (CH<sub>2</sub>), 120.8, 123.6 (C), 126.0 (CH), 126.7, 127.7, 130.3, 132.2 (C) 143.9 (CH), 165.3 (CON), 172.4 (C), 175.3, 176.2, 180.2 ppm (COOR). IR (ATR):  $\tilde{\nu}$  = 628, 745, 794, 809, 850, 900, 1101, 1191, 1249, 1343, 1384, 1442, 1542, 1594, 1643, 1691, 1980, 2163, 2542, 2939, 3053, 3273 cm<sup>-1</sup>. UV/Vis (H<sub>2</sub>O):  $\lambda$  (log  $\epsilon$ ) = 467 (4.40), 497 (4.48), 535 (4.61) nm; fluorescence (H<sub>2</sub>O):  $\lambda$  = 548, 588 nm;  $\Phi_F$  = 0.63. MS (ESI-QIT, methanol):  $m/z$  136.2 [C<sub>9</sub>H<sub>13</sub>NH]<sup>+</sup>, 193.1 [H<sub>2</sub>N(CH<sub>2</sub>)<sub>3</sub>NC<sub>9</sub>H<sub>13</sub>]<sup>+</sup>. MS<sup>2</sup>-CID (He):  $m/z$  = 193.1  $\rightarrow$  136.1,  $m/z$  = 58.6.

**18-Fold Charged *N,N'*-Substituted Perylene-3,4,9,10-tetracarboxdiimide (8b):** A procedure similar to that outlined for **8a** was used but with amine **2** instead of **1**. Dark red solid. Yield: 121 mg, (39%). <sup>1</sup>H NMR (300 MHz, D<sub>2</sub>O, r.t.):  $\delta$  = 1.28 (m, 166 H, CH<sub>3</sub> + CH<sub>2</sub>), 1.32 (m, 36 H, CH<sub>2</sub>), 1.63 (m, 36 H, CH<sub>2</sub>), 1.81 (m, 52 H, CH<sub>2</sub>), 1.93 (m, 36 H, CH<sub>2</sub>), 2.05 (m, 52 H, CH<sub>2</sub>), 2.93 (t,  $J$  = 9.4 Hz, 36 H, CH<sub>2</sub>), 4.44 (t,  $J$  = 7.3 Hz, 36 H, CH<sub>2</sub>), 7.93 (d,  $J$  = 6.7 Hz, 36 H, CH), 8.59 ppm (d,  $J$  = 6.7 Hz, 36 H, CH). <sup>13</sup>C NMR (100.5 MHz, D<sub>2</sub>O, r.t.):  $\delta$  = 22.7, 23.7, 25.8, 26.5, 27.5 (CH<sub>2</sub>), 29.5 (CH<sub>3</sub>), 30.3, 30.6, 31.1, 36.3 (CH<sub>2</sub>), 36.8 (C), 39.5, 58.3, 60.8 (CH<sub>2</sub>), 121.7, 124.4, 125.3 (C), 125.8 (CH), 127.5, 131.5, 133.7 (C), 143.8 (CH), 164.1 (CON), 172.0 (C), 175.4, 176.5, 181.7 ppm (COOR). IR (ATR):  $\tilde{\nu}$  = 630, 746, 793, 809, 850, 901, 1102, 1187, 1275, 1344, 1384, 1456, 1542, 1593, 1642, 1691, 1980, 2163, 2559, 2939, 3052, 3272 cm<sup>-1</sup>. UV/Vis (H<sub>2</sub>O):  $\lambda$  (log  $\epsilon$ ) = 466 (4.05), 499 (4.49), 534 (4.61) nm; fluorescence (H<sub>2</sub>O):  $\lambda$  = 550, 589 nm;  $\Phi_F$  = 0.79. MS (ESI-QIT, methanol):  $m/z$  = 136.2 [C<sub>9</sub>H<sub>13</sub>NH]<sup>+</sup>, 212.1 [H<sub>2</sub>N(CH<sub>2</sub>)<sub>5</sub>NC<sub>9</sub>H<sub>13</sub>]<sup>+</sup>. MS<sup>2</sup>-CID (He):  $m/z$  = 221.1  $\rightarrow$  136.0,  $m/z$  = 86.3.

**9-Fold Charged *N,N'*-Substituted Perylene-3,4,9,10-tetracarboxdiimide (10a):** In a round-bottomed flask, **9** (150 mg, 0.093 mmol) and HOBt (225 mg, 1.674 mmol) were dissolved in DMF (3 mL) under a N<sub>2</sub> atmosphere and cooled to 0 °C. A solution of DCC (345 mg, 1.674 mmol) in DMF (1 mL) was added, and stirring was continued for 15 min at 0 °C. Compound **1** (456 mg, 1.674 mmol) in DMF (1 mL) was added dropwise, and the mixture was stirred for 48 h at room temperature. DMF was distilled off under reduced pressure, and the residue was dissolved with a small amount of methanol/water (2:1). A red solid was precipitated by the addition of a large quantity of acetone. The suspension was centrifuged, and the precipitation procedure was repeated two more times. After drying in vacuo, **10a** was obtained as a dark red solid (256 mg, 0.066 mmol, 71%). <sup>1</sup>H NMR (300 MHz, D<sub>2</sub>O, r.t.):  $\delta$  = 1.08 (m, 17 H, CH<sub>2</sub> + CH<sub>3</sub>), 1.31 (m, 89 H, CH<sub>3</sub> + CH<sub>2</sub>), 1.88 (m, 30 H, CH<sub>2</sub>), 2.14 (m, 44 H, CH<sub>2</sub>), 3.17 (m, 18 H, CH<sub>2</sub>), 4.52 (m, 18 H, CH<sub>2</sub>), 8.05 (m, 18 H, CH), 8.77 ppm (m, 18 H, CH). <sup>13</sup>C NMR (100.5 MHz, D<sub>2</sub>O, r.t.):  $\delta$  = 14.5 (CH<sub>3</sub>), 23.3, 28.7 (CH<sub>2</sub>), 29.8 (CH<sub>3</sub>), 30.5, 32.7, 36.4 36.5, 52.6 58.1, 58.7 (CH<sub>2</sub>), 118.0–135.0 (br, C), 144.2 (CH), 162.8 (CON), 171.8 (C), 172.2, 175.8 ppm (COOR). IR (ATR):  $\tilde{\nu}$  = 746, 810, 849, 930, 1114, 1186, 1248, 1343, 1402, 1460, 1537, 1594, 1639, 1691, 2049, 2163, 2361, 2871, 2928, 3046, 3248 cm<sup>-1</sup>. UV/Vis (H<sub>2</sub>O):  $\lambda$  (log  $\epsilon$ ) = 466 (4.13), 497 (4.51), 534 (4.68) nm; fluorescence (H<sub>2</sub>O):  $\lambda$  = 547, 586 nm;  $\Phi_F$  = 0.68. MS (ESI-QIT, methanol):  $m/z$  = 475.2 [M – 7Br]<sup>7+</sup>, 567.8 [M – 6Br]<sup>6+</sup>, 697.5 [M – 5Br]<sup>5+</sup>, 891.6 [M – 4Br]<sup>4+</sup>, 1215.2 [M – 3Br]<sup>3+</sup>.

**9-Fold Charged *N,N'*-Substituted Perylene-3,4,9,10-tetracarboxdiimide (10b):** A procedure similar to that outlined for **10a** was used but with amine **2** instead of **1**. Dark red solid. Yield 236 mg (61%). <sup>1</sup>H NMR (300 MHz, D<sub>2</sub>O, r.t.):  $\delta$  = 1.05 (m, 17 H, CH<sub>2</sub> + CH<sub>3</sub>), 1.33 (m, 89 H, CH<sub>3</sub> + CH<sub>2</sub>), 1.95 (m, 74 H, CH<sub>2</sub>), 3.05 (m, 18 H,

CH<sub>2</sub>), 4.49 (m, 18 H, CH<sub>2</sub>), 8.05 (m, 18 H, CH), 8.75 ppm (m, 18 H, CH). <sup>13</sup>C NMR (100.5 MHz, D<sub>2</sub>O, r.t.):  $\delta$  = 14.6 (CH<sub>3</sub>), 23.3, 25.9, 26.7, 28.4, 29.7 (CH<sub>2</sub>), 29.9 (CH<sub>3</sub>), 30.6, 32.7 (CH<sub>2</sub>), 36.6 (C), 39.4, 58.3, 61.1 (CH<sub>2</sub>), 118.1–132.6 (br, C), 125.9, 144.1 (CH), 163.1 (CON), 171.7 (C), 175.2, 180.8, 182.6 ppm (COOR). IR (ATR):  $\tilde{\nu}$  = 627, 746, 794, 810, 850, 930, 1027, 1114, 1187, 1275, 1344, 1402, 1459, 1539, 1594, 1639, 1692, 1980, 2042, 2163, 2861, 2929, 3048, 3251 cm<sup>-1</sup>. UV/Vis (H<sub>2</sub>O):  $\lambda$  (log  $\epsilon$ ) = 466 (4.16), 496 (4.42), 533 (4.74) nm; fluorescence (H<sub>2</sub>O):  $\lambda$  = 547, 587 nm;  $\Phi_F$  = 0.69. MS (ESI-QIT, acetonitrile):  $m/z$  = 609.8 [M – 6Br]<sup>6+</sup>, 747.9 [M – 5Br]<sup>5+</sup>, 954.8 [M – 4Br]<sup>4+</sup>, 1299.7 [M – 3Br]<sup>3+</sup>, 1989.2 [M – 2Br]<sup>2+</sup>.

**Supporting Information** (see footnote on the first page of this article): <sup>1</sup>H NMR, <sup>13</sup>C NMR, and mass spectra of all compounds; additional absorption and fluorescence spectra.

## Acknowledgments

We thank the Deutsche Forschungsgemeinschaft (DFG) and the European Research Council (ERC) (Advanced Grant “Graphenochem”) for financial support.

- [1] T. E. Kaiser, H. Wang, V. Stepanenko, F. Würthner, *Angew. Chem.* **2007**, *119*, 5637–5640; *Angew. Chem. Int. Ed.* **2007**, *46*, 5541–5544; X. Zhang, Z. Chen, F. Würthner, *J. Am. Chem. Soc.* **2007**, *129*, 4886–4887; Z. Chen, V. Stepanenko, V. Dehm, P. Prins, L. D. A. Siebbeles, J. Seibt, P. Marquetand, V. Engel, F. Würthner, *Chem. Eur. J.* **2007**, *13*, 436–449; Z. Chen, M. G. Debije, T. Debaerdemaeker, P. Osswald, F. Würthner, *ChemPhysChem* **2004**, *5*, 137–140.
- [2] W. Zhou, Y. Wen, L. Ma, Y. Liu, X. Zhan, *Macromolecules* **2012**, *45*, 4115–4121.
- [3] C. Huang, S. Barlow, S. R. Marder, *J. Org. Chem.* **2011**, *76*, 2386–2407.
- [4] J. Qu, J. Zhang, A. C. Grimsdale, K. Müllen, F. Jaiser, X. Yang, D. Neher, *Macromolecules* **2004**, *37*, 8297–8306; X. Z. Jiang, Y. Q. Liu, S. G. Liu, W. F. Qiu, X. Q. Song, D. B. Zhu, *Synth. Met.* **1997**, *91*, 253–256.
- [5] J. Fortage, M. Séverac, C. Houarner-Rassin, Y. Pellegrin, E. Blart, F. Odobel, *J. Photochem. Photobiol. A: Chem.* **2008**, *197*, 156–169; L. Schmidt-Mende, A. Fechtenkötter, K. Müllen, E. Moons, R. H. Friend, J. D. MacKenzie, *Science* **2001**, *293*, 1119–1122; Y. Ooyama, Y. Harima, *Eur. J. Org. Chem.* **2009**, 2903–2934; C. Li, H. Wonneberger, *Adv. Mater.* **2012**, *24*, 613–636.
- [6] M. R. Hansen, T. Schnitzler, W. Pisula, R. Graf, K. Müllen, H. Spiess, *Angew. Chem.* **2009**, *121*, 4691–4695; *Angew. Chem. Int. Ed.* **2009**, *48*, 4621–4624; Y. Guan, Y. Zakrevskyy, J. Stumpe, M. Antonietti, C.-F. J. Charl, *Chem. Commun.* **2003**, 3, 1041–1044.
- [7] F. Nolde, W. Pisula, S. Müller, C. Kohl, K. Müllen, *Chem. Mater.* **2006**, *18*, 3715–3725; F. Würthner, *Pure Appl. Chem.* **2006**, *78*, 2341–2349.
- [8] S. Nakazono, S. Easwaramoorthi, D. Kim, H. Shinokubo, A. Osuka, *Org. Lett.* **2009**, *11*, 5426–5429; S. Nakazono, Y. Imazaki, H. Yoo, J. Yang, T. Sasamori, N. Tokitoh, T. Cedric, H. Kageyama, D. Kim, H. Shinokubo, A. Osuka, *Chem. Eur. J.* **2009**, *15*, 7530–7533.
- [9] a) C. D. Schmidt, C. Böttcher, A. Hirsch, *Eur. J. Org. Chem.* **2007**, *33*, 5497–5505; b) C. D. Schmidt, C. Böttcher, A. Hirsch, *Eur. J. Org. Chem.* **2009**, *31*, 5337–5349.
- [10] G. R. Newkome, Z. Yao, G. R. Baker, V. K. Gupta, *J. Org. Chem.* **1985**, *50*, 2003–2004; G. R. Newkome, H. J. Kim, C. N. Moorefield, H. Maddi, K.-S. Yoo, *Macromolecules* **2003**, *36*, 4345; G. R. Newkome, R. K. Behera, C. N. Moorefield, G. R.

- Baker, *J. Org. Chem.* **1991**, *56*, 7162–7167; M. Brettreich, A. Hirsch, *Synlett* **1998**, *12*, 1396–1398.
- [11] C. Backes, F. Hauke, A. Hirsch, *Adv. Mater.* **2011**, *23*, 2588–2601; C. Backes, C. D. Schmidt, K. Rosenlehner, F. Hauke, J. N. Coleman, A. Hirsch, *Adv. Mater.* **2010**, *22*, 788–802; C. Backes, F. Hauke, C. D. Schmidt, A. Hirsch, *Chem. Commun.* **2009**, *19*, 2643–2645.
- [12] Detailed mass spectra are shown in the Supporting Information.
- [13] A. E. Clark, C. Qin, A. D. Q. Li, *J. Am. Chem. Soc.* **2007**, *129*, 7586–7595.
- [14] S. Rehm, V. Stephanenko, X. Zhang, T. H. Rehm, F. Würthner, *Chem. Eur. J.* **2010**, *16*, 3372–3382.
- [15] B. Rybtchinski, L. E. Sinks, M. R. Wasielewski, *J. Am. Chem. Soc.* **2004**, *126*, 12268–12269.
- [16] G. D'Errico, D. Ciccarelli, O. Ortona, *J. Colloid Interface Sci.* **2005**, *286*, 747–754.
- [17] S. S. Berr, *J. Phys. Chem.* **1987**, *91*, 4760–4765.
- [18] R. F. Brown, G. H. Schmid, *J. Org. Chem.* **1962**, *27*, 1288–1294.

Received: August 6, 2012

Published Online: September 20, 2012